Fall 2024

Gems & Gemology

90th ANNIVERSARY

VOLUME LX

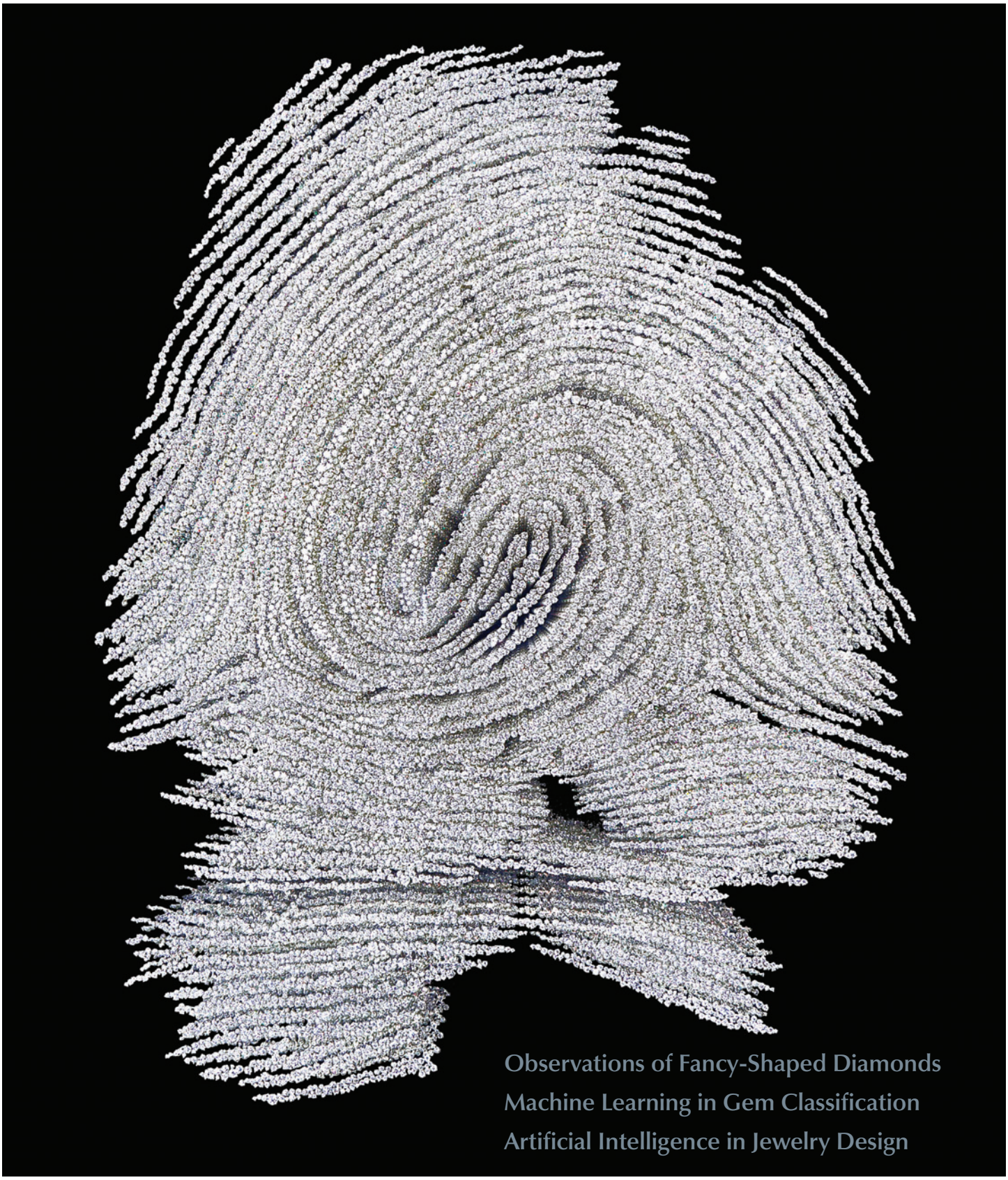

Observations of Fancy-Shaped Diamonds

Machine Learning in Gem Classification

Artificial Intelligence in Jewelry Design

The Quarterly Journal of the Gemological Institute of America

GEMS & GEMOLOGY®
Fall 2024
VOLUME 60, No. 3


p. 281


p. 335


p. 354

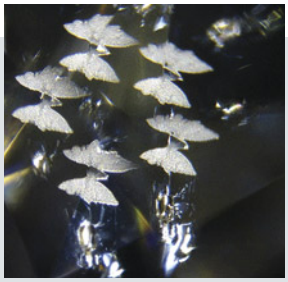
p. 383


p. 425


p. 440

Editorial

Feature Articles

Regular Features

GEMS & GEMOLOGY®

gia.edu/gems-gemology

Customer Service
(760) 603-4200
gandg@gia.edu

Subscriptions
Copies of the current issue may be purchased for $29.95 plus shipping. Subscriptions are $79.99 for one year (4 issues) in the U.S. and $99.99 elsewhere. Canadian subscribers should add GST. Discounts are available for renewals, group subscriptions, GIA alumni, and current GIA students. To purchase print subscriptions, visit store.gia.edu or contact Customer Service. For institutional rates, contact Customer Service.

Database Coverage
Gems & Gemology's impact factor is 1.6, according to the 2023 Journal Citation Reports by Clarivate Analytics (issued June 2024). *G&G* is abstracted in Thomson Reuters products (Current Contents: Physical, Chemical & Earth Sciences and Science Citation Index—Expanded, including the Web of Knowledge) and other databases. For a complete list of sources abstracting *G&G*, go to gia.edu/gems-gemology, and click on "Publication Information."

Manuscript Submissions
Gems & Gemology, a peer-reviewed journal, welcomes the submission of articles on all aspects of the field. Please see the Author Guidelines at gia.edu/gems-gemology or contact the Managing Editor. Letters on articles published in *G&G* are also welcome. Please note that Field Reports, Lab Notes, Gem News International, Micro-World, Colored Stones Unearthed, Diamond Reflections, Charts, and In the Spotlight are not peer-reviewed sections but do undergo technical and editorial review.

Gems & Gemology is published quarterly by the Gemological Institute of America, a nonprofit educational organization for the gem and jewelry industry.

Postmaster: Return undeliverable copies of *Gems & Gemology* to GIA, The Robert Mouawad Campus, 5345 Armada Drive, Carlsbad, CA 92008.

Our Canadian goods and service registration number is 126142892RT.

About the Cover

Designed by South African artist Johnathan Schultz, "Out of the Darkness" replicates Nelson Mandela's 1962 arrest warrant fingerprint using 9,225 near-colorless diamonds totaling 895.6 carats. The piece measures approximately 20 × 15 in. and is featured in this issue's Gem News International section. Photos by Carlton Davis (front cover) and Michael Craigwood (back cover); courtesy of Johnathan Schultz.

Printing is by L+L Printers, Carlsbad, CA.

GIA World Headquarters The Robert Mouawad Campus 5345 Armada Drive Carlsbad, CA 92008 USA

ISSN 0016-626X

Gems & Gemology at Ninety: A Look to the Future

In the previous issue of *Gems & Gemology*, Dr. James Shigley's editorial provided a thoughtful retrospective on the journal's evolution over its 90-year history. This editorial offers a glimpse into the future of gemology, as illuminated by three groundbreaking feature articles in this Fall 2024 issue.

In the lead article, GIA's Dr. Ilene Reinitz and fellow researchers present a paradigm-shifting approach to assessing the cut of oval-, pear-, and marquise-shaped diamonds. By combining rigorous research methods—including a large-scale international survey of observers over several years and the use of 3D modeling and virtual facet maps to analyze light behavior in diamonds—the authors lay the groundwork for implementing a useful cut grading system for fancy-shaped diamonds.

"From diamond cut evaluation to cutting-edge technological advancements, these articles highlight exciting transformations on the horizon."

Next, Dr. Matthew Hardman and GIA colleagues harness the power of machine learning algorithms to identify gemstones, determine their provenance, and detect treatments with remarkable accuracy and speed. Through meticulous testing and validation, they achieved error rates of less than 5% and a substantial reduction in indeterminate classifications. This pioneering work establishes machine learning as an effective tool to augment traditional microscopic, spectroscopic, and geochemical methods. As the global gemstone market navigates the complexities of treated and laboratory-grown products, this technology could be vital in maintaining the industry's integrity and consumer confidence.

Finally, GIA's Michael Magee explores the transformative potential of artificial intelligence in jewelry design. Magee systematically assesses five leading generative AI tools, demonstrating their ability to create stunningly realistic and diverse jewelry designs from simple text and image prompts. The article also addresses the emerging ethical, legal, and regulatory concerns surrounding the proliferation of AI-generated jewelry designs. But even as AI technology advances, the article reminds us that humans are still indispensable in conveying the stories of jewelry and gemstones.

From diamond cut evaluation to cutting-edge technological advancements, these articles highlight exciting transformations on the horizon. The use of machine learning and artificial intelligence in gemology will continue to advance and accelerate in the coming years. Deep mathematics is integral to GIA's work around revolutionizing the approach to fancy cut grading. As my longtime colleague Dr. Shigley noted in the Summer 2024 issue's editorial, advanced scientific techniques are now commonly used in gemological laboratories. He also wrote that sophisticated instruments will become more portable and accessible. But advanced technology alone won't solve all identification challenges—existing instruments and techniques will remain vital in maintaining the quality of the data.

While technology marches on, I believe we must continue to look backward. During his tenure as a Harvard professor, the well-known historian of business and strategy Alfred D. Chandler routinely asked his classes and colleagues, "How can you know where you're going if you don't know where you have been?" Fundamental observational gemology will be as important in the future as it has been in the past, not only as a check and balance with the proliferation of new instruments, AI, and machine learning, but also for the storytelling of gems. As the dynamic evolution of gemology continues, *Gems & Gemology* remains committed to bridging tradition and innovation.

Thomas M. Moses

Thomas M. Moses | Executive Vice President and Chief Lab & Research Officer, GIA

Observations of Oval-, Pear-, and Marquise-Shaped Diamonds: Implications for Fancy Cut Grading

Ilene M. Reinitz, Al Gilbertson, Troy Blodgett, Amanda Hawkes, James Conant, and Abhijith Prabhu

A cut grading system useful at all levels of the diamond trade must encompass the visual appeal of polished diamonds. This paper presents results from observations of oval-, pear-, and marquise-shaped diamonds for face-up appearance and outline appeal. In a controlled environment, an international cross section of diamond buyers, sellers, cutters, and appraisers observed sets of research diamonds in each shape; internal observation teams also examined diamonds submitted to GIA for grading services. Observers consistently disliked diamonds with prominent windowing but showed a broader range of opinions regarding the "bow tie" and "crushed ice" patterns typically found in these rounded fancy shapes. The distribution of opinions indicates significant differences in both regional preferences and personal taste for certain outlines and appearance patterns. Virtual facet maps, calculated from the three-dimensional wireframe file of a polished diamond, provide a quantitative visualization of these patterns. The geometric complexity of fancy shapes with multiple faceting arrangements requires the use of those same 3D files for assessing or predicting light behavior in a polished diamond.

GIA recognizes more than 40 distinct categories of fancy-shaped diamond,[1] each with unique characteristics and appearance qualities and continuously evolving facet arrangement variations. Brightness and fire remain important concepts for grading cut in fancy shapes, as they are for standard round brilliants. However, fancy-shaped diamond appearance patterns (figure 1) include aspects not displayed by the more constrained round brilliant at any proportion combination. Fancy shapes show more varied and pronounced changes to that patterning with motion than rounds, changes that produce scintillation—sparkle and liveliness. Further, rounded fancy shapes are cut with a number of outline variations beyond the length-to-width ratio (L:W), affecting both the face-up appearance and overall appeal of a diamond. It is clear that the cut grading methods applied to round brilliants cannot be simply transferred to fancy-shaped diamonds. Each fancy shape merits its own tailored approach to cut quality grading, taking into account its unique set of visual attributes.

A useful cut grading system should make visual sense. For round brilliants, Moses et al. (2004) found that most people agreed on the qualities that diminished a diamond's appearance. Some of these qualities apply equally well to fancy shapes. For example, all observers dislike dark or dull areas that reduce the overall brightness of the stone and mar its attractiveness. As these areas become more pronounced, they detract even further. Most observers expect to see some fire—dispersed light with sufficient intensity and covering large enough areas to be noticeable. People generally prefer distinct and orderly contrast patterns that are not overly blocky or highly fragmented. However, the diverse range of patterns found in fancy shapes tap into deeper levels of individual preference or personal taste and aesthetics that extend beyond the basic appearance requirements for a faceted dia-

See end of article for About the Authors and Acknowledgments.
Gems & Gemology, Vol. 60, No. 3, pp. 280–304,
http://dx.doi.org/10.5741/GEMS.60.3.280

[1]GIA uses the term *fancy shape* to include non-round outlines as well as facet arrangements of round shapes other than the 57/58-facet standard round.

Figure 1. Oval-, pear-, and marquise-shaped diamonds show more complex appearance patterns than standard round brilliants. Photos by Jian Xin (Jae) Liao.

mond. As some patterns are shape-specific, these taste factors also extend to a preference for a particular outline. Acknowledging varying taste factors[2] within a cut grading system is challenging for each fancy shape. Assessing overlap and differences among observers looking at a set of diamonds with different appearances is an essential first step for building such a system.

This article will discuss observations of oval, pear, and marquise shapes (described in box A).

In Brief

- Oval-, pear-, and marquise-shaped diamonds display more complex face-up appearance patterns than standard round brilliants, including bow ties and areas of crushed ice.
- Observers agree on some aspects of appearance in these shapes but show more variance regarding virtual facet patterns that contain significant areas of crushed ice.
- Regional and personal taste significantly influence evaluations, particularly among high-performing diamonds.
- Fancy-shaped diamonds need too many parameters for description to produce useful tables of proportion ranges for grading. Resolving their complexity requires three-dimensional wireframe files.

These three shapes share some geometric elements with the round brilliant. An oval is an elongated circle that can be modeled by a mathematical ellipse. A classic marquise is the intersection of two circular arcs (Watermeyer, 1980). A pear can be modeled by the combination of a marquise and an oval. Gem manufacturers utilize such mathematical models to help polish smooth and symmetrical outlines (Watermeyer, 1980). The similarities promote the reworking of concepts and tools from the round to these shapes, while the differences lead to additional factors to explore for the evaluation of cut. Oval, pear, and marquise shapes are found across a range of L:W, fashioned in a number of typical brilliant faceting arrangements and outline variations. Many parameters are required to describe the combination of variations of outline curvature, faceting arrangement, and proportions for those facets in each shape.

Variation among just six parameters for the round brilliant led to more than 38 million proportion combinations to encompass the proportions typically encountered in diamond grading. Fancy shapes require many more parameters, leading to an astounding number of possible combinations. For instance, a concise geometric description of one symmetrical faceting arrangement for an oval—eight bezels, four pavilion mains, and no painting or digging out (Blodgett et al., 2005)—requires 18 parameters, three times more than the round brilliant (box B). An oval arrangement with eight pavilion mains that includes painting variation increases the number of parameters to 28 (Conant, 2024). A symmetrical marquise with four pavilion mains requires all the parameters for the oval, plus the angle at the points, for a total of 19 parameters. Describing a pear shape with four

[2]During this study, it became obvious that observers who prefer a "hearts and arrows" appearance in round diamonds caused by observer reflection tend to dislike the same reflection pattern when it occurs in oval, pear, and marquise shapes, resulting in what the jewelry trade calls a "bow tie."

Box A: Describing Three Common Curved Outlines

The word *oval* means "egg-shaped" (from the Latin *ovus*, meaning egg), but oval gemstones are more symmetrical and elliptical in outline than most eggs. Most oval-outlined diamonds are slightly broader at the shoulders than an ellipse but more rounded than cushion shapes (figure A-1). Ovals that are flatter at the shoulders than an el-

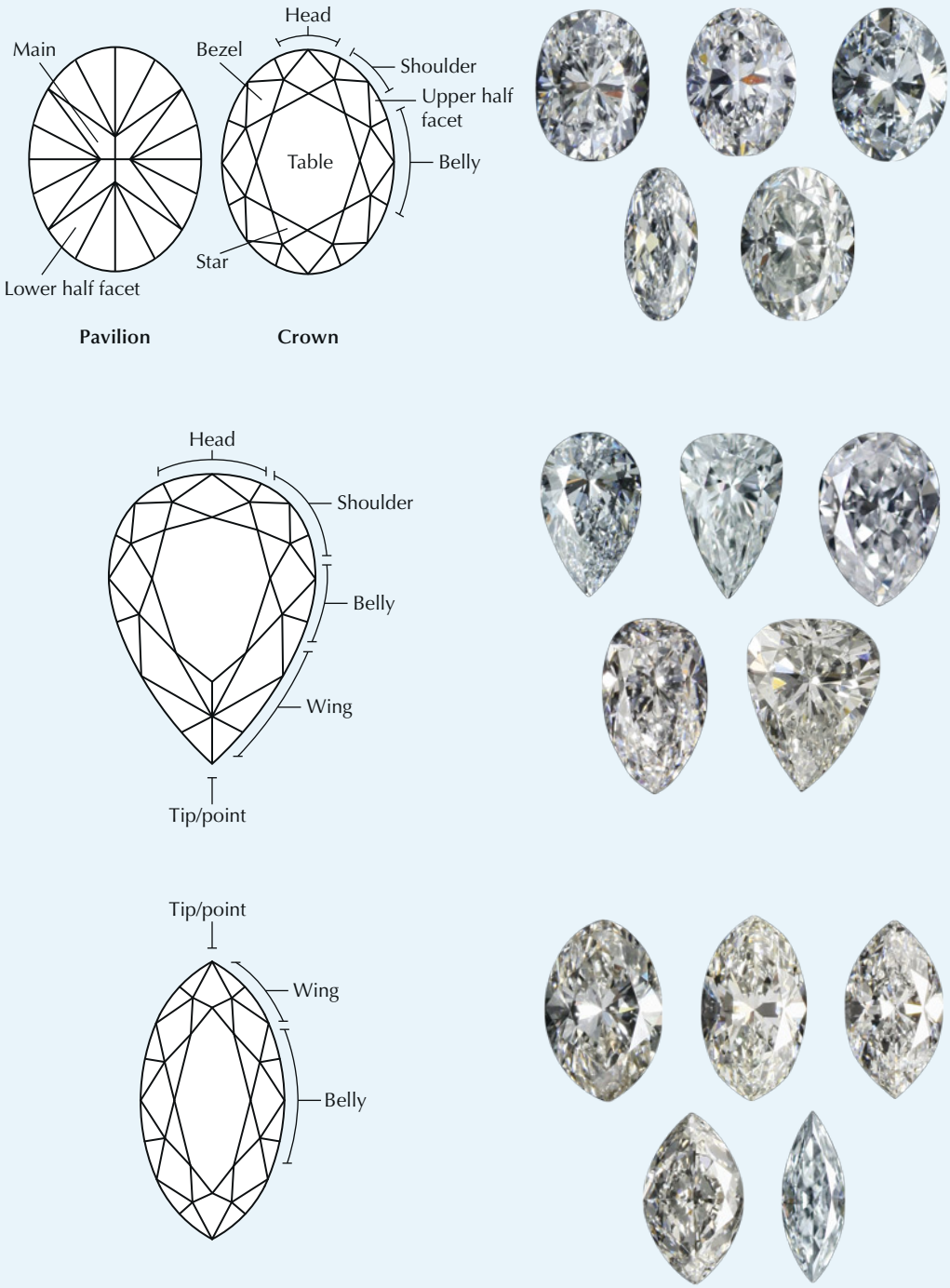

Figure A-1. These fancy shapes show a variety of outline variations beyond their different length-to-width ratios. Some have broad shoulders, and some have flat wings while others have wings that are plump. Point angles for both pear and marquise shapes vary independently from L:W.

lipse are often called "movals" by the trade, as the outline becomes closer to a marquise; ovals that are quite squat and almost round are called "rovals."

The outline of a pear-shaped diamond is rounded at one end (the head) and tapered to a point at the opposite end. A long, narrow pear is sometimes called a "pendeloque." The head shape can vary from semicircular to broad. The wings (see again figure A-1) can be plump or flat, and the angle of the point varies following the influence of the wing shape.

A marquise outline is an elongated elliptical shape with curved sides and two pointed ends. This is also called a "navette," from the Latin for "ship," because its face-up outline resembles a simple boat. Marquise shapes are fashioned with a range of point angles and wings that are either plump or flat (see again figure A-1).

Oval-shaped diamonds are commonly designed with L:W ranging from 1.2 to 1.7 (Blodgett et al., 2011). Pear shapes usually have L:W from 1.3 to 1.8. Marquise diamonds are typically longer with L:W from 1.5 to 2.5. All three shapes are usually cut with brilliant faceting, with many choices of facet arrangement (figure A-2). Many ovals have eight bezels matched with four, six, or eight pavilion mains, but some have ten or twelve bezels. Additional facet rows on the pavilion further add to the variety. Pear shapes typically have seven or eight bezels matched with anywhere from three to nine pavilion mains. (The single symmetry axis supports the odd-numbered main arrangements.) Pear and marquise shapes may have "French tips," in which several facets replace the bezel at a point. Marquise diamonds typically have six or eight bezels matched with four, six, or eight mains, and other more complicated pavilion arrangements. All three shapes can be fashioned with step faceting or as mixed cuts (step-cut crown and brilliant-style pavilion, or vice versa), but such diamonds are unusual and were not included in this investigation.

Figure A-2. Oval-, pear-, and marquise-shaped diamonds are commonly polished in a variety of faceting arrangements.

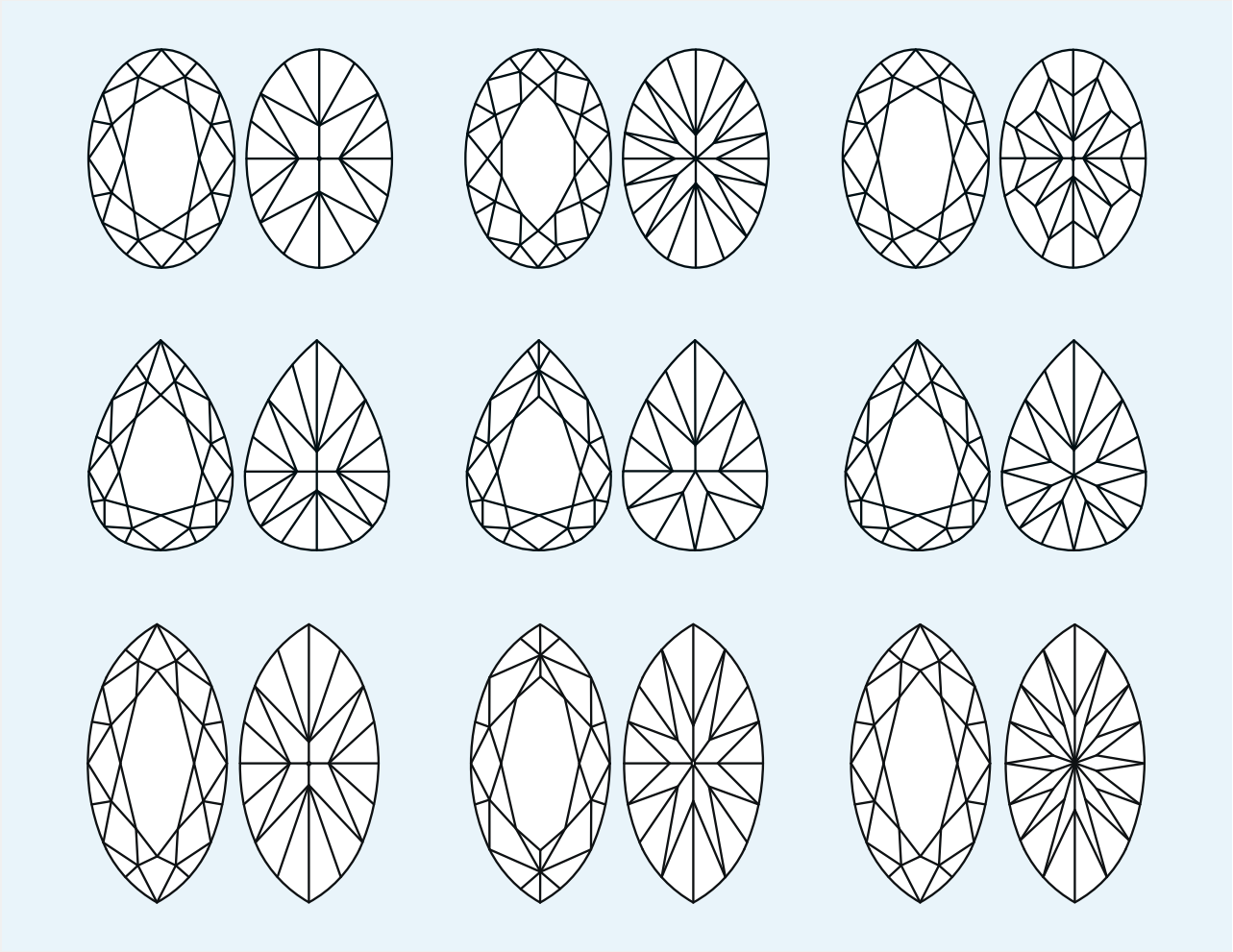

Box B: Parameter Descriptions for Outline and Proportions

Many parameters are required to describe just one fully symmetrical faceting arrangement with four pavilion mains in these three fancy shapes. The geometric parameters shown in figures B-1 and B-2 relate to gemological ways of describing the outline and proportions.

Curvature and L:W combine to describe whether an oval has large (broad) or slack (flatter) shoulders; adding in the point angle describes whether the wings of a marquise are plump or flat (see again box A). Girdle thickness indicates the separation of the crown from the

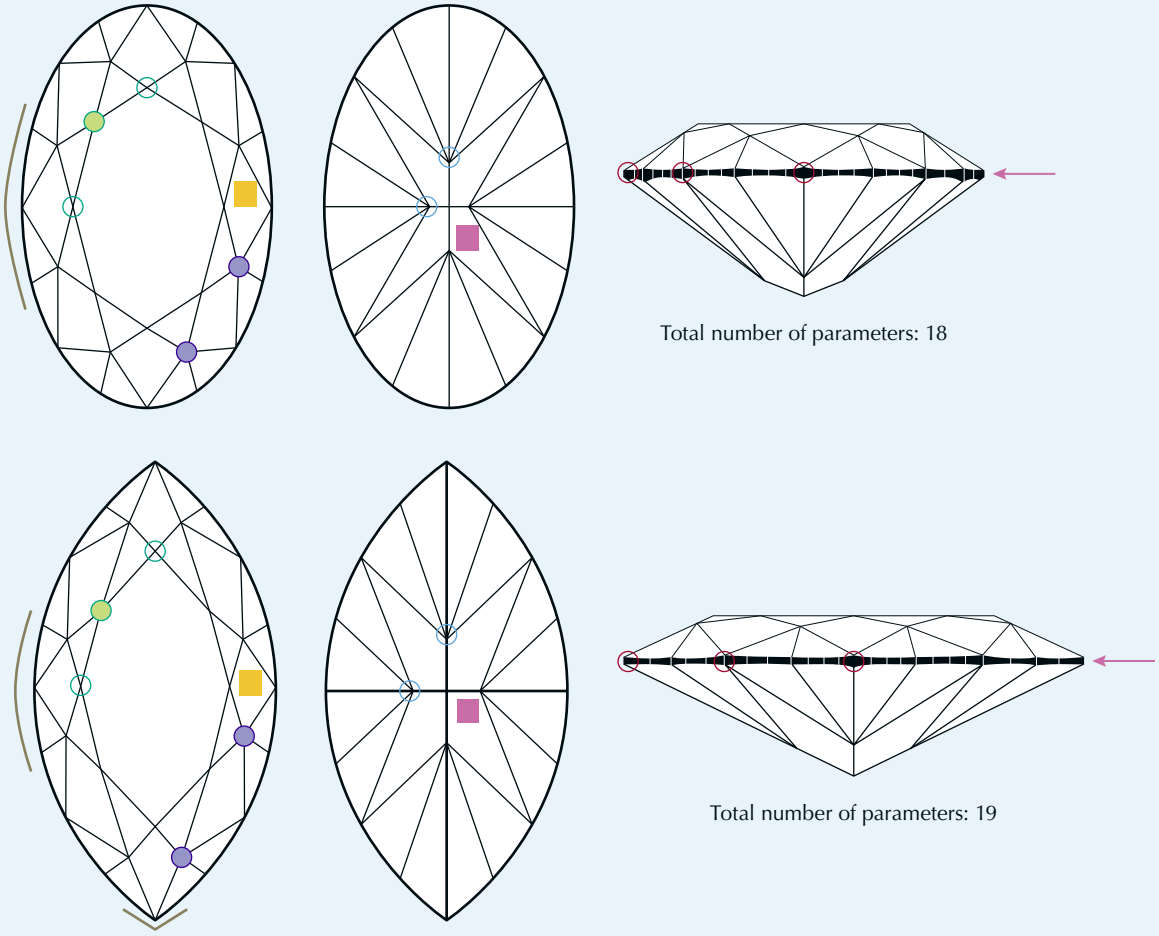

Figure B-1. A concise geometric description of a fully symmetric four-main oval brilliant requires 18 parameters, and describing a four-main marquise needs one more. Note that the meetpoints marked with filled circles (two colors) represent two parameters (azimuthal location around the outline and distance from the outline). A description using more conventional gemological proportions would yield an even longer list of parameters.

pavilion, while the sets of girdle vertices determine the outline positioning of the bezels and pavilion mains. The table vertex parameters describe the size and shape of the table and further constrain the position of the bezels. The distance parameter for the interior crown meetpoints describes the star lengths, and their position parameter affects the shapes of the bezel facets and stars. Given these constraints, a single crown angle value resolves the angles for the rest of the crown facets.

Similarly, the interior meetpoints in the pavilion describe the lower half facet lengths. With four pavilion mains, these meetpoints must lie along the length and width axes of oval and marquise shapes (see again figure B-1) and along the length axis of the pear (see again figure B-2). Since the girdle vertices constrain pavilion main positioning, only one pavilion angle is needed to solve for the others.

For the pear shape, the rounded portion and the pointed portion are mathematically independent. As illustrated in figure B-2, this shape needs two parameters for curvature and separate parameters for L:W of the head and L:W of the point. The pear needs a parameter for the displacement of the culet along the vertical axis because the culet is not constrained to lie at the width position. Eight table vertex parameters describe the length, width, and shape of a pear's table, and another eight crown meetpoints describe the star lengths and the shape of the bezel facets. Then, defining a single crown angle constrains the rest of the angles. The seven pairs of girdle vertices set the positions of the four pavilion mains and the lower half facet junctions, and the pavilion meetpoints constrain the lower half lengths and width of the pavilion mains. With these other parameters, a single pavilion angle constrains the rest of the angles.

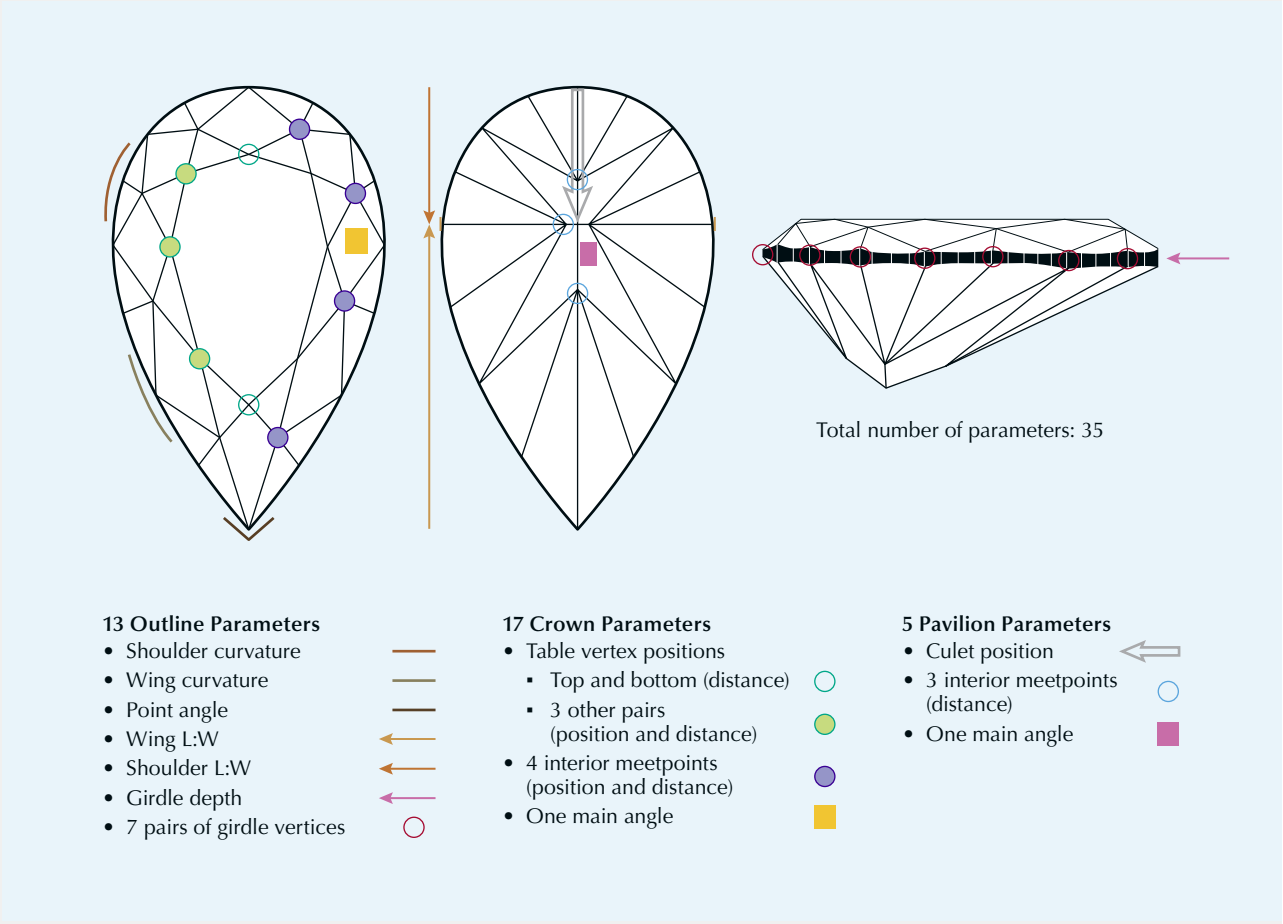

Figure B-2. A concise geometric description of a symmetrical four-main pear brilliant has 35 parameters. The pear shape has a single symmetry axis and fewer positional constraints and needs more parameters to describe its greater degrees of freedom. The two colors of filled symbols at some of the meetpoints represent two parameters (distance from the outline edge and azimuthal location around the outline).

mains requires 35 parameters because the curvature of the rounded portion and the pointed portion of the outline are independent, and the facet positions are less constrained. With eight pavilion mains and painting variations, the pear shape parameters increase to 57 (Conant, 2024). The much greater number of parameters for fancy shapes precludes any kind of grade prediction based on rounded proportion combinations. Any predictive cut grading for fancy shapes must be based on a 3D representation of the diamond, such as the wireframe files produced by non-contact measuring devices.

BACKGROUND

For many decades, the trade has debated which ranges of L:W, table percentage, and total depth percentage produce attractive fancy-shaped diamonds. As trade interest in proportion-based cut grading increased through the 1990s and into the 2000s, various ranges were promoted for some fancy shapes, along with parameter range charts for round brilliants. In 2005, the American Gem Society (AGS) unveiled its use of a three-dimensional ray-tracing model for light performance evaluation and produced corresponding ASET images (Sasian et al., 2007; Gilbertson, 2013). As research continued, some fancy-shaped diamonds were added to their Light Performance system. However, this approach required continual research to update reference standards for grading additional faceting arrangements among supported shapes. In support of the industry, manufacturers and retailers had access to proprietary software that could provide an estimated grade for a diamond by utilizing the 3D model created from a non-contact measuring device.

Octonus, in collaboration with Lexus Group, has applied various metrics for appearance aspects to fancy shapes; these metrics were originally developed for standard round brilliants (https://www.octonus.com/projects; see also https://legacy.octonus.com/oct/products/3dcalc/standard/diamcalc_2-0.phtml). This technology addresses several aspects of human vision, notably the effects of stereovision and the contribution of contrast to the perception of brilliance (Sivovolenko et al., 2013). Established by Lexus SoftMac in 2016, the Cutwise web platform is the chief source for this assessment of cut (https://cutwise.com). It accepts a wireframe file or imagery from the DiBox equipment suite and produces various images and videos along with an evaluation by the Cutwise metrics collection.

In the autumn of 2022, the International Gemological Institute (IGI) announced a cut grading service for nine fancy shapes (International Gemological Institute, 2022). They established proportion ranges "historically observed to produce positive beauty," hinted at additional shape-specific restrictions (e.g., bow tie factors), and left the final cut grade to a gemologist's visual evaluation of "how effectively the diamond reflects light back to the viewer" (International Gemological Institute, n.d.).

The visual appeal of polished diamonds is a critical factor for a fancy cut grading system. A useful system must also support the design and cutting of attractive fancy-shaped diamonds for traditional choices, as well as for new faceting arrangements, proportion combinations, and outline variations. Accurate cut grade estimation during rough planning allows manufacturers to make sound business decisions, and the large number of fancy-shape parameters (see again box B) requires wireframe files for the analysis that leads to a grade evaluation. However, a wireframe-based prediction is only as good as the fidelity of the wireframe (i.e., the degree to which it represents the diamond). Wireframes that do not closely match the stone's faceting produce anomalous results, as shown in box C.

While developing the GIA cut grading system for the round brilliant, we found that the face-up pattern—the distribution of bright and dark elements—was as important as the metrics for light return and fire in evaluating overall diamond appearance (Moses et al., 2004). This importance arises from the nature of human vision, which is more sensitive to the intensity and distribution of contrasting elements in a visual display than it is to the quantitative amount of light return (Yaguchi, 1987; Kingdom, 2003; Heeger, 2006; Gilbertson, 2013). Thus, the visual impression of brightness is largely drawn from these face-up patterns. Overall diamond appearance also includes how these patterns change with the motion of the diamond (or viewer, or light source), creating scintillation. Rounded fancy shapes display two pattern aspects of particular interest: "bow tie" and "crushed ice."

The elongation inherent to oval, pear, and marquise shapes tends to produce a bow tie as part of the visual pattern for most choices of brilliant faceting arrangement and wide ranges of proportions (figure 2). This area of dark contrast seen through the table across the width of the stone can vary from slight to thick, and it may be made up of disjointed segments or form a continuous dark bar. Some bow ties are per-

BOX C: WIREFRAME FIDELITY

Computer-driven gemstone measuring devices (such as the Lexus Helium system or the Sarine DiaVision) capture the skin of a polished diamond and construct a wireframe file—a mathematical representation of the vertices of the diamond and how they connect into facets. When this wireframe closely matches the measured diamond, it provides a model geometry for tracing how light moves through that stone (figure C-1). However, many fancy-shaped diamonds produce a wireframe file with significant differences from the actual stone. Shallow crown depth, shallow pavilion depth, and faceting designs that lead to small interfacial angles all make it more difficult for such measuring systems to render all the facets as seen on the diamond. Additional information about facet edges from a crown or pavilion view of the diamond is needed to correct such deficiencies. Ray-tracing light through a badly rendered wireframe may produce results that have little to do with the diamond's actual appearance.

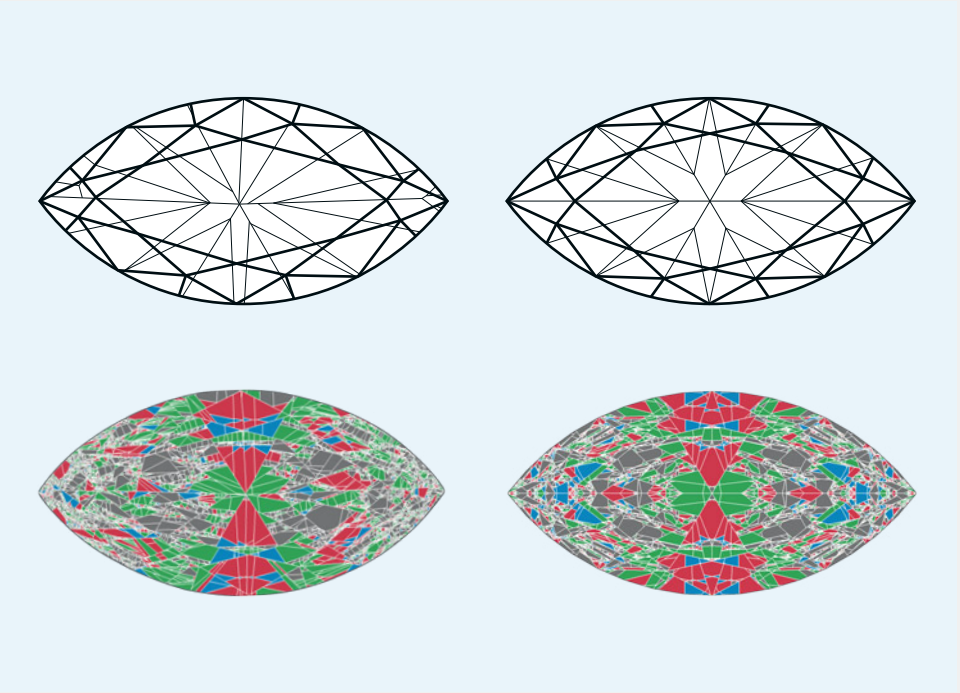

Figure C-1. The wireframe representation on the left has several problems with the rendering of the pavilion—note the missing mains (at the center and the wing on the upper right) and a lower half facet rendered in three pieces (at the left point). The wireframe on the right shows a symmetrical marquise with all of its facets, and proportions matched to the one on the left. ASET maps calculated from each wireframe file are shown on the bottom. The deficiencies in the wireframe on the left produce modeled results that differ in several areas from the complete wireframe.

sistent, while others brighten during motion of the diamond. The choice of faceting arrangement and faceting proportions can further accentuate or diminish bow ties.

These shapes generally produce areas with many small virtual facets (Sasian et al., 2007) often described by the trade as crushed ice (again, see figure 2). The size distribution of virtual facets in such "busy" areas can vary. Small virtual facets may dominate some diamonds, while others may show a broad range of virtual facet sizes. Crushed ice can also show differing amounts of contrast, from distinct and bright to muddled and gray. For most proportion combinations, all three shapes tend to show regions with this pattern, especially at points; with some facet arrangements, crushed ice dominates the pattern across the entire stone.

MATERIALS AND METHODS

Despite the daunting task of evaluating billions of possible fancy-shape combinations that manufacturers can produce, ultimately human observations provide the essential ground truth for tuning any predictive system. Both people and actual diamonds are required to collect human observations of diamond appearance. Using consistent lighting and observing conditions and the same set of diamonds for all observers provides the basis for exploring the variance (range of differences) among them. Quantitative

Figure 2. The patterns seen in oval-, pear-, and marquise-shaped diamonds often include a bow tie and areas of crushed ice. A: Pear shape RD133 shows a thin bow tie across the belly and small crushed ice in the point. B: Marquise RD101 displays a medium bow tie and medium to small crushed ice in both points. C: Oval RD118 has a strong bow tie and two arcs of medium to small crushed ice.

data can be drawn from such observations by having observers perform specific tasks, such as putting a set of stones in order from best to worst appearance or evaluating a group of stones in pairs until all have been compared.

The authors assembled an initial reference set of fancy-shaped diamonds containing 21 ovals, 16 pear shapes, and 16 marquise shapes, including examples with different numbers of pavilion mains in each shape (table 1). Each research diamond (RD) is designated by a unique number. For testing, we used 12 of each shape, in two sets of six stones for several kinds of observations, noted in table 1 as set A or B (figure 3). Since 2023, more stones have been added to the reference collection as research continues to include additional faceting arrangements, outline variations, and particular pattern elements.

A mobile lighting and viewing environment was developed to gather observations from trade members in six worldwide locations and from several teams of internal GIA observers. The chosen lighting and observing conditions were documented and standardized to ensure that each observing station was identical and observers followed a common procedure. The station consisted of a GIA DiamondDock, with GIA fluorescent bulbs set in the center position of the lighting cabinet and a diffusing plate below. Observation stones were set in neutral gray plastic trays on the floor of the DiamondDock. Observers held the tray close to the bottom of the viewing environment (with part of their hands touching the base) and centered 10 to 12 in. (25 to 30 cm) under the light source and 12 to 18 in. (30 to 45 cm) from their eyes. The tray with the stone or stones was gently rocked to add motion for some observations. For recent internal observations (described below), each observer wore a white lab coat and was asked to maintain a consistent hairstyle (whether down or pulled back). Although we acknowledge that not every condition experienced by a consumer in the real world is covered by these specifications, this environment was chosen as the standard because the appearance of the diamonds seems to be most fairly represented without exaggerating or deemphasizing the critical pattern elements.

Trade observations were gathered for several years at the gem shows in Tucson, Arizona, from diamond buyers, sellers, cutters, and appraisers, along with several non-jewelry trade individuals representing consumers. Trade observers took surveys about outline appeal, where each survey page displayed computer-generated outlines for oval, pear, or marquise. Both L:W and outline variations were included, and participants scored each outline from 1 (strongly disliked) to 10 (strongly liked). In 2013, 69 participants were instructed to arrange each set of six diamonds in order from most appealing to least appealing, first evaluating outline and a second time considering only face-up appearance. In 2015, 43 participants provided their comments as they observed reference diamonds of various shapes, including seven ovals, seven marquises, and nine pear shapes (the Tucson set is denoted by T in table 1). These observers evaluated face-up appearance, outline appeal, and durability factors on a scale from Excellent to Poor. Then the observers were asked whether specific features affected their decisions.

In 2014 and 2015, we took the same sets of six diamonds to Antwerp, Hong Kong, Mumbai, Tel Aviv, and New York and gathered observations and comments from 166 participants, all active as diamond buyers, sellers, or cutters. These observers evaluated each stone in a group of six diamonds of a particular shape on a scale from Excellent to Poor and made

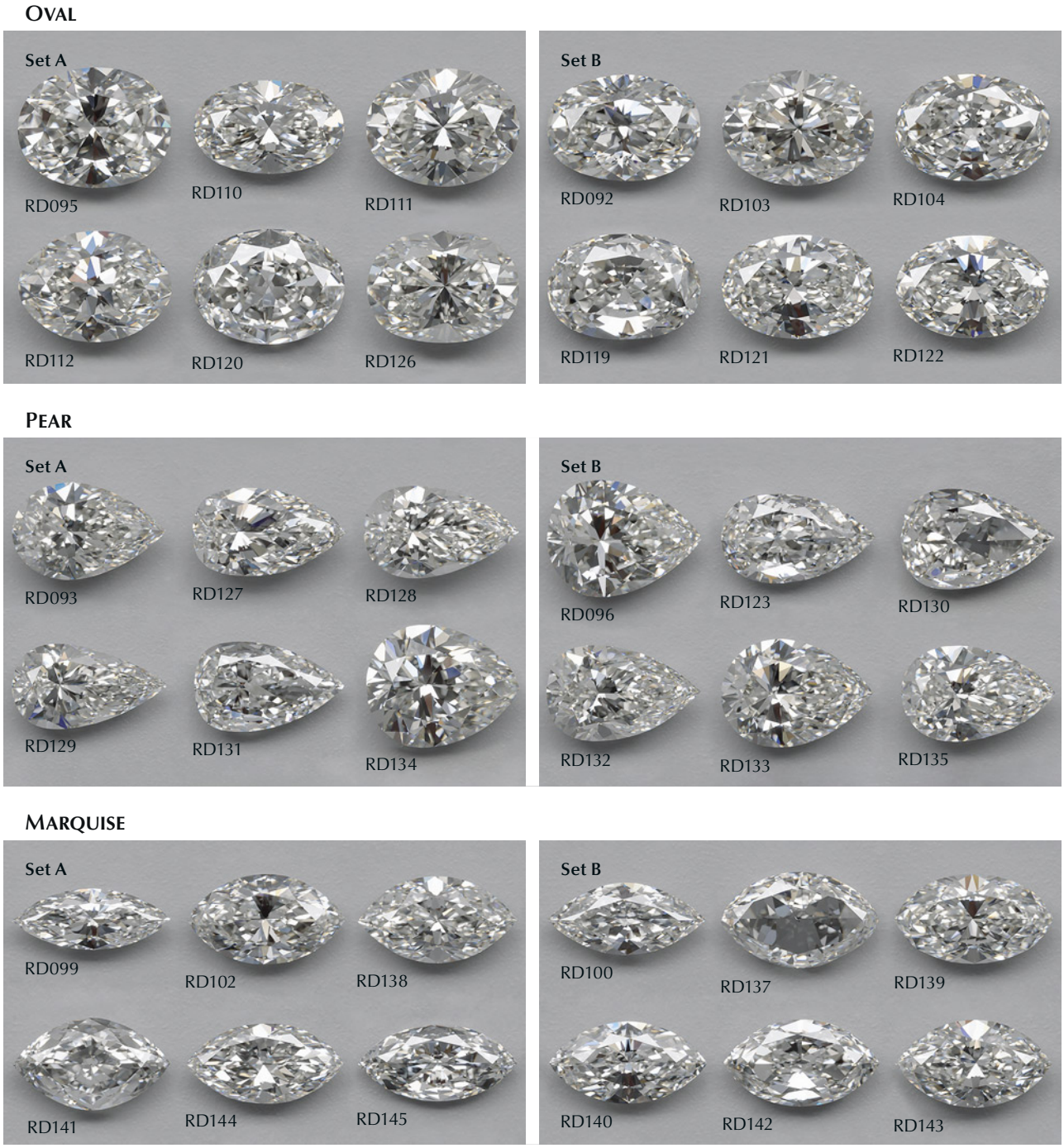

Figure 3. These virtual images display the 36 research diamonds used for observations, grouped into sets A and B for each shape. They range in size from 0.33 to 0.86 ct, have color grades between D and K, and have clarities between VVS_2 and I_1. Table 1 contains size and grading-report information for each diamond. The images were created with a proprietary rendering configuration, mimicking the DiamondDock environment. Still virtual images and videos of these stones in motion are available online (https://www.gia.edu/gems-gemology/fall-2024-fancy-shaped-diamonds).

comments on specific appearance aspects. Most of these observers looked at all 36 oval, pear, and marquise diamonds.

Additional visual observations were gathered from several teams of GIA staff (approximately 30 staff members over three years) adept at assessing outline

TABLE 1. Details of the reference diamonds.

Diamond	Shape	Set	Bezels/Mains	Weight (ct)	Color	Clarity
RD092	Oval	B, T	8/4	0.86	F	VS_1
RD095	Oval	A	8/8 s[a]	0.75	D	SI_2
RD103	Oval	B	8/6	0.74	H	VS_2
RD104	Oval	B	8/4	0.37	F	VS_2
RD110	Oval	A, T	8/6	0.47	G	I_1
RD111	Oval	A	8/8	0.47	G	SI_2
RD112	Oval	A, T	8/6	0.69	G	SI_2
RD113	Oval	—	8/6	0.39	F	VS_2
RD114	Oval	—	8/6	0.47	I	SI_2
RD115	Oval	—	8/6	0.41	G	VVS_2
RD116	Oval	T	8/6	0.45	I	SI_1
RD117	Oval	—	8/6	0.46	I	VS_2
RD118	Oval	—	8/6	0.44	H	VS_1
RD119	Oval	B	8/6	0.45	I	VVS_2
RD120	Oval	A, T	8/6	0.43	H	SI_1
RD121	Oval	B	8/6	0.45	G	VS_1
RD122	Oval	B	8/6	0.46	H	VS_2
RD126	Oval	A, T	8/6	0.66	H	SI_2
RD181	Oval	—	8/4	0.50	D	VS_2
RD185	Oval	—	8/6	0.87	F	SI_2
RD176	Oval	T	8/mod 4[b]	0.78	D	VS_2
RD093	Pear	A	7/6	0.72	F	VS_2
RD096	Pear	B, T	8/7	0.74	I	I_1
RD123	Pear	B, T	7/7	0.45	D	SI_2
RD124	Pear	—	8/7	0.38	H	I_1
RD125	Pear	—	8/7	0.47	H	SI_1
RD127	Pear	A, T	8/6	0.57	H	SI_2
RD128	Pear	A, T	8/7	0.63	G	I_1
RD129	Pear	A, T	8/7	0.65	K	SI_2
RD130	Pear	B, T	8/7	0.62	I	I_1
RD131	Pear	A, T	8/7	0.68	D	I_1
RD132	Pear	B	8/7	0.45	K	SI_1
RD133	Pear	B	8/7	0.47	K	VS_2
RD134	Pear	A, T	8/7	0.47	K	VS_1
RD135	Pear	B	8/7	0.46	I	VS_1
RD199	Pear	—	8/4	0.62	I	SI_2
RD200	Pear	—	8/7	0.70	F	VS_2

TABLE 1 (continued). Details of the reference diamonds.

Symmetry	Length (mm)	Width (mm)	Depth (mm)	Depth (%)	Table Size (%)	Girdle Min	Girdle Max
Good	7.43	5.17	3.24	62.7	54	THN	STK
Good	6.75	5.3	3.16	59.6	56	THN	STK
Good	6.52	4.97	3.40	68.4	62	STK	THK
Good	6.07	4.20	2.16	51.4	67	ETN	THK
Good	6.52	4.05	2.71	66.9	52	MED	VTK
Very Good	5.71	4.38	2.89	66.0	58	STK	VTK
Good	6.76	4.89	3.26	66.7	54	MED	VTK
Good	5.55	4.02	2.58	64.2	57	STK	ETK
Good	5.46	4.02	3.09	76.9	55	THN	ETK
Good	5.92	3.92	2.66	67.9	61	VTN	VTK
Good	5.92	4.38	2.57	58.7	58	THN	VTK
Good	6.43	4.19	2.40	57.3	57	VTN	VTK
Good	5.86	4.20	2.64	62.9	55	STK	VTK
Good	6.51	4.49	2.23	49.7	60	THN	THK
Very Good	6.28	4.77	2.08	43.6	65	THN	THK
Good	6.29	4.31	2.55	59.2	61	THN	THK
Good	6.50	4.35	2.54	58.4	64	VTN	STK
Good	6.38	4.71	3.28	69.6	62	STK	VTK
Very Good	6.32	4.51	2.56	56.8	59	MED	THK
Good	7.46	5.25	3.21	61.1	56	MED	THK
Good	6.90	5.15	2.80	54.4	66	MED	THK
Good	7.74	4.92	3.19	64.8	55	MED	VTK
Good	6.94	5.25	3.25	61.9	60	MED	ETK
Good	7.63	4.44	2.12	47.7	61	THN	THK
Good	6.69	3.99	2.38	59.6	57	THK	VTK
Good	6.08	4.52	2.82	62.4	60	THN	ETK
Good	7.64	4.41	2.69	61.0	63	MED	THK
Very Good	7.76	4.62	2.99	64.7	61	THN	THK
Good	8.12	4.49	3.13	69.7	62	THN	VTK
Good	7.57	4.96	2.37	47.8	63	THK	ETK
Good	8.55	5.14	2.35	45.7	61	STK	ETK
Good	6.54	4.07	2.81	69.0	57	MED	THK
Very Good	6.44	4.59	2.73	59.5	58	THN	MED
Good	5.71	4.57	2.87	62.8	56	STK	VTK
Good	6.88	4.26	2.66	62.4	57	VTN	VTK
Very Good	7.22	4.79	2.90	60.6	64	MED	VTK
Excellent	7.36	5.02	2.92	58.2	66	MED	VTK

TABLE 1 (continued). Details of the reference diamonds.

Diamond	Shape	Set	Bezels/Mains	Weight (ct)	Color	Clarity
RD099	Marquise	A, T	6/6	0.75	D	VS_2
RD100	Marquise	B, T	6/4	0.85	D	VVS_1
RD101	Marquise	—	6/6	0.79	D	VS_1
RD102	Marquise	A	8/6	0.82	D	VVS_1
RD136	Marquise	—	6/6	0.32	I	VS_2
RD137	Marquise	B	8/6	0.33	—	I_1
RD138	Marquise	A	8/6	0.46	F	SI_2
RD139	Marquise	B, T	8/6	0.39	I	SI_2
RD140	Marquise	B	8/6	0.39	H	VS_1
RD141	Marquise	A, T	8/4	0.44	G	SI_2
RD142	Marquise	B, T	8/4	0.40	H	SI_1
RD143	Marquise	B, T	8/6	0.44	I	VVS_1
RD144	Marquise	A	8/6	0.41	H	VVS_2
RD145	Marquise	A	8/6	0.39	I	SI_1
RD146	Marquise	T	6/6	0.43	I	VVS_1
RD197	Marquise	—	8/8	0.82	F	VVS_2

[a]*Indicates that the mains are four to each side, with none in the heads*
[b]*Modified brilliant pavilion with four short pavilion mains*

and appearance details in fancy shapes. Initially, these internal observers worked with the reference sets, forging consensus and refining the relative ranking within the sets. Next, they used the reference stones while observing diamonds submitted for grading reports in sizes from 0.60 to 2.20 ct, evaluating various appearance aspects. Later, two internal teams, one in Carlsbad and one in Las Vegas, observed 683 ovals, 430 pears, and 308 marquise shapes for overall appearance.

Our most recent work with one internal team (2023) has examined appearance details for more client diamonds—approximately 350 ovals, 230 pears, and 90 marquise shapes. Each diamond was observed in the tray, placed in both vertical and horizontal positions. The following were evaluated on scales with either four or five intervals: brightness; girdle reflection; appeal and boldness of the contrast pattern and the symmetry of that pattern; windowing or leakage; size of any bow tie along the stone's length and width; and the total amount of crushed ice, its sparkle size, definition, and appearance appeal. For some properties, that scale ranged from Excellent to Poor; for others, it ranged from None to Obvious. The contrast pattern was evaluated from Dispersed to Concentrated, and the amount of crushed ice ranged from 0% to 100%. Bow tie patterns were evaluated from Short to Long in one direction and Thin to Wide in the other direction. Crushed ice sparkle size ranged from Tiny to Large.

Direct observation data is presented in histograms by evaluation category. Groups of observations (for a single diamond) were analyzed for their mean and consensus values. Consensus, abbreviated as Cns(x), is a statistical measure developed specifically for ordinal data with arbitrarily assigned number values (Tastle and Wierman, 2007), such as choosing a grade category for an observed diamond. Unlike standard deviation, consensus assesses the frequency distribution of responses to derive a useful measure of agreement (or disagreement) among those responses. Consensus varies from 0 (complete disagreement) to 1 (complete agreement) and indicates the amount of spread among the responses—whether there are many or few of them.

Diamonds were photographed with a Vision 360° B2B Mini system, with lighting conditions comparable to those at the floor of a DiamondDock viewing cabinet. In addition, virtual diamond images have been created using a proprietary configuration with OctaneRender that models many details of the observing environment: the DiamondDock and its

TABLE 1 (continued). Details of the reference diamonds.

Symmetry	Length (mm)	Width (mm)	Depth (mm)	Depth (%)	Table Size (%)	Girdle Min	Girdle Max
Good	11.05	4.24	2.75	64.9	54	THN	VTK
Very Good	10.98	5.02	2.63	52.4	55	MED	ETK
Good	8.94	5.05	3.03	60.0	54	THN	THK
Very Good	9.02	5.13	2.99	58.3	57	THN	VTK
Fair	11.02	3.79	1.17	30.9	89	VTN	STK
Good	6.94	4.20	1.68	40.1	74	VTN	MED
Good	7.38	4.03	2.72	67.5	56	THN	VTK
Good	6.67	3.78	2.53	66.9	58	STK	VTK
Good	7.59	3.96	2.35	59.3	60	STK	THK
Good	7.89	4.63	2.04	44.1	63	MED	VTK
Good	7.58	4.22	2.13	50.5	64	ETN	THK
Good	7.25	4.06	2.65	65.3	55	THN	VTK
Good	7.44	3.78	2.43	64.3	67	MED	VTK
Good	8.38	4.05	1.91	47.2	61	THN	VTK
Fair	10.91	3.63	1.91	52.6	52	VTN	THK
Very Good	8.67	4.99	3.30	66.2	65	STK	THK

[a]*Indicates that the mains are four to each side, with none in the heads*
[b]*Modified brilliant pavilion with four short pavilion mains*

lighting, background room lighting, the observer's position, and even the texture and color of the tray (again, see figure 3). Our observation team compared such virtual images created from the wireframes of the research diamonds to the actual diamonds in the DiamondDock and found the images and diamonds to be nearly identical.

Virtual facet pattern maps (of secondary reflections) were calculated using typical ray-tracing techniques for our reference diamonds and for the 670 recently observed diamonds. These maps independently display a diamond's face-up visual pattern compared to photographic imaging. They are color-coded to show the size of virtual facets, ranging from light blue (smallest) to dark blue (largest). Figure 4 compares two such maps with virtual images of the diamonds they represent.

RESULTS

An important first step before conducting visual evaluation of fancy shapes was to assemble appropriate sets of oval-, pear-, and marquise-shaped diamonds that displayed a range of visual appearances. Arranging those sets was not difficult, but transforming them into a useful reference set for the evaluation of appearance and outline shape was a more challenging and iterative process. Selected results are presented here, and more comprehensive sets of results can be found online (https://www.gia.edu/gems-gemology/fall-2024-fancy-shaped-diamonds).

Table 2 shows the results from the observations in 2013 of face-up appearance for sets A and B in the three shapes. The stones are listed in the rank order for each set according to the internal observing team, next to the ranking derived from the averaged (mean) Tucson observations. Even for oval set B and pear set A, where this order is the same, the consensus values below 0.8 demonstrate the broad spread of opinions among observers. A notable exception is RD137, a marquise that nearly all observers ranked as Poor in appearance. In contrast, pear shape RD131 has a consensus of 0.36—half the observers thought it was Poor, but the other half were distributed from Fair to Excellent.

The outline evaluations (table 3) also show medium to small consensus values for most stones. Again, the reference diamonds are listed according to the ranking of the GIA internal team for outline appeal and can be compared to the mean values from the Tucson observations. (Note that this outline

Figure 4. Virtual facet maps of marquise RD197 and pear RD125 are displayed next to virtual images of the stones they represent. In these maps, color is used to classify the size of virtual facets, from small to large: light blue (<0.05 mm), blue (0.05–0.10 mm), and dark blue (>0.10 mm). These examples demonstrate how the virtual facet maps condense the dynamic face-up appearance of a diamond into a static distribution map.

order is different from the appearance order for the same stones within each set.) Pear shapes RD093, RD127, and RD128 (in set A) have higher consensus values for outline evaluation, and oval RD103 has the lowest value. Generally, observers showed considerable variation regarding which outlines were acceptable, let alone attractive. Outline surveys showed similar broad opinions, with some notable differences between what participants liked and outlines that are found in the market (figure 5).

In 2014 and 2015, we took these sets of reference stones to major diamond-cutting centers worldwide and gathered trade observations and comments (see Materials and Methods). The primary goal in collecting such data was to capture any regional differences between the centers. We found substantial agree-

Figure 5. L:W preference for oval shapes. Those surveyed in 2009 using outline sketches showed a spread of opinions that peaked around 1.7, tending toward larger L:W than the preferred range in GIA course material (gray shaded region). However, the peak L:W of oval diamonds submitted for grading was close to 1.4, and those with L:W greater than 1.7 are rarely seen due to the shape of the rough. At high L:W, it is more challenging to find angles that yield a scintillating, attractive diamond.

TABLE 2. Comparison of GIA internal team and Tucson observers for evaluations of face-up appearance.

	Set A				Set B			
Shape	GIA internal rank order	Tucson rank order	Tucson mean[a]	Consensus[b]	GIA internal rank order	Tucson rank order	Tucson mean	Consensus
Oval	RD112	RD112	2.4	0.66	RD092	RD092	1.9	0.61
Oval	RD111	RD111	2.5	0.59	RD121	RD121	3.4	0.63
Oval	RD110	RD095	4.1	0.55	RD104	RD104	3.0	0.50
Oval	RD126	RD126	3.6	0.61	RD122	RD122	4.0	0.68
Oval	RD095	RD110	3.4	0.44	RD103	RD103	3.8	0.43
Oval	RD120	RD120	5.0	0.51	RD119	RD119	4.9	0.61
Pear	RD128	RD128	2.7	0.69	RD135	RD132	2.3	0.60
Pear	RD093	RD093	1.8	0.74	RD132	RD123	3.3	0.67
Pear	RD127	RD127	3.4	0.69	RD133	RD135	2.2	0.76
Pear	RD131	RD131	4.4	0.36	RD123	RD096	4.6	0.63
Pear	RD129	RD129	4.8	0.74	RD096	RD133	2.7	0.58
Pear	RD134	RD134	3.9	0.39	RD130	RD130	5.6	0.79
Marquise	RD138	RD144	2.8	0.59	RD143	RD143	1.8	0.75
Marquise	RD144	RD238	2.5	0.61	RD139	RD140	3.2	0.60
Marquise	RD099	RD102	3.4	0.47	RD100	RD100	2.9	0.66
Marquise	RD102	RD099	3.0	0.47	RD140	RD139	2.6	0.67
Marquise	RD145	RD145	4.5	0.64	RD142	RD142	4.5	0.72
Marquise	RD141	RD141	4.9	0.60	RD137	RD137	5.9	0.96

[a]*Mean values range from a high of 1 (all observers ranked the stone first) to a low of 6 (all observers ranked it last).*
[b]*Even when the two groups yielded the same rank order, the consensus values indicate the wide spread of opinions among observers.*

ment for some diamonds, whether the appearance was pleasing or deficient, and marked disagreement for others. Figures 6, 7, and 8 show virtual images of some of the observed reference diamonds paired with histograms of observer appearance evaluations from different locations.

For the ovals in figure 6, observers from all locations agreed well on the high evaluation of RD092, which had minimal windowing, a mixture of virtual facet sizes, and no strong bow tie. RD120, with rather large windowing and low contrast in the center of the stone, was generally disliked, with less agreement about which lower evaluation it should receive. The remaining three diamonds showed a spread of opinions. RD103 and RD110 both received many evaluations of Very Good to Good, but RD103, with a radiating pattern in the table and scattered crushed ice elsewhere, received more high evaluations in all locations but New York; RD110, with heavy concentrations of tiny crushed ice in the wings and regions of contrast under the table, was viewed more favorably in India. Opinions of RD176, which had tiny crushed ice throughout and no sizeable dark regions of contrast, showed considerable variation between locations.

The five pear shapes in figure 7 have general agreement among observers for three diamonds and a wider spread of opinions for the other two. RD135, with a radiating center pattern and a variety of crushed ice zones, was well regarded by most and had a fairly consistent distribution of opinions across all locations. RD127 shows a similar consistency in the distribution but was preferred less overall than RD135. RD130, with significant windows under the table, was strongly disliked by most observers, but a few people in each location gave this stone a higher evaluation.

TABLE 3. Comparison of outline evaluations between the GIA internal team[a] and Tucson observers.

	Set A			Set B		
Shape	GIA internal rank order	Tucson mean	Consensus[b]	GIA internal rank order	Tucson mean	Consensus
Oval	RD111	2.6	0.54	RD103	3.0	0.39
Oval	RD095	3.6	0.42	RD092	2.6	0.48
Oval	RD112	3.6	0.49	RD121	2.6	0.63
Oval	RD120	3.2	0.62	RD104	3.2	0.57
Oval	RD126	3.0	0.59	RD119	5.0	0.63
Oval	RD110	5.0	0.50	RD122	4.3	0.63
Pear	RD093	1.3	0.86	RD096	3.9	0.45
Pear	RD128	2.4	0.77	RD133	2.4	0.60
Pear	RD127	2.9	0.77	RD135	2.4	0.57
Pear	RD129	4.6	0.73	RD132	3.2	0.57
Pear	RD134	5.2	0.73	RD123	4.5	0.61
Pear	RD131	4.6	0.61	RD130	4.5	0.60
Marquise	RD145	3.8	0.61	RD140	2.5	0.65
Marquise	RD144	2.5	0.60	RD142	3.4	0.58
Marquise	RD102	3.2	0.49	RD143	1.9	0.68
Marquise	RD141	4.5	0.52	RD100	3.7	0.47
Marquise	RD138	2.3	0.63	RD137	5.2	0.68
Marquise	RD099	4.6	0.46	RD139	4.2	0.59

[a]*Note that the internal team's rank order for outline is different than the order for face-up appearance.*
[b]*Tucson observers gave a broad spread of opinions (lower consensus values), with similar mean values for several diamonds within each set.*

The evaluation distributions of RD131 and RD123 show a strikingly broad range of overall opinions within and between different locations. RD131, with well-distributed crushed ice, was seen more favorably in Antwerp and Hong Kong by a percentage of the observers, though the absolute numbers of people were small. RD123 was seen less favorably in Israel, where 93% of observers gave it a lower evaluation.

Figure 8 shows observations for five marquise diamonds, and geographic differences in evaluation are noticeable for all of them. These differences are most pronounced for RD100, rated lower in Hong Kong and Israel, and RD141, rated higher in Hong Kong and India. Lower values of consensus were found for both bimodal distributions and those with broad spread.

In 2015, additional trade comments and evaluations of appearance and outline were gathered in Tucson. The comments echoed those from international observers and reminded us that an overall cut grading system should address design and craftsmanship issues, as well as appearance. Most trade observers disparaged prominent bow tie patterns and outlines with very large L:W. We also recorded many negative comments about inconsistent girdle thickness and girdle areas that were too thin, even though these factors may not directly affect either appearance or outline shape.

Figure 6. Trade observers in five global locations evaluated these ovals for face-up appearance. They agreed well on the high evaluation of RD092 but showed less agreement on the low evaluation of RD120 with its noticeable window. The combination of crushed ice and contrast elements found in RD103 and RD110 produced a spread of opinions and some notable differences among locations. The pattern of RD176, with crushed ice everywhere, produced the least agreement among observers. The highest total is highlighted in pink.

The internal observation team continued refining the RD sets and using them to evaluate diamonds submitted for grading services. These observations began delving into specific pattern aspects (see Materials and Methods), and even the well-trained internal team shows variance among observers, more for some visual properties than for others. Figure 9 displays histograms of consensus values of several appearance aspects for the hundreds of observed diamonds. The internal team agreed very strongly about the extent of windowing for most stones, and strongly for brightness evaluations. However, they showed some variance in the evaluation of the strength of bow tie patterns (contrast boldness) and still less agreement regarding the width of those patterns. Evaluation of whether the contrast pattern was concentrated or dispersed produced lower consensus values for ovals than for pears or marquise shapes. Levels of observer agreement for the amount of crushed ice, its definition, and the predominant sparkle size also show marked differences among the three shapes.

As we examined and considered all these observations, a common theme emerged. Diamonds with

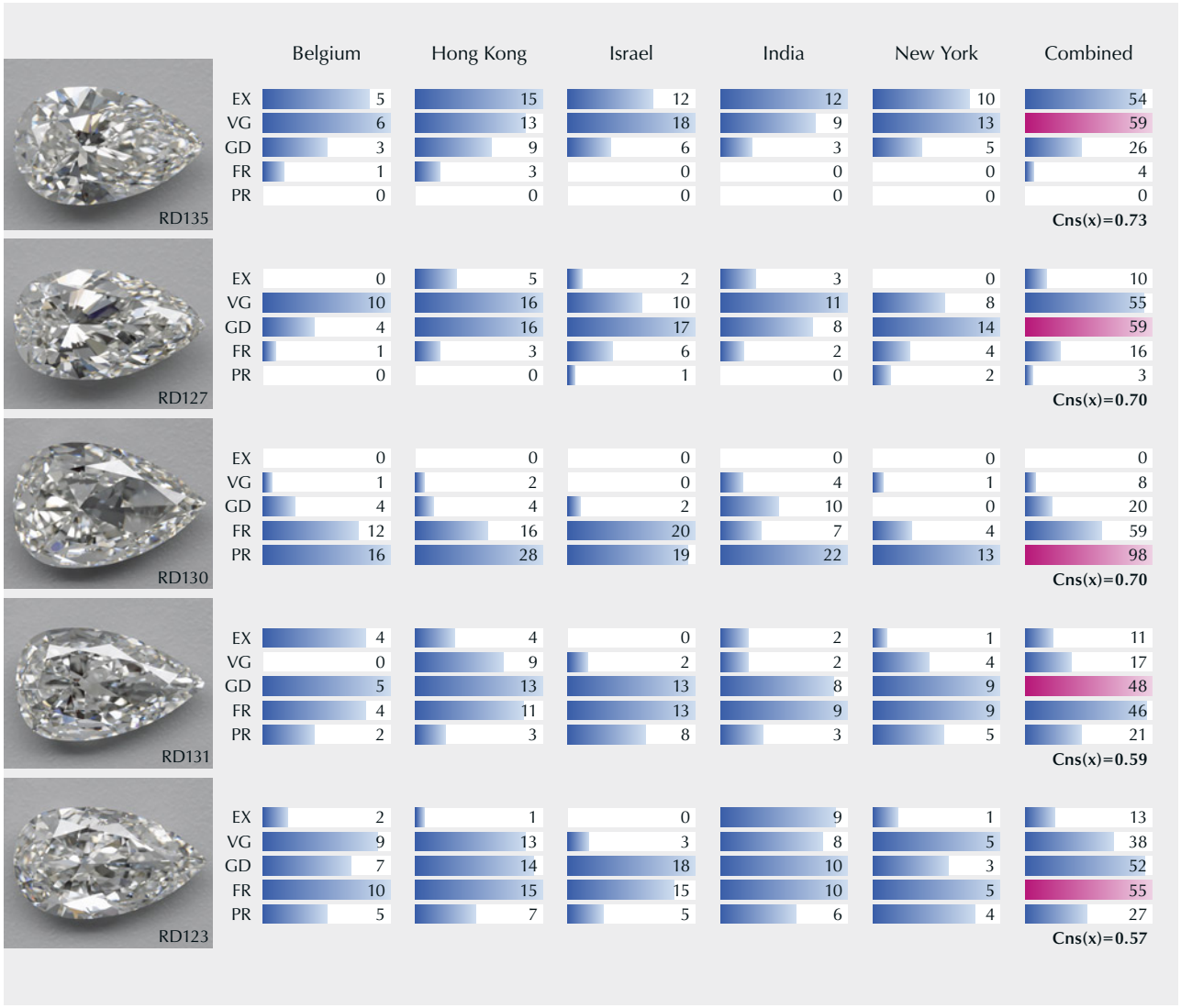

Figure 7. International trade observers evaluated these five pear-shaped diamonds for face-up appearance. They showed substantial agreement about the high evaluation of RD135, the medium evaluation of RD127, and the low evaluation of RD130 (a diamond with a large dark window). The patterns of RD131 and RD123, both dominated by crushed ice, yielded less observer agreement and more variation of opinion among locations.

substantial amounts of crushed ice in their pattern tended to yield less agreement for either overall face-up appearance or some specific aspects of appearance. The 2023 observations motivated us to develop the virtual facet map (described in figure 4) for displaying crushed ice and analyzing how virtual facets of various sizes are distributed across the stone.

Figure 10 shows virtual facet maps for several reference diamonds observed by both trade and in-house teams; virtual images of these diamonds are found in figures 3, 6, 7, and 8 for comparison. The table in figure 10 gives the evaluations and consensus values from Tucson observers in 2013 and the international observers in 2014/2015. Consensus values for RD143 and RD093 were higher among both groups of observers, with a notable difference in how each group evaluated the appearance of the two diamonds. Marquise RD143 has large virtual facets across the belly with a mixture of large, medium, and small virtual facets filling the points. Pear RD093 has large virtual facets across the head and belly of the stone, plus a few more mixed with medium and small virtual facets in the point.

Observations of oval RD092 and pear shapes RD129 and RD135 yielded strong but different consensus values for appearance between the Tucson

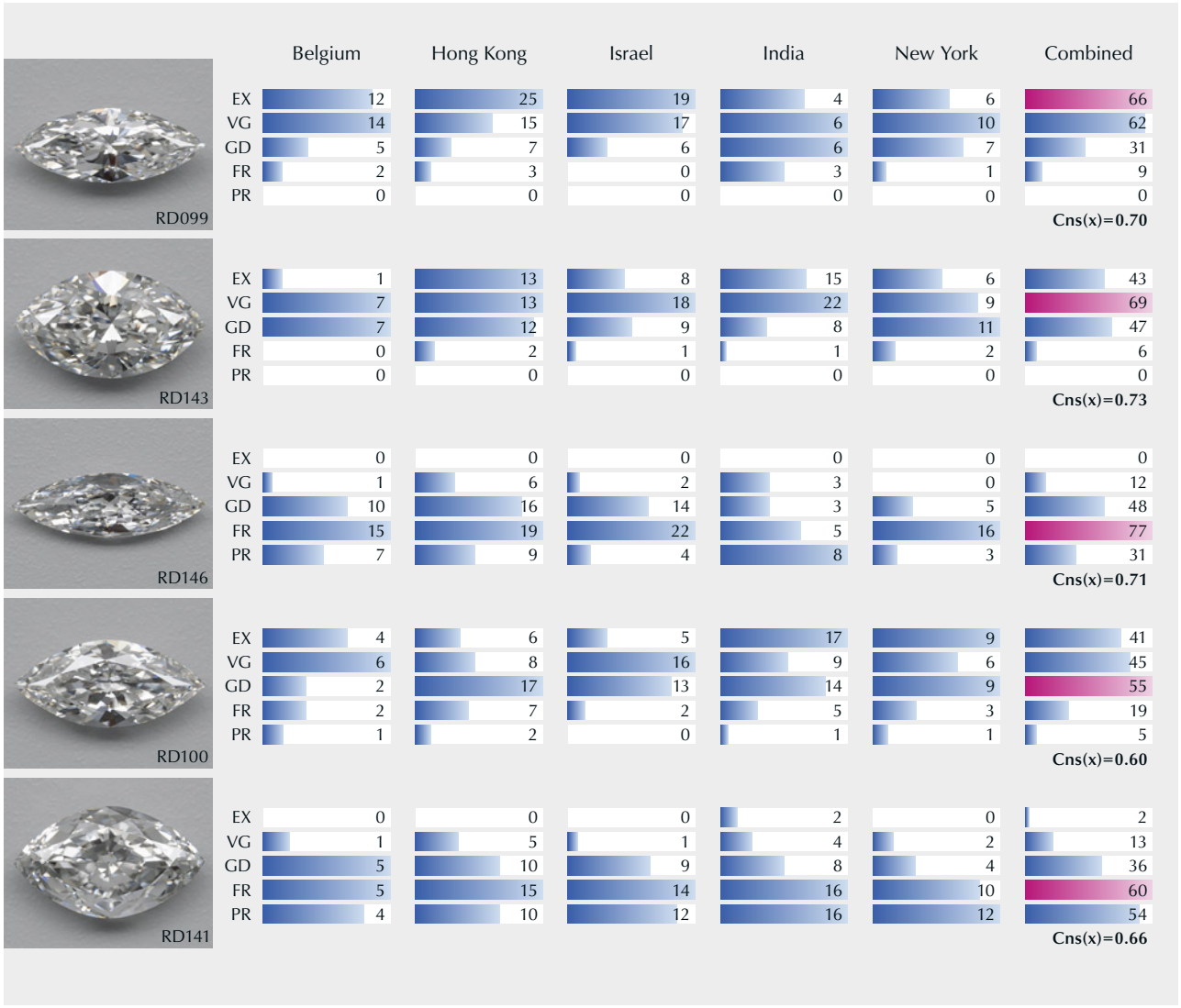

Figure 8. International trade observers also evaluated the face-up appearance of five marquise-shaped diamonds. Observers agreed well on the high evaluations of RD099 and RD143 and the low evaluation of RD146. The pervasive crushed ice pattern in RD100 produced less observer agreement, with noticeable differences among both India and New York observers. RD141 shows both windowing and crushed ice, and it yielded lower observer agreement.

group and the international group. Both pear shapes have areas of crushed ice in the head and filling the points. The oval shows two arcs of small virtual facets between the large ones in the belly and at both ends. The virtual facet maps for marquise RD099 and oval RD110 are not symmetrical, another pattern aspect that reduces observer agreement. RD099 has large virtual facets across the belly mixed with medium and small virtual facets toward the points. RD110 has more large virtual facets on the left side and top than on the right side or bottom, as well as large arcs of small virtual facets.

DISCUSSION

A great deal has been discovered about the mechanics of human vision over the last 40 years, but vision psychophysics remains a topic of active research (Murray, 2020). Much of that research is conducted with large visual stimuli—objects more than 10 times larger than gem diamonds—so the industry can learn more from the concepts of such research than from its specific experiments.

Further, people vary substantially in their appreciation of particular aspects of the visual display found in these fancy shapes. A useful cut grading system must make visual sense while acknowledging

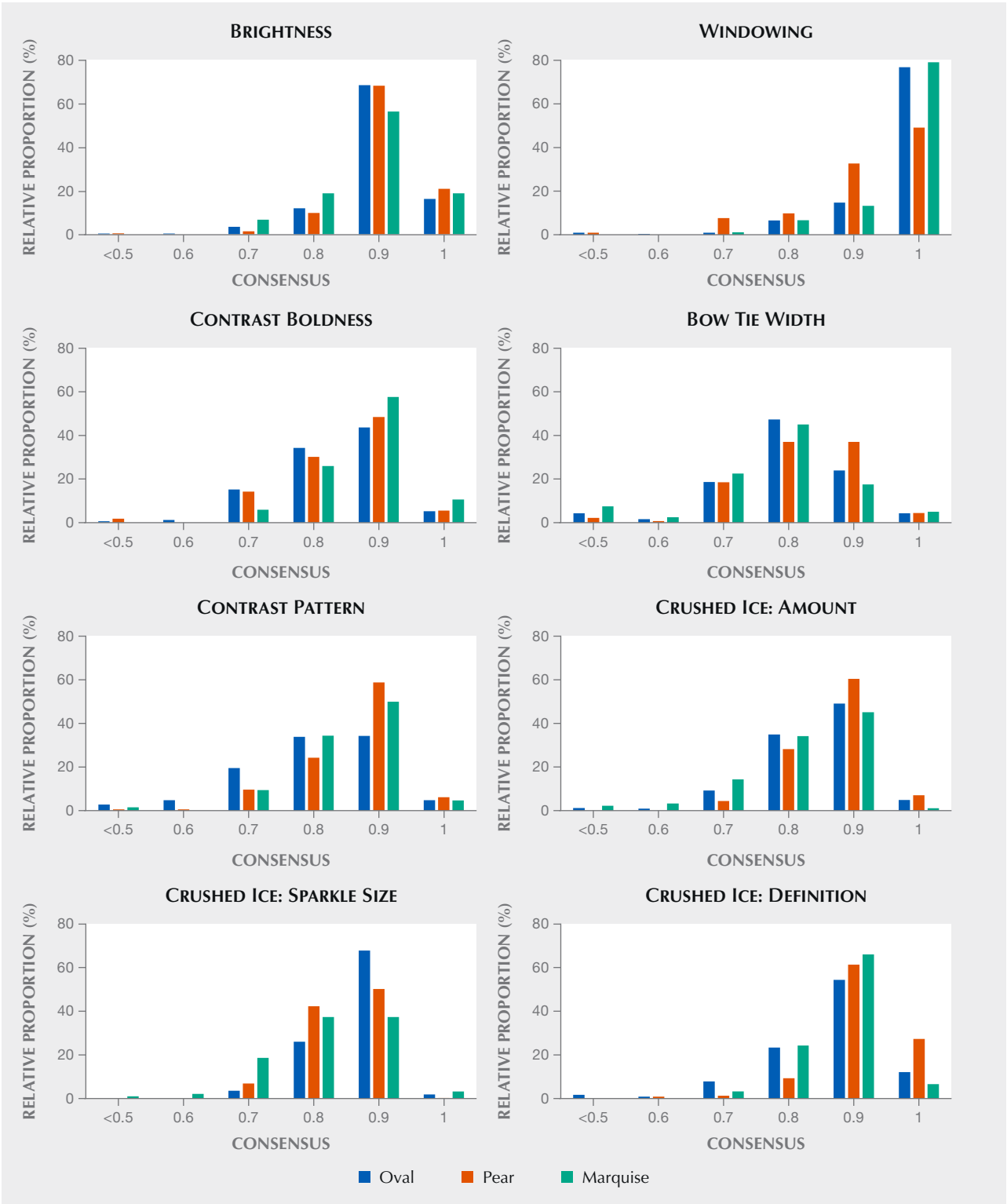

Figure 9. Histograms of consensus values from detailed 2023 observations from the internal team for approximately 350 ovals, 230 pears, and 90 marquise shapes show strong agreement for some visual aspects and more varied opinions on other aspects. Observers showed very strong agreement about the amount of windowing in most of the diamonds, and strong agreement about the assessment of brightness. They showed less agreement about the intensity (boldness) and size of bow tie patterns. Observations of the contrast pattern and properties related to crushed ice patterns show both varied opinions and some shape-related differences for the extent of disagreement.

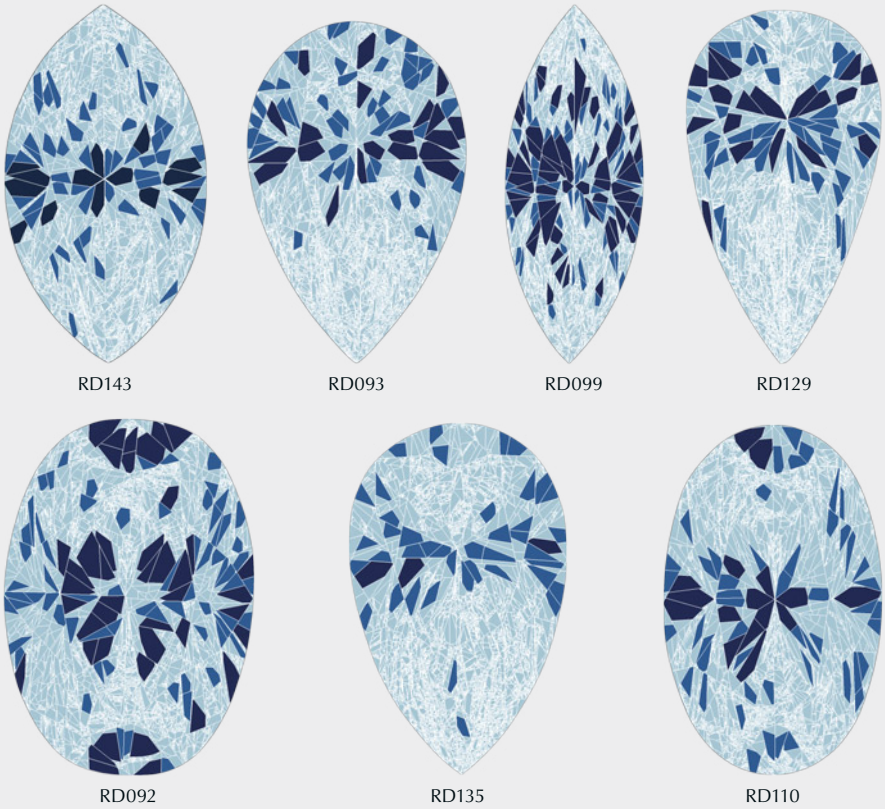

Tucson observers			International observers	
Diamond	Consensus	Avg. rank (among set)	Consensus	Avg. evaluation
RD143	0.75	First	0.73	VG–GD
RD093	0.74	Second	0.71	EX–VG
RD129	0.74	Fifth	0.69	GD
RD092	0.61	First	0.74	EX–VG
RD135	0.60	Third	0.73	EX–VG
RD110	0.55	Fifth	0.63	VG–GD
RD099	0.47	Fourth	0.70	EX–VG

Figure 10. Maps for these seven diamonds show different amounts of small, medium, or large virtual facets, as well as various distributions across the stones. Compare these maps to virtual images of the diamonds found in figures 3, 6, 7, and 8. Observers showed less agreement for diamonds with larger amounts of crushed ice (for the shape) and for those with lower pattern symmetry.

this variance in personal taste. A fancy cut grading system should support consumer confidence for diamond purchases rather than dictate preferred aesthetics. Human observations are thus essential for sorting out which appearance aspects are evaluated similarly by most observers and which are more subject to individual preference.

Observer preferences vary widely with respect to shape outline (see again table 3 and figure 3). Some observers prefer a narrow range of acceptable shape outlines, while others appreciate a greater variety of outlines, such as those with prominent shoulders, flat wings, and a range of point angles. Observer choices for attractive L:W differ significantly from what is commercially available. Given such a broad range of opinions, reporting L:W and some display of the actual outline shape may be more helpful for both the trade and consumer than setting strict grad-

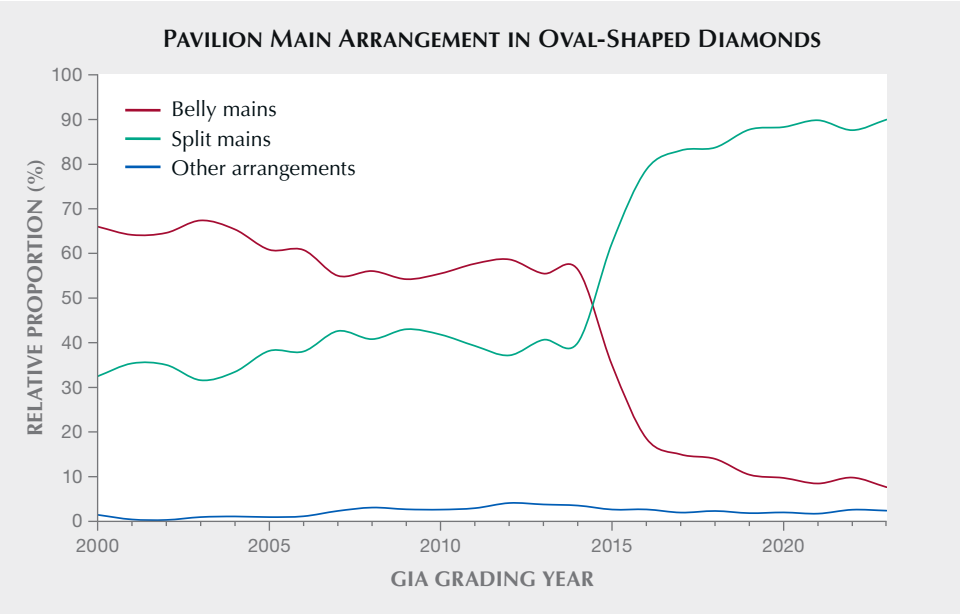

Figure 11. Oval diamonds submitted for GIA grading reports have shown a strong shift over time regarding choices for pavilion main faceting, which minimizes the appearance of bow ties. Before 2014, more than half of the ovals had pavilion mains across the stone width (at the belly). By 2016, that fraction dropped to 20%, with a comparable rise in stones with mains split on either side of the stone's belly. By 2023, nearly 90% of submitted ovals had no belly mains.

ing limits for these factors. An educational context for the outline variations that typically occur in each shape can help the report user understand how a particular diamond compares to others in the marketplace and assess their personal preference.

When GIA added patterns to evaluate round brilliant appearance (Moses et al., 2004), it was possible to define particular pattern deficiencies and scale them from Poor to Very Good based on observations. Diamonds with proportion combinations that produced none of those deficiencies displayed a range of face-up appearance patterns that were all considered attractive by the majority of the observation team or external observers. These observations show that large windows, especially dark-looking windows, are thoroughly disliked (for example, RD137, RD141, RD130, and RD120). However, an approach limited to winnowing out appearance faults will not account for differences in taste regarding the more complicated patterns seen in oval, pear, and marquise diamonds.

We learned that bow tie patterns that are particularly broad, dark, or persistent (as the stone moves) are generally disliked, but opinions diverge as this pattern becomes narrower, less intense, or changes from dark to light with motion. Some observers expect a bow tie pattern in these shapes, while others prefer a minimal bow tie or none at all. Faceting arrangements with pavilion mains across the stone width (at the belly) often enhance the bow tie. Interestingly, starting in 2014, the GIA laboratory saw a marked shift in the faceting arrangements of oval diamonds submitted for grading services (figure 11). Before that year, more than half of the submissions had faceting arrangements that included pavilion mains across the stone's width, while 30–40% did not. Since 2014, the percentage of ovals without belly mains has increased to nearly 90%. These arrangements minimize or eliminate the bow tie, and such diamonds sell more easily.

The results showed low consensus values for diamonds with patterns dominated by crushed ice (for example, RD176 from figure 6 and RD131 from figure 7 and table 2). For diamonds with more mixed patterns (containing areas with large virtual facets), some stones show strong agreement for both higher and lower stone evaluations (e.g., RD093 and RD129), while others show only moderate consensus values (see again figure 10). Lack of symmetry in the virtual facet pattern also leads to lower consensus among observers. The virtual facet map provides an analysis of the size and distribution of crushed ice patterns, and future research can examine more closely how the definition and contrast within such patterns contribute to face-up appearance.

Evaluating the cut fitness of each fancy shape—addressing a range of proportions, potential asymmetries, numerous faceting arrangements, and outline variations—is a vast undertaking. We are working toward an objective evaluation of the important aspects of light interplay with a faceted diamond. At the same time, we seek a grading system that accommodates differences in regional and personal taste among the more complex patterns of fancy shapes.

Diamonds that observers find similar in bright, fiery, and sparkly appearance can exhibit rather different patterns with more varied overall appeal (figure 12). Tools for analyzing and categorizing those patterns, such as the virtual facet map calculated from a diamond's measured wireframe file, may provide a valuable addition to a fancy cut grading system.

CONCLUSIONS

A useful cut grading system for fancy shapes must make visual sense for both the trade and consumer. Observations gathered under consistent conditions provide the foundation for developing such a system. Oval-, pear-, and marquise-shaped diamonds display more complex appearance patterns than standard round brilliants, and observation data reveals how that complexity affects the evaluation of appearance.

The elongation of oval, pear, and marquise shapes produces bow ties and areas of crushed ice for many proportion combinations, faceting arrangements, and outline variations. Observations varied regarding the impact of a bow tie on overall appearance, but large, dark, persistent bow ties are a negative factor. Observers disliked diamonds with large windowing but only showed strong agreement when that window was dark. Observer opinion was widely spread for diamonds with substantial areas of crushed ice (small virtual facets), providing evidence of both personal and regional preferences.

Detailed internal observations of pattern elements in these three shapes demonstrated that observers can agree on semiquantitative descriptions of a diamond's pattern while disagreeing about the appeal of that diamond's appearance. Matters of taste and personal preference for some pattern elements impact observers' evaluation of overall appearance. To serve both the trade and the consumer, a cut grading system for fancy-shaped diamonds should accommodate taste differences and provide clarity for understanding them, in addition to evaluating fundamental appearance aspects.

Mathematical representation of fancy shapes, particularly these three fancy shapes, requires more parameters than the six used for the standard round brilliant—far too many for any kind of proportion charts. Instead, an accurate wireframe representation and ray-tracing simulation must serve as the basis for cut grade evaluation and estimation. The virtual facet maps presented here, calculated from such wireframe files, demonstrate some of the advantages of this approach.

Figure 12. These oval diamonds are attractive—bright, fiery, and scintillating—yet the differences in their appearance patterns are profound, as displayed by the details in the virtual facet maps. Therefore, individual taste becomes an important factor for a grading system to acknowledge.

ABOUT THE AUTHORS
Dr. Ilene Reinitz and Dr. Troy Blodgett are senior research scientists at GIA in New York. Al Gilbertson is a senior research associate, and Dr. James Conant is a research mathematician, at GIA in Carlsbad, California. Amanda Hawkes is the manager of research support, and Abhijith Prabhu is a research engineer, at GIA in Las Vegas.

ACKNOWLEDGMENTS
We sincerely thank Brooke Goedert, Kate Waterman, and Ron Geurts for their contributions to this project. Their insights helped design an effective methodology for collecting useful observation data. Their active participation in the observation process, both locally and during international trips, was instrumental in gathering high-quality data. We thank all the members of the Everest project team for their comments and assistance with figures. We thank Curtis Berry for all his work on the virtual diamond images. Our deepest gratitude goes to the dedicated diamond experts who gave their time to make observations and share their insights.

REFERENCES

Blodgett T., Gilbertson A., Geurts R., Green B., Johnson M., Reinitz I., Yantzer P. (2005) Painting and digging out: Variations on standard brillianteering of round brilliant diamonds, *Rapaport Diamond Report*, June 3, pp. 239–245.

Blodgett T., Gilbertson A., Geurts R., Goedert B. (2011) Length-to-width ratios among fancy shape diamonds. *G&G*, Vol. 47, No. 2, p. 129.

Conant J. (2024) Enumerating diamond cuts. *MATCH (Communications in Mathematical and in Computer Chemistry)*, Vol. 91, No. 3, pp. 593–631, http://dx.doi.org/10.46793/match.91-3.593C

Gilbertson A. (2013) Optimizing face-up appearance in colored gemstone faceting. *G&G*, Vol. 49, No. 2, pp. 64–81, http://dx.doi.org/10.5741/GEMS.49.2.64

Heeger D. (2006) Perception 30 Lecture Notes: Brightness, https://www.cns.nyu.edu/~david/courses/perception/lecturenotes/brightness-contrast/brightness-contrast.html

International Gemological Institute (2022) IGI now issuing cut grade for fancy shapes. September 10, https://www.igi.org/igi-now-issuing-cut-grade-for-fancy-shapes/

International Gemological Institute (n.d.) The grading process. https://www.igi.org/grading-process/

Kingdom F.A.A. (2003) Levels of brightness perception. In L. Harris and M. Jenkin, Eds., *Levels of Perception*. Springer, New York.

Moses T.M., Johnson M.L., Green B., Blodgett T., Cino K., Geurts R.H., Gilbertson A.M., Hemphill T.S., King J.M., Kornylak L., Reinitz I.M., Shigley J.E. (2004) A foundation for grading the overall cut quality of round brilliant cut diamonds. *G&G*, Vol. 40, No. 3, pp. 202–228, http://dx.doi.org/10.5741/GEMS.40.3.202

Murray R.F. (2020) A model of lightness perception guided by probabilistic assumptions about lighting and reflectance. *Journal of Vision*, Vol. 20, No. 7, http://dx.doi.org/10.1167/jov.20.7.28

Sasian J.M., Quick J., Sheffield J., Caudill J., Yantzer P. (2007) Evaluation of brilliance, fire, and scintillation in round brilliant gemstones. *Optical Engineering*, Vol. 46. No. 9, article no. 093604, http://dx.doi.org/10.1117/1.2769018

Sivovolenko S., Shelementiev Y., Holloway G., Mistry J., Serov R., Zhulin S., Zipa K. (2013) How diamond performance attributes: Brilliance, scintillation and fire depend on human vision features. *Australian Gemmologist*, Vol. 25, No. 3, pp. 82–121.

Tastle W.J., Wierman M.J. (2007) Consensus and dissention: A measure of ordinal dispersion. *International Journal of Approximate Reasoning*, Vol. 45, No. 3, pp. 531–545, http://dx.doi.org/10.1016/j.ijar.2006.06.024

Watermeyer B. (1980) *Diamond Cutting: A Complete Guide to Diamond Processing*. Purnell, Cape Town, pp. 251–278.

Yaguchi H. (1987) Heterochromatic brightness matching with checkerboard patterns. *Journal of the Optical Society of America A*, Vol. 4, No. 3, pp. 540–544, http://dx.doi.org/10.1364/JOSAA.4.000540

GEMS & GEMOLOGY®

2024

CONGRATULATIONS

This year, readers from all over the world took the 2024 *Gems & Gemology* Challenge. Participants tested their knowledge by answering questions listed in the Spring 2024 issue. Those who earned a score of 75% or higher received a GIA Certificate of Completion. Participants who earned 96% and above are listed below.

G&G Challenge Winners

Australia
Barbara Wodecki

Canada
Wendy Jamieson
Duncan Parker

Czech Republic
Pavel Hladký

India
Raju Jain

Malaysia
Gam Peih Yinn

Myanmar
War War

Spain
Jose Antonio Gutiérrez Martinez

Ukraine
Maxim Achkasov
Nataliya Vovk

United Kingdom
Paula Santillana

United States
Martin Harmon
Jessica Kramer
Steffano Minetto
Jana Miyahira-Smith
Samantha Shor
Lee Steele
Teresa Tolbert
Kate Trunnell
Flora Walters
Kate Waterman
Elly Wedge
Thomas Wendt
Irma Willey

Answers

See pages 56–57 of the Spring 2024 issue for the questions.

1 (b), 2 (c), 3 (b), 4 (c), 5 (d), 6 (c), 7 (a), 8 (c), 9 (a), 10 (c), 11 (a), 12 (d), 13 (a), 14 (d), 15 (b), 16 (d), 17 (c), 18 (d), 19 (b), 20 (a), 21 (b), 22 (a), 23 (b), 24 (a), 25 (c)

Classification of Gem Materials Using Machine Learning

Matthew F. Hardman, Artitaya Homkrajae, Sally Eaton-Magaña, Christopher M. Breeding, Aaron C. Palke, and Ziyin Sun

Gemstones traded in markets globally can have extremely high values due to their physical appearance and, in some cases, their scarcity. Gemological laboratories provide identification services to determine gemstone species, growth origin, provenance, and the history of color- or clarity-enhancing treatments, all characteristics that can significantly affect gemstone values. These determinations are primarily conducted through microscopic analysis of the gem material and by identifying characteristic features in spectroscopic data acquired using nondestructive techniques. In addition, mildly destructive methods such as laser ablation–inductively coupled plasma–mass spectrometry may be employed to determine the trace element composition of a gem material. Traditionally, the diagnostic criteria used to determine geographic provenance or color/clarity treatment history are selected by trained specialists based on careful evaluation of large research datasets. Identifying the specific features that are useful for classification purposes can be time-consuming, and subtle diagnostic features may be overlooked. Machine learning enables rapid exploration of large, complex datasets in new ways. Hence, the application of machine learning algorithms may complement existing microscopic, spectroscopic, and geochemical approaches.

This study examines the application of several machine learning models to gemstone classification problems involving natural alexandrite, laboratory-grown diamonds, and natural saltwater pearls. Using machine learning in a number of test cases, the authors achieved classification error rates as low as 5% or less for determination of provenance and detection of color treatment and were able to reduce the number of samples classified as indeterminate using conventional techniques by more than 50%.

The market value of diamonds, pearls, and colored stones can be influenced strongly by the species of the material, its physical features (e.g., cut, color, clarity, and size), and its rarity. However, value can also be driven by other factors, such as the geographic provenance of the material, growth origin (natural or laboratory-grown), or its history of color- or clarity-enhancing treatments. Gemological laboratories offer identification services that provide consumers with this type of information, as it can aid in defining the value of a gem. This process also protects consumers by reducing the number of erroneously or fraudulently traded gems, such as laboratory-grown diamonds that are marketed as natural.

See end of article for About the Authors and Acknowledgments.
Gems & Gemology, Vol. 60, No. 3, pp. 306–329,
http://dx.doi.org/10.5741/GEMS.60.3.306

At GIA, geographic provenance and treatment history are determined by comparing unclassified gems against large curated databases of samples from the same species, for which the provenance or treatment history are independently known. Microscopic examination is generally the first stage of analysis, identifying diagnostic physical features (e.g., mineral inclusions indicative of certain localities; Palke et al., 2019a,b). The gem material can also be characterized using a variety of nondestructive analytical techniques including photoluminescence (PL), Raman scattering, ultraviolet/visible/near-infrared (UV-Vis-NIR) absorption, and Fourier-transform infrared (FTIR) absorption spectroscopy. GIA's traditional approaches to comparison of these data include visual inspection of spectra, identifying peaks and bands as well as their relative intensities, and in some cases using automated software for spectral matching (e.g., the WiRE package for Renishaw Raman devices). For diamonds, these features reflect atomic defects in the

lattice, which are created or destroyed during growth and color- or clarity-enhancing treatments (Martineau et al., 2004; D'Haenens-Johansson et al., 2022).

For some colored stones and pearls, minimally destructive methods such as laser ablation–inductively coupled plasma–mass spectrometry (LA-ICP-MS) can determine the elemental composition. This technique removes a small amount of material from the stone, which may leave a tiny crater approximately 55 µm in diameter. These chemical data are compared with gem databases using bivariate scatterplots or "selective plotting," as research has shown that trace element compositions can indicate geographic origin (e.g., Groat et al., 2019; Palke et al., 2019a,b). Selective plotting is an advanced classification technique that can reduce the compositional overlap between gemstones in bivariate diagrams by filtering the reference data to only those samples with similar elemental concentrations as the unclassified stone, considering multiple trace elements simultaneously. For example, unclassified and reference stones might be plotted on a bivariate diagram using magnesium and iron concentrations; the reference stones shown on the plot would be filtered to those with similar compositions of other elements as well, such as titanium or gallium (see Palke et al., 2019a for a detailed overview). This approach reduces the compositional overlap between gemstones of different provenance when applied to alexandrite, ruby, and sapphire (Sun et al., 2019; Palke et al., 2019a,b).

In Brief

- Machine learning methods including random forest, artificial neural networks, and support vector machines can enhance classification of gem materials.
- Machine learning methods are effective tools for determining the provenance of alexandrite and saltwater pearls.
- Subtle indicators of post-growth treatment in some laboratory-grown diamonds can be identified using machine learning.

To determine geographic provenance or treatment history using these approaches, each group of samples must have sufficiently distinct characteristics to allow separation. In practice, however, a single characteristic is generally not diagnostic enough for determination, and multiple forms of evidence are needed. This becomes much more difficult when samples lack a particular set of characteristic features (e.g., a lack of inclusions). When gemological specialists cannot observe clear diagnostic features, even after careful examination of all data, a classification of "undetermined" may be given.

To address this challenge, we investigate machine learning (ML) as a complementary tool to existing classification approaches. The criteria used for gemstone classification at GIA—physical features, spectroscopic characteristics, and elemental compositions—are selected based on years of detailed examination, resulting in recognizing patterns related to gemstone characteristics and their provenance or treatment history. Directing computer algorithms to identify patterns among large datasets, in a manner similar to that of a gem specialist, may provide new insights.

BACKGROUND

Gemological laboratories have acquired spectroscopic and trace element data for millions of diamonds, colored gemstones, and pearls collectively. By carefully inspecting these databases, trained specialists can identify characteristic features that can be used to determine geographic provenance or treatment history for new samples. However, the massive scale of available data, coupled with the complexity of different gem materials and the constantly evolving techniques for growing and treating them (e.g., Eaton-Magaña et al., 2024), make it time-consuming to identify the most useful classification criteria through manual inspection. As a result, subtle diagnostic features may be overlooked. Computers can rapidly parse large datasets, and some software already provides functions that enable users to match features in acquired data (such as Raman spectra) to extensive reference databases. Hence, computers are powerful tools that complement existing traditional approaches.

Artificial intelligence (AI) is the use of computer systems to emulate the way humans think, process information, and learn. ML is a subfield of AI associated with developing algorithms to learn from datasets in order to identify patterns or solve particular problems without requiring explicit programming (Xu et al., 2021). The application of ML in the physical sciences has increased in recent years, with successful uses in fields including the evaluation of the mantle and exploration for diamonds and kimberlites (Dawson and Stephens, 1975; Griffin et al., 2002; Hardman et al., 2018a,b), as well as mineral

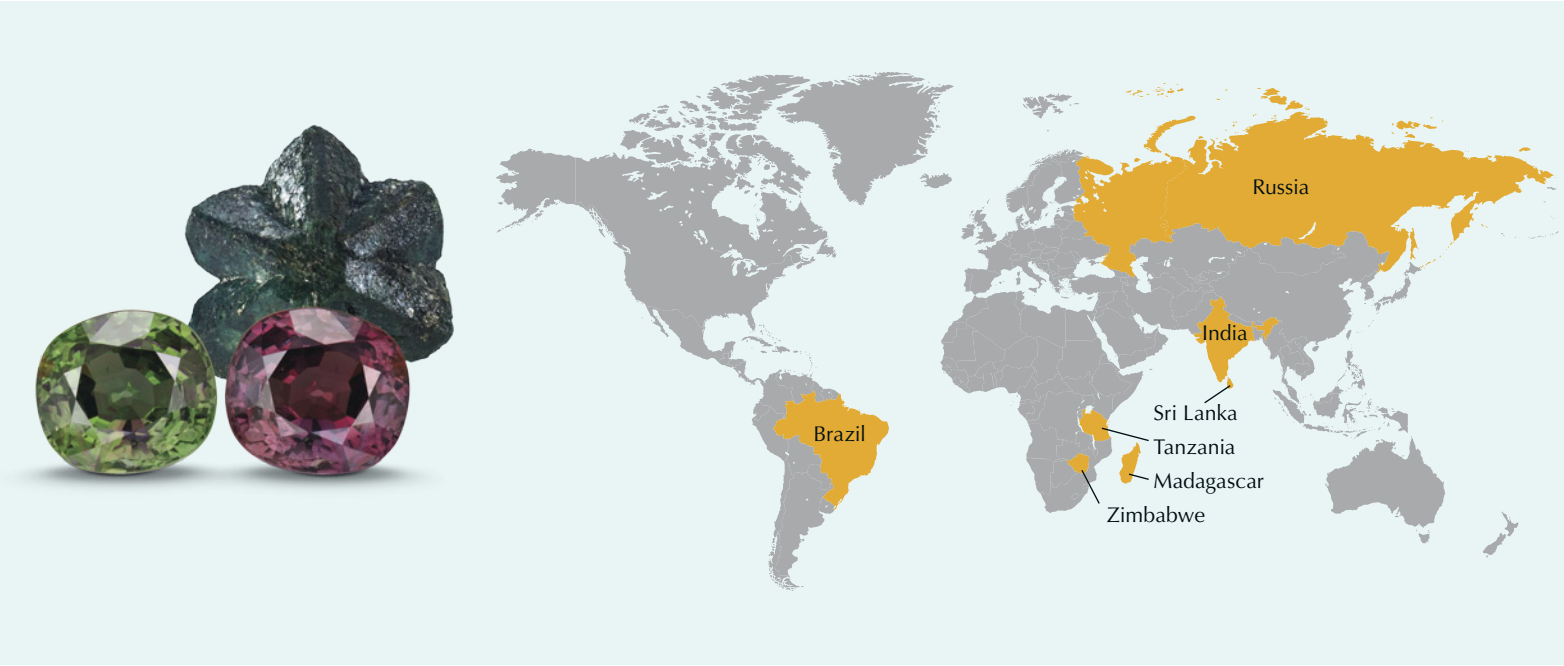

Figure 1. Left: Faceted alexandrite with color-change effect, with a rough crystal for comparison. The green color of the faceted stone is visible when exposed to daylight-equivalent illumination, while the red color is visible when exposed to incandescent illumination. Photos by Robert Weldon; rough crystal courtesy of William F. Larson and faceted stone courtesy of GIA's Dr. Edward J. Gübelin collection, no. 34767. Right: World map indicating seven major alexandrite sampling localities. Other sampling localities are not discussed in this study (e.g., Sun et al., 2019).

chemistry and characterization (Schönig et al., 2021; Hazen and Morrison, 2022). The application of ML to gemological problems—including provenance determination—has also increased over time (e.g., Blodgett and Shen, 2011; Luo et al., 2015; Homkrajae et al., 2019; Krebs et al., 2020; Hardman et al., 2022; Bassoo et al., 2023; Bendinelli et al., 2024).

Applying ML to gemological research can yield significant benefits. For example, while the selective plotting approach surpasses bivariate scatterplots for classifying some colored stones, some samples still cannot be classified. ML allows the comparison of even more variables simultaneously and can reveal subtle classification criteria involving multiple variables with complex relationships that may not be apparent using bivariate scatterplots or selective plotting. Using these criteria, ML models can be automated to assist gemologists by suggesting a classification. This opinion can be quite valuable in making a confident judgment. However, some samples will still exhibit too much compositional overlap to be classifiable even with ML.

This study provides an overview of ML approaches to gem classification, including some that are in active use at GIA. We examine the applications of ML to three distinct gem materials for which GIA offers laboratory report services (alexandrite, laboratory-grown diamonds, and natural saltwater pearls) and discuss the advantages of ML over traditional approaches.

MATERIALS

Alexandrite. Alexandrite, a variety of the mineral chrysoberyl ($BeAl_2O_4$), has a unique color-change property when exposed to different light sources (for example, from green or green-blue in daylight to red in incandescent lighting; figure 1, left). This property is caused by trace concentrations of Cr^{3+} replacing Al^{3+} in the crystal lattice (Gübelin and Schmetzer, 1982). GIA provides services for determining the geographic origin of alexandrite (figure 1, right).

Alexandrite provenance determination is conducted at GIA using microscopic analysis to identify physical features such as mineral inclusions that may be characteristic of different sampling localities (Sun et al., 2019). Trace element compositions offer additional information. While alexandrite from different localities can have very similar compositions, possibly due to similar geological processes, the compositions can also vary significantly between localities (Sun et al., 2019). Data acquired for unknown stones are compared to curated databases of alexan-

TABLE 1. Summary of gem materials classified in this study.[a]

Gem	Locality	Samples	Analyses
Alexandrite[b]	Brazil	174	528
	India	27	81
	Madagascar	38	132
	Russia	42	153
	Sri Lanka	33	170
	Tanzania	27	80
	Zimbabwe	5	13
	Treatment	**Samples/spectra**	
CVD-grown diamond[c]	As-grown/untreated	300	
	Post-growth treated	1,795	
	Locality	**Samples**	**Analyses**
Natural saltwater pearl[d]	Bahrain	268	843
	Kuwait	188	588
	Oman	148	444

[a]*Between 3 and 5 spots were measured on each pearl, and between 2 and 10 spots on each alexandrite. A single spectrum was acquired for each CVD-grown diamond.*
[b]*Sun et al. (2019)*
[c]*Hardman et al. (2022)*
[d]*This study*

drite with known provenance, using bivariate scatterplots and selective plotting. As it is uncommon for one or even two chemical variables to separate a group of samples from all others, selective plotting offers significant advantages over bivariate techniques by enabling comparison of more variables simultaneously. Despite these techniques, the provenance of some stones remains unclear.

To test the capability of ML to improve alexandrite provenance determination, the authors compiled the concentrations of the trace elements boron, magnesium, vanadium, chromium, iron, gallium, germanium, and tin for samples from mines located in seven countries. These alexandrites, detailed by Sun et al. (2019), represent a portion of the samples in GIA's colored stone reference collection, consisting of stones with known sampling locality that were loaned to GIA by individual donors. The number of stones from each sampling locality is given in table 1. Trace element compositions were acquired by LA-ICP-MS, originally reported by Sun et al. (2019) and summarized in table 2. We have compiled data for 10 additional samples with chemical compositions yielding inconclusive provenance determinations using traditional bivariate scatterplot and selective plotting approaches. We calibrated new ML models using samples with known provenance and applied these models to classify the population of "undetermined" alexandrites.

CVD-Grown Diamonds. Diamonds can be grown using chemical vapor deposition (CVD) by placing a diamond substrate within a vacuum chamber at moderate temperatures (approximately 700° to 1300°C) and subatmospheric pressures (generally 20–500 mbar; figure 2); see Arnault et al. (2022) and D'Haenens-Johansson et al. (2022) for reviews on CVD growth. CVD-grown diamonds can be treated

TABLE 2. Trace element concentrations (in ppmw) of alexandrite from global localities, determined by LA-ICP-MS.[a]

Element	Brazil (174 samples, 528 analyses)		India (27 samples, 81 analyses)		Madagascar (38 samples, 132 analyses)	
	Range	Average ± 2σ	Range	Average ± 2σ	Range	Average ± 2σ
B	bdl–42.7	2.5 ± 12.5	bdl–68.9	10.9 ± 29.6	0.78–225	54.9 ± 84.4
Mg	2.5–46.7	11.9 ± 10.8	38.4–203	104.3 ± 55.9	4.92–337	64.5 ± 125.1
V	56.8–201	136.1 ± 52.7	314–1210	722.0 ± 365.6	13.6–468	132.6 ± 187.2
Cr	424–6050	2955 ± 1993	192–2120	1090 ± 907	43.4–3430	875 ± 1206
Fe	4180–11500	6352 ± 2048	829–4610	2898 ± 2108	1060–12100	5771 ± 4221
Ga	53.3–145	72.8 ± 21.1	168–284	199.4 ± 41.8	50.9–1070	383.8 ± 385.4
Ge	bdl–2.55	0.71 ± 0.77	bdl–1.68	0.32 ± 0.45	bdl–2.55	0.38 ± 0.94
Sn	87.4–4470	870.6 ± 824.2	0.28–6.01	1.7 ± 2.4	0.82–327	43.8 ± 133.4

[a]*Between 2 and 10 spots were measured on each alexandrite.*

after growth under high-pressure, high-temperature (HPHT) or low-pressure, high-temperature (LPHT) conditions to improve their color grade. Several of GIA's grading reports for laboratory-grown diamonds document any evidence of post-growth treatment.

Lattice defects form during CVD growth and may manifest as peaks or bands in PL spectra (e.g., figure 3;

Figure 2. Left: A 0.21 ct HPHT-treated CVD-grown diamond. Photo by Robison McMurtry. Right: Schematic diagram of a CVD reactor. From D'Haenens-Johansson et al. (2022).

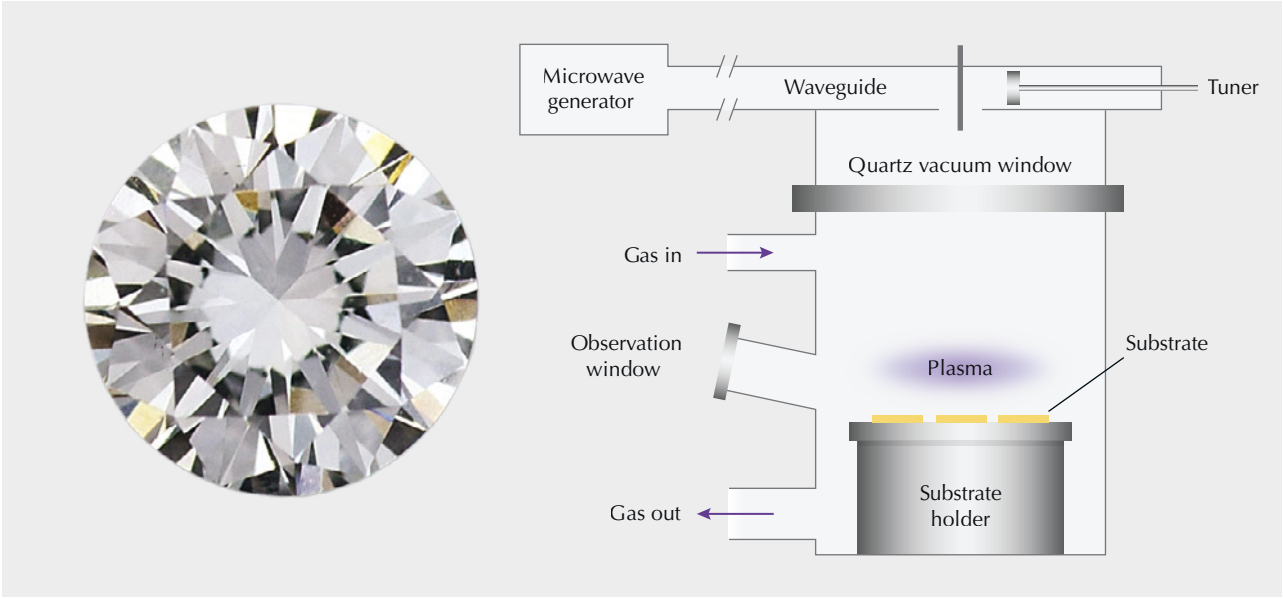

TABLE 2 (continued). Trace element concentrations (in ppmw) of alexandrite from global localities, determined by LA-ICP-MS.[a]

Element	Russia (42 samples, 153 analyses)		Sri Lanka (33 samples, 170 analyses)		Tanzania (27 samples, 80 analyses)		Zimbabwe (5 samples, 13 analyses)		Detection limit (ppmw)
	Range	Average ± 2σ	Range	Average ± 2σ	Range	Average ± 2σ	Range	Average ± 2σ	
B	15.5–208	45.0 ± 83.6	23.1–400	81.6 ± 114.2	4.21–87.8	28.3 ± 33.9	bdl–12.4	7.95 ± 8.14	0.12
Mg	4.47–3140	93.0 ± 718.7	2.95–987	169.7 ± 390.3	24–270	53.3 ± 67.6	10.9–38.3	20.5 ± 16.5	0.024
V	21.5–347	101.7 ± 132.1	29.8–1190	210.9 ± 373.0	33.2–241	76.1 ± 75.1	19.1–50.6	31.2 ± 21.4	0.015
Cr	156–14200	3092 ± 6352	24.1–3200	702 ± 1202	232–8270	1991 ± 2763	2550–15600	8704 ± 8807	0.21
Fe	1390–8610	2784 ± 2359	1720–12200	7676 ± 4801	2470–9210	5623 ± 2732	7480–25000	14064 ± 10164	1.3
Ga	171–406	262.9 ± 107.4	246–1580	731.4 ± 720.5	54.9–212	94.1 ± 59.4	269–343	312.5 ± 48.2	0.019
Ge	1.08–76.4	10.3 ± 32.1	0.1–2.7	0.59 ± 1.08	bdl–4.48	0.87 ± 1.49	bdl–3.19	1.81 ± 2.14	0.074
Sn	37.9–1550	324.1 ± 523.5	7.35–785	57.9 ± 217.0	3.56–192	22.9 ± 66.4	338–2110	1204 ± 1144	0.046

[a]*Between 2 and 10 spots were measured on each alexandrite.*

Martineau et al., 2004). The post-growth treatment process may create, destroy, or alter the concentration or distribution of lattice defects (figure 3; Martineau et al., 2004; D'Haenens-Johansson et al., 2022). Therefore, treatment can be detected by interpreting PL spectroscopic data. However, the full suite of potential treatments applied to CVD-grown diamonds is not always disclosed by manufacturers, and these processes can change over time. GIA seeks to identify all forms of post-growth treatment. This

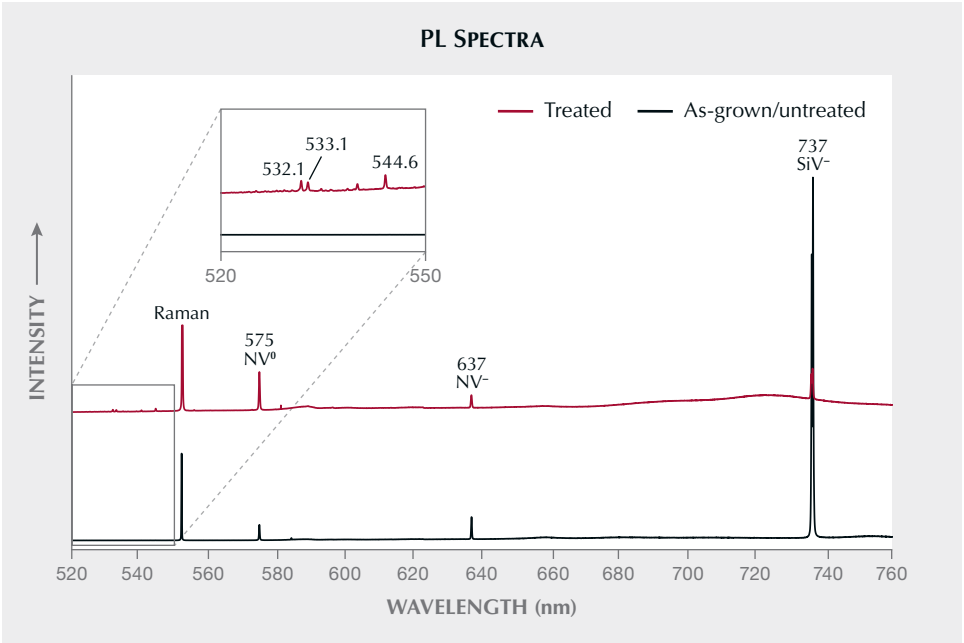

Figure 3. Example PL spectra for different as-grown (untreated) and post-growth treated CVD diamonds acquired at liquid nitrogen temperature (approximately 77 K) using 514 nm laser excitation. The spectra are offset vertically for clarity and scaled so that the Raman peaks (at 552.4 nm) have equal intensity. Inset: An enlarged view highlights the occurrence of multiple weak features in some diamond spectra in the 520–550 nm range. NV = nitrogen-vacancy and SiV = silicon-vacancy defects, with neutral (^{0}) or negative ($^-$) charge states.

Figure 4. Left: Representative natural saltwater nacreous (light-colored) and non-nacreous (dark-colored) pearls produced by Pinctada radiata *mollusks from Kuwait in the Persian (Arabian) Gulf. Photo by Robert Weldon; courtesy of Ahmad Abdullah Alomaish Alajmi. Right: Map showing the location of Bahrain, Kuwait, and Oman.*

study assesses the capability of ML in establishing new criteria for the identification of post-growth treatment in CVD-grown diamonds. PL spectra were compiled for 300 as-grown (untreated) and 1,795 HPHT-treated CVD-grown diamonds (D–Z color range), measured during routine analysis of diamonds submitted by clients to GIA. Each determination of treated or untreated was made by trained specialists based on inspection and comparison of PL spectra and surface fluorescence patterns. These spectra were acquired with 514 nm laser excitation at liquid nitrogen temperature (approximately ~77 K) using a Renishaw inVia Raman microscope at 5× magnification. They were previously compiled by Hardman et al. (2022).

Natural Saltwater Pearls. Pearls differ from many other gem materials in that they are formed organically from a mollusk. Shells and pearls are composed of calcium carbonate ($CaCO_3$) together with organic substances called *conchiolin*, plus a small volume of water. Pearls have a wide variety of trace element compositions that can be inherited from different growth-related processes and the environment in which they formed (Fuge et al., 1993). They can also have nacreous surfaces (featuring a layered structure of aragonite platelets in "brick-and-mortar" formation and commonly with pearly luster) or non-nacreous surfaces (lacking pearly luster; figure 4). Calcite and aragonite are polymorphs, minerals having the same chemical composition (i.e., $CaCO_3$) but different structure. Pearls are produced by a variety of different mollusk species and can form in a variety of freshwater and saltwater environments globally. They can form naturally or be cultured, grown through human intervention. This complex set of features increases the difficulty of evaluating the relationships between pearl compositions and growth conditions.

GIA's pearl identification services include a determination of natural or cultured identity, mollusk species, saltwater or freshwater formation environment, and the presence of any treatment. ML has been previously applied to determine the provenance of freshwater pearls using trace element compositions (Homkrajae et al., 2019), while pearls formed in saltwater environments have not been tested as thoroughly. To evaluate whether the provenance of saltwater pearls can be determined, the authors compiled trace element compositions measured by LA-ICP-MS for a set of 604 new natural saltwater pearls sampled from Oman, Bahrain, and Kuwait (table 3). Pearls from all three localities were sourced from local pearl divers and classified as C1 samples according to the GIA pearl classification codes (see table 1 in Homkrajae et al., 2021). The Bahrain and Kuwait pearls reportedly originated from *Pinctada radiata* mollusks from the Persian (Arabian) Gulf, while the Oman pearls were derived from *Pinctada margaritifera* mollusks in the Gulf of Oman region. Trace element compositions were determined using a Thermo Fisher Scientific iCAP Qc ICP-MS coupled with a New Wave Research UP-213 laser ablation unit using the same analytical parameters as Homkrajae et al. (2019). We analyzed between three and five spots on each sample and report the compositions of six elements (sodium, magnesium, potassium, manganese, strontium, and barium) in table 3.

METHODS

Data Processing. For this study and for statistical analysis in general, datasets need to be reprocessed from their original form into a format that is better

TABLE 3. Trace element concentrations (in ppmw) of natural saltwater pearls from Bahrain, Kuwait, and Oman, determined by LA-ICP-MS.[a]

Element	Bahrain (268 samples, 843 analyses)		Kuwait (188 samples, 588 analyses)		Oman (148 samples, 444 analyses)		Detection limit (ppmw)
	Range	Average ± 2σ	Range	Average ± 2σ	Range	Average ± 2σ	
Na	2710–10000	5887 ± 1700	2880–8050	6316 ± 1779	3350–9910	5154 ± 1162	3.9
Mg	27.8–12300	839.0 ± 4458.3	26.2–13300	533.5 ± 3564.5	43–7850	280 ± 1111	0.25
K	bdl–289	48.19 ± 64.62	bdl–501	51 ± 83	bdl–153.0	24.4 ± 21.5	1.3
Mn	bdl–42.8	1.35 ± 1.72	0.05–12.30	1.13 ± 3.40	bdl–17.7	3.0 ± 4.3	0.05
Sr	604–2330	1012 ± 423	610–3020	998 ± 389	746–2040	1150 ± 399	0.1
Ba	v0.12–4.83	0.66 ± 1.18	0.11–8.81	0.78 ± 1.16	bdl–1.19	0.37 ± 0.34	0.005

[a]*Between three and five spots were measured on each pearl.*

suited to a particular statistical method. Trace element concentrations reported in units of parts per million by weight (ppmw) can be used in comparisons, including in bivariate scatterplots. For some statistical models, however, trace elements with very low concentrations—near or below the instrument's detection limit—must be identified. We replace these values with the respective detection limit for each element so they can be processed using statistical methods. This reduces uncertainties for values near the analytical detection limit, but it is worth noting that the data distribution will be shifted slightly higher than if all such values were replaced with zero. During trace element analysis of pearls and colored gemstones, GIA typically tests three spots on each sample to ensure data quality and to assess the diversity of compositions that some samples may have: Some samples may have significant compositional heterogeneity that cannot be characterized with a single analytical spot.

Spectroscopic data is often presented graphically, with measured intensity (on the y-axis) for a variety of wavelengths (on the x-axis; e.g., figure 5). The

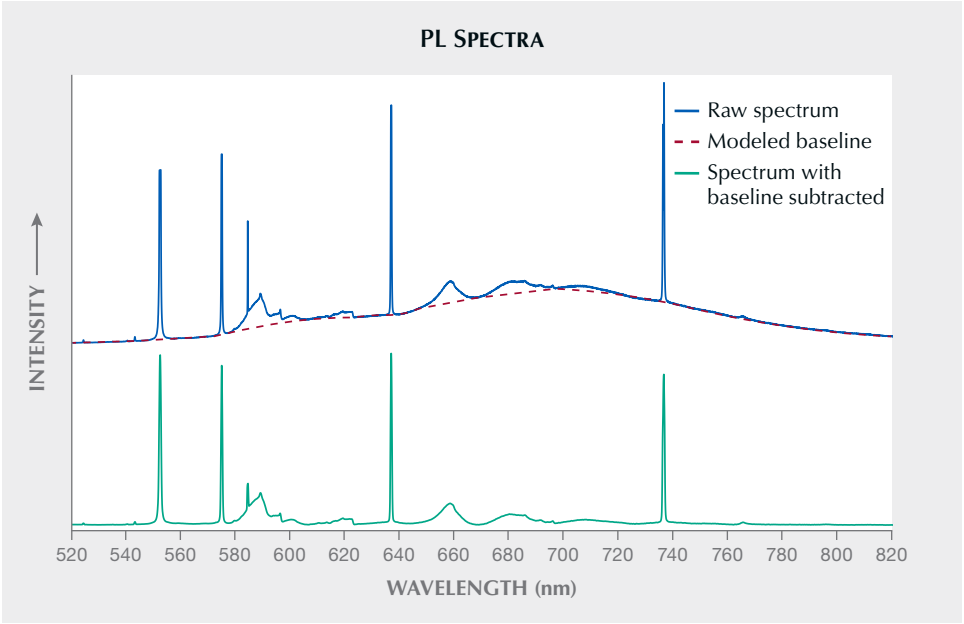

Figure 5. Example PL spectra measured using 514 nm laser excitation, before and after subtraction of a modeled baseline.

spectra may display bands and/or peaks corresponding to particular defects or features in the material being analyzed. Some spectra may have significant "backgrounds," appearing as broad bands in certain regions of the spectrum (figure 5). To determine the areas of some peaks, this background must first be removed. To reduce the background effects in this study, a modeled baseline was subtracted from each spectrum (figure 5). Background effects can also introduce noise, or generally weak spectroscopic features unrelated to the sample itself. Under some circumstances, noise can be strong enough to be confused with an actual peak. If noise is inadvertently used to calibrate a statistical model, the model outputs may be unpredictable or meaningless, so it is very important to identify these features. We have screened all spectra in this study to identify actual peaks, but note that distinguishing a weak peak from noise may be difficult or impossible in some cases.

For CVD-grown diamonds, peak heights above background levels can be calculated and compared with other spectra, including those from CVD-grown diamonds previously classified as treated or untreated. However, PL spectra are semiquantitative, and peak heights can vary due to factors such as changes in laser power during analysis. To compare peak heights across different spectra, the peak height can be normalized by dividing it by the height of the diamond Raman line (with a peak position of 552.4 nm when measured with a 514 nm laser; figure 3). This line corresponds to diamond's intrinsic Raman peak at 1332 cm^{-1}.

Data can also be transformed into a different structure to better fit the requirements of particular ML models. In reality, data populations can have nonsymmetrical distributions (figure 6, left), skewing toward high or low values rather than a clear central value (as is expected for normal or Gaussian distributions). For example, iron concentrations in an alexandrite database may have a nonnormal distribution similar to that in figure 6, left. However, some statistical models require that calibration data have approximately symmetrical distributions. Log transformation, which replaces all values in a dataset with their logarithms, can shift a population of nonnormal data closer to normality while preserving the relative distribution of their values (figure 6, right). In addition, variables in some datasets may have very different scales. For example, some elements may have concentrations at the parts per thousand level and others at the parts per million

Figure 6. Left: An arbitrary dataset with a nonsymmetrical distribution that has a negative skew (tail to the left) compared to an ideal normal (Gaussian) distribution. Right: The same set of values following log transformation.

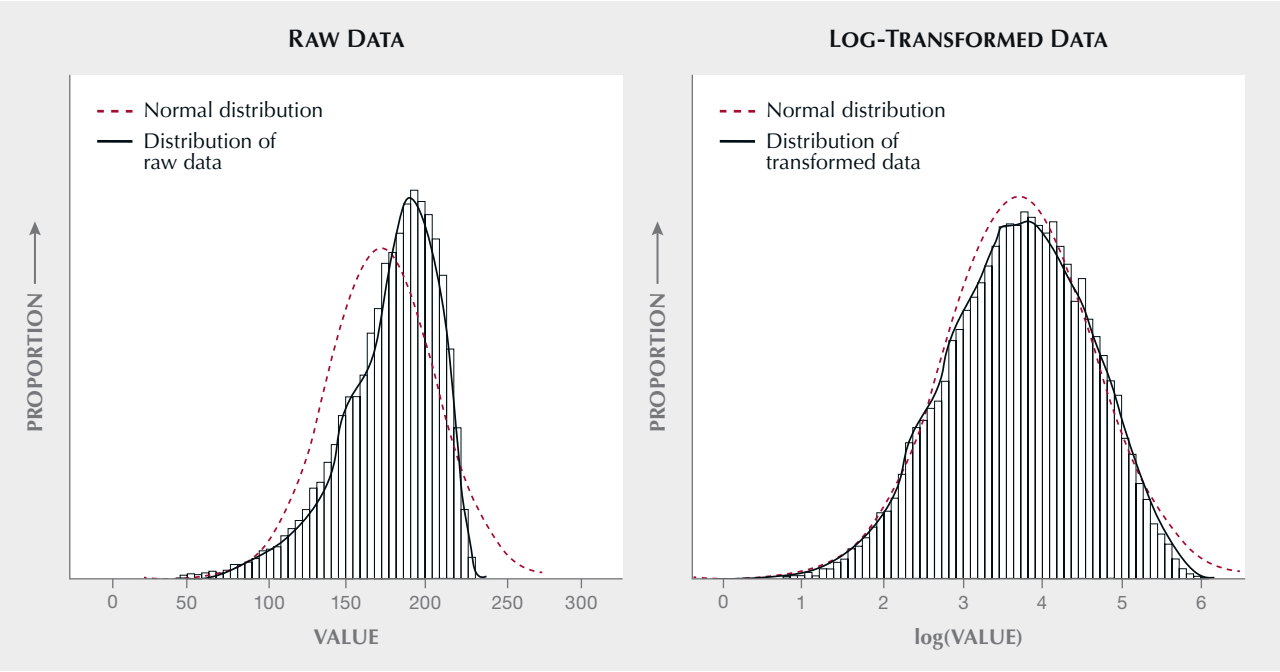

level. These data can be rescaled to improve the comparability of all data by preserving their relative order but adjusting their distributions to cover approximately the same range.

To perform statistical analysis in this study, we imported trace element and spectroscopic data files into the R statistical freeware package (v4.3.2; R Core Team, 2024). Using R, all trace element and spectroscopic data were rescaled and log transformed. Example scripts can be accessed in the appendix available online (https://www.gia.edu/gems-gemology/fall-2024-machine-learning).

Model Calibration and Validation. At GIA, traditional approaches to colored stone classification include the use of bivariate scatterplots and selective plotting to compare trace element compositions. For stones with compositions that overlap with multiple populations using these methods, statistical models can add more classification variables to enhance discrimination. For trace elements, this may mean considering larger numbers of elements, as compositional overlap in analyzing the concentrations of two elements may be reduced by using three or more elements.

An initial step is dataset *simplification*, particularly if the dataset contains many samples, each with a large number of variables. Principal component analysis (PCA) and linear discriminant analysis (LDA) are techniques that can simplify a dataset by projecting the relationships between many variables onto fewer dimensions for easier interpretation (box A). The dataset can then be visualized using bivariate scatterplots with the transformed variables as axes (see box A), or PCA or LDA can be used to preprocess a dataset for subsequent use in more complex ML models.

The choice of ML model depends on the goals of the user (see box B). Some models are extremely interpretable and intuitive, such as decision trees where the logic of decision-making is provided directly to the user for easy application. Other models are more "black box" in nature, involving complex computational, mathematical, or statistical logic hidden from the user. In these cases, the user inputs data and receives an outcome from an opaque computer model. In general, the more complex models are much more difficult to interpret but also more powerful and capable of producing better results. ML models discussed in this study include random forest (RF), support vector machines (SVM), and artificial neural networks (ANN). Box B provides an overview of all three. Previous research has documented the advantages and disadvantages of these models when applied to different problems, with RF in particular performing extremely well in many different fields (e.g., Fernández-Delgado et al., 2014; Bolton et al., 2019).

Feature selection is an application of ML that objectively analyzes a dataset to identify variables that have a strong influence on classification. The "Boruta" algorithm, for instance, ranks all statistically significant variables in a dataset by testing whether their exclusion leads to a significant decrease in model performance (box B; Kursa et al., 2010). This list can then be inspected more closely by a user. For datasets with hundreds or thousands of variables, feature selection saves significant time and effort.

Validation is extremely important. ML models are often reported with *error rates*, values that indicate their success in making correct classifications. Ideally, models with low error rates will produce more accurate results when testing new samples. One approach to accurately evaluate model quality is *k*-fold cross-validation, in which a dataset is partitioned into a random subset for model calibration (e.g., 80%) and the remainder is allocated to testing the model (e.g., 20%). This process is repeated k times, with k chosen by the user. The error rates of all folds are averaged to provide a measure of model quality. By using a larger k value, the average error rate of all folds will generally be less biased toward the results of individual folds (Hastie et al., 2009). ML models can be recalibrated and retested to improve model quality and reduce error rates.

An additional measure of quality is classification *confidence*, which indicates the probability that an individual result produced by the ML model is accurate. Some ML models will output a classification probability with every decision, indicating the model's confidence in its own decision. When testing an unclassified sample using an ML model, the user can accept or reject the classification based on this probability value. For classification problems with two possible outcomes, a probability value of approximately 50% indicates low certainty for either outcome, possibly due to the unclassified sample having similar characteristics to both groups. The threshold probability that users will set during decision-making is subjective and may be chosen by comparing with the probabilities assigned to stones with known origin. It is important to consider confidence values before accepting ML results.

Box A: Dimensionality Reduction

Analyzing large datasets with many different variables per sample can make it difficult or impossible to uncover complex relationships or subgroups of samples hidden among the data. Principal component analysis and linear discriminant analysis are dimensionality reduction techniques that can be used to simplify large datasets, identifying key relationships and condensing meaningful information into fewer variables.

PCA reduces the number of dimensions in a dataset by transforming the data, producing a new list of variables called principal components. These components retain as much information as possible from the original data but are much simpler to visualize. Principal components are linear combinations of the starting variables, structured in such a way that the first principal component represents the majority of the variance of the data, with the second principal component representing additional variance, but less than the first. Additional components represent progressively less variance. Therefore, most of the variation in a dataset can be explored or visualized using fewer variables. PCA results shown in a bivariate scatterplot can be a valuable tool (e.g., figure A-1). The relative distribution of data highlights differences and similarities between samples. Vectors superimposed

Figure A-1. Example plot of principal components 1 and 2 in two-dimensional space. Vectors corresponding to five variables used to generate the PCA solution are indicated. Variables 3 and 5 may be positively correlated (as they have similar length and direction), and both strongly influence principal component 1. Variables 2 and 4 may be negatively correlated, given their opposing direction; both variables strongly influence principal component 2 (positively and negatively, respectively). Each principal component is a linear combination of the original variables. The numerical values for each principal component do not have any physical meaning but convey the level of variation between data points.

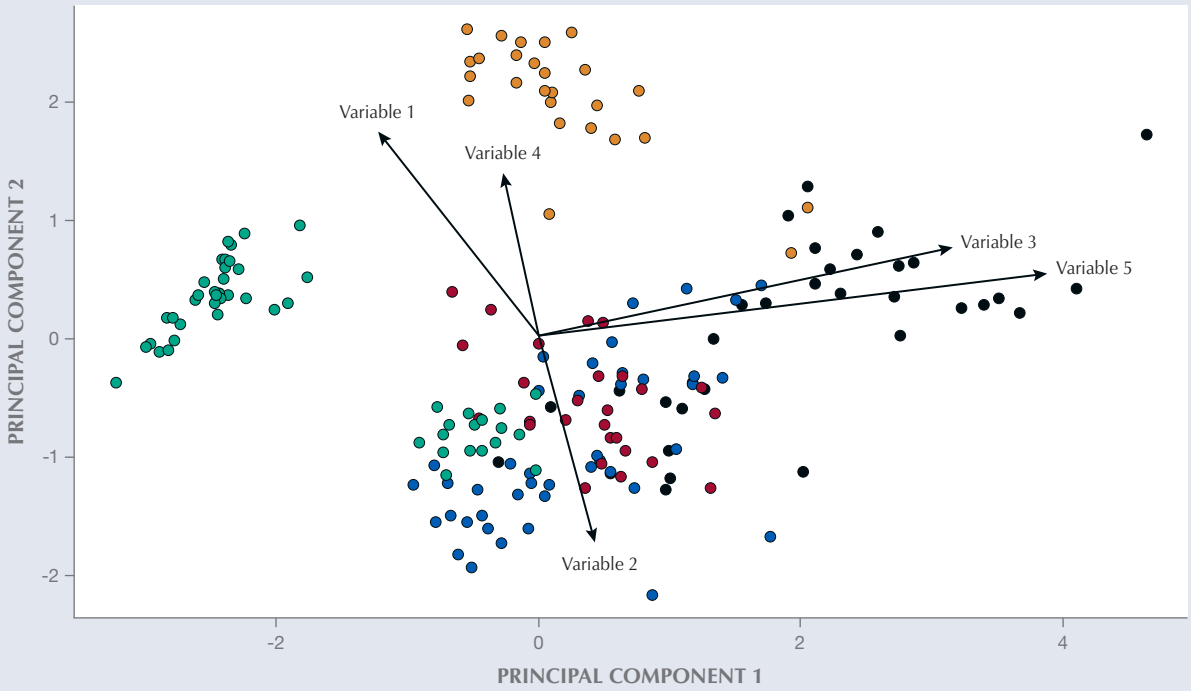

GIA's research department uses R, Python, and MATLAB software to construct scripts and models that are used to classify gem materials. These software tools are computationally complex, with commands written using scripts, and can be difficult for general users to navigate. Therefore, models calibrated using these tools are exported and integrated into existing software already being used for gemological classification. This reduces the complexity of the ML logic and provides laboratory gemologists with the rapid and concise classification outputs they need.

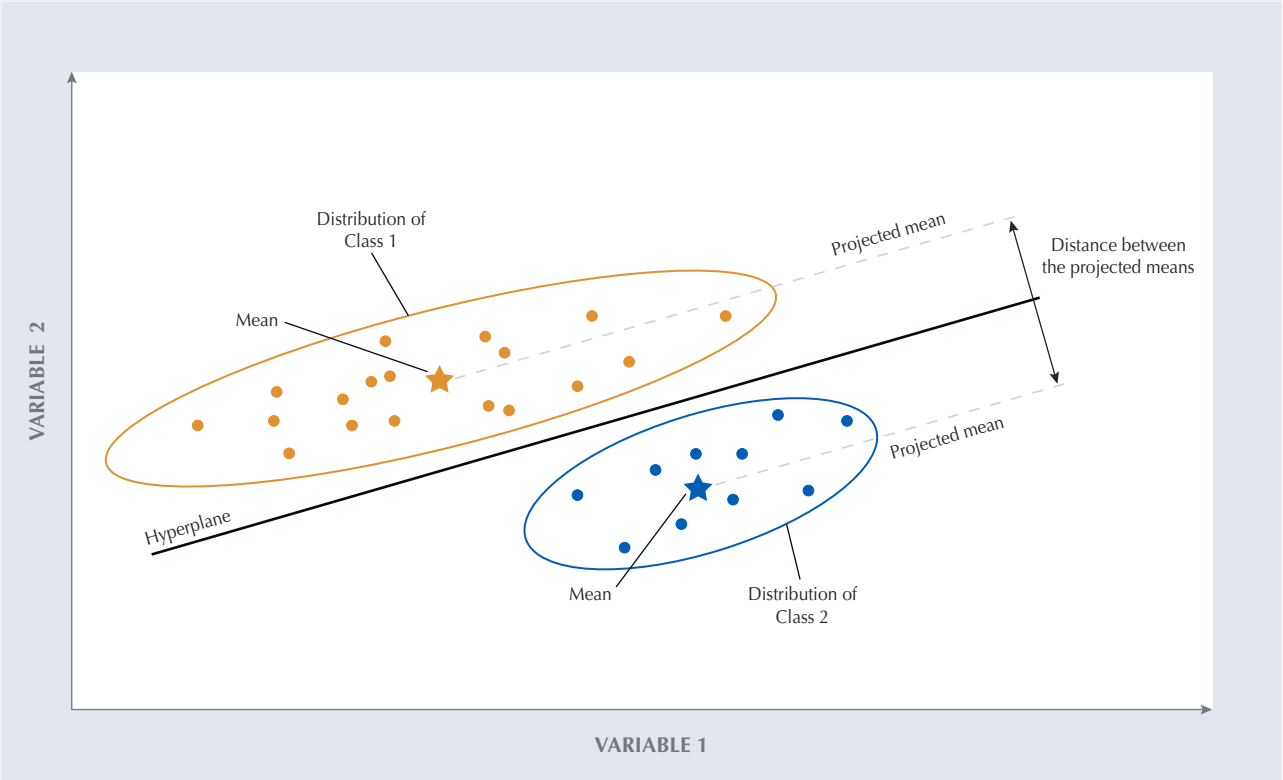

Figure A-2. Example linear discriminant analysis plot. Populations of data can be separated using a hyperplane, a linear equation constructed from variables perpendicular to the maximum separation between the projected means of the two groups. New samples can be classified using the hyperplane equation.

on the data graphically show how each variable or feature influences each principal component. Vector length indicates the intensity of the influence, and vector direction shows whether it is oriented positively or negatively toward one or both of principal components 1 and 2. Broadly speaking, correlated vectors may indicate features that are correlated to one another.

LDA reduces the dimensionality of a dataset by projecting it into a lower-dimensional space, maximizing the separation between labeled groups. It produces a series of linear equations from the initial starting variables (Zhao et al., 2020). Unlike PCA, LDA explicitly determines the best combination of features for classifying data into different groups. These linear boundaries can then be used to classify new samples. LDA results can also be shown in bivariate scatterplots (e.g., figure A-2).

Like all statistical methods, PCA and LDA have particular stipulations. For example, LDA assumes a normal distribution of variables (Hastie et al., 2009). Both are linear techniques and thus appropriate when the data are linearly separable. The outputs from PCA and LDA can be used as inputs to calibrate machine learning models, as the restructuring of the database using PCA and LDA may allow the data to be more effectively processed by machine learning. In this case, the user may select a small number of principal components that collectively describe a large amount of the variance of the original data.

This study examines GIA's application of PCA, LDA, RF, ANN, SVM, and Boruta to gem-related classification problems. The authors used R to construct all of the machine learning models and to validate each one using *k*-fold cross-validation. For alexandrite and natural saltwater pearls, we applied PCA, LDA, RF, ANN, and SVM to build new models for provenance determination. For CVD-grown diamonds, the authors applied the Boruta algorithm to identify their spectroscopic features and identify those that could enhance the detection of post-growth treatment.

BOX B: MACHINE LEARNING MODELS

Machine learning is the process of training computer algorithms to solve complex problems or identify patterns without explicit programming. ML models are characterized by complex mathematics, and each is suited to particular types of datasets, with specific advantages and disadvantages. Several ML models are summarized here. For each model, the algorithm learns to identify the best combination of features to separate samples into groups by predefined criteria (e.g., species and provenance). These criteria can then be applied to classify new samples.

Decision trees are intuitive ML models consisting of successive binary true or false statements drawn as trees (figure B-1A; Hastie et al., 2009). New samples can be tested and classified rapidly using the logic of the decision tree. However, the method of generating a decision tree can lead to "overfitting," in which samples are split into groups based on random features in the data, leading to poor results when tested against new samples. The random forest method builds many decision trees (potentially thousands) from the initial dataset; the outcomes from all trees are aggregated, and the majority vote determines the classification (figure B-1B; Breiman, 2001). As an ML model, RF often outperforms the others, being less sensitive to analytical noise than models such as single decision trees (Breiman, 2001; Fernández-Delgado et al., 2014; Bolton et al., 2019).

For datasets where a linear boundary can separate populations of data, linear discriminant analysis can be applied (see box A). LDA produces multiple linear boundaries that separate different groups within a dataset. In cases where data cannot be separated clearly by a linear boundary, other models such as support vector machines can be applied (Boser et al., 1992; Cristianini and Shawe-Taylor, 2000). SVM uses a mathematical function (known as a "kernel function") to transform the original data and remap it to a new coordinate space where the data can be separated using a linear equation (figure B-1B). Artificial neural networks are another option, organized in a fashion similar to the human brain. Information about variables in the dataset passes through successive layers of "artificial neurons" at each layer, and the neurons transform the dataset and pass it through to other layers (LeCun et al., 2015). After repeated transformation and classification stages, the original data receives a classification outcome (figure B-1C).

Some ML models cannot extrapolate to new data that differ significantly from the data used during the initial calibration. In these cases, new types of samples tested against ML models—such as RF—may produce unpredictable outcomes (Hengl et al., 2018). But if the new data have a linear relationship with other available samples, linear models such as LDA may be capable of accurately predicting the outcome class. The choice of ML model is critical, and all ML outcomes should be considered carefully. Model performance can be improved by iteratively testing combinations of parameters until finding the combination that produces the model with the best performance.

Finally, feature selection is a statistical approach for investigating large databases and identifying the variables that are most important for successful classification of a particular dataset. For spectroscopic data, feature selection can be used to pinpoint the most useful peaks for solving a specific classification problem. The Boruta algorithm, for example, ranks the importance of all variables based on how the error rate of the model changes when each variable is excluded from model calibration (Kursa et al., 2010). Although feature selection algorithms are useful time-saving tools, all "important" variables should be scrutinized to ensure their value. The Boruta approach has been previously applied in determining the importance of geological and environmental processes (e.g., Amiri et al., 2019; Prasad et al., 2021).

Figure B-1. Schematic overviews of three machine learning methods: random forest, support vector machine, and artificial neural network. A: Individual decision trees within RF consist of nodes (circles) representing true or false decisions where unclassified data are tested and then filtered down the tree until assigned a class at the bottom. The outcome for a test dataset is the majority vote from all trees (in this example, Group C). B: In SVM, data that are separable by a nonlinear boundary can be transformed into linearly separable data using a kernel function, a mathematical function that projects the data into a new remapped coordinate space. Support vectors are data points that define the orientation of the boundary (or hyperplane) between groups. C: ANNs consist of input variables and successive hidden layers. Decisions are made at the artificial neurons, where weights indicate the relative importance of different variables at each layer. This is a "feedforward" neural network, where the data are processed in one direction without recursive feedback loops.

RESULTS

Alexandrite. PCA was applied to the trace element concentrations for alexandrite in this study; the results are shown in a bivariate scatterplot with principal components 1 and 2 as axes (figure 7). Principal components are linear combinations of the initial variables in a database, serving to summarize and simplify complex datasets; the vectors in figure 7 in-

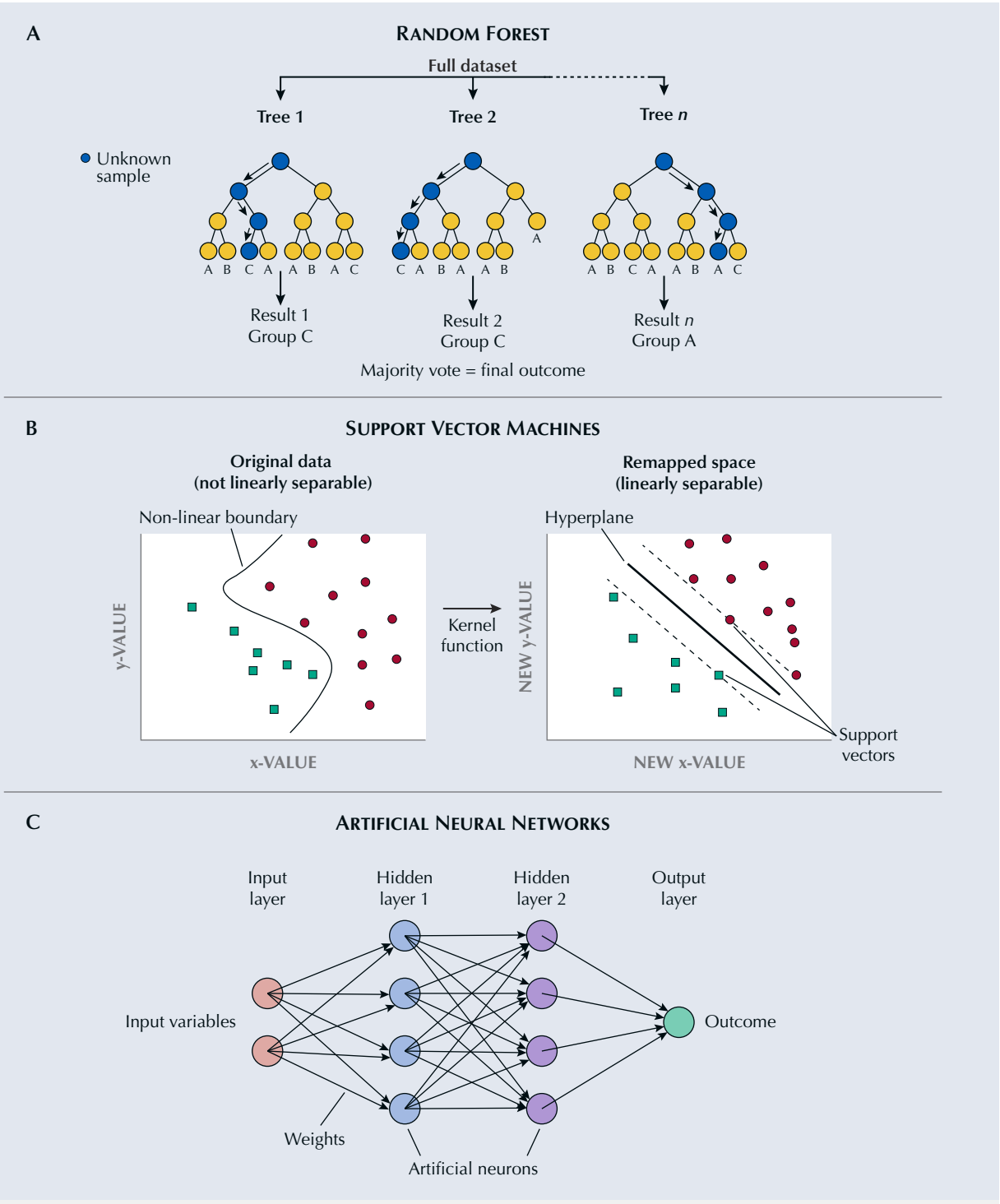

dicate the relative concentrations of each element and highlight samples with elevated concentrations of each (see box A). The scatterplot reveals separation between several populations of alexandrite from different localities—such as India, Brazil, and Russia—though alexandrite from other localities overlaps to different degrees. Alexandrite from some localities have different compositions than those from other

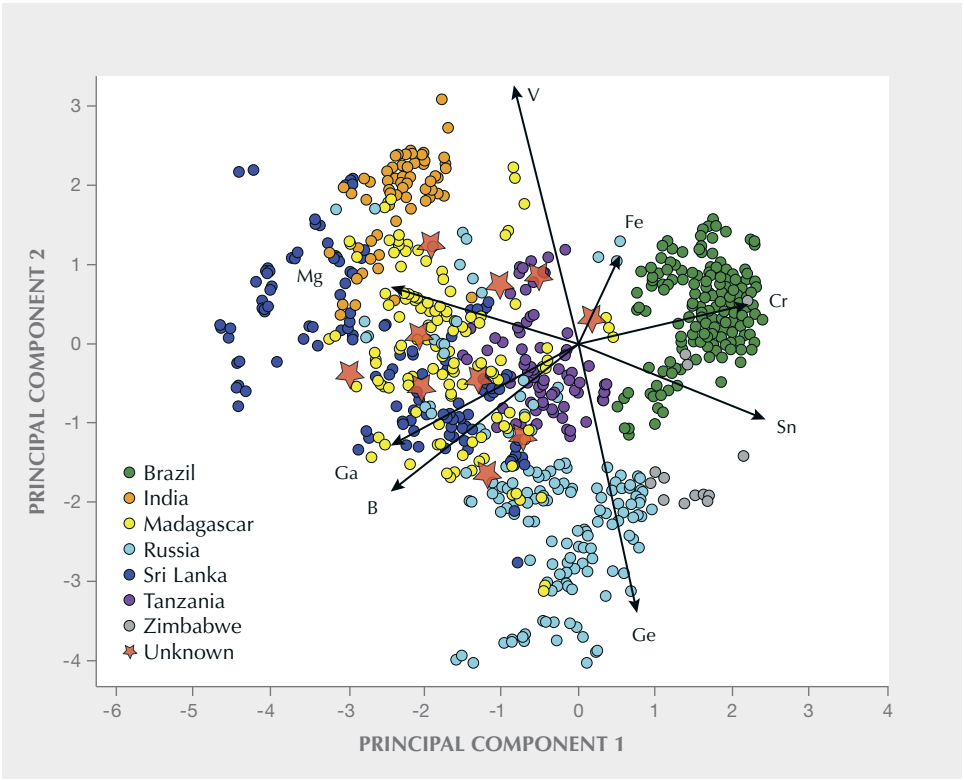

Figure 7. Plot of principal components 1 and 2 for alexandrite samples in this study. The stars denote alexandrite with an "undetermined" provenance using traditional approaches. The values for principal components 1 and 2 convey the relative variation between data points, but the values themselves do not have physical meaning.

localities; for example, samples from India have relatively elevated vanadium concentrations, and those from Sri Lanka have elevated gallium concentrations (figure 8). Calibrated models using LDA, RF, SVM, and ANN achieved cross-validated error rates <4% for alexandrite provenance determination, within error of one another (table 4). A set of 10 alexandrite samples with elemental compositions previously considered inconclusive using traditional approaches is plotted relative to alexandrite with known prove-

Figure 8. Box and whisker diagrams for the concentrations of vanadium (left) and gallium (right) in alexandrite from the seven localities in this study. The colors match the groups in figure 7.

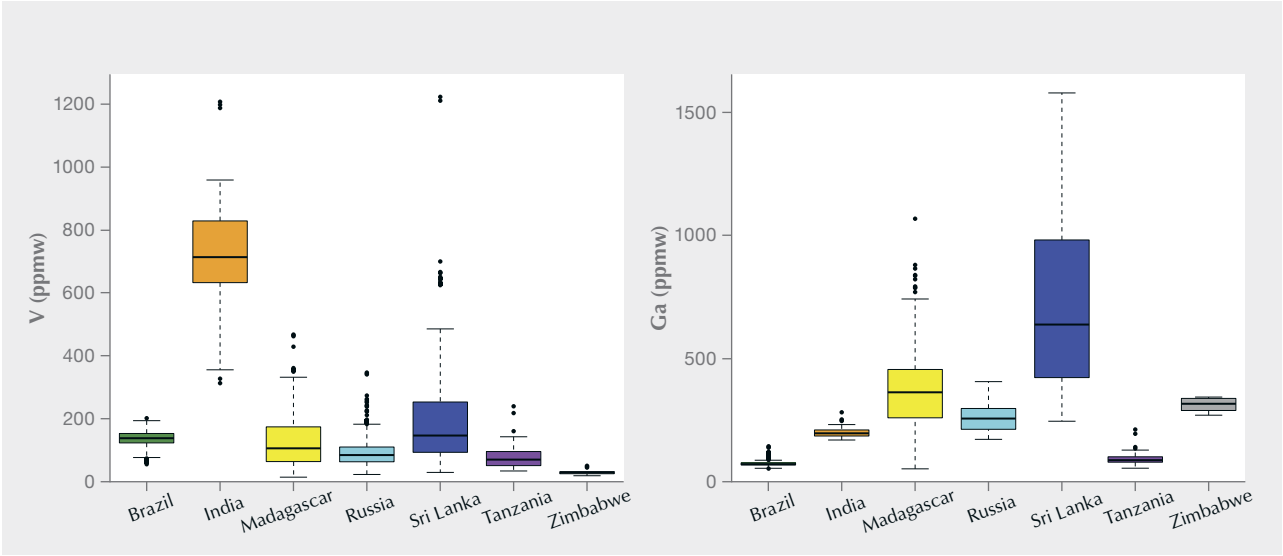

nance using PCA (figure 7) and classified using the four calibrated models (table 5). The inconclusive alexandrite samples fall within areas of the plot where multiple localities overlap. When tested using the four ML models, half of the samples yielded consistent classifications and the remainder produced contradictory results.

CVD-Grown Diamonds. A previous study (Hardman et al., 2022) applied machine learning to the detection of treatment in CVD-grown diamonds using PL spectra with the Raman-normalized peak intensities of 13 different features as variables. The diamond spectra are complex and many other peaks occur, but their value as indicators of treatment has not been assessed. When the Boruta algorithm is applied to feature selection for CVD-grown diamond PL spectra, it produces a ranked list of peaks. Each peak is evaluated for its ability to improve detection of treated or untreated stones when included in the statistical model. We have tabulated the peaks considered most important by Boruta, and these are presented in figure 9 and table 6. For treated CVD-grown diamonds, the majority of these features occur in the range of 520–550 nm in PL spectra.

TABLE 4. Error rates[a] for statistical models applied to alexandrite and natural saltwater pearl provenance determination.

Machine learning model	Alexandrite (346 samples, 1,157 analyses)	Natural saltwater pearl (604 samples, 1,875 analyses)
Linear discriminant analysis	3.7 ± 3.0%	24.2 ± 4.0%
Random forest	1.3 ± 3.2%	12.1 ± 3.6%
Artificial neural networks	2.0 ± 2.5%	13.2 ± 3.0%
Support vector machines	3.4 ± 3.1%	17.3 ± 3.3%

[a]*Error rates represent mean ±2σ determined by tenfold cross-validation.*

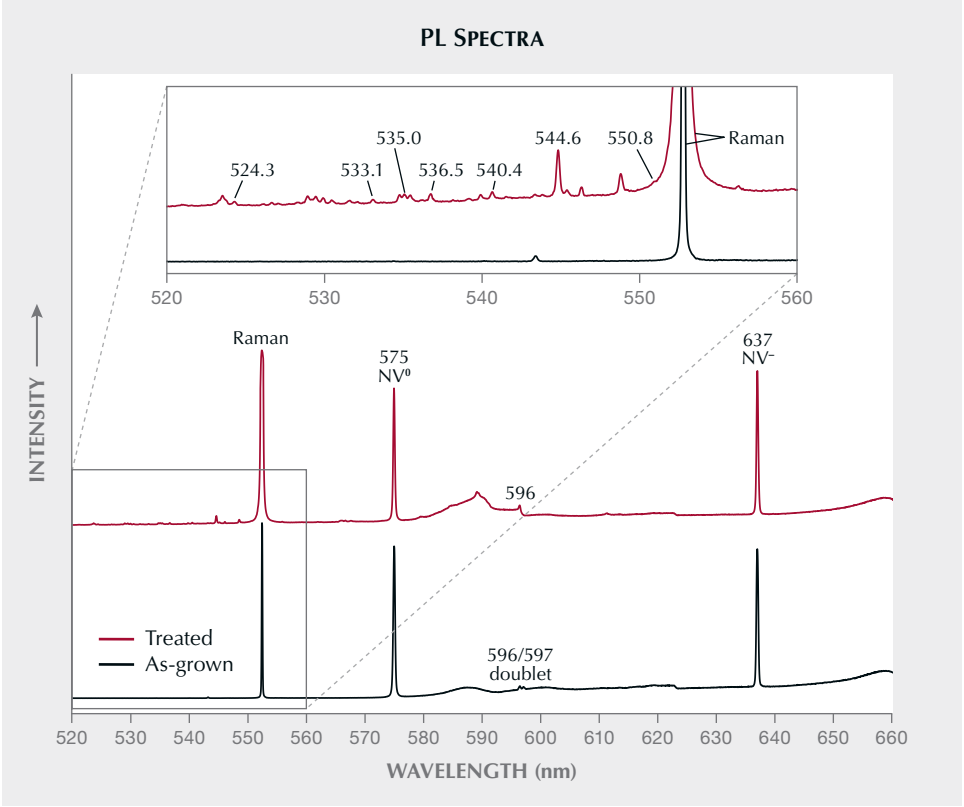

Figure 9. Example PL spectra for as-grown and HPHT-treated CVD-grown diamonds. A subset of 10 peaks whose Raman-normalized intensities are identified as important by the Boruta feature selection algorithm are labeled. The spectra are offset vertically for clarity and scaled so that the Raman peaks have equal intensity. Note that not all peaks appear in every spectrum. For example, the 596/597 nm peak doublet is present in some but not all as-grown *CVD diamonds (whereas only 596 nm is present in some* treated *CVD-grown diamonds).*

TABLE 5. Classification outcomes for ten alexandrite samples with previously inconclusive provenance, determined using four calibrated ML models.

Sample	Linear discriminant analysis	Random forest	Artificial neural networks	Support vector machines
1	Madagascar	Madagascar	Madagascar	Russia
2	Madagascar	Madagascar	Madagascar	Madagascar
3	Tanzania	Madagascar	Madagascar	Tanzania
4	Tanzania	Madagascar	Madagascar	Madagascar
5	Sri Lanka	Madagascar	Madagascar	Madagascar or Sri Lanka[a]
6	Madagascar	Madagascar	Madagascar	Madagascar
7	Madagascar	Madagascar	Madagascar	Madagascar
8	Madagascar	Madagascar	Madagascar	Madagascar
9	Tanzania	Tanzania	Tanzania	Tanzania
10	Madagascar or Brazil	Madagascar	Madagascar	Madagascar or Russia

[a]*Samples with multiple outcomes are those with subequal probabilities for each.*

Natural Saltwater Pearls. There are varying levels of population separation when PCA results are shown using bivariate scatterplots and when pearls are color-coded based on different classification variables (figure 10, A and B). Many pearls reportedly fished from Kuwait and Bahrain (with relatively close spatial proximity) and produced by the same *Pinctada radiata* mollusk species have similar compositions and overlap; Oman pearls, which were reportedly produced by *Pinctada margaritifera* mollusks, are separated from Kuwait and Bahrain pearls (figure 10A). The population of Bahrain pearls is broadly bimodal, with one subgroup having strong overlap with Kuwait pearls and the other showing elevated magnesium and manganese concentrations (figure 10A). Moreover, nacreous and non-nacreous pearls differ in composition, with non-nacreous pearls (mostly from Bahrain) having higher magnesium concentrations (figure 10, B and C). The magnesium concentrations of non-nacreous pearls from Bahrain, Kuwait, and Oman largely overlap with each other (figure 10C).

Using models based on LDA, RF, SVM, and ANN, geographic provenance can be determined with model error rates <25%, with RF performing the best (<13% error rate; table 4). For outcomes produced using the RF model, the misclassification of natural saltwater pearls is tabulated in table 7. The most significant misclassifications are between Kuwait and Bahrain pearls: 13% of Bahrain and 18% of Kuwait

TABLE 6. Ranking of top 10 peaks in CVD-grown diamond spectroscopic data collected using 514 nm PL, identified by the Boruta algorithm.

Rank[a]	Approximate peak position (nm)
1	524.3
2	575
3	540.4
4	535.0
5	544.6
6	596/597 doublet
7	536.5
8	533.1
9	637
10	550.8

[a]*Ranked importance of the Raman-normalized intensities of each peak when used as a classification variable in machine learning models. These ranks are produced by examining PL spectra for 300 as-grown and 1,795 post-growth treated CVD diamonds.*

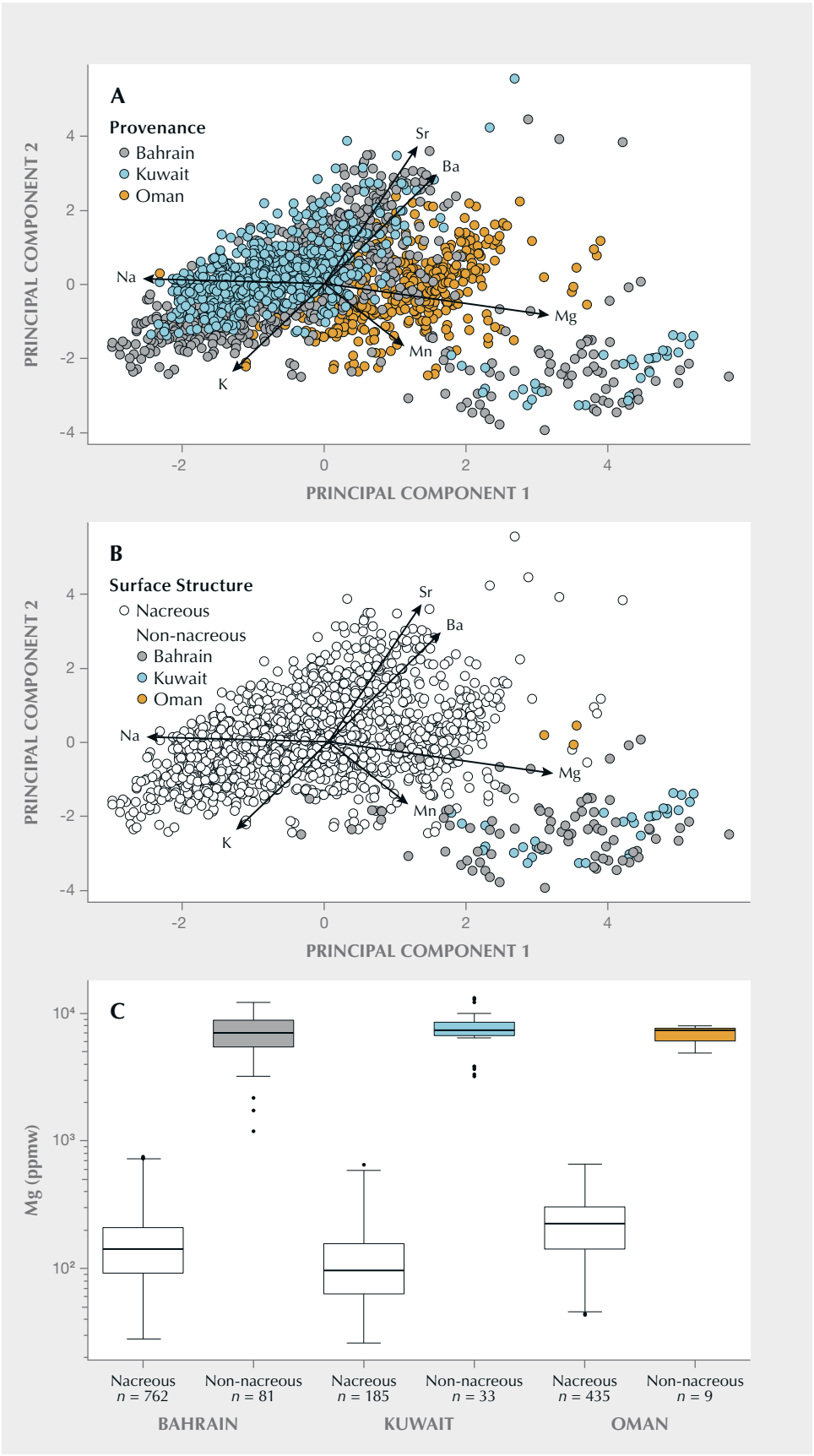

Figure 10. Plot of principal components 1 and 2 for natural saltwater pearls, based on (A) geographic provenance (Bahrain, Kuwait, and Oman) and (B) surface structure (nacreous and non-nacreous). C: Box and whisker plot of magnesium concentrations for all analyses of nacreous and non-nacreous pearls in this study, divided by locality. Solid lines correspond to median values, boxes represent the range from the 1st to 3rd quartile (interquartile range; IQR), the vertical lines are whiskers that range from IQR ± (1.5 × IQR), and the black dots correspond to pearls with values beyond the whiskers, considered to be outliers.

pearls misclassify, primarily as one another, with very few misclassifications as "Oman." Conversely, only 4% of pearls from Oman receive an incorrect provenance determination, all as "Bahrain."

DISCUSSION

Alexandrite Provenance Determination. When alexandrite trace element compositions are transformed using PCA, separation between samples from different localities becomes apparent, enabling the broad classification of several alexandrite samples with previously inconclusive provenance (figure 7). PCA indicates several elements that may discriminate alexandrite from different localities, such as high vanadium in Indian alexandrite and gallium concentrations that are elevated in Sri Lankan alexandrite and low in Brazilian samples. These differences are also resolved in box and whisker plots for these elements (figure 8). Alexandrite from Sri Lanka and Madagascar display overlapping compositions that may be differentiated using additional principal components. PCA also indicates that Brazilian alexandrites are compositionally diverse, with some having higher germanium despite reportedly originating from the same mine (Sun et al., 2019). This underscores the importance of compiling representative databases for accurate provenance determination of unclassified stones. The compositional variability of alexandrite within a particular country may increase as stones from other mines are collected.

A moderately strong positive correlation between the elements boron and gallium for the full dataset is inferred from the vectors with similar length and direction shown in figure 7. The primary advantage of applying PCA to alexandrite is its ability to consider each of these aspects simultaneously, enabling efficient visualization and interpretation of alexandrite compositional data. If alexandrite samples from different localities are formed through distinct geological processes, PCA plots may reveal detectable differences in their compositions.

Machine learning models produced using the LDA, RF, SVM, and ANN methods can determine alexandrite provenance with error rates <4% (table 4). Of the 10 alexandrite samples with inconclusive provenance determinations using traditional approaches, 50% received a consistent classification using all four methods, while others were classified similarly using three different models (table 5). However, some samples received conflicting outcomes or classification probabilities (not shown) that were intermediate. These samples should be referred to a trained specialist before the ML outcome is accepted. Discrepancies between models calibrated using the same dataset may arise from the underlying mathematical properties of each model, some of which are more suitable for particular datasets, combined with the fact that some alexandrite samples have elemental compositions that are transitional between stones from different localities. This may be further complicated by changes in quality and consistency of data collection methods over time, including changes in standard reference materials. Previous studies have shown RF to be a particularly powerful method (Fernández-Delgado et al., 2014; Bolton et al., 2019), a finding consistent with model error rates in this study (table 4). In cases of conflicting outcomes, the RF model results may carry more weight with trained specialists than LDA, for example.

TABLE 7. Summary of classification results for natural saltwater pearls in this study using the random forest model. Samples with matching known and predicted provenance are considered to be correctly classified.

Known provenance	Predicted provenance			
	Bahrain	Kuwait	Oman	Error rate
Bahrain (268 samples)	233	28	7	13.1%
Kuwait (188 samples)	33	155	0	17.6%
Oman (148 samples)	6	0	142	4.1%

For alexandrite from different localities with similar compositions, it can be difficult to accurately determine provenance even with very robust ML models. To reduce model error rates and improve provenance determination for more stones, new compositional variables can be added. While the addition of ML to traditional approaches failed to definitively classify all samples in this study, it reduced the number of "undetermined" results by 50%, using existing data routinely acquired during gemological assessment.

CVD-Grown Diamond Treatment Detection. Machine learning approaches previously applied to detecting treatment in CVD-grown diamonds achieved error rates <5%, using the intensities of 13 peaks in PL spectra as variables in RF models (Hardman et al., 2022). The models described by Hardman et al. (2022) are currently used at GIA to aid in treatment detection for CVD-grown diamonds. For each stone analyzed, a confidence value is provided to the user, reflecting the model's level of certainty in the classification outcome. This is very important for accurate detection of treatment: Accepting ML outcomes without careful consideration, even with error rates of 1%, can scale to a large number of misclassifications as more stones are tested.

Laboratory-grown diamond producers are continually exploring new approaches to post-growth treatment (Eaton-Magaña et al., 2024). These developments may introduce new defect distributions, rendering existing classification criteria obsolete and necessitating the development of new criteria. Beyond the 13 peaks used by Hardman et al. (2022), the spectroscopic signatures of CVD-grown diamonds contain many other peaks, not all of which have been fully characterized. As many peaks occur in different combinations in thousands of available spectra, machine learning offers a powerful tool to mine these data. By applying ML to diamonds with known treatment histories, researchers can identify potential new classification criteria significantly faster.

Applying Boruta to the CVD-grown diamond database in this study produced a ranking of the PL spectra peaks considered statistically useful for treatment detection. For brevity, we have listed only the top 10 important peaks as identified by the feature selection algorithm (table 6), shown graphically in figure 9. The majority of these peaks (e.g., 524.3 and 575 nm) were previously used for treatment detection by Hardman et al. (2022). The peak doublet at 596/597 nm has a high ranking and was previously reported as an important indicator of untreated CVD-grown diamonds (Wang et al., 2003; Martineau et al., 2004). Other peaks, such as 536.5 nm, are assigned high importance using Boruta but were not applied directly by Hardman et al. (2022). This feature occurs in the 520–550 nm spectral range, which contains many previously documented peaks associated with post-growth treatment of CVD-grown diamonds (Wang et al., 2012; Barrie, 2020; Hardman et al., 2022). With further validation and testing, this peak—and others identified using feature selection—may become new criteria for detection, complementing existing variables. Boruta analysis also provides a sense of comparative importance that is useful for classification. For example, a 524.3 nm peak may be very important for identifying HPHT treatment. In its absence, the relative intensity of the 575 nm peak—which is present in nearly all CVD-grown diamonds and ranked as the second most important variable (table 6)—becomes an even more important variable. New variables identified by Boruta must be validated before they are added into new ML models for treatment detection: Future studies can evaluate how strongly new variables improve classification error rates. Regardless, the feature selection procedure as a whole represents a significant time savings for objectively parsing large datasets and identifying subtle variations in available data that may be difficult for a human to quantify without computer software.

Natural Saltwater Pearl Provenance Determination. PCA applied to trace element compositions of natural saltwater pearls reveals that many pearls from Oman are compositionally distinct from those of Kuwait and Bahrain, driven in part by elevated magnesium concentrations (figure 10, A and B). By comparison, many pearls from Kuwait and Bahrain are compositionally similar to each other. The elemental compositions of pearls are the result of complex biological processes related to mollusk species, water chemistry, and nutrient sources (Homkrajae et al., 2019). Therefore, it is difficult to specify which biogenic processes cause the compositional similarity between pearls from Kuwait and Bahrain. For example, while the Kuwait and Bahrain pearls are derived from *Pinctada radiata* mollusks, their nutrient sources might differ. There is also no guarantee that

all mollusks from a single locality and from the same species had similar nutrient sources. This may account for the compositional spread in pearls from each locality (figure 10).

For example, non-nacreous pearls have higher magnesium concentrations than nacreous pearls from the same locality (figure 10C). When analyzing pearls using LA-ICP-MS, it is important to accurately record the position of the analysis within the pearl, along with other useful descriptive information about the material (such as the presence or absence of nacre). These observations provide important context for compositional variation displayed in PCA plots.

Despite the compositional overlap of pearls from Bahrain and Kuwait using PCA (figure 10, A and B), the LDA, RF, SVM, and ANN models can still determine the provenance of many pearls (table 4). Each model has a moderate error rate for the classification of pearl provenance (>10%), indicating compositional differences between many pearls from different localities. However, some compositional overlap remains unresolved using the current set of elemental variables, even when using ML techniques. These error rates are higher than those observed for the classification of alexandrite (table 4), reflecting the nature of biological and growth environment conditions—some problems cannot be fully resolved even with powerful statistical methods such as RF. Nevertheless, the majority of Oman pearls from this study received a correct classification using RF, whereas classifications for Bahrain and Kuwait were less conclusive (table 7). When finalizing a provenance determination, pearls classified by ML as "Oman" tend to be more accurate. The similar compositions of some pearls from Bahrain and Kuwait may be attributed to the fact that they are produced by the same mollusk species (*Pinctada radiata*) located within the Persian (Arabian) Gulf, which provides similar biological and growth environment conditions. Conversely, Oman pearls form in *Pinctada margaritifera* mollusks found in the Gulf of Oman region.

Trace element composition also provides insight into the biogenic processes that formed the pearls. Freshwater pearls have much higher manganese content than saltwater pearls (Homkrajae et al., 2019). Among the natural saltwater pearls in this study, we noted several other variations in elemental compositions that may reflect local environmental conditions, such as varying concentrations of strontium, sodium, potassium, and barium (figure 10, A and B). Pearls harvested over time from a variety of environments may also be sensitive to small- and large-scale climate changes. Consequently, analyzing pearl compositional data using ML may be complicated by temporal changes in environment.

Pearl research is an active area of study at GIA, one that relies on acquiring pearls for which the provenance and culturing history are known and well characterized. Findings from ML will help shape future research projects by identifying important elemental variables and highlighting populations of pearls that would benefit from expanded sampling. Adding more elements into the ML models in this study—if these elements are shown to be free of analytical interferences (compare to Homkrajae et al., 2019)—may further improve the determination of pearl provenance.

CONCLUSIONS

Traditional approaches to gem classification at GIA encompass microscopic examination and the acquisition of trace element or spectroscopic data. Trace element data can be compared using bivariate scatterplots and selective plotting, while spectroscopic data are assessed through visual inspection to pinpoint key classification features. Unclassified materials are compared to curated datasets of samples for which the classification has been independently verified (figure 11). Machine learning complements these approaches, enhancing the determination of provenance and detection of color treatment in gem materials. The ML models in this study can successfully determine the provenance of alexandrite and reduce the number that may otherwise receive an inconclusive outcome. For CVD-grown diamonds, ML identifies peaks in spectroscopic data that offer valuable indicators of post-growth treatment. For natural saltwater pearls, principal component analysis helps to assess biogenic processes related to growth environment, enabling preliminary provenance determination.

Despite high success rates for some classification problems (>95%; table 4), ML models still provide incorrect answers sometimes. For certain natural gemstones, this could be associated with geology—similar geological processes occurring at different localities may result in samples with very similar properties and elemental compositions, complicating provenance determination (e.g., Smith et al., 2022). In these cases, ML does not always provide a confident provenance determination, no matter how robust the approach. If a decision cannot be made after classification by ML

Figure 11. Double-strand natural saltwater pearl necklace. Photo by Robert Weldon; courtesy of Karmshil Enterprise. Alexandrite exposed to incandescent illumination (left, red) and daylight-equivalent illumination (right, green). Photos by Robert Weldon; courtesy of GIA's Dr. Edward J. Gübelin collection, no. 33805. Ring containing a CVD-grown diamond. Photo by Johnny Leung.

and review by a trained specialist, the sample may receive a final decision of "undetermined." Nevertheless, ML successfully minimizes the small number of "undetermined" outcomes by leveraging data that is already part of routine gemological practices. These techniques are powerful complements to existing laboratory practices, offering substantial time and cost savings.

ABOUT THE AUTHORS

Dr. Matthew F. Hardman is a research scientist, Artitaya Homkrajae is supervisor of pearl identification, Dr. Sally Eaton-Magaña is senior manager of diamond identification, Dr. Christopher M. Breeding is senior manager of analytics, Dr. Aaron C. Palke is senior manager of research, and Ziyin Sun is a senior research associate, at GIA in Carlsbad, California.

ACKNOWLEDGMENTS

We thank Troy Ardon for software development, as well as Chunhui Zhou, Abeer Al-Alawi, Mei Yan Lai, Ulrika D'Haenens-Johansson, James Shigley, and three anonymous reviewers for useful comments and suggestions that improved the quality of this manuscript.

REFERENCES

Amiri M., Pourghasemi H.R., Ghanbarian G.A., Afzali S.F. (2019) Assessment of the importance of gully erosion effective factors using Boruta algorithm and its spatial modeling and mapping using three machine learning algorithms. *Geoderma*, Vol. 340, pp. 55–69, http://dx.doi.org/10.1016/j.geoderma.2018.12.042

Arnault J.-C., Saada S., Ralchenko V. (2022) Chemical vapor deposition single-crystal diamond: A review. *Physica Status Solidi Rapid Research Letters*, Vol. 16, No. 1, article no. 2100354, http://dx.doi.org/10.1002/pssr.202100354

Barrie E. (2020) Lab Notes: HPHT-processed CVD laboratory-grown diamonds with low color grades. *G&G*, Vol. 56, No. 2, pp. 289–290.

Bassoo R., Eames D., Hardman M.F., Befus K., Sun Z. (2023) Topaz from Mason County, Texas. *G&G*, Vol. 59, No. 4, pp. 414–431, http://dx.doi.org/10.5741/GEMS.59.4.414

Bendinelli T., Biggio L., Nyfeler D., Ghosh A., Tollan P., Kirschmann M.A., Fink O. (2024) Gemtelligence: Accelerating gemstone classification with deep learning. *Communications Engineering*, Vol. 3, article no. 110, http://dx.doi.org/10.1038/s44172-024-00252-x

Blodgett T., Shen A.H. (2011) Application of discriminant analysis in gemology: Country-of-origin separation in colored stones and distinguishing HPHT-treated diamonds. *G&G*, Vol. 47, No. 2, p. 145.

Bolton M.S.M., Jensen B.J.L., Wallace K., Praet N., Fortin D., Kaufman D., Batist M.D. (2019) Machine learning classifiers for attributing tephra to source volcanoes: An evaluation of methods for Alaska tephras. *Journal of Quaternary Science*, Vol. 35, No. 1-2, pp. 81–92, http://dx.doi.org/10.1002/jqs.3170

Boser B.E., Guyon I.M., Vapnik V.N. (1992) A training algorithm for optimal margin classifiers. In *Proceedings of the Fifth Annual Workshop on Computational Learning Theory*, pp. 144–152.

Breiman L. (2001) Random forests. *Machine Learning*, Vol. 45, pp. 5–32, http://dx.doi.org/10.1023/A:1010933404324

Cristianini N., Shawe-Taylor J. (2000) *An Introduction to Support Vector Machines and Other Kernel-Based Learning Methods*. Cambridge University Press, Cambridge, UK.

Dawson J.B., Stephens W.E. (1975) Statistical classification of garnets from kimberlite and associated xenoliths. *Journal of Geology*, Vol. 83, No. 5, pp. 589–607, http://dx.doi.org/10.1086/628143

D'Haenens-Johansson U.F.S., Butler J.E., Katrusha A.N. (2022) Synthesis of diamonds and their identification. *Reviews in Mineralogy & Geochemistry*, Vol. 88, No. 1, pp. 689–754, http://dx.doi.org/10.2138/rmg.2022.88.13

Eaton-Magaña S., Hardman M.F., Odake S. (2024) Laboratory-grown diamonds: An update on identification and products evaluated at GIA. *G&G*, Vol. 60, No. 2, pp. 146–167, http://dx.doi.org/10.5741/GEMS.60.2.146

Fernández-Delgado M., Cernadas E., Barro S., Amorim D. (2014) Do we need hundreds of classifiers to solve real world classification problems? *Journal of Machine Learning Research*, Vol. 15, No. 1, pp. 3133–3181.

Fuge R., Palmer T.J., Pearce N.J.G., Perkins W.T. (1993) Minor and trace element chemistry of modern shells: A laser ablation inductively coupled plasma mass spectrometry study. *Applied Geochemistry*, Vol. 8, Supplement 2, pp. 111–116, http://dx.doi.org/10.1016/S0883-2927(09)80020-6

Griffin W.L., Fisher N.I., Friedman J.H., O'Reilly S.Y., Ryan C.G. (2002) Cr-pyrope garnets in the lithospheric mantle 2. Compositional populations and their distribution in time and space. *Geochemistry Geophysics Geosystems*, Vol. 3, No. 12, pp. 1–35, http://dx.doi.org/10.1029/2002GC000298

Groat L.A., Giuliani G., Stone-Sundberg J., Sun Z., Renfro N.D., Palke A.C. (2019) A review of analytical methods used in geographic origin determination of gemstones. *G&G*, Vol. 55, No. 4, pp. 512–535, http://dx.doi.org/10.5741/GEMS.55.4.512

Gübelin E., Schmetzer K. (1982) Gemstones with alexandrite effect. *G&G*, Vol. 18, No. 4, pp. 197–203, http://dx.doi.org/10.5741/GEMS.18.4.197

Hardman M.F., Pearson D.G., Stachel T., Sweeney R.J. (2018a) Statistical approaches to the discrimination of crust- and mantle-derived low-Cr garnet – Major-element-based methods and their application in diamond exploration. *Journal of Geochemical Exploration*, Vol. 186, pp. 24–35, http://dx.doi.org/10.1016/j.gexplo.2017.11.012

——— (2018b) Statistical approaches to the discrimination of mantle- and crust-derived low-Cr garnets using major and trace element data. *Mineralogy and Petrology*, Vol. 112, No. S2, pp. 697–706, http://dx.doi.org/10.1007/s00710-018-0622-7

Hardman M.F., Eaton-Magaña S.C., Breeding C.M., Ardon T., D'Haenens-Johansson U.F.S. (2022) Evaluating the defects in CVD diamonds: A statistical approach to spectroscopy. *Diamond and Related Materials*, Vol. 130, article no. 109508, http://dx.doi.org/10.1016/j.diamond.2022.109508

Hastie T., Tibshirani R., Friedman J. (2009) *The Elements of Statistical Learning: Data Mining, Inference, and Prediction*, 2nd ed. Springer-Verlag, New York.

Hazen R.M., Morrison S.M. (2022) On the paragenetic modes of minerals: A mineral evolution perspective. *American Mineralogist*, Vol. 107, No. 7, pp. 1262–1287, http://dx.doi.org/10.2138/am-2022-8099

Hengl T., Nussbaum M., Wright M.N., Heuvelink G.B.M., Graler B. (2018) Random forest as a generic framework for predictive modeling of spatial and spatio-temporal variables. *PeerJ*, Vol. 6, article no. e5518, http://dx.doi.org/10.7717/peerj.5518

Homkrajae A., Sun Z., Blodgett T., Zhou C. (2019) Provenance discrimination of freshwater pearls by LA-ICP-MS and linear discriminant analysis (LDA). *G&G*, Vol. 55, No. 1, pp. 47–60, http://dx.doi.org/10.5741/GEMS.55.1.47

Homkrajae A., Manustrong A., Nilpetploy N., Sturman N., Lawanwong K., Kessrapong P. (2021) Internal structures of known *Pinctada maxima* pearls: Natural pearls from wild marine mollusks. *G&G*, Vol. 57, No. 1, pp. 2–21, http://dx.doi.org/10.5741/GEMS.57.1.2

Krebs M.Y., Hardman M.F., Pearson D.G., Luo Y., Fagan A.J. (2020) An evaluation of the potential for determination of the geographic origin of ruby and sapphire using an expanded trace element suite plus Sr-Pb isotope compositions. *Minerals*, Vol. 10, No. 5, article no. 447, http://dx.doi.org/10.3390/min10050447

Kursa M.B., Jankowski A., Rudnicki W.R. (2010) Boruta – a system for feature selection. *Fundamenta Informaticae*, Vol. 101, No. 4, pp. 271–285, http://dx.doi.org/10.3233/FI-2010-288

LeCun Y., Bengio Y., Hinton G. (2015) Deep learning. *Nature*, Vol. 521, No. 7553, pp. 436–444, http://dx.doi.org/10.1038/nature14539

Luo Z., Yang M., Shen A.H. (2015) Origin determination of dolomite-related white nephrite through IB-LDA. *G&G*, Vol. 51, No. 3, pp. 300–311, http://dx.doi.org/10.5741/GEMS.51.3.300

Martineau P.M., Lawson S.C., Taylor A.J., Quinn S.J., Evans D.J.F., Crowder M.J. (2004) Identification of synthetic diamond grown using chemical vapor deposition (CVD). *G&G*, Vol. 40, No. 1, pp. 2–25, http://dx.doi.org/10.5741/GEMS.40.1.2

Palke A.C., Saeseaw S., Renfro N.D., Sun Z., McClure S.F. (2019a) Geographic origin determination of blue sapphire. *G&G*, Vol. 55, No. 4, pp. 536–579, http://dx.doi.org/10.5741/GEMS.55.4.536

——— (2019b) Geographic origin determination of ruby. *G&G*, Vol. 55, No. 4, pp. 580–612, http://dx.doi.org/10.5741/GEMS.55.4.580

Prasad P., Loveson V.J., Das S., Chandra P. (2021) Artificial intelligence approaches for spatial prediction of landslides in mountainous regions of western India. *Environmental Earth*

Sciences, Vol. 80, No. 21, article no. 720, http://dx.doi.org/10.1007/s12665-021-10033-w
R Core Team (2024) R: A language and environment for statistical computing. R Foundation for Statistical Computing, Vienna, https://www.R-project.org
Schönig J., von Eynatten H., Tolosana-Delgado R., Meinhold G. (2021) Garnet major-element composition as an indicator of host-rock type: A machine learning approach using the random forest classifier. *Contributions to Mineralogy and Petrology*, Vol. 176, No. 12, article no. 98, http://dx.doi.org/10.1007/s00410-021-01854-w
Smith E.M., Smit K.V., Shirey S.B. (2022) Methods and challenges of establishing the geographic origin of diamonds. *G&G*, Vol. 58, No. 3, pp. 270–288, http://dx.doi.org/10.5741/GEMS.58.3.270
Sun Z., Palke A.C., Muyal J., DeGhionno D., McClure S.F. (2019) Geographic origin determination of alexandrite. *G&G*, Vol. 55, No. 4, pp. 660–681, http://dx.doi.org/10.5741/GEMS.55.4.660
Wang W., Moses T., Linares R.C., Shigley J.E., Hall M., Butler J.E. (2003) Gem-quality synthetic diamonds grown by a chemical vapor deposition (CVD) method. *G&G*, Vol. 39, No. 4, pp. 268–283, http://dx.doi.org/10.5741/GEMS.39.4.268
Wang W., D'Haenens-Johansson U.F.S., Johnson P., Moe K.S., Emerson E., Newton M.E., Moses T.M. (2012) CVD synthetic diamonds from Gemesis Corp. *G&G*, Vol. 48, No. 2, pp. 80–97, http://dx.doi.org/10.5741/GEMS.48.2.80
Xu Y., Liu X., Cao X., Huang C., Liu E., Qian S., Liu X., Wu Y., Dong F., Qiu C.-W., Qiu J., Hua K., Su W., Wu J., Xu H., Han Y., Fu C., Yin Z., Liu M., Roepman R., Dietmann S., Virta M., Kengara F., Zhang Z., Zhang L., Zhao T., Dai J., Yang J., Lan L., Luo M., Liu Z., An T., Zhang B., He X., Cong S., Liu X., Zhang W., Lewis J.P., Tiedje J.M., Wang Q., An Z., Wang F., Zhang L., Huang T., Lu C., Cai Z., Wang F., Zhang J. (2021) Artificial intelligence: A powerful paradigm for scientific research. *The Innovation*, Vol. 2, No. 4, article no. 100179, http://dx.doi.org/10.1016/j.xinn.2021.100179
Zhao H., Lai Z., Leung H., Zhang X. (2020) Linear discriminant analysis. In *Feature Learning and Understanding: Algorithms and Applications*. Information Fusion and Data Science Series. Springer Nature, Cham, Switzerland, https://doi.org/10.1007/978-3-030-40794-0_5

Generative Artificial Intelligence as a Tool for Jewelry Design

Michael D. Magee

While the jewelry industry is deeply rooted in traditional tools and techniques, generative artificial intelligence (AI) must be recognized today as a revolutionary tool to assist jewelers. The intersection between AI and the creative arts is especially controversial, and the use of generative AI in jewelry design is no different. This paper examines how generative AI creates designs based on text and image prompts, comparing five of the more common AI programs (Midjourney, DALL.E, Stable Diffusion, Leonardo, and Firefly) with a focus on generating realistic jewelry images. It addresses the ethical, legal, and regulatory questions that have arisen around AI-generated art. Lastly, it explores how this new technology can best be used by jewelry designers to enhance creative expression.

The allure of jewelry lies in its intricate design, the craftsmanship behind each piece, and the significance and lore we attach to particular jewels. From the skilled hands of ancient goldsmiths to the precision of modern-day artisans, the creation of jewelry has always been a deeply human endeavor. But as we stand on the brink of a new era, the time-honored traditions of jewelry design are converging with the cutting-edge advancements of artificial intelligence. This convergence has opened up a new frontier in design and creation, with generative AI making its way into the designer's workshop alongside traditional tools and techniques.

For decades, computer-aided design and manufacturing (CAD/CAM) and other digital design tools have been widely used by jewelry designers. However, generative AI reaches into a new realm where computers have become capable of generating unique designs with seemingly little to no direction or human input. In the context of jewelry design, this technology offers the potential to redefine the boundaries of creativity and production.

Despite the exciting possibilities, this fusion of AI with the creative arts is not without controversy. Concerns range from the potential displacement of skilled artisans to the ethical implications of AI-generated art. As one U.S.-based digital advertising agency noted, "AI-generated content, while impressive in its ability to analyze trends and produce designs quickly, may lack the nuanced touch and emotional connection that is often conveyed through a human designer's work. This could lead to a homogenization of design styles, as AI algorithms tend to optimize for efficiency and patterns in data rather than the bespoke artistry that clients seek" (JEMSU, n.d.).

"AIdeation" AND "HALLUCINATION"

One of the most powerful opportunities that AI technology presents is the ability to brainstorm design ideas at incredible speed. Sometimes referred to by the play on words "AIdeation," quickly creating

In Brief

- Generative artificial intelligence programs can create highly detailed, photorealistic images of gems, jewelry, or any other subject in seconds.
- Designers may use these tools to create wholly new concepts for jewelry or to create variations on an existing idea.
- The legal and regulatory framework for AI-generated art is not yet settled. There are a wide range of copyright concerns and legal cases around source material still in question.
- This technology is rapidly advancing and already impacting the field of jewelry design.

See end of article for About the Author and Acknowledgments.
This article was originally published in a different form by The Jewelry Symposium for the Advancement of Jewelry Manufacturing Technology and is published with permission of The Jewelry Symposium.
Gems & Gemology, Vol. 60, No. 3, pp. 330–347,
http://dx.doi.org/10.5741/GEMS.60.3.330

Figure 1. Midjourney 5.2 image variations produced from the prompt "a pair of 18 karat yellow gold earrings featuring a fusion of Art Deco and ancient Egyptian styles." At each stage in this figure, the user selects one of the images (marked here by the colored square boundary) and feeds it back into the AI, which generates four new variations. In this manner, the image is further refined to suit the tastes of the designer or the client.

ideas as starting points is becoming the most common use case for AI in design. With an input consisting of only a few words, AI can generate many iterations from a single concept or idea.

As an example of a potential "AIdeation" workflow, consider the design of a pair of earrings for a client who is passionate about both ancient Egyptian and Art Deco styles. After a short description, or "prompt," is entered into Midjourney (docs.midjourney.com/docs/prompts), the program quickly returns four original images blending these styles for the user to choose from (figure 1). These images are simply stepping stones to more variations. The user can choose any of the options to explore and create variations based on that image, making widely varied options at first and then refining the image through minor alterations. In approximately five minutes, Midjourney can generate 16 or more variations to begin designing around.

"Hallucination" is a common term used in reference to the popular ChatGPT or other text-based AI chatbot programs, where the program makes up patently false information in its answers. While this understandably poses a significant problem when attempting to collect and summarize factual information, it is actually a benefit where image generation is concerned. The images created by generative AI are not collages cut and pasted from different images in the training data: They are original "hallucinated" compositions. A simple prompt can generate entirely new designs, such as the collection of white gold earrings in figure 2 or the rose gold pendants in figure 3.

The tools are far from perfect, and for now they are better suited for generating new ideas than perfecting an existing image or design. So far, AI is no substitute for a trained designer, and it has no concept of what can actually be manufactured. Examples of AI design irregularities can be seen in the odd miniature diamond rings on the ends of the baguettes in figure 4 and the "floating" bezels in figure 5.

UNDERSTANDING GENERATIVE AI

The good news for most jewelry designers is that knowing the technical details of the AI model is not at all important to using the tool effectively. A complete grasp of the underlying programming will not give the casual user better results.

Figure 2. Images from Midjourney 5.2 using the prompt "a pair of white gold earrings displaying a sense of asymmetrical balance."

Figure 3. Images generated by Midjourney 5.2 from the prompt "a rose gold pendant with contrasting round gems."

Broadly speaking, generative AI refers to a type of artificial intelligence that can generate new content, including text, images, music, or even videos that previously did not exist. Generative AI essentially oper-

Figure 4. DALL.E 3 generated this image from the prompt "create a halo of tapered baguette diamonds, also set in platinum, which are attached to the gallery of the Paraiba's setting." Circled in red is a design oddity: miniature diamond rings placed on the ends of the baguettes.

Figure 5. Another image output from Midjourney 5.2, using the prompt "watercolor style, pear-shaped Paraiba tourmaline brooch set in platinum with a halo of diamonds surrounding it." Circled in red are irregularly shaped gems and "floating" bezels.

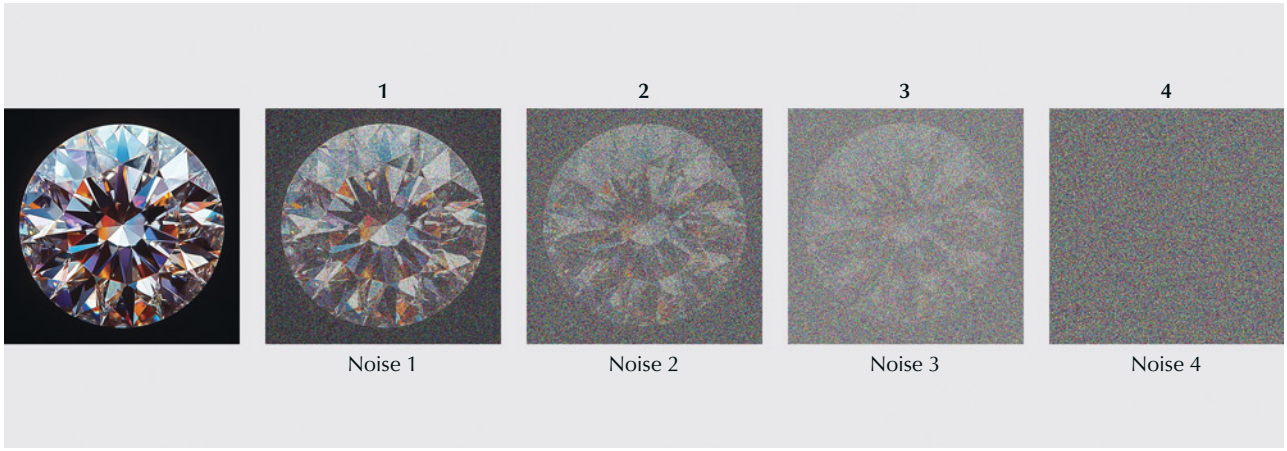

Figure 6. Steps of forward diffusion. Noise is added to the image at each step until it is completely randomized.

ates using complex algorithms and large amounts of data. What makes the process unique is the machine learning used to find patterns within that data.

Machine learning is the science of developing models that computer systems use to perform complex tasks without explicit instructions. This is where the AI learns from the data, absorbing information and performing better over time. The system processes large quantities of data in order to identify patterns. Then the AI analyzes the data with algorithms and makes predictions based on that data analysis. The AI makes many attempts to process the data, testing itself and measuring its performance after each round of data processing. In this way, the AI "learns" from mistakes and gradually improves its ability to generate increasingly sophisticated and realistic new content. Given enough text, images, or other data, generative AI can find patterns linking similar concepts together and then create a new result that follows the same patterns (Sanderson, 2017; see also https://www.youtube.com/@3blue1brown).

Creating Images. So how does generative AI actually produce images? AI image creation models are a specific application of generative AI that focuses on visual content, such as pictures or graphics. These models have captured global media attention for their ability to create stunning, sometimes surreal images based on simple text descriptions. One of the most prevalent image creation models for generative AI is the diffusion model. To understand how this model works, it is helpful to understand that the diffusion referred to in the name is similar to the concept of particle diffusion in physics. In an image, this "particle diffusion" is represented by each pixel moving or changing in a random direction, slowly transforming the image into static or visual noise.

For example, consider the image of a diamond in figure 6. A user might start with this to train a model to create other diamond or gem images. Step by step, a little bit of noise is added to the training image. Eventually, the training image is completely unrecognizable as a diamond, showing only randomness. This forward diffusion process takes the original image and adds noise, gradually transforming it into an unrecognizable noise image (Stable Diffusion Art, 2024).

Both the original diamond image and the images for each step of added noise are fed into a neural network model, which attempts to calculate exactly how much and what kind of noise was added at each step. With enough data, this neural network model can create a working noise prediction model. Once this is accomplished, the noise prediction model can be applied in reverse.

In reverse diffusion, the process begins with a randomly generated image. The noise predictor then calculates the amount of noise that has been added to the image. That noise is subtracted from the original randomized image. The process is repeated until it resolves into the image of a diamond, as shown in figure 7 (Stable Diffusion Art, 2024).

These models are trained not on a single image, but on trillions of images. With enough data, the generative AI can assign reverse diffusion pathways for any type of image or prompt it is trained on. A properly trained model will produce many different images of diamonds, or any other subject, based on the learned pathways from each of the training images,

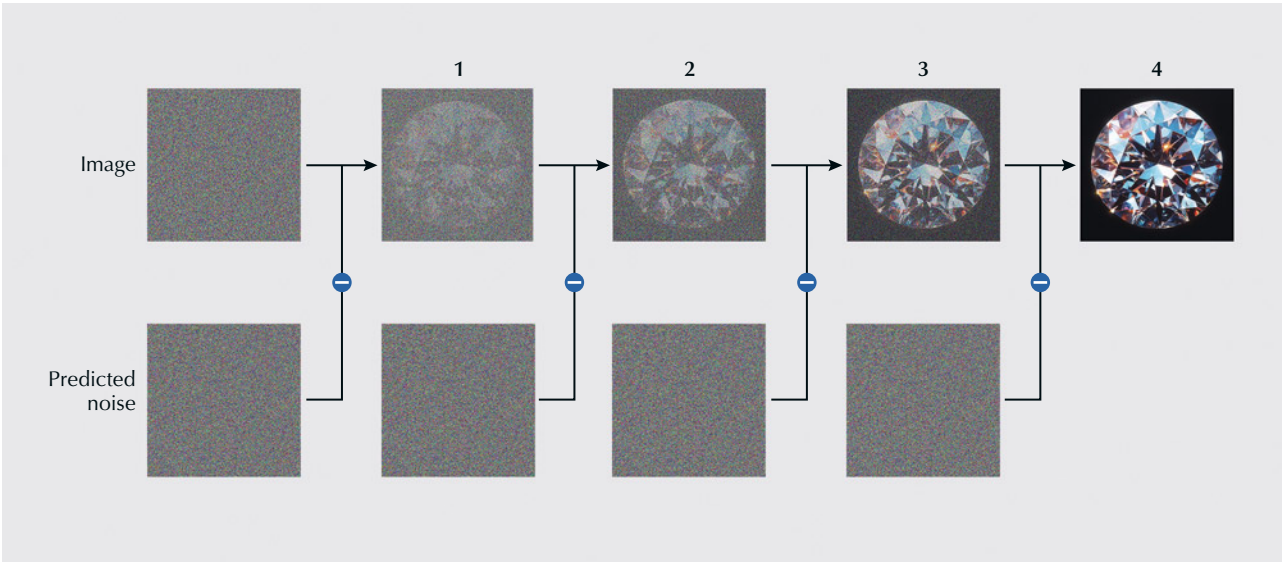

Figure 7. Steps of reverse diffusion. Predicted noise is removed step by step from a randomly generated image until it resolves into a recognizable image.

and a model trained on jewelry images will be able to generate entirely new images of gems and jewelry.

Prompts. At the time of this writing, text prompts are still the most common way of interacting with any generative AI program. Somewhere between a coding language and regular sentence structure, each word in a text prompt is converted into its own set of weighted vectors, which are used to "steer" the noise toward a desired outcome. Each program has its own language requirements and idiosyncrasies that can be used to optimize the user's control over the image.

When given a text description, the AI applies what it learned during training to translate those words into a visual format. For example, if the user prompts it for an image of a "sunset over the ocean," the AI combines its understanding of "sunset" and "ocean" to create an entirely new image that fits the description. By assigning a weight to each part of a prompt, the model will use a different noise prediction. Combining those prompt weights with a starting image of randomly generated noise will return a near-infinite number of possible outcomes.

Figure 8. Left: A sterling silver "River" brooch by Dolmen Metalworks featuring Mississippi River stone cabochons. Photo by Michael Magee. Right: Eight necklace variations created in Dream Studio SDXL v1.0 using the prompt "silver necklace, water motif, sandblast and high-polish, cabochons." The sixth image was generated without stones.

Figure 9. Pendant design from Midjourney 5.2 using the prompt "enamel and yellow gold pendant, Alphonse Mucha style, Art Nouveau, African American woman in profile, on a background of flowers, sketch on white paper, drawn by a master designer."

Rather than creating an image using only text, most platforms allow the user to upload an image as a starting point or use a combination of image and text prompts. This prompt can be an original image input by the user or an image previously generated by an AI. In figure 8, we see an example of a photograph used in conjunction with a text prompt to create variations based on the original image's identifiable content, color scheme, and style.

Beyond creating entirely new images such as the one in figure 9, generative AI's capabilities can be focused on a particular aspect of an existing image. Four of the commonly used tools are *outpainting*, *inpainting*, *upscaling*, and *blending*. Each generative AI program also has its own proprietary features, abilities, and specialties in addition to these common tools.

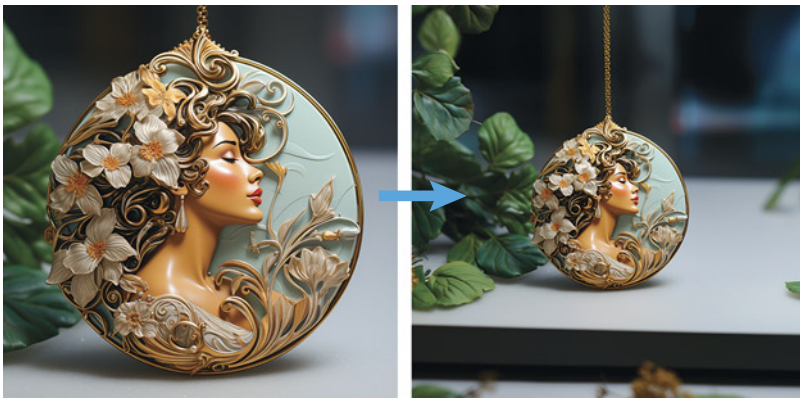

Figure 10. Images from Midjourney 5.2, before and after outpainting.

Outpainting expands the image, effectively zooming out and then filling in what the AI expects to be found in the scene around the original image (figure 10). This can typically be done with or without an additional text prompt explaining what should fill the outer portion.

Inpainting requires the user to identify a portion of the image that should be replaced (figure 11). The AI then updates that selected subsection of the image. This can also be done either with or without an additional text prompt to define what should change within the image.

Figure 11. Images from Midjourney 5.2 using the inpainting prompt "more plants on the table."

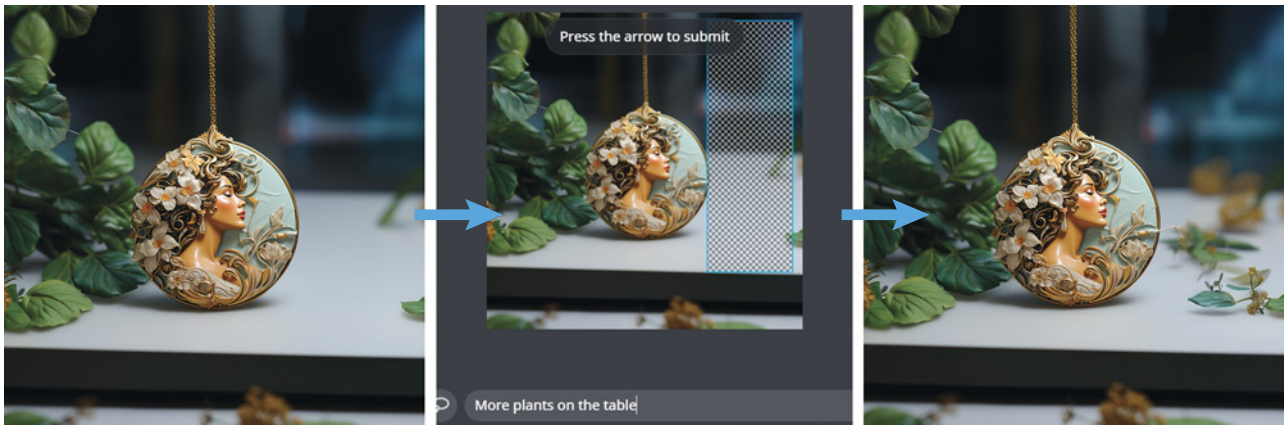

Figure 12. Images from Midjourney 5.2, before and after upscaling.

Upscaling allows the user to enlarge an image without reducing its resolution (figure 12). When the image is upscaled, the AI divides each pixel into the appropriate number of new pixels, adding new information while increasing overall image size. The end result is an image that is both larger in overall size and has increased definition. No additional text prompt is used, as the AI is not adding or subtracting any prompted subject matter. Instead, the AI uses the image itself as the prompt to fill in the details at a finer resolution.

Blending takes two or more existing images and creates a new image that combines aspects of each of the originals (figure 13), with or without an additional text prompt.

REVIEW OF POPULAR GENERATIVE AI PROGRAMS

This section briefly looks at five of the most popular generative AI programs: Midjourney, Stable Diffusion, DALL.E, Leonardo.AI, and Firefly. Each platform has its own pros and cons, described below and compared in box A.

Midjourney is currently one of the most popular and robust AI image generators available. The images can be highly detailed, creative, and realistic, and the responses to prompts reflect a reasonable understanding of common jewelry terminology (see figures 1–3 and 9–13).

Subscription plan pricing varies depending on the membership tier. The speed of image generation varies

Figure 13. Two images created with Midjourney 5.2 (left and center) and their resulting blend image (right). Prompt 1 (left): "enamel and yellow gold pendant, Alphonse Mucha style, Art Nouveau, African American woman in profile, on a background of flowers, sketch on white paper, drawn by a master designer." Prompt 2 (center): "a jewelry designer and an AI computer drafting a new design on paper together in a jewelry designer's workshop."

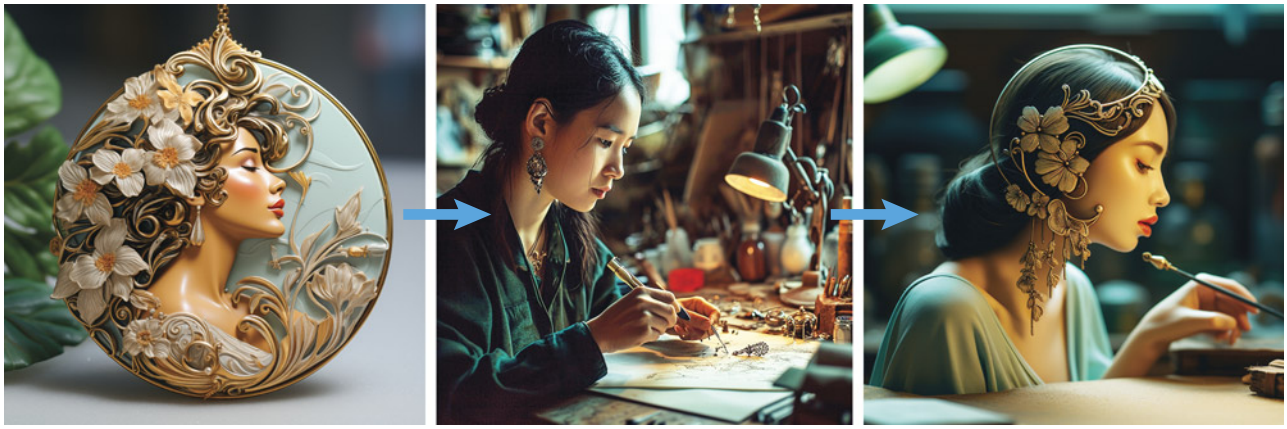

Figure 14. Dream Studio SDXL v1.0 AI-generated image using the prompt "platinum three-stone ring, tanzanite center gem, diamond side gems, photorealistic" (left) and variations with 25% and 50% image strength (right).

accordingly, but even the basic plan can generate a set of four images within 30 seconds. Typically, all of the images created are made publicly available on Midjourney's website and are visible to all other users. The two highest membership tiers offer a privacy mode that does not share generated images.

The main disadvantage of Midjourney is that currently it can only be accessed through the Discord interface. Initially created as a chat and messaging app for video gamers to interact with one another, the Discord community has branched out into many areas beyond gaming. However, the Discord interface can be daunting to new users, especially those unfamiliar with video gaming chats and streaming platforms. To alleviate this challenge, Midjourney is developing a web-based interface. At the time of this writing, however, the web version is in a closed development stage and only open to select users.

Stable Diffusion, by Stability AI, is an open-source generative AI program. The online interface is easy to use and is accessed through the website interface, called DreamStudio. Users are given free credits to start with and can purchase more as needed.

The most common criticism of DreamStudio is that the images are less creative than those generated by other programs, particularly Midjourney, which is thought to have more of an artistic flair.

One area where DreamStudio excels is in making variations on an existing image (see figure 8). Once a starting image is uploaded, a slider can be set to determine how closely or loosely the variations should follow the original (figure 14). A higher image strength value will make any new images adhere more strictly to the original, while a lower image strength will give the AI more "creative license" to make variations.

Stable Diffusion is offered as an open-source program and can be installed locally on a computer rather than using it through the DreamStudio webpage. While running Stable Diffusion locally on a computer may slow down the generative process, depending on the computer's specifications, it does offer several key advantages. One is that all the images created are kept private from other users and the Internet at large. Most other programs charge users a premium to keep their data private. The other significant advantage is that an advanced user can customize the diffusion process with samplers. A sampler is an add-on to the diffusion model that can nudge the image creation toward specific styles or results (Gilgamesh, 2023). This grants the user greater control over the specific qualities and details of the images generated.

DALL.E is made by OpenAI, the same company that created the well-known ChatGPT. The latest version of DALL.E is fully integrated with ChatGPT, which means users can prompt it with a written or spoken conversation instead of a code-like prompt (see figure 4).

While the images created can be extremely detailed, the process is typically slower and less customizable than other programs. Free accounts are available for both programs; however, at the time of this writing, a monthly subscription is necessary to access the latest versions of ChatGPT and DALL.E.

Box A: Comparison of AI Programs

To compare the five most widely used generative AI programs, the same prompt was used to create four variations of a tanzanite three-stone ring using each program (figures A-1 through A-5). The prompt used was "platinum three-stone ring, tanzanite center gem, diamond side gems, photorealistic." For DALL.E, a complete sentence structure was used for the same prompt.

Figure A-1. Images generated by Midjourney 6. These designs feature intricate details, including organic scrolls and fine milgrain. The gems are in the appropriate color range for tanzanite and diamonds. The images also feature a certain amount of depth of field, making them more photorealistic.

Figure A-2. Images generated by DreamStudio SDXL v1.0. These designs are less detailed but still mainly accurate depictions of jewelry. The metal and gemstones show the appropriate color range for their materials. The image on the bottom left shows some inaccuracies on the prong settings, blurring between prongs and diamonds on the center setting and adding extra prongs to the side setting on the left. Again, a certain amount of depth of field is apparent, making the images more photorealistic.

Figure A-3. Images generated by DALL.E 3 using the prompt "create a photorealistic image of a platinum three-stone ring, with a tanzanite center gem and diamond side gems." These images show some detail and creativity in the designs and feature a wider variety of gem shapes. However, in the bottom left image, some of the details are poorly defined, such as the milgrain along the channel setting, the engraving on the inside of the shank, and the detail on the sides of the pear setting. In all of the images, the colors are reasonably accurate for the materials. The images are less photorealistic and more closely resemble digital renderings from a CAD program. This stylistic rendering seems to be consistent across images created with DALL.E.

Figure A-4. Images generated by Leonardo.AI Phoenix. The rings in these images are remarkably similar, with little variation in design or positioning. The designs are also very simple in comparison to the previous three examples. A greater variety of prompts would be needed to create more design variations. All the images show some degree of depth of field, and the bottom left image also displays a particular blurring of lights in the background, creating a photorealistic effect.

Figure A-5. Images generated by Adobe Firefly 2. These rings are less accurate depictions of the "three-stone ring" concept given in the prompt—particularly the top left image, which has no side stones at all. The desired materials, tanzanite and platinum, are also poorly depicted and could easily be confused for blue sapphire and white gold. Upon closer inspection, the center "tanzanite" gems show an oversimplified faceting patten not common in commercial cuts. The bottom right ring also appears to be slightly out of round. These inaccuracies are likely due to the smaller amount of jewelry-specific training data available to Firefly.

DALL.E can also remember previous conversations and write its own prompts when asked to describe uploaded images. Since integrating with ChatGPT, DALL.E has quickly become a popular contender to Midjourney.

Leonardo.AI is another image generator that has recently become a very popular rival to Midjourney. While Leonardo has a more complicated web interface than Dream Studio, DALL.E, and Firefly, it offers more variety and control over both the types of prompts available and the style of the images created.

Leonardo's base memberships are free with a limited number of generations per month. Several tiers of paid memberships are available, offering greater generation speed and other options. At the lower membership tiers, all images uploaded to and created by Leonardo become part of the program's dataset, with private accounts available for a monthly fee.

Like Midjourney, Leonardo has a well-developed understanding of jewelry terminology and is likely to create images that technically match the prompt. Part of what makes Leonardo unique is the ability to combine text prompts with a live sketching program, called Realtime Canvas. The generated image constantly updates, within the parameters of the text prompt, as the user sketches through their web interface or through the iOS app. Leonardo also allows users to "train" their own image models by uploading up to 40 images. The AI then uses this custom dataset to fine-tune its results for the user.

Adobe Firefly is a relative latecomer to the generative AI field but offers a unique set of assets, namely Adobe's existing Creative Cloud suite. The Firefly

tool is both a stand-alone image generator and a built-in plugin to Photoshop, where it can be used to generatively fill areas of a composition with excellent inpainting and outpainting capabilities.

Firefly can be purchased as a stand-alone product or bundled into the cost of Photoshop or Creative Cloud. The Firefly website is easy to use to quickly generate and modify images.

One of Firefly's main advantages is also its biggest disadvantage for creating jewelry: Adobe's unique sources of training data. Most other generative AI programs have been trained on trillions of images pulled from all over the Internet, which includes a vast quantity of jewelry images. In comparison, Firefly has been trained on hundreds of millions of Adobe Stock images, openly licensed content, and public domain images. Therefore, the regulatory landscape is clearer for Adobe Firefly, which will be discussed in depth in the next section. However, this is a considerably smaller dataset than the other programs, and an even smaller proportion of it is trained on jewelry. Consequently, Firefly has less of an understanding of jewelry forms and terminology.

ETHICAL, LEGAL, AND REGULATORY CHALLENGES

As with any technological revolution, the introduction of generative AI into jewelry design brings a new set of challenges that must be navigated with care. This section will delve into the ethical considerations, legal implications, and evolving regulatory landscape surrounding AI-generated art.

How we think about AI—whether as a tool or as a cocreator—adds a layer of complexity to the question of ownership and copyright. Anthropomorphizing AI (attributing human qualities to it) can pose additional philosophical and moral dilemmas. It is helpful to consider generative AI as a tool used to support human creators rather than as an independent creator with its own ideas (Epstein et al., 2023). In navigating this uncharted territory, it is imperative to understand both the opportunities and challenges posed by generative AI. By understanding these issues, jewelry designers can make informed decisions about how to responsibly integrate AI into their processes.

Ethical Considerations. The use of AI in creative industries raises important ethical questions. One primary concern is the authenticity of the designs. When a piece of jewelry is created with the heavy involvement of AI, who becomes the true author? This is a crucial question for designers who pride themselves on the uniqueness and originality of their work. Moreover, there are concerns over the potential for AI to create and proliferate designs that closely resemble original artworks without proper attribution or compensation to the original designers. Indeed, users can prompt the AI to generate images in the style of a specific artist (Yup, 2023). As a response to this criticism, many programs are beginning to place guardrails against directly referencing living artists in their prompts.

Another ethical issue involves the impact of AI on craftsmanship. Jewelry design is an art form that traditionally requires a high degree of skill and years of practice. If anyone can use AI to generate intricate designs in a matter of minutes, then what becomes of the skilled artisan? There is a significant risk that the value placed on manual skills and craftsmanship could diminish, leading to a loss of heritage and tradition within the field.

Fortunately, the jewelry industry is fundamentally about tangible goods. While AI may be able to create extraordinary images, at some point the design still needs to be manufactured. By making the tools of design more easily accessible, greater value could potentially be placed on the skills needed to turn those designs into reality. A designer's understanding of gems and precious metals, manufacturing processes, ergonomics, and typical wear are instrumental in creating jewelry that is both beautiful and functional.

Legal Landscape and Regulatory Implications. The current legal issues for generative AI revolve predominantly around copyright and intellectual property (IP) rights. The current legal frameworks were established in a pre-AI era and are thus not fully equipped to handle the nuances of AI-generated works. For instance, if an AI creates a jewelry design based on a prompt from a human designer, who owns the copyright? At the time of this writing, the U.S. Copyright Office has brought some clarity to this scenario:

> In the Office's view, it is well-established that copyright can protect only material that is the product of human creativity. Most fundamentally, the term "author," … excludes non-humans. … For example, when an AI technology receives solely a prompt from a human and produces complex written, visual, or musical works in response, the "traditional elements of authorship" are determined and executed by the technology—not the human user. (United States Copyright Office, 2023)

In short, art generated solely by an AI program cannot be copyrighted or attributed to any author. However, the U.S. Copyright Office went on to say that "an artist may modify material originally generated by AI technology to such a degree that the modifications meet the standard for copyright protection. In these cases, copyright will only protect the human-authored aspects of the work" (United States Copyright Office, 2023).

There is also the complication of derivative works. If an AI is trained on a dataset that includes copyrighted jewelry designs, there is the possibility that its outputs will infringe on the IP rights of the original creators. To address these remaining questions about copyright and ownership, the U.S. Copyright Office is conducting a study regarding the copyright issues raised by generative AI. This same matter is being addressed in U.S. district courts, where several high-profile intellectual property lawsuits are currently in progress (Appel et al., 2023).

Some of the larger AI companies are taking steps to help their customers address the risks of copyright infringement. In 2023, OpenAI announced that it would pay the legal costs incurred by enterprise-level customers who face claims around copyright infringement as it pertains to ChatGPT and DALL.E (Wiggers, 2023).

One notable exception to the intellectual property battles in generative AI is Adobe Firefly. As previously mentioned, Adobe has trained its generative AI model using only licensed Adobe Stock and public domain images where copyright has expired (https://www.adobe.com/products/firefly/enterprise.html). This means Adobe is able to guarantee that its AI images do not violate any existing copyrights, and it can offer limited IP indemnification for enterprise-level customers using Firefly (https://helpx.adobe.com/legal/product-descriptions/adobe-firefly.html). However, it has more recently come to light that the Firefly model was trained partially on images generated by other AI platforms—about 5% in all (Metz and Ford, 2024). While this somewhat complicates the issue of intellectual property practices, Adobe stands by its moderation process and insists that its training data does not include intellectual property.

Adobe also automatically adds specific metadata to any AI-modified or -generated image created with its software. These "content credentials" can also store the content creator's information, establishing a more durable record of ownership. To further this goal of content transparency, Adobe founded the Content Authenticity Initiative (https://opensource.contentauthenticity.org), a nonprofit group for creating tools to verify the provenance of digital images.

Adobe is also a cofounder of the Coalition for Content Provenance and Authenticity (C2PA, https://c2pa.org), an organization that develops open global standards for sharing information about AI-generated media across platforms and websites beyond Adobe products. Other members of C2PA include Microsoft and Google, both of which are currently the subject of lawsuits for allegedly extracting data indiscriminately from the Internet to train their own AI products.

The regulatory environment for AI in creative arts is still in its infancy. Governments and international bodies are only beginning to grapple with the implications of AI and are in the process of developing laws and guidelines to govern its use. This includes ensuring that AI-generated works respect copyright and IP laws and setting standards for transparency and accountability in AI use.

For jewelry designers, staying informed about these regulations is critical. As laws evolve, new compliance requirements may affect how designers can use AI tools. Designers will need to stay abreast of these changes to ensure that their use of AI remains within legal boundaries. Furthermore, there is a clear need for education within the jewelry design community about the legal and ethical implications of AI. Designers should be equipped with the knowledge to use AI responsibly, respecting both the letter and the spirit of intellectual property laws.

AI-ENHANCED DESIGNERS

As with any new technology, early adopters are already using generative AI to enhance their design and sales workflows. Many of the tools listed in this paper are being used to drive sales, either by creating marketing content, inspiring the final designs, or producing images to close sales. At the time of this writing, AI-generated images are still error-prone, and designers may wish to create the images in private to cull any unworkable results before showing them to a client. However, as this technology advances, it will undoubtedly open up new options for designers who enjoy working in live sessions in front of their clients.

One of the most promising AI methods being pioneered to enhance a designer's workflow is called "sketch to render." This approach takes a loose sketch of a design as an image prompt and then uses

Figure 15. Hand-sketched bracelet design by Devyani Shah (left) and a Dzine.ai "rendering" (right) created using the sketch along with the text prompt "white gold bracelet with pave set diamonds in leaf-shaped clusters. A large oval emerald is set in the center of the bracelet. Art Deco inspiration. Photorealistic rendering. Dazzling light reflection on the gems. Neutral background."

a generative AI program to create a fully rendered image, filling in the color, materials, lighting, and shading of a 3D object based on the original sketch and an accompanying text prompt (figure 15). A talented designer or salesperson can use "sketch to render" to quickly turn their sketched ideas into realistic images for a client to review. Some promising examples of this technology are Dzine.ai and Vizcom.ai. In figure 15, a hand sketch is used along with a detailed text prompt to create a more photorealistic version of the original sketch in Dzine. Looking closely at the AI-generated image shows some blending between the diamonds and the metal materials in the bracelet links. Dzine recently began training their models on jewelry-specific images in order to remove these kinds of inaccuracies.

The "sketch to render" method introduces significant enhancements to the design workflow. First, it brings the focus of the design process back into the hands of the human designer or salesperson. Designs can be drawn by hand and scanned, or drawn on a digital application on a tablet, computer, or even phone. Once drawn, an AI program can quickly process the sketch into a more photorealis-

Figure 16. Digital sketch (left) and a Dzine.ai "rendering" (right) using the original image and adding the text prompt "intricate yellow gold earrings, adorned with scintillating diamonds, dangle elegantly from the ear, their wavy design evoking a sense of fluidity, as if dancing in the light; photorealistic rendering, the warm golden hue and flecks of diamond sparkle radiating a sun-kissed glow, perfect for a summer evening soiree or a vintage-inspired bridal look, with hints of Art Deco sophistication and bohemian flair, every detail meticulously captured in the rendering's subtle nuances."

tic image, similar to the digital rendering of a CAD model (figure 16).

With the prevalence of CAD programs in the industry, custom jewelry purchasers have come to expect photorealistic renderings of their jewelry before giving approval. This means a designer often spends hours developing a CAD model for approval without first receiving a deposit on their time and work. When a design goes through many iterations before client approval, this CAD modeling time can add up to a significant cost.

By using AI to create a photorealistic image from only a sketch, a salesperson can get approval and potentially a deposit on a design before investing any time modeling in CAD. The photorealism of the AI-generated image can help the client better visualize the final product, while the designer can save the labor-intensive CAD modeling for the final design. The salesperson can even use AI to create variations of the original sketch to quickly explore design options.

Another significant benefit of this "sketch to render" method is that it creates a copyrightable foundation for the design early in the process. Instead of creating an uncopyrighted AI design with copyrightable human-made modifications, the designer creates a copyrighted original sketch and later adds AI modifications that may or may not be copyrightable. While not a guarantee of copyright protection, starting with a human-created drawing can help establish the "human authorship" requirement for a copyright.

Much of the effort of custom sales is the selling of jewelry from pictures—sketched by hand, digitally sketched, or CAD-rendered—as the desired jewelry does not yet exist. Now a designer can use AI to enhance their natural creativity, reduce unnecessary labor on unwanted designs, protect their creative ideas, and help their clients realize their ideal design faster.

FUTURE DEVELOPMENTS

The technology involved in generative AI is moving at a tremendous pace. The speed of image generation, as well as the complexity and accuracy of the prompts, improve with every update released. While these changes may make AI more accessible and accepted for jewelry design, they may not fundamentally alter how this technology changes our industry. However, there are several growth areas that bear watching: *text to video*, *image to depth map*, and *text to mesh* generation.

Text to Video takes the text-to-image format one step further, creating short videos solely from a text prompt. It often requires multiple images from dif-

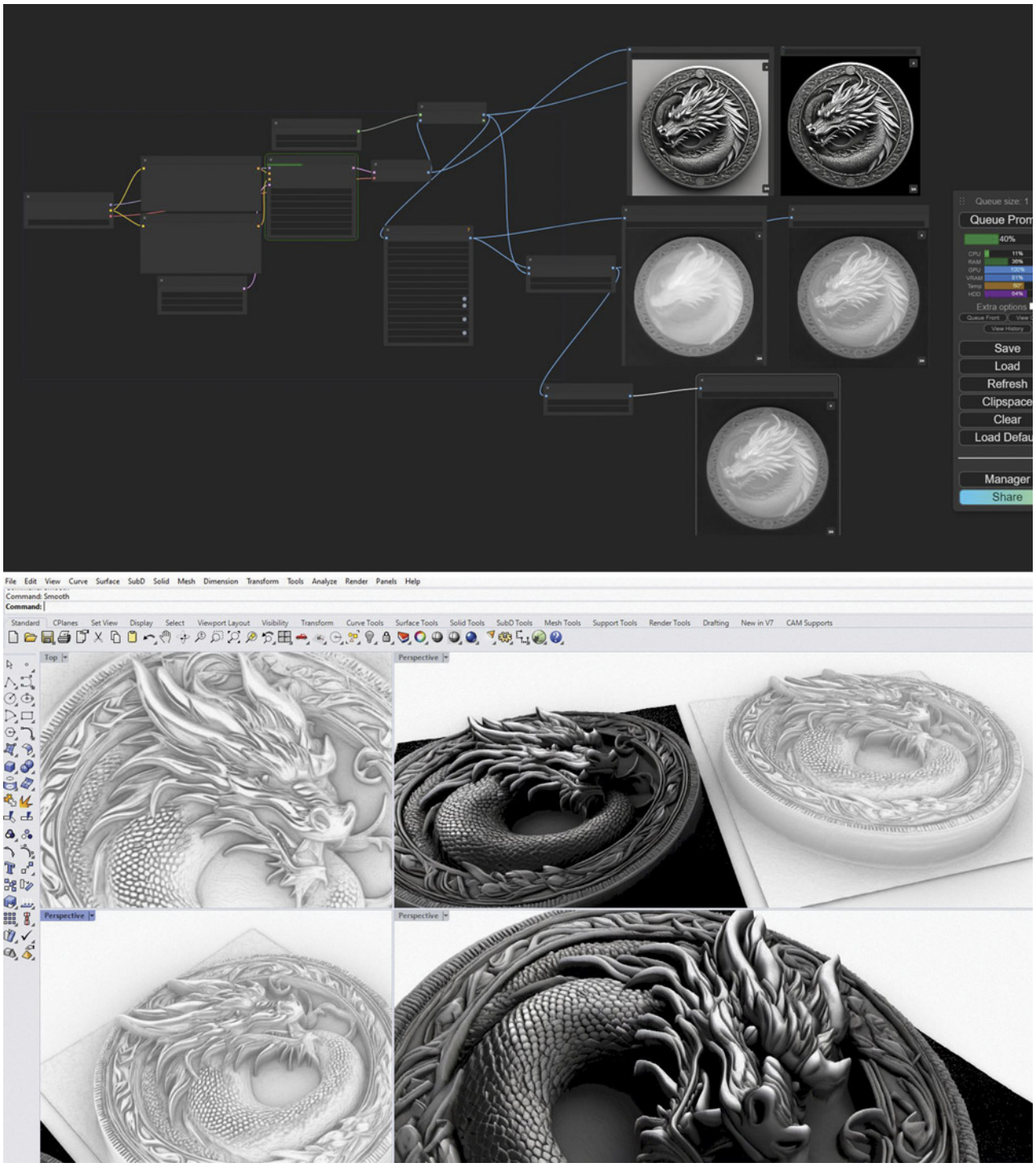

Figure 17. "Dragon Coin" by Chris Botha. Stable Diffusion image and depth map; 3D design in ZoeDepth and Rhinoceros 3D. The top image shows a customized program for Stable Diffusion using the ComfyUI user interface. ComfyUI allows the user to control Stable Diffusion with a visual programming language. Each piece of code is represented as a box with specific inputs and outputs. The boxes are connected together via these input and output connectors to modify the code, creating detailed images from the text prompt and then transforming the detailed images into heightfield images suitable for ZoeDepth. The bottom image uses Rhinoceros to show the 2.5D object created from this image by ZoeDepth.

ferent angles to properly describe a jewelry object. Many designers are familiar with the top, front, and side views found in many CAD programs, as well as hand-drafting techniques. A simple video rotating 360° can describe a ring more accurately than any single image. Several of the major AI platforms, such as Leonardo.AI and Stability AI, have already offered this capability in more recent upgrades, although at the time of this writing, these models still have a limited ability to rotate a complex jewelry design accurately (see video at www.gia.edu/gems-gemology/fall-2024-artificial-intelligence-in-jewelry-design).

Image to 2.5D Depth Map is an interesting step toward creating producible models directly from AI. With some additional training, programs such as Stable Diffusion can be modified to create not only black-and-white images but also depth maps, which are grayscale images where the shades of gray denote the relative depth of a three-dimensional object. Other programs, such as ZoeDepth (Bhat et al., 2023), can translate those images into actual 2.5D geometry, which can be manipulated directly in a CAD program such as Rhinoceros or ZBrush (figure 17).

Text to 3D may take longer to properly develop as a technology, but it has the potential to dramatically impact the jewelry industry. Instead of training on the trillions of images found on the Internet, these programs are trained on multitudes of 3D models. While these programs currently exist and can be found at sites such as Meshy.ai (figure 18), they are geared toward building props and avatars for the video game industry. The low-resolution quality of these models makes them not yet suitable for producing jewelry. One of the biggest hurdles for this technology is the relative paucity of 3D models available to train the AI compared to the number of images used to train the 2D models.

Figure 18. Images from Meshy.AI using the prompt "green emerald amulet, yellow gold, high detail, organic leaf and vine design." This program creates fully three-dimensional models from a text prompt, as opposed to the flat 2D images of other programs. Some of the finer details are "painted" onto the model with a colored image that is applied to a simpler 3D object. Finer details suggest that the gem and pendant are separate objects (left). The same object with the colored image removed (right) reveals the actual 3D geometry created. Note that the gem and pendant are actually one object painted as different materials.

Several major 3D players, including TurboSquid, Autodesk, and Meta, are currently developing their own 3D modeling generative AI tools. TurboSquid, owned by Shutterstock, is the largest online 3D model marketplace, with over a million 3D models available for purchase, although most of the models are not jewelry specific. Autodesk, the maker of many of the most popular CAD programs, announced its Project Bernini for generative AI 3D shape creation in May 2024 (Autodesk, 2024). Meta (the parent company of Facebook, Instagram, and WhatsApp) recently published a paper about a new Gen3D program designed to create 3D objects from text for its Metaverse applications (Siddiqui et al., 2024). Each of these companies would have a collection of high-resolution models large enough to properly train a text-to-mesh program to generate high-quality 3D meshes that could be imported into any CAD program.

SUMMARY

How can jewelry designers best use this new technology to enhance creative expression? Generative artificial intelligence is already having a profound effect on the fields of art and design. Its impact on the jewelry design industry has begun as well.

The two greatest assets of generative AI today are accessibility and speed. Anyone can now create jewelry images in a matter of seconds using only a few words and the right program. However, there is more to real jewelry product design than just a picture. Going forward, the two greatest assets for a designer using these tools will be the ability to translate images into actual models, acting as a "reality check" on the designs, and the ability to personalize or customize, pushing designs further toward a specific direction or purpose.

Images from generative AI may be eye-catching, but they still must be made into physical objects to become jewelry. A designer's expertise is needed to translate any 2D jewelry image into a 3D model by using CAD or traditional hand-carving or fabrication methods. To be effective, designers must still possess a deep understanding of the metal and gem materials, manufacturing processes, the dimensions and tolerances needed for durability, and the ergonomics of how jewelry interacts with the wearer's body.

Personalization will continue to add a human touch. Whether a designer is brainstorming ideas for a new jewelry line using prompts crafted from marketing predictions for the upcoming year or designing a one-of-a-kind, bespoke jewelry piece for a single client, the AI images may only be the beginning. A good designer can take these AIdeation starting points and refine the design, whether to tie it into an existing brand, tell the design story for one individual, or simply push the boundaries of design even further. Likewise, a creative designer can start with their own designs and use AI to explore variations and transform their quick sketches into photorealistic images. These personal touches also help ensure that the final design is unique and copyrightable.

Given the overlap between AI tools, they can be chosen based on what works best for an individual business. However, a jewelry designer using AI tools must be vigilant to ensure that their use of AI does not inadvertently violate the IP rights of others. Using AI to create variations of one's own preexisting work ensures that the main input for the generated image comes from personal creativity.

For a company willing to invest greater resources, there may be another interesting pathway. A company with a large collection of designs could potentially create its own private generative AI platform, trained on its own designs. This would allow that company to generate new images based solely on its own existing portfolio, solving any copyright or intellectual property concerns. Even a designer with a limited number of designs could use them to train an existing generative AI model to create images that are heavily influenced by their modest portfolio.

Lastly, an industrywide push is needed for transparency in AI tools. Designers should have a clear understanding of how AI models are trained, the data they use, and the potential for bias or infringement within these models. This transparency will help designers make more informed choices about the tools they use. Many unanswered legal and regulatory questions regarding this new technology remain, waiting for their respective day in court.

As with any new technology, each individual ultimately decides whether to become an early adopter, taking on the possibilities of both risk and reward, or to wait, watching and learning from the accomplishments and missteps of others.

ABOUT THE AUTHOR
Michael Magee is a senior subject specialist in jewelry manufacturing arts at GIA in Carlsbad, California.

ACKNOWLEDGMENTS
The author would like to thank the jeweler community at the online forum CADCAMTrav and Ian McAskill in particular for being an early adopter of AI technology and helping to pave the path. Thanks to Greg Stopka for his excellent peer review and insights. Chris Botha shared his work in figure 17, and the author's colleague Devyani Shah shared her manual design skills in figure 15. Thanks also to The Jewelry Symposium for the inspiration to write and present this paper.

REFERENCES

Appel G., Neelbauer J., Schweidel D.A. (2023) Generative AI has an intellectual property problem. *Harvard Business Review*, April 7, https://hbr.org/2023/04/generative-ai-has-an-intellectual-property-problem

Autodesk (2024) Autodesk unveils Research Project Bernini for generative AI 3D shape creation. *ADSK News*, May 8, https://adsknews.autodesk.com/en/news/research-project-bernini/

Bhat S.F., Birkl R., Wofk D., Wonka P., Müller M. (2023) ZoeDepth: Zero-shot transfer by combining relative and metric depth. *arXiv*, article no. 2302.12288, http://dx.doi.org/10.48550/arXiv.2302.12288

Epstein Z., Hertzmann A., Herman L., Mahari R., Frank M.R., Groh M., Schroeder H., Smith A., Akten M., Fjeld J., Farid H., Leach N., Pentland A., Russakovsky O. (2023) Art and the science of generative AI: A deeper dive. *arXiv*, article no. 2306.04141, http://dx.doi.org/10.48550/arXiv.2306.04141

Gilgamesh (2023) Tutorial: What is a sampler in Stable Diffusion? *Medium*, https://gilgam3sh.medium.com/tutorial-what-is-a-sampler-in-stable-diffusion-d5c16875b898

JEMSU (n.d.) What potential drawbacks could interior designers face with AI-generated content in 2024? https://www.jemsu.com/what-potential-drawbacks-could-interior-designers-face-with-ai-generated-content-in-2024

Metz R., Ford B. (2024) Adobe's "ethical" Firefly AI was trained on Midjourney images. *Yahoo Finance*, April 12, https://finance.yahoo.com/news/adobe-ethical-firefly-ai-trained-123004288.html

Sanderson G. (2017) Neural networks. *3blue1brown*, https://www.3blue1brown.com/topics/neural-networks

Siddiqui Y., Monnier T., Kokkinos F., Kariya M., Kleiman Y., Garreau E., Gafni O., Neverova N., Vedaldi A., Shapovalov R., Novotny D. (2024) Meta 3D AssetGen: Text-to-mesh generation with high-quality geometry, texture, and PBR materials. *arXiv*, article no. 2407.02445, https://doi.org/10.48550/arXiv.2407.02445

Stable Diffusion Art (2024) How does Stable Diffusion work? https://stable-diffusion-art.com/how-stable-diffusion-work

United States Copyright Office (2023) Artificial Intelligence and Copyright. *59942 Federal Register*, Vol. 88, No. 167, https://www.copyright.gov/ai/docs/Federal-Register-Document-Artificial-Intelligence-and-Copyright-NOI.pdf

Wiggers K. (2023) OpenAI promises to defend business customers against copyright claims. *TechCrunch*, November 6, https://techcrunch.com/2023/11/06/openai-promises-to-defend-business-customers-against-copyright-claims

Yup K. (2023) What AI art means for society, according to Yale experts. *Yale Daily News*, January 23, https://yaledailynews.com/blog/2023/01/23/what-ai-art-means-for-society-according-to-yale-experts/

AMETHYST FROM NEWFOUNDLAND, CANADA: GEOLOGY, INTERNAL FEATURES, AND FLUID INCLUSION MICROTHERMOMETRY

Joshua William Lloyd Maloney, Philippe M. Belley, and James Conliffe

Gem-quality amethyst at the La Manche deposit in the Avalon Zone of Newfoundland, Canada, occurs in a calcite-galena-barite-quartz vein adjacent to a historical lead mine containing similar mineralization. The deposit has produced mineral specimens as well as medium to medium-dark purple (up to 11 ct) and light purple (<3 ct) faceted stones. Amethyst is interpreted to have formed as the final stage of hydrothermal mineral deposition in the veins. Variable color, zoning, and crystal size in different but contiguous crystal-lined pockets suggest relatively closed-system behavior within pockets where amethyst/quartz was deposited from trapped silica- and iron-bearing hydrothermal fluid. Microthermometry of primary fluid inclusions revealed an average homogenization temperature of 75.5 ± 6.9°C, cooler than in fluid inclusions within sulfide-bearing zones of similar veins in the region. Average fluid salinity estimated from primary inclusions in amethyst, recorded in weight % NaCl equivalent, was 10.7 ± 1.8 eq. wt.% NaCl. This was similar to the salinity of fluid in sulfide-bearing veins in the region and significantly higher than in quartz-chlorite veins in the region. Secondary fluid inclusions suggest a late influx of lower-salinity fluids (~7 eq. wt.% NaCl) associated with post-crystallization deformation that internally fractured amethyst crystals, reducing the volume suitable for faceting. Mineral inclusions are most abundant in the final purple and colorless growth stages in amethyst. They consist of black to red hematite spherulites, acicular "beetle-leg" inclusions (likely hematite), pyrite, chalcopyrite, and sprays of ochre goethite. Late iron-rich accessory mineral deposition may have depleted the hydrothermal fluid of iron, the chromophore in amethyst, during the final growth stage. La Manche amethyst's inclusion mineralogy is similar to that of amethyst from the deposits at Thunder Bay (Ontario, Canada), but the morphology of accessory sulfide minerals is different.

A new discovery of gem- and specimen-quality amethyst was made in Newfoundland, Canada, by Jason White in 2017 while conducting near-surface exploration in the proximity of a historical epigenetic vein-hosted lead deposit at La Manche, near Arnold's Cove. Amethyst, the purple variety of quartz colored by interstitial Fe^{3+} (Cohen, 1985), forms in a number of geological settings, but always at relatively low temperature (≤400°C) and shallow crustal depth (Cohen, 1985; McArthur et al., 1993; Yang et al., 2001; Kievlenko, 2003; Gilg et al., 2014). While gem-quality amethyst is known to occur in miarolitic granite pegmatites and skarns (Yang et al., 2001; Kievlenko, 2003; Ontiveros et al., 2004), commercially important deposits are hosted either in geodes within basalt or in epigenetic hydrothermal veins (Kievlenko, 2003). The purpose of this study is to (1) describe the amethyst gemstones and mineralization at La Manche, (2) identify amethyst's position in the paragenetic sequence of the veins, (3) characterize the mineral inclusions, (4) gain insights into formation temperature and hydrothermal fluid salinity by conducting fluid inclusion microthermometry on primary and secondary inclusions, and (5) use these data to develop an understanding of this new gem-quality amethyst occurrence and how it compares, geologically and gemologically, to others.

Regional Geology. La Manche is located in the Clarenville area of southeastern Newfoundland and situated in the Avalon Zone, a geological terrane that makes up the southeast part of Newfoundland (figure 1). Bedrock in this area is late Proterozoic in age, con-

See end of article for About the Authors and Acknowledgments.
GEMS & GEMOLOGY, Vol. 60, No. 3, pp. 348–367,
http://dx.doi.org/10.5741/GEMS.60.3.348

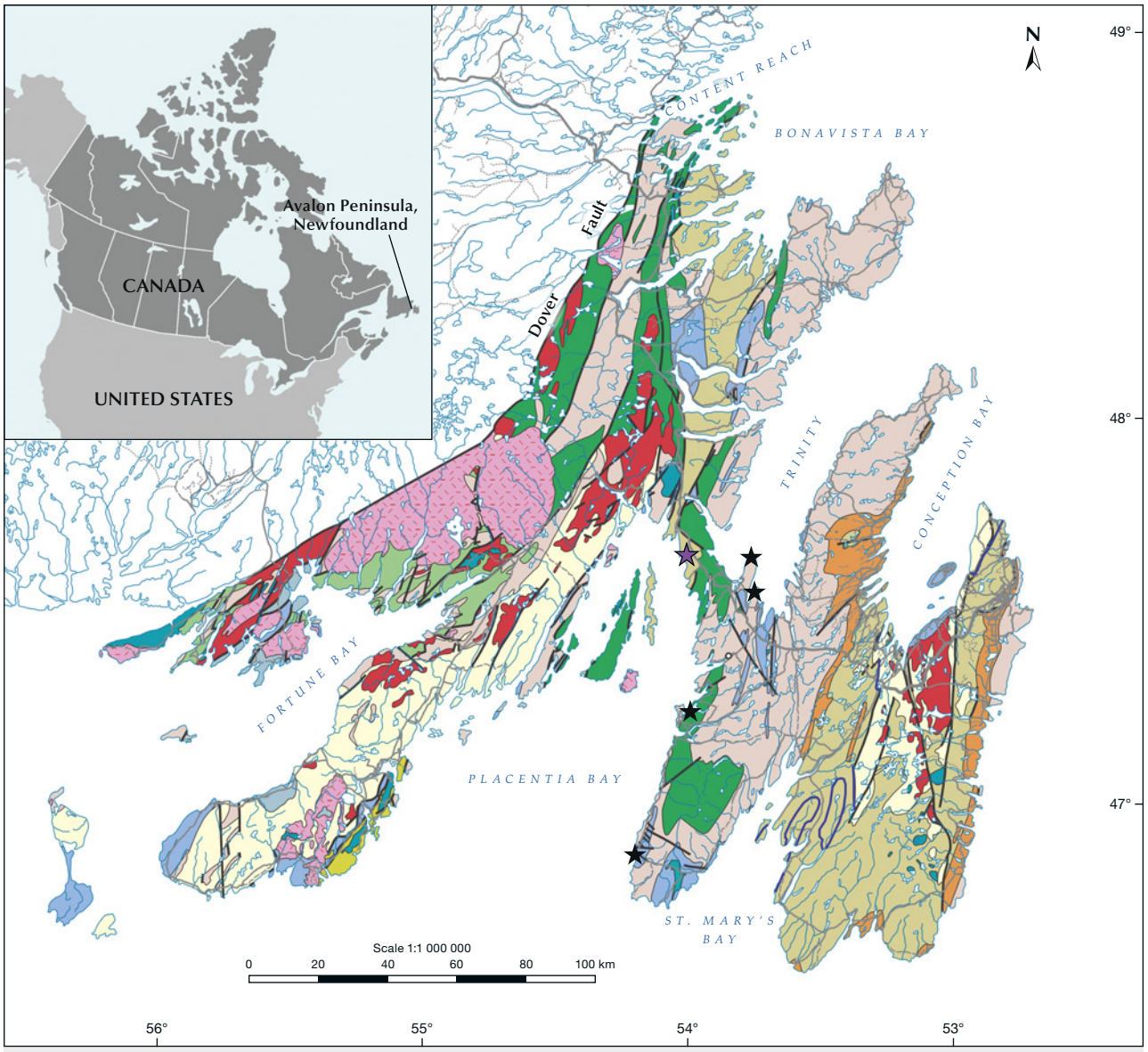

Figure 1. Geological map of the Avalon Zone showing the location of the La Manche vein system and other barite-bearing veins. Modified after Mills et al. (2021) and Colman-Sadd et al. (1990), with data from Maloney (1990).

sisting of clastic sedimentary rocks (turbidites formed in a marine basin; Mills et al., 2021) from the Connecting Point Group that are overlain by subaerial bimodal volcanic rocks of the Bull Arm Formation (Maloney, 1990). The Connecting Point Group consists of turbidites from a preserved marine sedimentary basin. Its oldest portion is constrained by the age of the underlying Love Cove Group, determined as 620 million years (Ma), and the 605 Ma age of a Bull Arm Formation rhyolite overlying the angular unconformity with the Connecting Point Group (O'Brien et al., 1989; Mills et al., 2016, 2021).

In Brief

- Gem-quality amethyst occurs as a late-stage mineral in an epigenetic hydrothermal calcite-galena-barite-quartz vein at La Manche on Placentia Bay in Newfoundland, Canada.
- Faceted stones from the occurrence range from light purple (<3 ct) to medium-dark purple (up to 11 ct). Color zoning is present but usually not very apparent in cut stones.
- Fluid inclusion microthermometry indicates that the amethyst formed at low temperature (<100°C) in NaCl-bearing fluids of moderate salinity (10.7 ± 1.8 eq. wt.% NaCl).
- Mineral inclusions in La Manche amethyst consist of spherulitic and acicular hematite, goethite sprays, pyrite, and chalcopyrite.

Within the Avalon Zone, a number of hydrothermal mineral veins occur (figure 1), consisting of barite, calcite, and sulfides—primarily galena with minor to trace sphalerite and chalcopyrite (Maloney, 1990). Maloney recognized two varieties of veins in the region: an early set of quartz ± chlorite veins (formed as a result of low-grade metamorphism) and a later set of barite ± calcite ± sulfide veins. Sulfide-bearing veins in La Manche and Silver Cliff (45 km south of La Manche, also in the Avalon Zone) are part of the subsequent set. Both deposits occur proximal to each other and are relatively rich in galena. Barite-bearing veins occur in other areas of the Avalon Peninsula such as Collier Point and Bellevue. Vein formation is interpreted to have taken place during or after the Acadian Orogeny (Devonian Period), when Avalon Zone rocks were weakly metamorphosed to sub-greenschist facies (prehnite-pumpellyite facies; Papezik, 1974), folded, faulted, and intruded by syntectonic to post-tectonic granites (Maloney, 1990).

La Manche Geology. The La Manche vein consists of an epigenetic vein-hosted lead deposit. Due to the abundance of galena, underground mining for lead was conducted by Ripley & Company, Placentia Bay Lead Company, and La Manche Mining Company from 1857 to 1873, followed by several unsuccessful attempts to resume mining operations between 1873 and 1948 (Tibbo, 1983). Large vugs described as containing "amethystine" quartz crystals along with transparent quartz were encountered during underground mining in the 1800s (Murray, 1869; Howley, 2009). The La Manche vein consists primarily of calcite and galena with subordinate barite, quartz, sphalerite, and chalcopyrite, and it is confined to the Connecting Point Group siltstone. The vein ranges from several centimeters to 3 m wide and occurs mostly within or at the contact of an amygdaloidal[1] basic dike (Maloney, 1990).

Maloney described various stages of white, gray, and purple calcite occurring in the vein. Previous research focused on the calcite along with barite and subordinate sulfides. He concluded, based on geological, geochemical, isotopic, and fluid inclusion evidence, that the sulfide-rich veins such as La Manche (and Silver Cliff) formed by a later and hotter hydrothermal fluid pulse closer to the source of fluids relative to the earlier quartz-chlorite veins in the Avalon Peninsula. Exsolved fluid from crystallizing magma belonging to nearby granitoids (Late Proterozoic; Colman-Sadd et al., 1990) is hypothesized to be the source of hydrothermal fluids forming barite- and sulfide-bearing veins in the region (Maloney, 1990).

In the early 1980s, exploration, trenching, and drilling identified a parallel vein 185 m north of the trace of the main La Manche vein. Amethyst was discovered in a drill core at approximately 18.5 m depth (Tibbo, 1983), in what has now been recognized as a significant amethyst occurrence described below.

Description of the Amethyst Occurrence. Jason White's 2017 discovery of amethyst occurred in a vein similar to the historically mined vein and is located near that deposit. The La Manche amethyst occurrence is currently in the exploration stage, with several test samples taken to evaluate mineral specimen and gem rough distribution and potential. A preliminary assessment of gemstone potential at La Manche was briefly described by Wilson (2020).

[1]An igneous dike containing amygdules, which are formed from the late filling of vesicles by minerals.

Figure 2. View of the amethyst-bearing trench looking west-southwest into Placentia Bay. The vein is exposed in the right side of the trench, and overburden is displaced to the left. Aerial drone photo by Philippe Belley.

Faceted amethyst from La Manche is occasionally found in the Canadian market as loose stones or set in silver jewelry. Future production potential is still under evaluation.

The strike and dip of the new amethyst-bearing vein is similar to that of the mined vein. No amygdaloidal dike was observed in outcrop at this location. The amethyst-producing vein is exposed by a 150 m long trench (figures 2 and 3). The vein dips steeply to the northwest and has a variable strike ranging from 203° to 264° based on measurements taken in four different segments of the trenched area. The average strike is similar to the orientation of the northern boundary of the trench (~244°), which appears to define the contact with the hanging wall. Amethyst was recovered mainly in the elongated flooded trench on the central-eastern part of the pit (figure 3), and small amounts were observed in the western part. Between these zones, the vein appears to pinch down to approximately 20 cm in width, but the poor exposure makes it difficult to follow the trace across the pit. The hanging wall consists of the host Connecting Point Group siltstone, which also occurs sparsely as fragments within the vein overgrown by layered calcite.

The vein exposed in the main area has a thickness of at least 2 m and consists of approximately 10–30 cm thick layers of columnar calcite (often highly weathered) containing localized galena masses, some up to ~1 m in diameter and 20 cm thick. The galena is extremely coarse-grained (5–15 cm) with a light greenish alteration coating likely composed of anglesite and subordinate pyromorphite. Galena masses, radiating white barite blades, and rare chalcopyrite occur in the calcite. Crystal-lined pockets are primarily hosted within the calcite—rarely do these pockets contain only euhedral calcite. More commonly, they are lined with a layer of barite followed by amethyst or colorless quartz (figure 4). Amethyst rarely forms directly over galena and uncommonly

Figure 3. Left: The trench face in the main zone (in 2021) showing amethyst-bearing black mud in front of the vein's hanging wall. Right: Freshly recovered amethyst cluster in black and tan mud. Many clusters are completely obscured by the thick black to brown clay. Photos by Philippe Belley.

does so on granular massive white quartz. Quartz crystals consist of short-prismatic points dominated by termination faces oriented growing inward in open cavities. Bright medium purple to dark intense purple (e.g., figure 3, right) amethyst crystals averaging 2–3 cm wide and up to 6 cm wide are the most common, and these colors are found in approximately equal proportions at the locality. Less common are smaller light purple (light purple core with thick colorless outer zone) and colorless quartz crystals, which may occur in pockets relatively close to those containing the more saturated colors of amethyst. An individual pocket tends to contain only one type of amethyst (i.e., colorless, light purple, medium purple, or dark purple) except for small (<1 cm) secondary colorless quartz crystals that are uncommonly found in small amounts over main generation quartz/amethyst of any color. These pockets are usually elongated roughly parallel to the vein and reach at least 1.5 m in length. Much of the calcite is intensely weathered into black clay with local, tan-colored zones and is mixed with masses of galena, barite, and quartz. There is considerable evidence of amethyst pocket collapse, movement, and resettling within the black clay. Post-formation collapse is suggested by a specimen of amethyst covered by cemented "crystal mush," which appears to precede calcite weathering and black clay formation. This deformation and the displacement of crystal clusters within the black clay resulted in damage to many amethyst crystals. Undamaged specimens are more common in less affected areas of the vein, especially near the hanging wall.

Figure 4. A portion of the vein showing thick calcite (Cal) and massive galena (Gn) surrounding a pocket of barite (Brt) and amethyst (Qtz). Photo by Joshua Maloney.

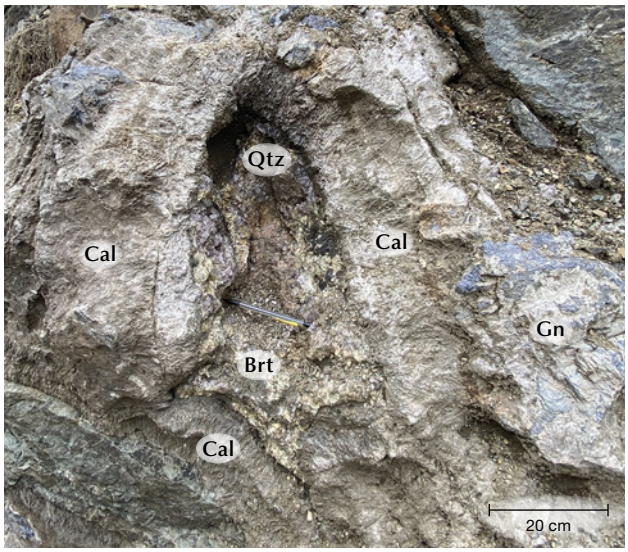

MATERIALS AND METHODS

Samples. More than 100 amethyst clusters were examined in addition to hundreds of faceted gemstones. These were collected by the claim owner and some of the authors (PB and JM) as part of a test sampling program, with rough being faceted in a commercial cutting factory. Approximately 2.4 kg out of a 7.0 kg sample of loose amethyst crystals recovered from the main zone consisted of facetable rough. The rough amethyst crystals were mostly medium-dark purple, with some medium purple varieties. These were faceted as calibrated round brilliant stones, each 5 mm in diameter or larger. Custom precision cutting was reserved for higher-quality rough. The 2.4 kg of amethyst loose crystals produced a total of 357 faceted stones: 164 stones weighing ≥1.0 ct (custom cuts and 7–10 mm round brilliants, maximum 6.42 ct, average 1.66 ct) and 193 stones weighing <1.0 ct (5–6 mm round brilliants, average 0.59 ct). Gemstones are described further in the Results section below. A subset of samples was selected for more detailed study: Seven crystals were prepared as polished sections for fluid inclusion analysis (samples LM-Ame-1 to LM-Ame-7, five of which contained fluid inclusions suitable for analysis), and 12 gemstones with characteristic inclusions were selected for photography and characterization.

Sample Examination and Preparation. Selected gemstones were observed under magnification with a binocular microscope. Three amethyst crystals and two barite-calcite contacts were polished into slide-mounted polished sections and studied using a petrographic microscope and a scanning electron microscope. These sections as well as included gemstones (broken and repolished to expose inclusions) were carbon coated (coating thickness 5–10 nm) and examined using Memorial University of Newfoundland's FEI Quanta 650 SEG scanning electron microscope (SEM). The SEM was equipped with two Bruker XFlash 5030 energy-dispersive X-ray spectrometers (EDS) for mineral identification using an operating voltage of 25 kV and an X-ray acquisition time of 30 s. Reference examples of hematite and goethite were mounted and polished together with included amethyst samples in a 25 mm epoxy puck so that the inclusions could be accurately identified. Refractive indices were measured using a Kruss professional refractometer with a monochromatic sodium light source (an RI liquid with a high value of 1.81, consisting of methylene iodide and tetraiodoethylene, was used at the contact face). Specific gravity was measured hydrostatically.

Fluid Inclusion Petrography and Microthermometry. Fluid inclusion assemblages (FIA) were identified and classified using criteria outlined by Goldstein (2003):

1. Primary inclusions are trapped during crystal growth and commonly found along growth layers and elongate in the direction of crystal growth.
2. Secondary inclusions form after crystal growth from fractures or deformation features that heal, thereby trapping the inclusions. These inclusions cut across growth zones.
3. Pseudosecondary inclusions are similar to secondary inclusions but form before crystal growth has finished. They form along deformation features that occur before the crystal has finished growing.

In addition, some clusters of inclusions have no clear relationship to growth zones but are not in fractures of clearly secondary or pseudosecondary origin. These inclusions are classified as having an indeterminate origin.

Seven saturated medium-dark purple amethyst crystals (LM-Ame-1 to LM-Ame-7) were fabricated into doubly polished wafers for fluid inclusion examination and analysis. Microthermometric data was collected using a Linkam THMSG600 heating/cooling stage attached to an Olympus BX51 microscope at Memorial University of Newfoundland. The heating/cooling stage was calibrated using synthetic water and carbon dioxide–water fluid inclusion standards. Following procedures outlined by Shepherd et al. (1985), the temperature of homogenization (T_h), temperature of first ice melting (T_{fm}), and final ice-melting temperature ($T_m ice$) were measured in two-phase liquid (L) + vapor (V) inclusions. During freezing at a cooling rate of 50°C/minute, the temperature at which the inclusions froze under metastable conditions (T_{mf}) was also recorded.

Due to the low measured homogenization temperature and high liquid content of the measured inclusions (>90% liquid at 25°C), fluid inclusion homogenization temperatures were recorded prior to low-temperature measurements in order to minimize the possible effects of stretching during freezing. The salts present in fluids were estimated by comparing recorded first ice melting temperatures with the known eutectic temperatures of common

aqueous-salt systems (Steele-MacInnis et al., 2016). In inclusions where the final ice-melting temperature was recorded, salinities were calculated for the water–sodium chloride system using the formula established by Bodnar (1993). Fluid salinities were also calculated based on the metastable freezing temperature using the equations of Wilkinson (2017). Although salinities calculated by metastable freezing temperatures likely have a higher degree of error (up to 3.2 eq. wt.% NaCl), they provide an estimate of fluid salinity in inclusions where vapor bubbles do not reappear prior to final ice melting. All fluid salinities are reported in weight % NaCl equivalent. Equivalent weight % NaCl is used as a measurement of salinity where precise speciation of salts in a sample has not been determined.

RESULTS

Description of Amethyst Mineralization. The amethyst found in the vein at La Manche occurs as scattered but locally abundant clusters in black clay found within a brecciated zone that appears to have formed in part from the subaerial weathering of calcite. The clusters are often loosened from the wall rock and may display broken points because of post-formation deformation. Three different types of amethyst can be found in the vein, sometimes close to each other but in different amethyst-lined cavities. The first is light purple to colorless and smaller than the other varieties, with an average crystal size of 1 cm (4 cm maximum). This has the least potential for gemstone cutting and mineral specimens due to its low color saturation and size. The remaining two amethyst varieties are more similar in size but vary in depth of color. One is saturated medium-dark purple in color (figure 5, A and B) while the other is saturated medium purple (figure 5C). Both varieties have significantly higher gemstone and specimen potential due to their more attractive appearance. These varieties are also much larger than the light purple amethyst to colorless quartz, with crystals averaging 2–3 cm in diameter and reaching up to 6 cm in maximum dimension. All coarsely crystalline quartz and amethyst observed at La Manche occurs only as a single final layer of mineralization in open cavities. Rarely, trace amounts of later colorless

Figure 5. Amethyst from La Manche. A: 9 cm wide with the largest crystal 4 cm tall. B: 11 cm wide. C: Medium purple amethyst, with the largest crystal measuring 4 cm wide. Photos by Philippe Belley.

Figure 6. A 32 × 7 mm polished section of amethyst from La Manche showing oscillatory zoning and weak sector zoning. The c-axis is indicated by the dashed line. Photo by Philippe Belley.

quartz (<2 cm) grow on top of the amethyst and generally show no preferential orientation with the underlying amethyst.

La Manche amethyst displays oscillatory and subtle sector zoning. A 7 mm thick cross section of medium-dark purple amethyst was cut and polished to display this zoning (figure 6). As is typical at La Manche, the outermost layer is colorless. The highest-quality gem material is generally found in the upper half to one-third of the crystals, from the broadest area to the termination. The edge of the amethyst crystals—where they contacted other crystals on the wall of a vug—tends to have an abundance of secondary fluid inclusions. Mineral inclusions (described in a subsequent section) are by far the most abundant in the final purple growth stage and the outer colorless zone.

Description of La Manche Amethyst Gemstones. Roughly half of the 357 faceted stones examined were light purple (all below 3 ct), and half were an attractive medium to medium-dark purple (with the most attractive color found in stones over 1 ct), while fewer than a dozen stones were colorless. The light purple stones were comparable in color to what is marketed as "rose de France" amethyst (figure 7, right faceted gem). While oscillatory and sector color zoning is present in La Manche amethyst, most faceted gemstones show uniform color when viewed table-up, though some examples show diffuse color

Figure 7. La Manche amethyst rough and faceted stones. The cut stone on the left (5.94 ct) shows diffuse color zoning. The one on the right (2.57 ct) is an example of light purple amethyst. Photo by Philippe Belley.

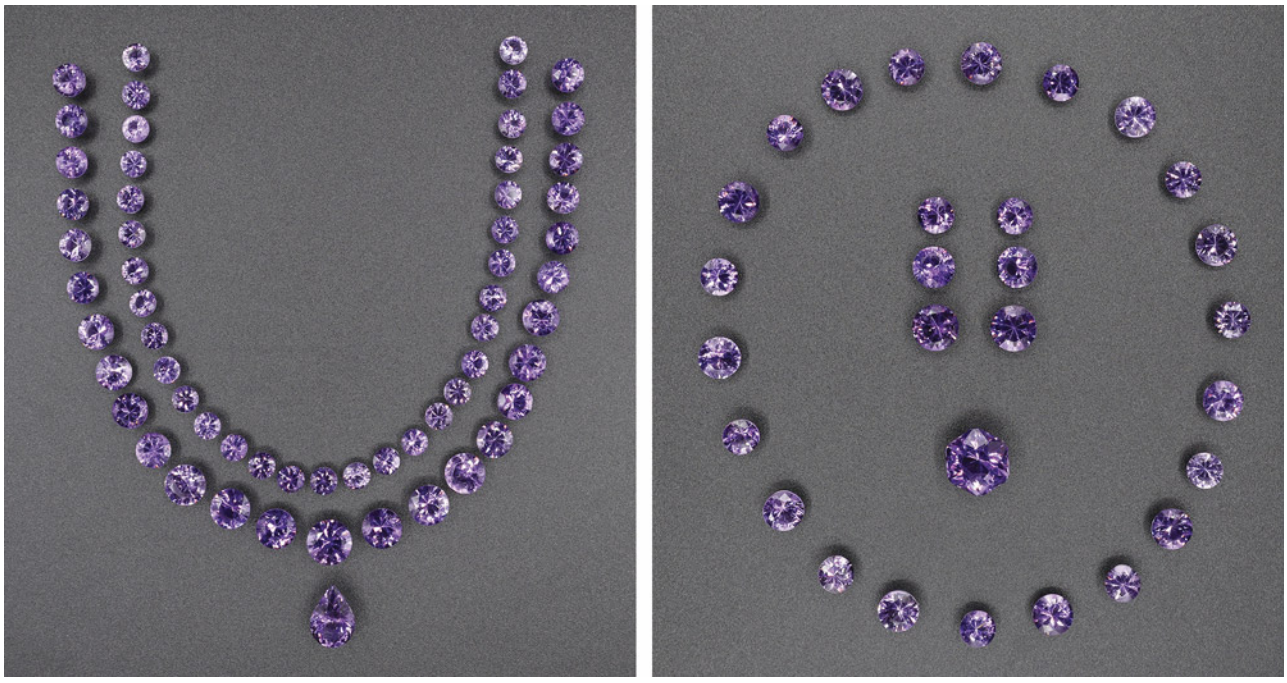

Figure 8. La Manche amethyst suite, 109.6 carats total. Left: Necklace set comprising round brilliants from 6 mm to 10 mm and a 3.69 ct pear cut. Right: Stones for a bracelet (7–8 mm rounds), earrings (7, 8, and 9 mm rounds), and a custom-cut hexagon (6.42 ct). Photos by Philippe Belley.

zoning where the depth of color changes slightly and progressively from one part of the stone to the other (figure 7, left faceted gem). The largest faceted gem examined weighed 6.42 ct, although an 11.0 ct oval faceted stone is known from the occurrence. Of particular note is a matching set of La Manche amethyst, 109.6 carats total (figure 8). The specific gravity, measured on a large transparent crystal fragment, was 2.66. Refractive indices, measured on three stones, were consistent: 1.541 (n_ω) and 1.550 (n_ε), with a birefringence of 0.009. Brazil twinning, a common feature in natural amethyst (Crowningshield et al., 1986), was generally visible in a simple polariscope, though sometimes difficult to observe depending on the orientation at which the gemstone was cut.

Fluid Inclusion Petrography and Microthermometry. Non-secondary fluid inclusions were rare, but FIA of primary, pseudosecondary, or indeterminate origin were observed in five of the seven samples studied. These were most common at the base and sides of the crystals, but some FIA of primary or indeterminate origin were also observed in the transparent and sparsely fractured amethyst near crystal terminations. Unequivocal primary FIA were observed in two samples, in trails parallel to the growth zones, and individual inclusions were generally elongate parallel to the *c*-axis growth direction (figure 9A). Pseudosecondary FIA were hosted in short trails that ran perpendicular to and terminated at growth zones. Indeterminate FIA occurred as clusters or short trails with no obvious relationship to growth zones.

Secondary FIA were observed in all samples and were much more abundant than other FIA types (>90% of total inclusions observed). They formed curvilinear trails (figure 9B) that crosscut growth zones and had a ribbon-like appearance parallel to the trend of the trail. Other secondary ribbon-like inclusions lined fractures that are not associated with secondary fluid inclusions (e.g., figure 9B): These can be difficult to observe when examining rough or preforms, and they can cause a stone to fracture during faceting (J. Henman, pers. comm., 2022).

Fluid inclusions hosted in primary, pseudosecondary, and indeterminate FIA were very similar in appearance and are described together. Inclusions ranged in size from <3 µm up to 30 µm. They were typically two-phase (liquid + vapor) at room temperature, but some monophase liquid inclusions were also observed. Two-phase inclusions were liquid rich with <10% vapor (figure 9, C and D) and did not show evidence of post-entrapment modification (i.e., leaking, stretching, decrepitation, necking down; Bodnar, 2003). All two-phase inclusions in individual FIA showed a consistent degree of fill. Secondary in-

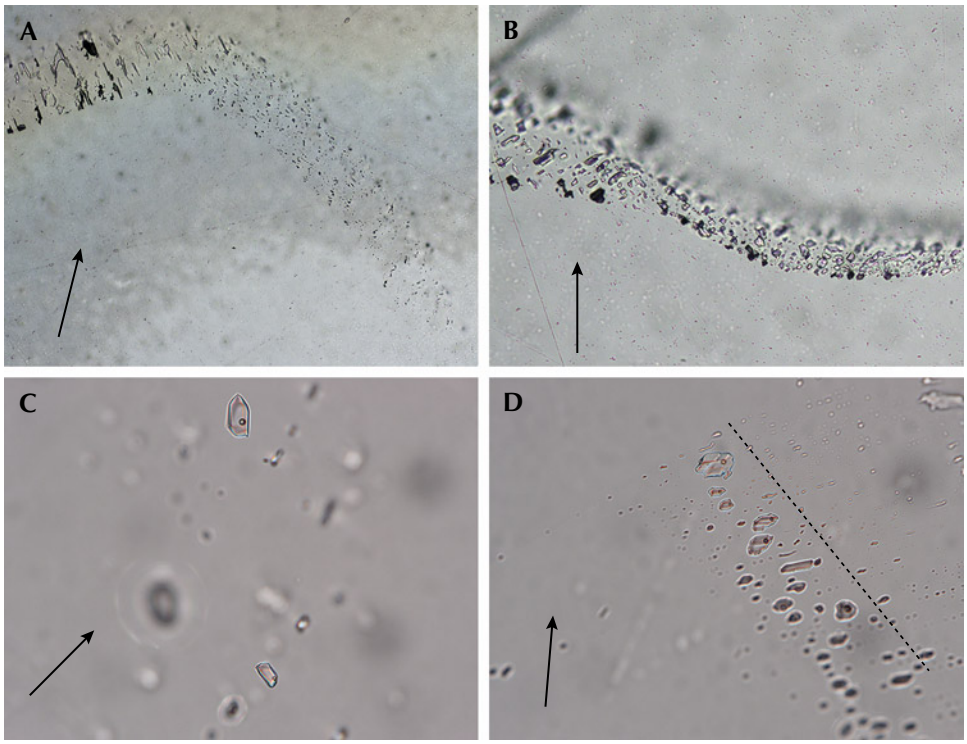

Figure 9. Fluid inclusions in La Manche amethysts viewed in transmitted light, with the arrow parallel to the c*-axis. A: Primary FIA in sample LM-Ame-01, located along a growth zone centered on what would be the point of the crystal. B: Secondary FIA in sample LM-Ame-01, occurring in a curvilinear, rehealed fracture. C: Typical two-phase (liquid + vapor) fluid inclusions in pseudosecondary FIA, sample LM-Ame-05. D: FIA of indeterminate origin in sample LM-Ame-07, with two-phase inclusions orientated perpendicular to the edge of the crystal (represented by dotted line). Photomicrographs by Joshua Maloney and James Conliffe; fields of view 1.11 mm (A), 0.36 mm (B), and 0.24 mm (C and D).*

clusions were smaller (<10 µm, generally <3 µm), and both monophase liquid and two-phase liquid-rich inclusions were observed. Some inclusions showed evidence of leaking with highly variable degrees of fill in individual FIA (monophase liquid to >20% vapor phase).

Microthermometric data recorded from 11 FIA in five samples is reported in table 1. Microthermometric data for inclusions hosted in primary, secondary, or indeterminate FIA was very similar (figure 10, left), and these results are reported together. Upon heating, all two-phase inclusions homogenized to the

Figure 10. Bivariate plots showing homogenization temperatures and salinities of amethyst from La Manche (this study) and associated sulfide, barite, and quartz-chlorite veins (Maloney, 1990). Data from individual FIA in amethyst showing average values with error bars denoting standard deviation.

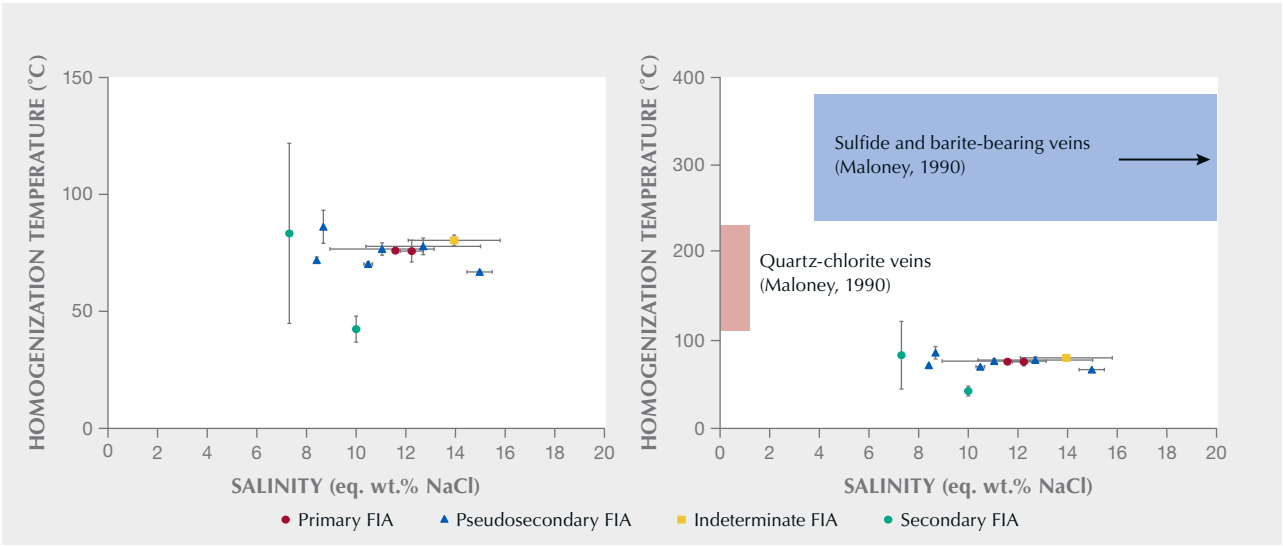

TABLE 1. Summary of fluid inclusion microthermometric data in amethyst from La Manche, Newfoundland.

Sample no.	Fluid inclusion assemblage	Setting	n[a]		T_{mf} (°C)	T_{fm} (°C)	$T_m$ice (°C)	Salinity (eq. wt.% NaCl)[b]	Salinity (eq. wt.% NaCl)[c]	T_h (°C)
LM-Ame-1	1	Primary	11	Avg	–52.0	–22.6	–8.5	12.2	10.0	75.7
				Std Dev[d]	0.0	na	0.4	0.5	0.0	4.6
	2	Secondary	6	Avg	–48.0	—	–4.6	7.3	6.9	83.3
				Std Dev	0.0	—	na	na	0.0	38.5
LM-Ame-4	1	Indeterminate	2	Avg	–58.2	–22.8	–5.9	9.1	13.9	80.4
				Std Dev	3.1	0.0	na	na	1.9	2.3
	2	Pseudosecondary	6	Avg	–53.1	–23.0	–7.0	10.5	10.8	70.2
				Std Dev	0.7	na	0.1	0.2	0.5	0.9
	3	Secondary	4	Avg	–52.0	—	—	—	10.0	42.4
				Std Dev	0.0	—	—	—	0.0	5.6
LM-Ame-5	1	Pseudosecondary	6	Avg	–59.8	–20.5	–4.1	6.6	15.0	66.9
				Std Dev	0.9	na	na	na	0.5	0.6
	2	Pseudosecondary	4	Avg	–56.3	–22.2	–8.1	11.8	12.7	77.8
				Std Dev	3.9	0.2	na	na	2.3	3.6
LM-Ame-6	1	Primary	2	Avg	–54.0	–21.1	–7.9	11.6	11.4	76.0
				Std Dev	0.0	0.1	na	na	0.0	1.1
	2	Pseudosecondary	7	Avg	–57.0	–21.0	–5.6	8.7	13.3	86.1
				Std Dev	0.0	na	na	na	0.0	7.0
LM-Ame-7	1	Indeterminate	5	Avg	–58.4	—	–5.4	8.4	14.1	71.9
				Std Dev	0.5	—	na	na	0.3	1.3
	2	Pseudosecondary	6	Avg	–53.7	—	—	—	11.0	76.6
				Std Dev	3.1	—	—	—	2.1	2.6

[a]*Number of inclusions analyzed in the assemblage*
[b]*Salinity calculated from* $T_m$ice *using equations of Bodnar (1993)*
[c]*Salinity calculated from* T_{mf} *using equations of Wilkinson (2017)*
[d]*Standard deviation of 0.0 indicates multiple inclusions with identical measured values; na indicates phase changes only observed in a single inclusion.*

liquid phase between 66.2° and 98.0°C (average 75.5°C, standard deviation 6.9°C, n = 47). Inclusions in individual FIA showed a narrow range of homogenization temperatures (generally <5°C), consistent with both trapping of a single-phase homogenous fluid and the absence of post-entrapment re-equilibration (Fall and Bodnar, 2018). Upon subsequent freezing at a rate of 50°C/minute, total freezing under metastable conditions occurred between –50° and –63°C. First ice melting (the eutectic temperature measured at the initiation of ice melting) was only observed in 10 inclusions between –23.0° and –20.5°C (average –21.9°C). These are close to the eutectic temperatures of pure H_2O-NaCl (–21.2°C) and H_2O-NaCl-KCl (–23°C) systems, indicating that NaCl (± KCl) is the most dominant salt in these inclusions, and they contain no significant amounts of $CaCl_2$ or $MgCl_2$ (Steele-MacInnis et al., 2016). Final ice melting, when no ice

Figure 11. A veil of secondary fluid inclusions along a rehealed fracture. Note the small black hematite spherulites. Photomicrograph by Philippe Belley; field of view 3.7 mm.

remains, in the presence of a vapor bubble was observed in 15 inclusions in the present study. This occurred between –8.7° and –4.1°C and was used to calculate fluid salinities between 6.6 and 12.5 eq. wt.% NaCl (average 10.7 eq. wt.% NaCl, standard deviation 1.8 eq. wt.% NaCl). In addition, fluid salinities from metastable ice melting temperatures were calculated using the equation of Wilkinson (2017). These range from 8.5 to 16.7 eq. wt.% NaCl (average 12.1 eq. wt.% NaCl, standard deviation 2.1 eq. wt.% NaCl), consistent with salinities calculated from $T_m ice$ and that the indicating fluids present during crystallization were of moderate salinity.

Microthermometric data was also collected from two secondary FIA to determine fluid flow history after crystal growth. They had a wide range of homogenization temperatures ranging from 38.0° to 144.0°C (homogenization to the liquid phase), with individual FIA having variations of >100°C indicating significant post-entrapment modification (i.e., leaking). Although eutectic temperatures were not observed, these inclusions freeze to form a clear ice before –50°C, suggesting that fluid compositions are dominated by NaCl ± KCl (Shepherd et al., 1985). A final ice melting temperature of –4.6°C was recorded in a single inclusion, corresponding to a salinity of 7.6 eq. wt.% NaCl and consistent with salinities calculated using metastable freezing temperatures (7.6 ± 1.1 eq. wt.% NaCl).

Inclusions in Faceted Stones. Due to their low abundance and generally very small size, primary fluid inclusions are rarely observed in cut gems using a standard gemological microscope. One rare example consisted of two very elongated primary fluid inclusions up to 1 mm long. Secondary fluid inclusions occur as subtle to prominent "veils" of inclusions along rehealed fractures. Subtle examples, consisting of relatively small and localized veils, occur commonly in faceted stones (figure 11). More prominent rehealed fractures are avoided by faceters but are common in amethyst crystals (e.g., figures 6 and 9).

La Manche amethyst contains multiple types of mineral inclusions that may occur together (figure 12) and are listed in order of abundance:

1. Black to red-orange spherical to globular hematite aggregates ("spherulites") from 5 to 100 µm in diameter (EDS confirmed against reference hematite and goethite samples mounted in the same polished puck; figure 12, A–C)
2. Needle-like and "beetle-leg" (figure 12B) to rod-like black to reddish inclusions that penetrate spherical aggregates, thought to be hematite
3. Radial bladed to acicular goethite clusters up to 1 mm long (EDS-confirmed)
4. Euhedral pyrite crystals showing complex habits, sometimes with parallel growth, up to 1 mm (EDS-confirmed; figure 12C)
5. Euhedral chalcopyrite crystals up to 0.4 mm (EDS-confirmed; figure 12D)

Hematite spherulites occur in many faceted stones. Like other mineral inclusions in La Manche amethyst, they are often restricted to one area of the faceted stone—the part of the outer zone of amethyst crystals that is richest in mineral inclusions. In most stones containing spherulites, these inclusions are only apparent upon close examination, especially with 10× magnification. Goethite and sulfide inclusions are less common and more prominently visible due to their larger average size.

DISCUSSION

Genetic Model. Layers of columnar calcite containing large, coarse-grained masses of galena in addition to dispersed barite clearly formed coevally: The minerals are found together in discrete layers of mineralization. Locally abundant masses of granular white quartz may also have formed in this stage, though no samples of this material were seen *in situ*. In many open cavities in the vein rock, barite occurs as later-stage layers where it is the dominant mineral preceding amethyst. Euhedral quartz crystals, generally as the amethyst variety, commonly overgrow the barite,

and barite has not been observed as intergrowths with quartz crystals. Therefore, amethyst crystallization occurred later than the other minerals in the vein. The restriction of amethyst to open cavities within layered calcite suggests that amethyst is a late-stage mineral genetically related to the lead-bearing hydrothermal veins. The presence of crystals with distinctive color, zoning, and sizes in separate but proximal pockets suggests the precipitation of quartz from trapped silica- and iron-bearing hydrothermal fluids where individual pockets behaved as relatively closed systems.

In a fluid inclusion study of barite-, sulfide-, and quartz-bearing veins in the Avalon Peninsula, Maloney (1990) found that sulfide-bearing and barite-bearing veins formed between 240°–370°C, with moderate to high salinity (~4.5–39 eq. wt.% NaCl, which includes NaCl, $CaCl_2$, and $MgCl_2$). In contrast, quartz-chlorite veins in the region formed as a result of regional low-grade metamorphism, where fluid inclusions have homogenization temperatures in the 110°–230°C range and extremely low salinity (average 0.6 eq. wt.% NaCl; Maloney, 1990). Fluid inclusion data from amethyst shows much lower homogenization temperatures (75.5° ± 6.9°C) relative to sulfide-barite-calcite in the region, as well as quartz-chlorite veins not associated with sulfide mineralization (figure 10, right). Although these homogenization temperatures represent minimum trapping temperatures, the low-grade regional metamorphism and open vuggy nature of the amethyst veins suggest that formation took place at relatively shallow crustal levels and the formation temperature of the La Manche amethyst was relatively low compared to other barite-, sulfide-, and quartz-bearing veins in the Avalon Peninsula. The salinity of fluid in primary inclusions in amethyst is considerably higher than in fluid in the quartz-chlorite veins, and

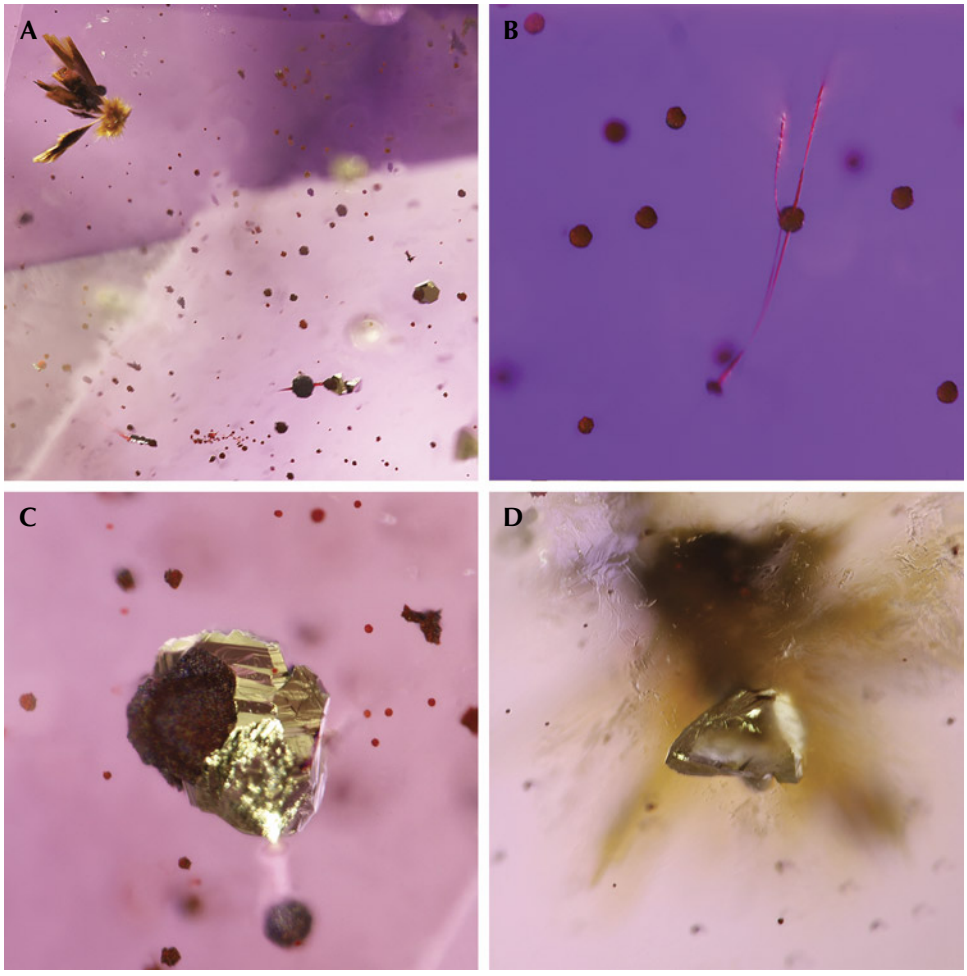

Figure 12. Mineral inclusions in La Manche amethyst. A: A cluster of acicular ochre goethite, black to red hematite spherulites, and euhedral sulfide crystals. B: Thin wiry "beetle-leg" type inclusion (probably hematite) associated with hematite spherulites in the emerald-cut gemstone pictured in figure 7. C: Pyrite showing parallel growth features in association with hematite. D: Pseudo-tetrahedral chalcopyrite crystal associated with goethite and hematite in amethyst. The color of the chalcopyrite inclusion was not apparent until it was later exposed by polishing and verified with reflected light microscopy and EDS. Photomicrographs by Philippe Belley; fields of view 2.10 mm (A), 0.77 mm (B), 0.80 mm (C), and 0.70 mm (D).

within the range of the ones associated with sulfide and barite veins. Therefore, vein structure, mineral textural relationships, and primary fluid inclusion homogenization temperatures and salinity suggest that La Manche amethyst formed in the final stage of mineral deposition by hydrothermal fluids at relatively low temperature (likely <100°C).

The thin colorless quartz rims on La Manche amethyst are an interesting feature. In the light purple amethysts, the purple zone is relatively small and limited to the core of the crystal, while the colorless layer is relatively thick (up to 80% of the crystal's radius). In the crystal-lined pockets of greatest commercial interest, most of the amethyst is medium to medium-dark purple in color with only a thin colorless rim (<20% of the crystal's radius). In all examples, iron-rich mineral inclusions (hematite, goethite, sulfides) occur principally in the outer purple zone as it transitions into colorless. Since amethyst color is generated by an interstitial Fe^{3+} impurity in quartz, we hypothesize that changing physicochemical conditions led to the precipitation of dissolved iron, and therefore iron was no longer available in the mineralizing fluids during the final stages of amethyst/quartz growth.

Comparison of Mineral Inclusions to Other Sources. Some primary inclusions in La Manche amethyst are common in amethyst from numerous sources, in particular "beetle-leg" habit black or reddish strands (likely hematite) and radiating aggregates of ochre-colored bladed to acicular goethite (see summary in table 2 and references therein). These inclusions are known to occur in amethyst in epigenetic hydrothermal veins (both hematite and goethite), geodes in basalt (goethite only), pockets in pegmatites (hematite only), and miarolitic cavities (hematite only; see table 2). Some inclusions known from basalt-hosted amethyst geode deposits (fluorite, calcite, and anhydrite; Gilg et al., 2003; Hyršl, 2006) and volcanic/volcaniclastic-hosted epithermal occurrences (microcline and baryte; Voudouris et al., 2018) were not observed at La Manche. The amethyst deposit containing the most similar inclusion assemblage is in Thunder Bay, Ontario, Canada, which (like La Manche) contains spherulitic hematite, acicular goethite, as well as pyrite and chalcopyrite (Kile, 2019). Hematite spherulites at Thunder Bay are generally reddish and occur in very high concentrations in late growth layers of some amethyst, causing an opaque red-brown coloration (Kile, 2019)—a significant contrast to the dominantly black color (likely due to larger crystallite size) and localized but low density of hematite spherulite inclusions in La Manche amethyst. The crystal habit of sulfides also differs between these two Canadian localities. Pyrite inclusions are cubic at Thunder Bay, while at La Manche they are either flattened or have more complex morphology (showing a combination of cubic, octahedral, and possibly pyritohedral faces). At Thunder Bay, chalcopyrite occurs as aggregates of fine-grained crystals (Kile, 2019), while at La Manche they occur as individual euhedral crystals. Sulfides are, however, very uncommon as inclusions in La Manche amethyst and therefore unlikely to be a useful discriminator of origin. The species and habit of more common mineral inclusions in La Manche amethyst overlap significantly with numerous other deposits.

Factors Affecting Amethyst Quality. A number of factors impact the quality of the amethyst found in the La Manche vein and affect their value as gemstones and specimens. In terms of primary features, the color zoning in amethyst results in faceted gemstones of varying lightness and saturation, with the more sought-after medium-dark intense purple as well as the lighter-colored "rose de France" type of amethyst. Some faceted stones contain small clusters of tiny hematite spherulites that are visible without magnification or under low magnification, but these are usually not apparent without close inspection.

The most significant factors affecting gem quality are secondary: Post-crystallization deformation has resulted in the formation of common rehealed fractures that contain secondary fluid inclusions, and post-formation pocket collapse resulted in damaged points on some mineral specimens. With regard to secondary fluid inclusions, the temperature of formation and salinity are unclear, but it is possible that they were formed by a relatively low-salinity fluid not related to hydrothermal mineralization.

Considering these factors, the La Manche occurrence has produced numerous beautiful faceted stones and mineral specimens with only minor test sampling. Its amethysts far surpass those from Thunder Bay with regard to the abundance of transparent facet-quality material (Wilson, 2014).

Geological Comparison with Other Deposits. Amethyst deposits are divided into the following categories:

1. Epigenetic hydrothermal veins, where mineralization crosscuts diverse rock types (e.g.,

TABLE 2. Summary of mineral inclusion types and fluid inclusion data in amethyst from La Manche, Newfoundland, and other localities.[a]

		Deposit type						
		Epigenetic hydrothermal veins						
Mineral inclusions	**Habit**	**Canada (La Manche)**	**Canada (Thunder Bay)**	**Brazil[b]**	**Kazakhstan[b]**	**Madagascar[b]**	**Morocco (Boudi)**	**Rwanda[b]**
Hematite	Acicular	x		x	x	x	x	x
	Spherulites	x	x					
	Flakes							
	Dendrites							
Goethite	Acicular/sprays	x	x	x	x	x		
Pyrite	Cubes		x					
	Complex forms	x						
	Platy	x						
Chalcopyrite	Single crystals	x						
	Crystal aggregates		x					
Fluorite								
Calcite								
Anhydrite								
Baryte								
Cristobalite								
Microcline								
Hydrocarbon	(liquid secondary inclusions)							
Fluid Inclusions								
Primary and Pseudosecondary	T_h (°C)	66.9–86.1	40.0–91.2	—	—	—	154–330	—
	Salinity (NaCl eq. wt.%)	10.0–15.0	15.3–22.9	—	—	—	5.7–13.9	—
Secondary	T_h (°C)	42.4–83.3	—	—	—	—	—	—
	Salinity (NaCl eq. wt.%)	6.9–10.0	—	—	—	—	—	—

[a]*Data sources: Yang et al. (2001); Gilg et al. (2003, 2014); Lowell and Koivula (2004); Hyršl (2006); Morteani et al. (2010); Commin-Fischer et al. (2010); Troilo et al. (2015); Dumańska-Słowik (2017); Feely et al. (2017); Schmetzer and Williams (2018); Voudouris et al. (2018); Kile (2019); Dias et al. (2021).*
[b]*Only the deposit type and country of origin are listed for these occurrences by Hyršl (2006).*
[c]*Hydrothermal breccia in granite*

TABLE 2 (continued). Summary of mineral inclusion types and fluid inclusion data in amethyst from La Manche, Newfoundland, and other localities.[a]

		Deposit type					
		Epigenetic hydrothermal veins			Geodes in basalt	Pegmatite	Miarolitic cavities
Mineral inclusions	**Habit**	**United States (Four Peaks, Arizona)**	**United States[c] (Green Ridge, Washington)**	**Greece (various occurrences)**	**Brazil/ Uruguay**	**Brazil[b]**	**South Korea**
Hematite	Acicular					x	x
	Spherulites						
	Flakes	x					
	Dendrites						x
Goethite	Acicular/sprays			x	x		
Pyrite	Cubes						
	Complex forms						
	Platy						
Chalcopyrite	Single crystals						
	Crystal aggregates						
Fluorite					x		
Calcite					x		
Anhydrite					x		
Baryte				x			
Cristobalite					x		
Microcline				x			
Hydrocarbon	(liquid secondary inclusions)		x				
Fluid Inclusions							
Primary and Pseudosecondary	T_h (°C)	—	270–311	189–275	50–120	—	273–288
	Salinity (NaCl eq. wt.%)	—	5.4–9.5	0.9–8.0	0.3–5.3	—	4
Secondary	T_h (°C)	—	—	—	—	—	—
	Salinity (NaCl eq. wt.%)	—	—	—	—	—	—

[a]*Data sources: Yang et al. (2001); Gilg et al. (2003, 2014); Lowell and Koivula (2004); Hyršl (2006); Morteani et al. (2010); Commin-Fischer et al. (2010); Troilo et al. (2015); Dumańska-Słowik (2017); Feely et al. (2017); Schmetzer and Williams (2018); Voudouris et al. (2018); Kile (2019); Dias et al. (2021).*
[b]*Only the deposit type and country of origin are listed for these occurrences by Hyršl (2006).*
[c]*Hydrothermal breccia in granite*

Kievlenko, 2003; Lowell and Koivula, 2004; Troilo et al., 2015; Dumańska-Słowik et al., 2017; Voudouris et al., 2018; Kile, 2019), sometimes also as hydrothermal breccias (Feely et al., 2017)
2. Basalt-hosted deposits, where amethyst is precipitated from hydrothermal fluid in geodes (Gilg et al., 2003, 2014; Morteani et al., 2010; Commin-Fischer et al., 2010; Dias et al., 2021)
3. Pegmatites and miarolitic cavities, in which late-stage amethyst crystallizes from hydrothermal fluids in the final stages of magmatic crystallization (e.g., Yang et al., 2001; Kievlenko, 2003)
4. Skarns, where amethyst forms in vugs as a late-stage mineral (Ontiveros et al., 2004)

Epigenetic hydrothermal amethyst deposits, such as that at La Manche, form in faults, joints, or breccias, often in rocks experiencing structural extension that creates structures along which hydrothermal fluids can travel. Most epigenetic hydrothermal vein-type amethyst deposits are nearly monomineralic (with the exception of some Russian deposits containing locally abundant calcium and iron carbonates; Kievlenko, 2003), and multiple growth stages of quartz deposition—often colorless, smoky, and later-stage amethyst—occur successively (Epstein, 1988; Garland, 1994; Kievlenko, 2003; Lowell and Koivula, 2004). The association of amethyst with an epigenetic hydrothermal base metal sulfide deposit at La Manche (galena with minor sphalerite and chalcopyrite; Maloney, 1990) is more similar to mineralization at Thunder Bay and at the Madjarovo gold-polymetallic deposit in Bulgaria. The La Manche occurrence is distinct in that individual quartz- or amethyst-lined pockets only contain one generation of crystals, with no repeated layers of quartz as found in many other hydrothermal deposits such as Thunder Bay and Madjarovo.

Two types of amethyst-bearing veins occur in the Thunder Bay area (Garland, 1994). In the west, amethyst is a minor constituent in vein systems consisting of three stages of mineralization: (A) calcite + sulfides; (B) quartz, including amethyst (if present); and (C) barite and fluorite (if present), with small quantities of silver-bearing minerals. In the east, there are notable amethyst deposits consisting of layers of white sugary quartz transitioning to episodic bands of white, smoky, and amethyst quartz, with sulfide minerals (galena, chalcopyrite, pyrite, and sphalerite) forming sparse lenses below the final layers of amethyst and occasionally containing late barite or fluorite overgrowths on euhedral amethyst (Garland, 1994; Kile, 2019). Gem-quality amethyst at Thunder Bay is extremely rare, and facet-quality material has only been reported from the quartz/amethyst-dominated type of vein (see Wilson, 2014). It is important to highlight that barite at Thunder Bay generally formed later than the amethyst, while it formed exclusively prior to amethyst deposition at La Manche. Furthermore, amethyst pockets at La Manche are enclosed within host calcite in the main vein, while the largest and most commercially important pockets in Thunder Bay occur at intersections between sets of mineralized faults (Garland, 1994).

In the Madjarovo deposit of Bulgaria, the crystallization of prismatic amethyst crystals occurred at the end of the hydrothermal process, with amethyst postdating copper, lead, and zinc sulfide mineralization in the same vein (Kievlenko, 2003, and references therein). The formation of amethyst in the final stage of mineral precipitation from hydrothermal fluids in a base metal sulfide deposit is common to both Madjarovo and La Manche. However, late-stage quartz in the Madjarovo deposit occurs as multiple discrete layers, a common feature in most amethyst deposits that is absent at La Manche. Principal gangue minerals at Madjarovo are quartz and calcite, whereas the dominant gangue mineral at La Manche is calcite with subordinate barite and locally abundant quartz that was not observed *in situ*.

The occurrence of amethyst in the latest stage of quartz growth is likely due to its relatively low temperature of formation (approximately 40°–250°C) and to the occurrence of oxidizing conditions required to form trivalent iron, which causes the purple color when incorporated into quartz and subsequently exposed to natural background radiation (Dennen and Pucket, 1972; Cohen, 1985; McArthur et al., 1993; Morteani et al., 2010). Amethyst crystallization at La Manche occurred at relatively low temperatures (<100°C), comparable to formation temperatures at Thunder Bay (range 40.0°–91.2°C, average 68.4°C), and lower than at Madjarovo and the numerous Russian deposits (100°–220°C; Kievlenko, 2003). The fluid inclusion entrapment temperature at La Manche is also lower than for amethyst in epithermal occurrences in Greece (approximately 200°–250°C; Voudouris et al., 2018) and New Zealand (170°–253°C; Braithwaite and Faure, 2002). The high-

est temperatures determined for two-phase fluid inclusions in a hydrothermal vein–type deposit are in the Boudi deposit in Morocco (154°–330°C; Dumańska-Słowik et al., 2017), and temperatures of 273°–288°C are known in amethyst from miarolitic cavities (Yang et al., 2001). Gilg et al. (2003) suggests a similar low formation temperature (<100°C) for geode-hosted amethyst in basalt (Brazil), but this is contradicted by estimates of 152°–238°C in primary fluid inclusions by Proust and Fontaine (2007). However, most fluid inclusions in Brazilian/Uruguayan basalt-hosted amethyst are monophase, and the two-phase inclusions used by Proust and Fontaine (2007) may have leaked, giving unreliable results, which is supported by the low formation temperatures inferred from oxygen isotope data (Gilg et al., 2014). In the basalt-hosted amethyst in Uruguay, Morteani et al. (2010) estimated formation temperatures between 50° and 120°C.

Hydrothermal fluid salinity at La Manche is moderate (10.7 ± 1.8 eq. wt.% NaCl), which is comparable to higher values from Boudi (5.7–13.9 eq. wt.% NaCl; Dumańska-Słowik et al., 2017) and epithermal amethyst occurrences in Greece (0.9–8.0 eq. wt.% NaCl; Voudouris et al., 2018), and significantly higher than in geode-type basalt-hosted amethyst in Brazil (0.3–5.3 eq. wt.% NaCl; Gilg et al., 2014) and epithermal amethyst in New Zealand (≤4.5 eq. wt.% NaCl; Braithwaite and Faure, 2002). Amethyst from miarolitic cavities in aplite cutting granite at the Eonyang deposit in South Korea contains lower-salinity fluid inclusions (4 eq. wt.% NaCl) that also contain CO_2 as well as H_2O and NaCl (Yang et al., 2001). Amethyst in Thunder Bay formed in fluids containing a higher salinity than all the aforementioned deposits, ranging between 15.3 and 22.9 eq. wt.% NaCl (McArthur et al., 1993).

Figure 13. The second- and third-largest faceted stones produced from the La Manche amethyst occurrence to date: 9.09 ct (left) and 8.46 ct (right). Photo by Philippe Belley.

CONCLUSIONS

La Manche amethyst features a range of colors, including saturated medium to medium-dark purple and light purple. The deposit has produced numerous beautiful faceted gemstones in exploration test samples, with a few as large as 8–11 carats (figure 13). The occurrence is a new example of an epigenetic hydrothermal-type deposit and one of the few examples where amethyst formed as a final-stage hydrothermal mineral in open cavities within a vein-hosted base metal sulfide deposit. La Manche is different from most vein-hosted amethyst deposits in that vugs generally contain only one discrete layer of amethyst rather than multiple banded layers—and the fact that this layer primarily occurs over calcite and barite. Based on microthermometry of two-phase primary inclusions, amethyst at La Manche formed at relatively low temperature (<100°C) and moderate salinity dominated by NaCl (approximately 11 eq. wt.% NaCl). It contains mineral inclusions similar to those found in many other deposits (i.e., acicular and spherulitic hematite and radiating acicular goethite) as well as others known only from the Thunder Bay deposits (pyrite and chalcopyrite). Pyrite and chalcopyrite inclusions in La Manche amethyst are relatively rare and can be differentiated by morphology from those reported in Thunder Bay amethyst. Due to the similar appearance of La Manche faceted amethyst gemstones to that from other sources, and the scarcity of inclusions unique to La Manche, they cannot be reliably differentiated. Origin would therefore require to be certified by mine-to-market supply chain management.

ABOUT THE AUTHORS

Joshua Maloney is a recent graduate of the B.Sc. Honours Geology program at Memorial University of Newfoundland (MUN), St. John's, Canada, and is now working as an exploration geologist. Dr. Philippe Belley is an assistant professor and manages the Gem Science Research Group at MUN. Dr. James Conliffe is a project geologist in the Mineral Deposits Section, Department of Mines & Energy, Government of Newfoundland and Labrador.

ACKNOWLEDGMENTS

The authors are extremely grateful for the support of claim owner Jason White, who guided multiple site visits, allowed sampling, and shared information. We thank Jaimy Henman for precision faceting the gemstones in figure 7 and providing feedback on the material, Andrea Mills (Government of Newfoundland and Labrador) for providing a high-resolution copy of the geological map of the Avalon Peninsula, Matt Crocker (MUN) for polished section preparation, and Dylan Goudie (MUN) for help with SEM-EDS.

REFERENCES

Bodnar R.J. (1993) Revised equation and table for determining the freezing point depression of H_2O-NaCl solutions. *Geochimica et Cosmochimica Acta*, Vol. 57, No. 3, pp. 683–684, http://dx.doi.org/10.1016/0016-7037(93)90378-A

——— (2003) Reequilibration of fluid inclusions. In I. Samson, et al., Eds., *Fluid Inclusions: Analysis and Interpretation*. Mineralogical Association of Canada, Short Course Series 32, pp. 1–8.

Braithwaite R.L., Faure K. (2002) The Waihi epithermal gold-silver-base metal sulfide-quartz vein system, New Zealand: Temperature and salinity controls on electrum and sulfide deposition. *Economic Geology*, Vol. 97, No. 2, pp. 269–290, http://dx.doi.org/10.2113/gsecongeo.97.2.269

Cohen A.J. (1985) Amethyst color in quartz, the result of radiation protection involving iron. *American Mineralogist*, Vol. 70, No. 11-12, pp. 1180–1185.

Colman-Sadd S.P., Hayes J.P., Knight I. (1990) Geology of the Island of Newfoundland (digital version of Map 90-01); Scale: 1:1,000,000. Government of Newfoundland and Labrador, Department of Mines and Energy, Geological Survey Branch. Open File GS# NFLD/2192.

Commin-Fischer A., Berger G., Polvé M., Dubois M., Sardini P., Beaufort D., Formoso M. (2010) Petrography and chemistry of SiO_2 filling phases in the amethyst geodes from the Serra Geral Formation deposit, Rio Grande do Sul, Brazil. *Journal of South American Earth Sciences*, Vol. 29, No. 3, pp. 751–760, http://dx.doi.org/10.1016/j.jsames.2009.10.002

Crowningshield R., Hurlbut C., Fryer C.W. (1986) A simple procedure to separate natural from synthetic amethyst on the basis of twinning. *G&G*, Vol. 22, No. 3, pp. 130–139, http://dx.doi.org/10.5741/GEMS.22.3.130

Dennen W.H., Puckett A.M. (1972) On the chemistry and color of amethyst. *Canadian Mineralogist*, Vol. 11, pp. 448–456.

Dias C.H., de Sa Carneiro Chaves M.L., Figueiredo e Silva R.C., Dutra Gomes S. (2021) Fluid inclusions in amethyst quartz of different geological environments from Brazil. *Mineralogical Magazine*, Vol. 85, No. 3, pp. 332–347, http://dx.doi.org/10.1180/mgm.2021.38

Dumańska-Słowik M., Toboła T., Jarmołowicz-Szulc K., Naglik B., Dylag J., Szczerba J. (2017) Inclusion study of hourglass amethyst from Boudi (Morocco) by Raman microspectroscopy and microthermometric measurements. *Spectrochimica Acta Part A: Molecular and Biomolecular Spectroscopy*, Vol. 187, pp. 156–162, http://dx.doi.org/10.1016/j.saa.2017.06.053

Epstein D.S. (1988) Amethyst mining in Brazil. *G&G*, Vol. 24, No. 4, pp. 214–228, http://dx.doi.org/10.5741/GEMS.24.4.214

Feely M., Costanzo A., Lindner F., George J., Parnell J., Bowden S., Baba M., Owens P. (2017) Quartz-amethyst hosted hydrocarbon-bearing fluid inclusions from the Green Ridge Breccia in the Snoqualmie Granite, North Cascades, WA, USA. *Minerals*, Vol. 7, No. 9, article no. 174, http://dx.doi.org/10.3390/min7090174

Garland M.I. (1994) Amethyst in the Thunder Bay area. Ontario Geological Survey, Open File Report 5891, 197 pp.

Gilg H.A., Krüger Y., Taubald H., van den Kerkhof A.M., Frenz M., Morteani G. (2014) Mineralisation of amethyst-bearing geodes in Ametista do Sul (Brazil) from low-temperature sedimentary brines: Evidence from monophase liquid inclusions and stable isotopes. *Mineralium Deposita*, Vol. 49, No. 7, pp. 861–877, http://dx.doi.org/10.1007/s00126-014-0522-7

Gilg H.A., Morteani G., Kostitsyn Y., Preinfalk C., Gatter I., Strieder A.J. (2003) Genesis of amethyst geodes in basaltic rocks of the Serra Geral Formation (Ametista do Sul, Rio Grande do Sul, Brazil): A fluid inclusion, REE, oxygen, carbon, and Sr isotope study on basalt, quartz, and calcite. *Mineralium Deposita*, Vol. 38, No. 8, pp. 1009–1025, http://dx.doi.org/10.1007/s00126-002-0310-7

Goldstein R.H. (2003) Petrographic analysis of fluid inclusions. In I. Samson et al., Eds., *Fluid Inclusions: Analysis and Interpretation*, Mineralogical Association of Canada, Short Course Series 32, pp. 9–54.

Howley J.P. (2009) *Reminiscences of Forty-Two Years of Exploration in and About Newfoundland*. Edited by W.J. Kirwin and P.A. O'Flaherty. Memorial University of Newfoundland, St. John's, Canada. 2053 pp.

Hyršl J. (2006) Gemological Abstracts: Genetic classification of mineral inclusions in quartz. *G&G*, Vol. 42, No. 3, pp. 97–98.

Kievlenko E.Y. (2003) *Geology of Gems*, English edition. Ocean Pictures Ltd., Littleton, Colorado.

Kile D.E. (2019) Mineralogy of the amethyst mines in the Thunder Bay area, Thunder Bay, Ontario, Canada. *Rocks & Minerals*, Vol. 94, No. 4, pp. 306–343, http://dx.doi.org/10.1080/00357529.2019.1595939

Lowell J., Koivula J.I. (2004) Amethyst from Four Peaks, Arizona. *G&G*, Vol. 40, No. 3, pp. 230–238, http://dx.doi.org/10.5741/GEMS.40.3.230

Maloney J.A. (1990) The origin of barite and related veins on the Avalon Peninsula of Newfoundland. Unpublished master's thesis, Memorial University of Newfoundland. St. John's, Canada.

McArthur J.R., Jennings E.A., Kissin S.A., Sherlock R.L. (1993) Stable-isotope, fluid-inclusion, and mineralogical studies relating to the genesis of amethyst, Thunder Bay Amethyst Mine, Ontario. *Canadian Journal of Earth Sciences*, Vol. 30, No. 9, pp. 1955–1969, http://dx.doi.org/10.1139/e93-172

Mills A.J., Dunning G.R., Langille A. (2016) New geochronological

constraints on the Connecting Point Group, Bonavista Peninsula, Avalon Zone, Newfoundland. In *Current Research*, Newfoundland and Labrador Department of Natural Resources, Geological Survey, Report 16-1, pp. 153–171.
Mills A.J., Dunning G.R., Sandeman H.A. (2021) Lithogeochemical, isotopic, and U-Pb (zircon) age constraints on arc to rift magmatism, northwestern and central Avalon Terrane, Newfoundland, Canada; implications for local lithostratigraphy. *Canadian Journal of Earth Sciences*, Vol. 58, No. 4, pp. 332–354, http://dx.doi.org/10.1139/cjes-2019-0196
Morteani G., Kostitsyn Y., Preinfalk C., Gilg H.A. (2010) The genesis of the amethyst geodes at Artigas (Uruguay) and the paleohydrology of the Guaraní aquifer: Structural, geochemical, oxygen, carbon, strontium isotope and fluid inclusion study. *International Journal of Earth Sciences*, Vol. 99, pp. 927–947, http://dx.doi.org/10.1007/s00531-009-0439-z
Murray A. (1869) *Report upon the Geological Survey of Newfoundland for the Year 1868*. Robert Winton, printer to the Hon. House of Assembly, St. John's, Newfoundland, Canada, 68 pp.
O'Brien S.J., Dunning G.R., Knight I., Dec T. (1989) Late Precambrian geology of the north shore of Bonavista Bay (Clode Sound to Lockers Bay). Government of Newfoundland and Labrador, Department of Mines, Geological Survey Report of Activities, pp. 49–50.
Ontiveros M., Wilson W.E., Megaw P.K.M. (2004) Famous mineral localities: The Guerrero amethyst deposits, Mexico. *Mineralogical Record*, Vol. 35, No. 6, pp. 29–37.
Papezik V.S. (1974) Prehnite-pumpellyite facies metamorphism of late Precambrian rocks of the Avalon Peninsula, Newfoundland. *Canadian Mineralogist*, Vol. 12, pp. 463–468.
Proust D., Fontaine C. (2007) Amethyst geodes in the basaltic flow from Triz quarry at Ametista do Sul (Rio Grande do Sul, Brazil): Magmatic source of silica for the amethyst crystallizations. *Geological Magazine*, Vol. 144, No. 4, pp. 731–739, http://dx.doi.org/10.1017/S0016756807003457
Schmetzer K., Williams B. (2018) Gem-quality amethyst from Rwanda: Optical and microscopic properties. *Journal of Gemmology*, Vol. 36, No. 1, pp. 26–36.
Shepherd T.J., Rankin A.H., Alderton D.H.M. (1985) *A Practical Guide to Fluid Inclusions*. Blackie, London.
Steele-MacInnis M., Ridley J., Lecumberri-Sanchez P., Schlegel T.U., Heinrich C.A. (2016) Application of low-temperature microthermometric data for interpreting multicomponent fluid inclusion compositions. *Earth-Science Reviews*, Vol. 159, pp. 14–35, http://dx.doi.org/10.1016/j.earscirev.2016.04.011
Tibbo H.G. (1983) Report on a diamond drilling program on mineral claim 12072, License No. 12014, La Manche Project, Placentia Bay, Newfoundland. Tasu Resources Ltd., Newfoundland and Labrador exploration report file 001N-0448.
Troilo F., El Harfi A., Mouaddib S., Bittarello E., Costa E. (2015) Amethyst from Boudi, Morocco. *G&G*, Vol. 51, No. 1, pp. 32–40, http://dx.doi.org/10.5741/GEMS.51.1.32
Voudouris P., Melfos V., Mavrogonatos C., Tarantola A., Götze J., Alfieris D., Maneta V., Psimis I. (2018) Amethyst occurrences in Tertiary volcanic rocks of Greece: Mineralogical, fluid inclusion and oxygen isotope constraints on their genesis. *Minerals*, Vol. 8, No. 8, article no. 324, http://dx.doi.org/10.3390/min8080324
Wilkinson J.J. (2017) Metastable freezing: A new method for the estimation of salinity in aqueous fluid inclusions. *Economic Geology*, Vol. 112, No. 1, pp. 185–193, http://dx.doi.org/10.2113/econgeo.112.1.185
Wilson B.S. (2020) Colored gemstones from Canada: An update. *InColor*, No. 45, pp. 78–85.
——— (2014) Colored gemstones from Canada. In L.A. Groat, Ed., *Geology of Gem Deposits*, 2nd ed., Mineralogical Association of Canada, Short Course Series 44, pp. 375–405.
Yang K.H., Yun S.H., Lee J.D. (2001) A fluid inclusion study of an amethyst deposit in the Cretaceous Kyongsang Basin, South Korea. *Mineralogical Magazine*, Vol. 65, No. 4, pp. 477–487, http://dx.doi.org/10.1180/002646101750377515

Lab Notes

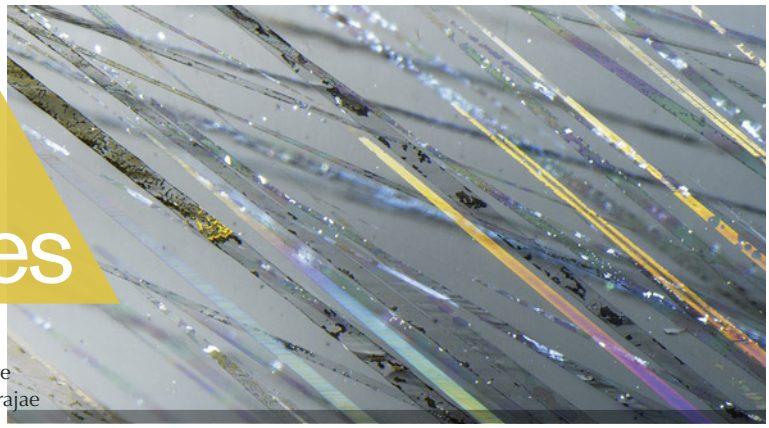

Editors

Thomas M. Moses | Shane F. McClure
Sally Eaton-Magaña | Artitaya Homkrajae

Green HAÜYNE

The Carlsbad laboratory recently examined a suite of seven yellowish green to bluish green gems ranging in weight from 0.24 to 1.44 ct (figure 1), which were identified as haüyne, a member of the sodalite group. Gem-quality haüyne is most notable for its intense blue color, especially in material of German origin, so the striking green color of these stones was unexpected. However, a deposit of green haüyne was reported from Afghanistan earlier this year (B. Srisataporn et al., "Green haüyne: A rarity among sodalite gems," *Journal of Gemmology*, Vol. 39, No. 1, 2024, pp. 13–16).

Standard gemological testing revealed properties consistent with haüyne, including an average refractive index of 1.50 and a hydrostatic specific gravity of 2.41. The stones also fluoresced orange to long-wave UV and were inert to short-wave UV. Microscopic examination revealed interesting whitish inclusions, which have been previously reported as mica (figure 2). This was confirmed by Raman spectroscopy. No evidence of clarity enhancement was observed in any of the stones examined. Raman spectroscopy further confirmed the identity of the green gems as haüyne.

This suite represents the first green gem-quality haüyne examined by GIA and is an interesting and rare collector stone.

Nathan Renfro, Maxwell Hain, and Wim Vertriest

Figure 1. These seven stones (0.24–1.44 ct) ranging in color from yellowish green to bluish green were identified as the rare gem haüyne.

Figure 2. A large mica cluster was observed in the 1.44 ct green haüyne; field of view 1.83 mm. Courtesy of Bill Vance.

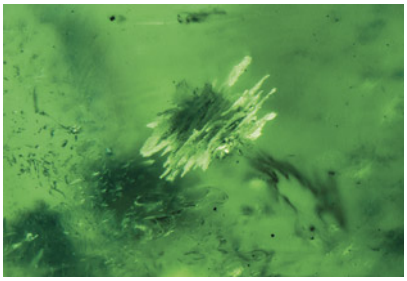

LABORATORY-GROWN DIAMOND

Colored Bands in CVD-Grown Diamond

The Surat laboratory recently examined a 3.14 ct F-color oval brilliant diamond grown by chemical vapor deposition (CVD). The diamond featured a single dark brown band measuring ~2.2 mm in length that resembled graining in natural diamond (figure 3). The band was visible under the microscope as well as with a 10× loupe. The clarity grade was VVS_2 based on this colored band, which was visible through multiple bezels and affected the transparency at that location. Through the pavilion, parallel whitish bands were also observed (figure 4A).

Editors' note: All items were written by staff members of GIA laboratories.

Gems & Gemology, Vol. 60, No. 3, pp. 368–380.

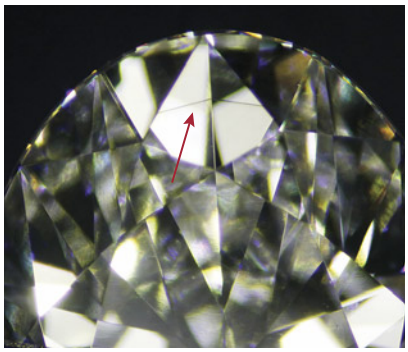

Figure 3. A growth remnant appeared as a color band (arrow) in a 3.14 ct CVD-grown diamond. Field of view ~11.75 mm.

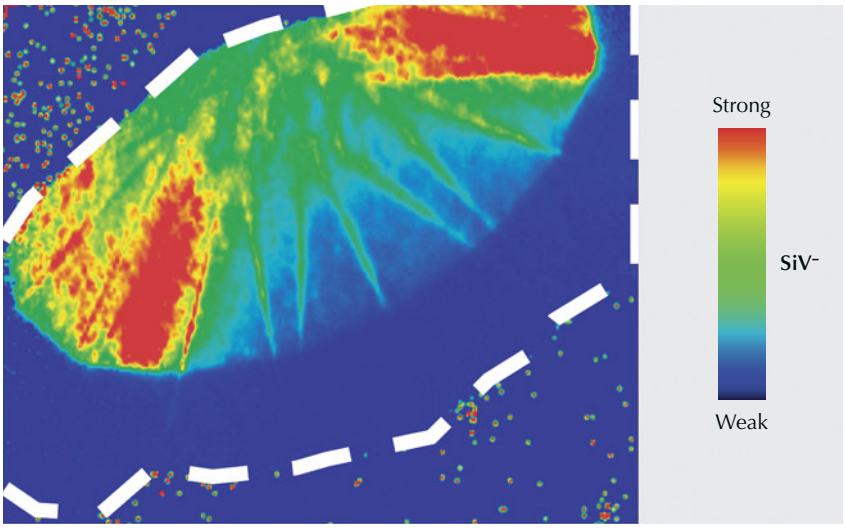

Figure 5. False-color PL map of the SiV^- defect at 736.6/736.9 nm using 633 nm laser excitation, normalized to the diamond Raman area on the pavilion. The dashed line indicates the approximate outline of the diamond.

The subtle banding seen in this diamond differed from a cloud of graphite inclusions at a growth interface previously reported in a CVD-grown diamond (Summer 2023 Lab Notes, pp. 213–214). The fluorescence image collected by the DiamondView revealed a layered growth structure that did not coincide with the color banding, indicating a start-stop cycling growth process typical of CVD synthesis (figure 4B). Deep UV fluorescence with green and blue coloration as well as strong green phosphorescence seen in the DiamondView image (figure 4C) indicated high-pressure, high-temperature treatment. The SiV^- defect at 736.6 and 736.9 nm, a common feature of CVD laboratory-grown diamond and only rarely seen in natural diamond, was observed in photoluminescence (PL) spectra using 457, 514, and 633 nm laser excitation. PL mapping (figure 5) revealed that the concentration of SiV^- was higher near the culet of the pavilion and dramatically lower near the table.

GIA has documented growth remnants in thousands of CVD-grown diamonds. But with a multitude of manufacturers, recipes, and treatments, a wide variety of clarity characteristics are encountered, including the unusual color band observed here.

Srushti Tanti and Raju Jain

Irradiated HPHT-Grown Diamonds with Blue-Green Color Zonation

The Carlsbad laboratory received two diamonds grown by the high-pressure, high-temperature (HPHT) process that contained interesting color

Figure 4. A: Hazy parallel lines (indicated by arrows) resembling whitish internal graining; field of view ~6.31 mm. DiamondView imaging of the pavilion facets showed blue growth layers in green fluorescence (B), as well as strong green phosphorescence (C).

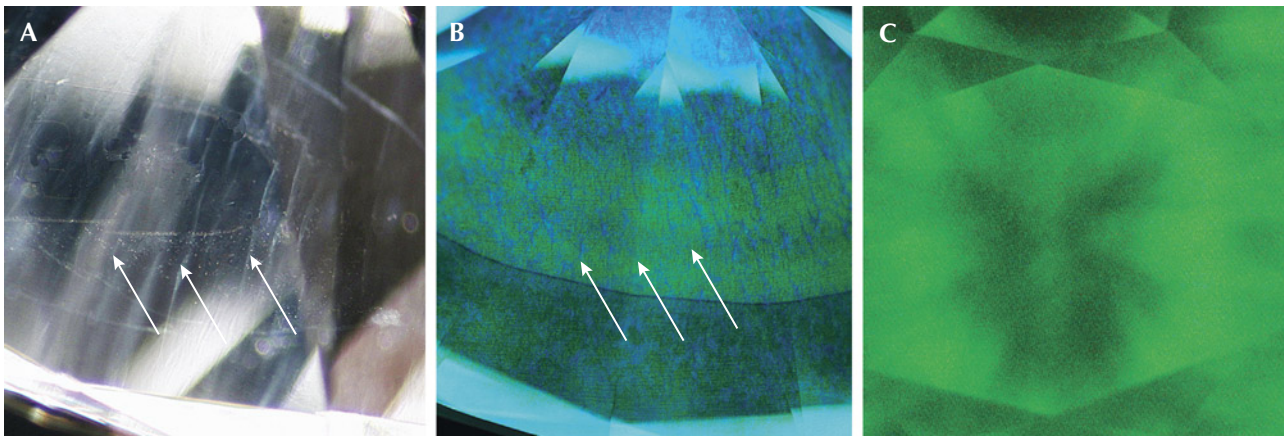

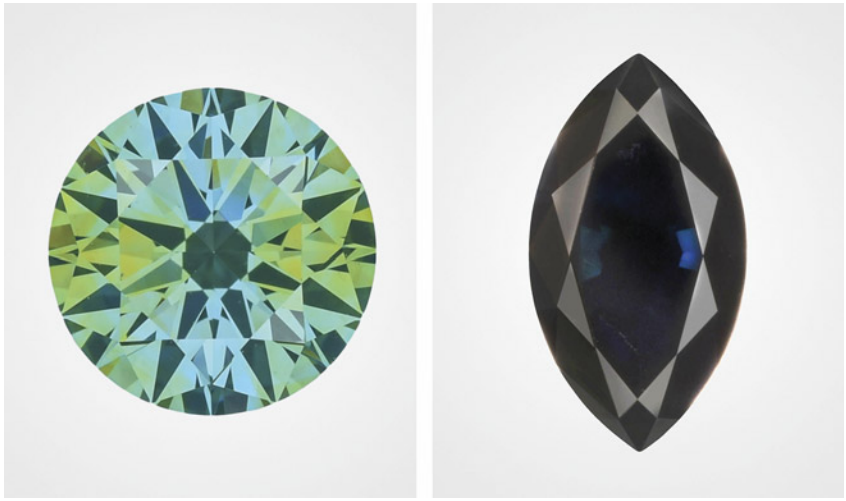

Figure 6. Two HPHT-grown diamonds: a 0.51 ct round brilliant with Fancy Deep bluish green color (left) and a 1.56 ct Fancy black marquise (right).

zonation. The 0.51 ct round brilliant (figure 6, left), submitted for a laboratory-grown colored diamond report, received a Fancy Deep bluish green color grade. The 1.56 ct marquise (figure 6, right), submitted for the same LG-CD service, was Fancy black. Both stones were determined to be artificially irradiated. The high concentration of defects created by laboratory irradiation led to extensive absorption in the marquise, causing a black appearance that is fairly uncommon for laboratory-grown diamonds. When viewed through the pavilion, sector-dependent color zonation was visible in both stones (figure 7).

Dramatic color zonation corresponding with growth sectors is a feature of some fancy-color HPHT-grown diamonds (J.E. Shigley et al., "Gemesis laboratory-created diamonds," Winter 2002 *G&G*, pp. 301–309; J.E. Shigley et al., "Lab-grown colored diamonds from Chatham Created Gems," Summer 2004 *G&G*, pp. 128–145; S. Eaton-Magaña et al., "Observations on HPHT-grown synthetic diamonds: A review," Fall 2017 *G&G*, pp. 262–284; Winter 2023 Lab Notes, pp. 489–490). In these particular irradiated stones, the areas of transmitted blue color were due to the GR1 defect, which created absorption primarily in the red portion of the visible spectrum (e.g., C.D. Clark et al., "The absorption spectra of natural and irradiated diamonds," *Proceedings of the Royal Society of London A: Mathematical, Physical, and Engineering Sciences*, Vol. 234, No. 1198, 1956, pp. 363–381). Nitrogen can cause absorption in the blue portion of the visible spectrum to contribute to yellow color in some of the growth sectors, and together these can lead to a combined green color. From the pavilion of the round brilliant diamond (figure 7, left), the yellow sectors appeared to be distinct from blue, but these color components combined to appear green face-up (figure 6, left). Similarly, green coloration resulting from yellow Ib and blue IIb sectors was described in some early HPHT-grown diamonds (Shigley et al., 2004).

These stones offer examples of fun and distinctive features that can be observed in laboratory-grown colored diamonds.

Taryn Linzmeyer and Sally Eaton-Magaña

PEARLS

Fashioned Queen Conch Shell Bead

Conch pearls are prized for their porcelaneous surface and distinctive flame-like pattern, characterized by a regular arrangement of parallel elongated crystals that create a silky sheen (H.A. Hänni, "Explaining the flame structure in non-nacreous pearls,"

Figure 7. Viewed through the pavilion, sector-dependent color zones were apparent in both the round brilliant (left) and the marquise (right; field of view 7.19 mm).

SSEF, 2009). Highly valued Queen conch pearls, produced by the *Aliger gigas* species (formerly *Strombus gigas* or *Lobatus gigas*), are known for their exquisite pink coloration, flame structure, and porcelaneous luster. Queen conch shells are widely used for crafting and jewelry accessories and sometimes used to simulate the appearance of natural pearls.

Recently, GIA's Mumbai laboratory received a drilled light pink bead for pearl identification, measuring 10.20 mm in diameter and weighing 7.50 ct (figure 8). Most Queen conch pearls are oval, semi-baroque, or baroque, and it is very rare to find a perfectly round conch pearl similar to the submitted specimen. In addition, an obvious banded structure was observed on the surface, which raised suspicions of a fashioned shell (E. Fritsch and E.B. Misiorowski, "The history and gemology of Queen conch 'pearls'," Winter 1987 *G&G*, pp. 208–221). The banded structure was arranged in a distinct concentric ring pattern resembling a bull's-eye (figure 9A), with alternating white, cream, and light pink bands covering half of its surface. The parallel band lines appeared to run throughout the bead when observed using transmitted fiber-optic illumination (figure 9B), consistent with the parallel striations revealed by real-time X-ray microradiography imaging (figure 9C). Under high magnification, prominent flame structures with long, slender linear striations were visible (figure 9D).

Figure 8. This round light pink bead fashioned Queen conch shell (10.20 mm and 7.50 ct) resembled a Queen conch pearl.

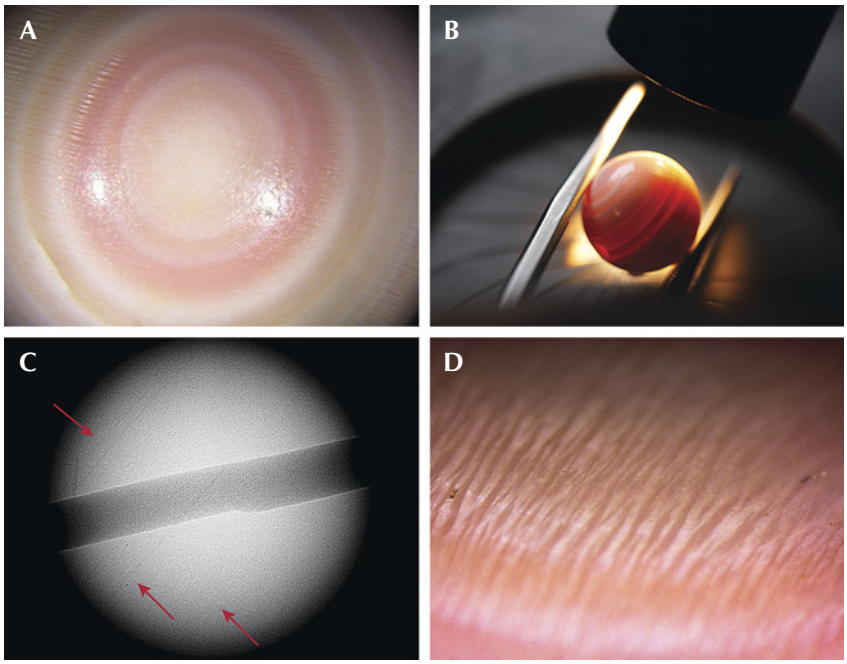

Figure 9. A: Concentric rings with alternating white, cream, and light pink color bands resembling a bull's-eye; field of view 3 mm. B: Banded structure observed under fiber-optic illumination. C: Internal banding lines (red arrows) correlating to the external bands visible in image A. D: A pattern of parallel elongated slender flames imparting a silky sheen effect; field of view 1 mm.

Ultraviolet/visible/near-infrared reflectance spectra showed absorption features at 280 and 368 nm and a broad band centered at 512 nm, similar to those seen in natural orangy pink conch pearls, confirming their natural color origin (figure 10). Raman analysis using 514 nm laser excitation revealed a doublet at 702/704 cm^{-1} and a peak at 1086 cm^{-1}, indicative of aragonite. Significant polyenic pigment peaks were previously observed at 1125 and 1514 cm^{-1}, indicative of natural color (S. Karampelas et al., "Raman spectroscopy of natural and cultured pearls and pearl producing mollusc shells," *Journal of Raman Spectroscopy*, Vol. 59, No. 1, 2019, pp. 1813–1821). After thorough analysis, the specimen was confidently determined to be a fashioned shell bead imitation originating from the shell of an *Aliger gigas* gastropod (Queen conch).

Shell imitations of pearl hold a long-standing history as fashionable jewelry pieces targeting a wide consumer base. These imitations are occasionally misrepresented as "shell pearls" or simply "pearls," potentially misleading less experienced buyers (Summer 2014 Lab Notes, pp. 153–154). Their close resemblance to natural and cultured pearls often leads consumers to seek laboratory testing. The fashioned shell specimen under examination was relatively straightforward given the distinctive banded structure, a feature normally absent in pearls. However, it is crucial to observe subtle traits and compositions that can distinguish genuine pearls from imitations. Shell is the most popular material used for porcelaneous pearl imitations, and sometimes it is sourced from the same mollusk

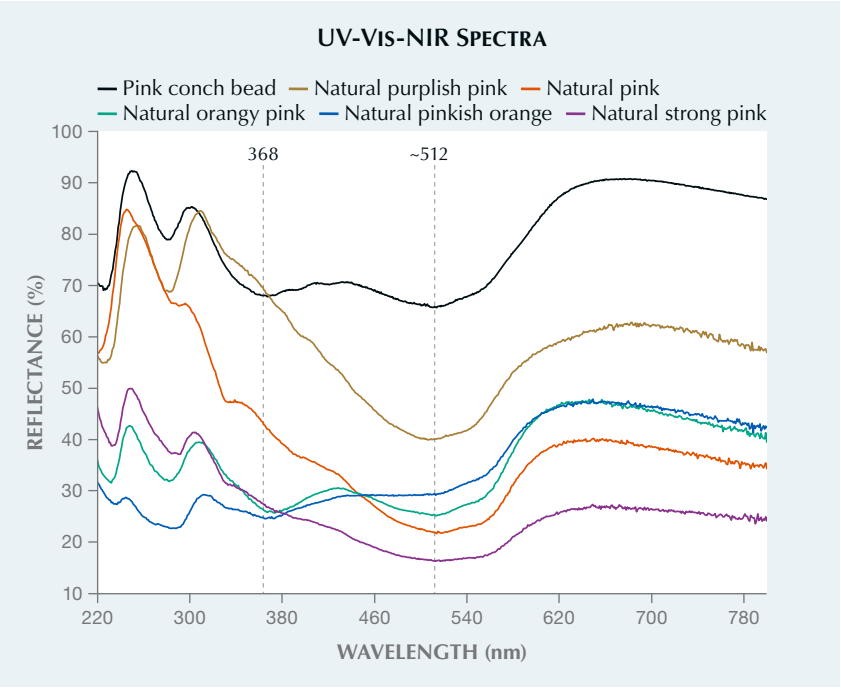

Figure 10. UV-Vis-NIR spectra comparison of the conch bead imitation with five naturally colored conch pearls from GIA reference samples. The natural orangy pink and pinkish orange samples displayed a feature at 368 nm with a broad reflectance band centered around 512 nm similar to that observed in the examined specimen.

species as the pearl being imitated, causing similar color and surface appearance. Therefore, caution and scrutiny are always essential when purchasing pearl products.

Gauri Sarvankar, Abeer Al-Alawi, and Roxane Bhot Jain

Two Imitation Melo Pearls

Flame structures are a surface characteristic of Melo pearls produced from mollusks belonging to the *Melo* species. The flame pattern is a result of the interaction of light with an interwoven aragonite lamellae microstructure of the pearl (H.A. Hänni, "Explaining the flame structure of non-nacreous pearls," *Australian Gemmologist*, Vol. 24, No. 4, 2010, pp. 85–88). Melo pearls are valued for their rarity, large sizes, attractive yellowish orange to orange colors, and flame structures. Therefore, it is not surprising that there have been attempts to imitate these pearls (M.S. Krzemnicki, "A worked shell bead as an imitation of a melo pearl," *Gemmological Journal Hong Kong*, Vol. 27, 2006, pp. 31–33; Summer 2006 Lab Notes, pp. 166–167; N. Sturman et al., "An imitation 'Melo pearl,'" *GIA Research News*, January 21, 2011). Most imitations of Melo pearl are dyed fashioned shells from the *Tridacna* species. However, two recent samples submitted to GIA for pearl identification were unusual.

The Hong Kong laboratory received a 140.58 ct orange sphere measuring 27.23 mm. At first glance, its orange bodycolor and non-nacreous surface appearance with a blotchy pattern resembled the flame-like surface structure of a Melo pearl (figure 11, left). However, high magnification revealed a mosaic structure and concentrations of an orange dye substance (figure 12). While aragonite and polyenic pigments are commonly observed in naturally colored Melo pearls, Raman spectroscopy indicated a calcite composition with diagnostic peaks at 282, 713, and 1088 cm^{-1}. Photoluminescence spectroscopy showed clear peaks at 552 and 560 nm, proving the presence of color treatment. This combined evidence confirmed the specimen was dyed calcite.

Meanwhile, another orange sphere (figure 11, right) weighing 89.81 ct and measuring 23.27 × 23.00 mm that appeared to be a Melo pearl was submitted to the Bangkok laboratory. The sample's color and appearance were similar to that of the specimen tested in Hong Kong, but its surface texture was mottled. Magnification revealed a patchy structure of unnat-

Figure 11. A 140.58 ct dyed calcite sphere (left) and an 89.81 ct round dyed and coated shell (right), both resembling Melo pearls.

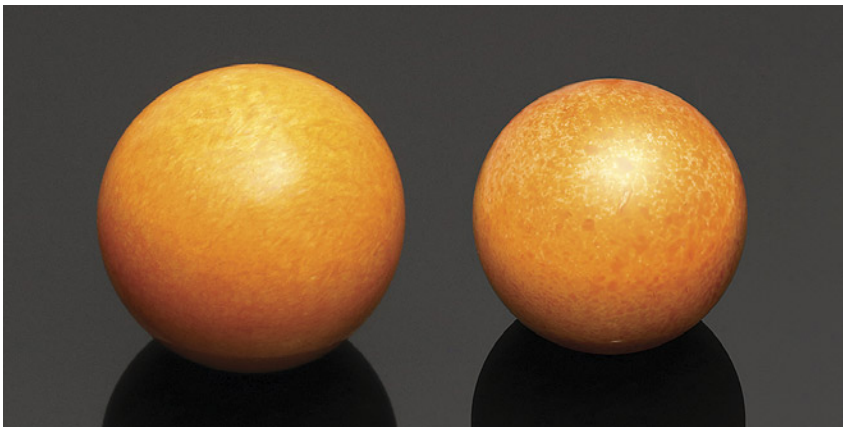

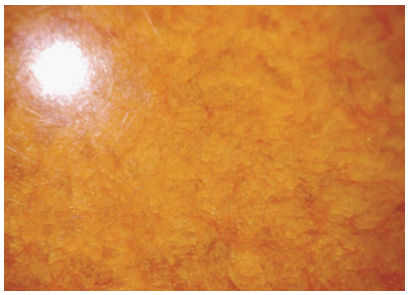

Figure 12. The 140.58 ct sphere exhibited a mosaic structure, and orange color concentration was noted within areas under magnification. Field of view 6.92 mm.

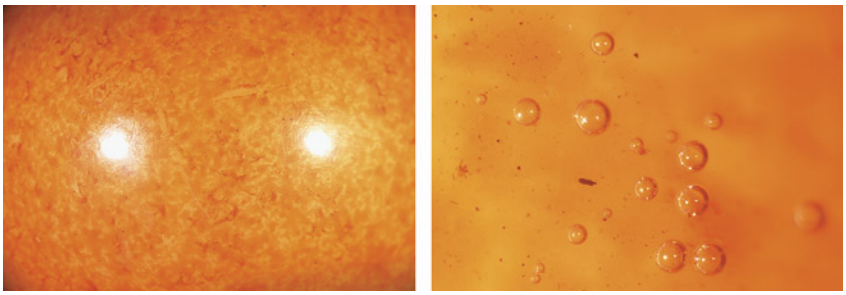

Figure 13. Microscopic observation of the 89.81 ct sphere revealed unnatural color patches (left) and gas bubbles and trapped dirt (right). Fields of view 19.20 and 1.80 mm.

ural orange coloration and a lack of flame patterns (figure 13, left). The sample possessed a resinous luster, and gas bubbles and trapped dirt suggested a colorless coating on the outermost surface (figure 13, right). The Raman spectroscopy of the coated surface showed distinct peaks around 1582, 1602, 2945, 3004, and 3065 cm^{-1}, indicative of an artificial resin (L. Kiefert et al., "Identification of filler substances in emeralds by infrared and Raman spectroscopy," *Journal of Gemmology*, Vol. 26, No. 8, 1999, pp. 501–520; Fall 2005 Gem News International, pp. 272–273). Under strong fiber-optic illumination, the item exhibited obvious banding typical of shell-related materials (figure 14, left). Furthermore, one area seemed to have been ground down, revealing a white material underneath the coated and dyed layers (figure 14, right). Raman analysis on the area showed peaks at 703, 1085, and 1460 cm^{-1}, identifying the material as aragonite. All the data obtained led to the conclusion that this was a Melo pearl imitation made of a dyed and coated shell.

While pearl imitations are not new to the market, these two samples appear strikingly similar to natural Melo pearls. Careful inspection under high magnification and advanced analytical procedures employed by gemological laboratories are sometimes needed to provide accurate and comprehensive results.

Wing Kiu Fan and Ravenya Atchalak

Metallic Core in a Natural Freshwater Pearl

Although cultured pearls dominate the freshwater pearl industry, the rarer natural freshwater pearls are still encountered during routine laboratory testing. The majority of these have been handed down through generations, and recent finds are limited due to heavy regulations in the mussel shelling industry and lower demand for mother-of-pearl. Recently, GIA's Mumbai laboratory received for identification a white circled button-shaped nacreous pearl measuring 5.74 × 3.98 mm and weighing 0.97 ct (figure 15).

The pearl displayed circular bands on its upper portion with minor sub-surface-reaching cracks and a translucent nacreous layer with

Figure 14. Left: A "banding test," performed using strong transmitted lighting to reveal banding, indicated the item was fashioned from shell. Right: The underlying white surface was exposed in one polished area; field of view 3.60 mm.

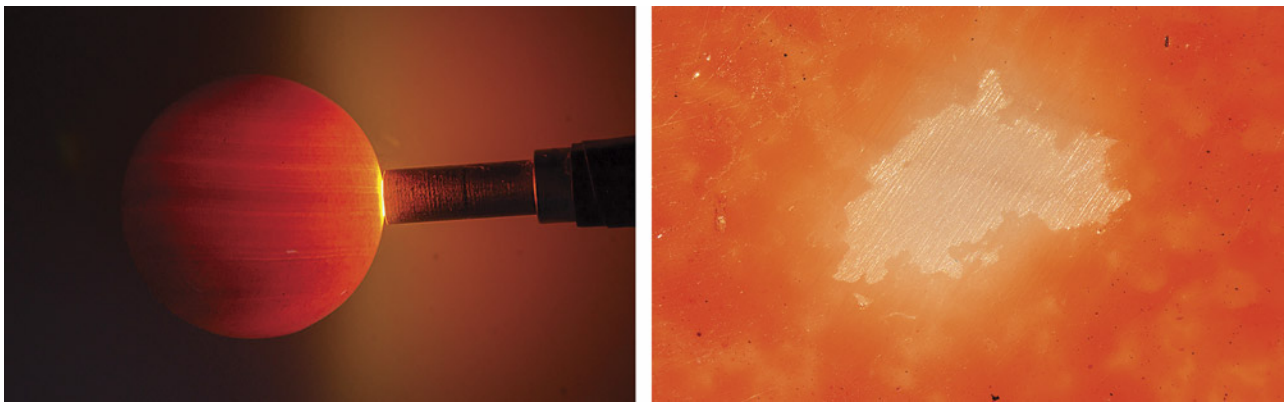

Figure 15. The white natural freshwater pearl measuring 5.74 × 3.98 mm and weighing 0.97 ct.

overlapping platelets of aragonite. The pearl showed a strong yellowish green reaction when exposed to X-ray fluorescence. Energy-dispersive X-ray fluorescence analysis conducted on two spots revealed manganese levels of 348 and 390 ppm and strontium levels of 470 and 694 ppm, respectively. The results of both analyses are characteristic of pearls from a freshwater environment. Under long-wave ultraviolet light, the pearl exhibited a moderate greenish yellow reaction, which is typical for unprocessed white pearls. White cultured freshwater pearls are routinely processed and show moderate to strong blue reactions under long-wave UV.

Real-time X-ray microradiography (RTX) imaging revealed a small near-round radiopaque white core, measuring approximately 0.20 × 0.15 × 0.12 mm, surrounded by concentric growth arcs extending to the pearl's edge (figure 16). The core's radiopacity suggested it was composed of a material of higher density than the surrounding nacreous area. This resembled the opacity typically observed in metals during X-ray radiography and was similar to metal cores previously noted in saltwater pearls (M.S. Krzemnicki, "Pearl with a strange metal core," *SSEF Facette*, No. 24, 2018, p. 27; Summer 2023 Gem News International, pp. 244–246). Another metal remnant was observed in the pearl's drill hole, initially presumed to be a fragment of a broken needle used during drilling (figure 16).

Upon closer examination using X-ray computed microtomography (µ-CT), the metal feature within the drill-hole area appeared similar to the metallic core found within the pearl and seemed to be partially embedded within the pearl's growth arcs. Both metal features exhibited undulating outlines and a lack of sharp edges typically associated with a broken metal fragment. Given the similar properties of both metal fea-

Figure 16. Left: RTX imaging from the side reveals a near-round metallic core (yellow arrow) surrounded by growth arcs and a small metal feature within the drill hole (red arrow). Right: RTX imaging from the top reveals slight distortion to the metal core and a small metal feature embedded inside the wall of the drill hole.

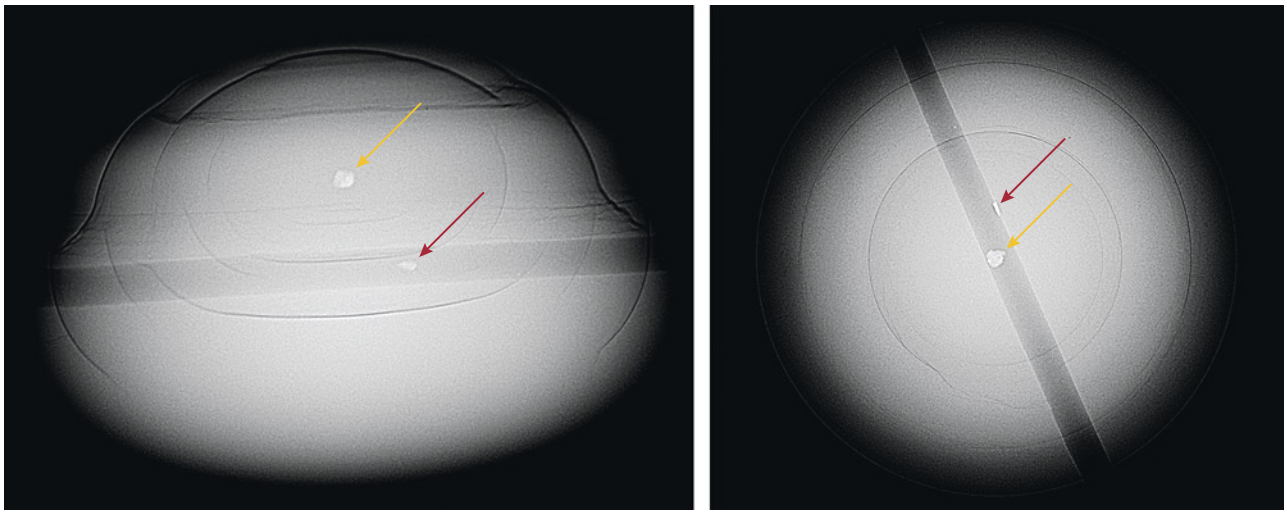

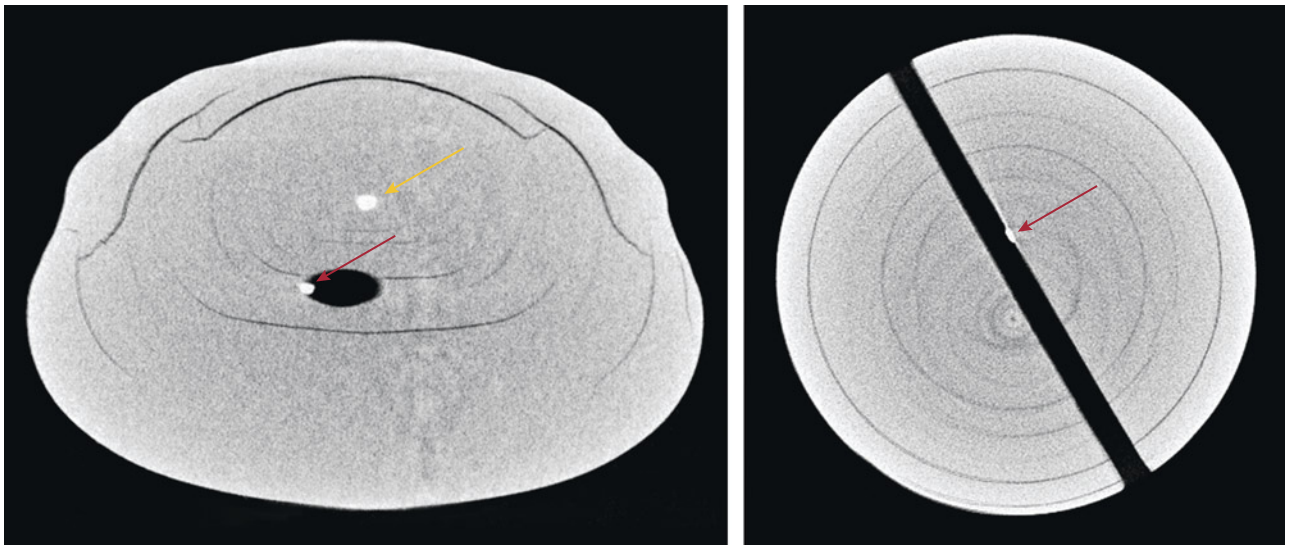

Figure 17. Left: µ-CT image showing the metallic core (yellow arrow) and the small metal feature crossing the boundary of the drill hole (red arrow). Right: µ-CT image showing only the metal feature protruding from a nacreous area in the drill hole (red arrow).

tures, the metal feature at the drill hole may have been present prior to the drilling process, rather than a remnant from a drilling needle (figure 17).

Because RTX and µ-CT imaging did not reveal any suspicious irregular linear or void structures typically found at the center of freshwater cultured pearls, the sample was identified as a natural freshwater pearl (K. Scarratt et al., "Characteristics of nuclei in Chinese freshwater cultured pearls," Summer 2000 *G&G*, pp. 98–109). The structure present was comparable to that of natural freshwater pearls previously studied by GIA (Summer 2021 Gem News International, pp. 167–171). The only difference noted was the metallic core at the center of this pearl, a feature not commonly observed in natural freshwater pearls.

These observations suggest environmental contamination during the pearl's formation, potentially due to the presence of a foreign object around which the pearl formed. The process of pearls forming around such foreign objects remains a topic of ongoing scientific research.

Jayesh Surve and Abeer Al-Alawi

A Multicore Non-Bead Cultured Pearl

Recently, the Mumbai laboratory received a lot consisting of 101 variously shaped, white to cream saltwater nacreous loose pearls for identification services. When exposed to X-ray fluorescence (XRF), the pearls showed an inert to weak yellowish green reaction. Energy-dispersive X-ray fluorescence confirmed the saltwater origin of these pearls; however, an unusually high concentration of strontium was detected on the surface, which will be the subject of a separate study.

Real-time X-ray microradiography (RTX) imaging showed typical non-bead cultured pearl structures, mostly with central dense cores surrounded by concentric growth rings and associated light gray calcium carbonate ($CaCO_3$) "seed" features, elongated linear structures, and sizeable spindle-shaped voids (A. Homkrajae et al., "Internal structures of known *Pinctada maxima* pearls: Cultured pearls from operated marine mollusks," Fall 2021 *G&G*, pp. 186–205). Some of the pearls contained multiple nuclei that showed varied combinations of multicore structures. One of these was a light cream near-oval pearl weighing 1.69 ct and measuring 6.83 × 5.34 mm that exhibited a bumpy cluster-like formation (figure 18). Under long-wave ultraviolet radiation, the pearl displayed a moderate yellowish green reaction typical of white pearls from the *Pinctada* species.

Figure 18. A semi-baroque non-bead cultured pearl weighing 1.69 ct and measuring 6.83 × 5.34 mm.

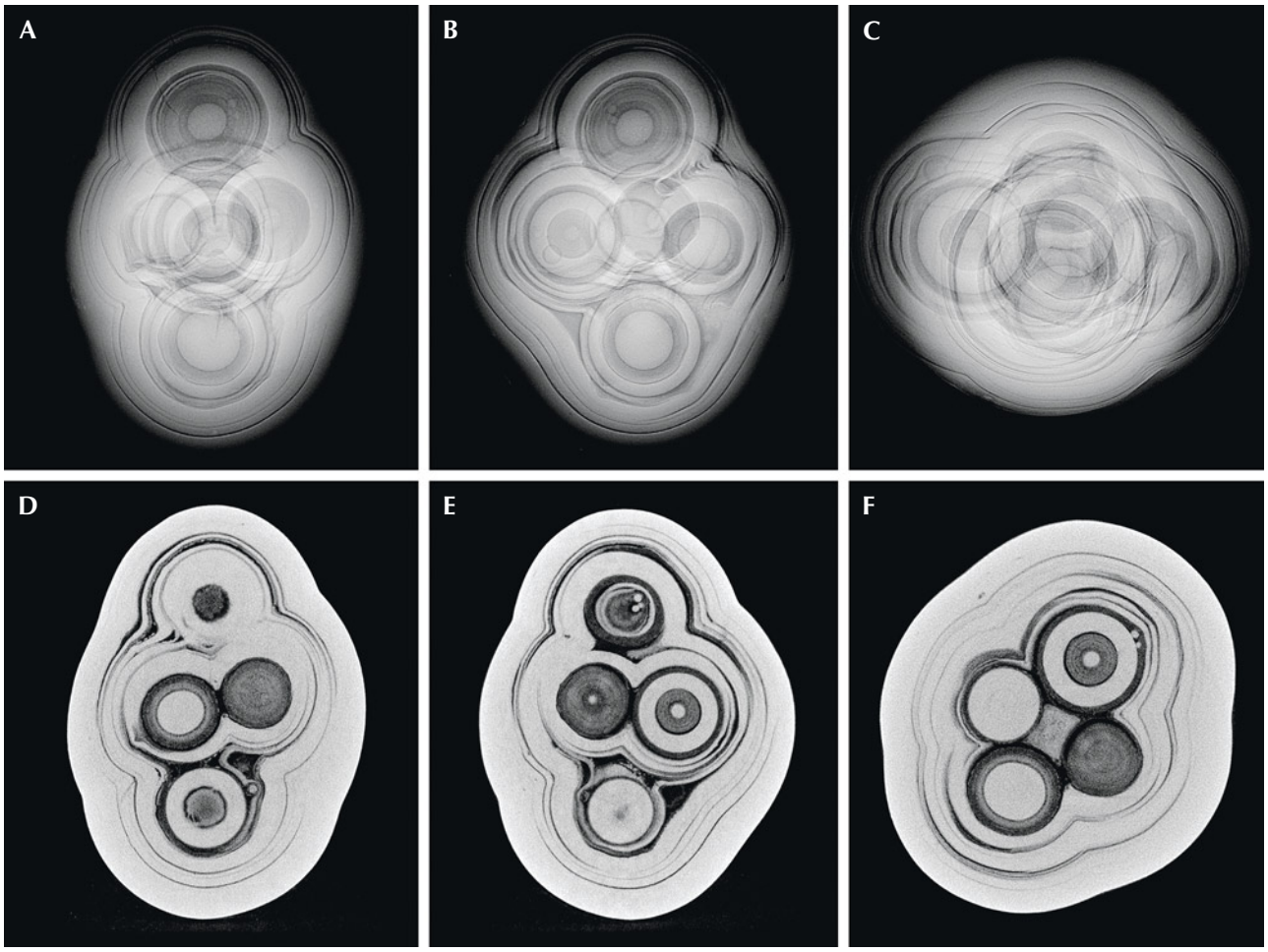

Figure 19. Top: RTX images revealing the pearl's complex multicore internal structure. Bottom: µ-CT images displaying the six cores present inside the pearl.

The pearl showed an inert reaction when subjected to XRF, consistent with others in the group and characteristic of a saltwater environment. Raman spectroscopy using 514 nm laser excitation detected a doublet at 701 and 704 cm^{-1}, along with a main peak at 1086 cm^{-1}, indicating the presence of aragonite.

RTX imaging in three directions revealed a complex interconnected structure within the pearl, and several cores of varying sizes and radiopacities overlapped, making it difficult to count the number of cores (figure 19, A–C). X-ray computed microtomography (µ-CT) analysis displayed the structure more clearly, showing a total of six medium to large light gray dense cores engulfed by distinct conchiolin-rich layers (figure 19, D–F). Four cores exhibited prominent light gray calcium carbonate "seed" features in the organic-rich concentric growth rings. Such features are commonly observed in non-bead cultured pearls from the *Pinctada maxima* species (Homkrajae et al., 2021). Notably, two of the cores were encircled by thick alternating concentric growth rings with radiopacities of lighter and darker shades of gray. All the cores were surrounded by growth layers conforming to the pearl's shape, and the "seed" features were also observed in between the layers, as shown in the video at www.gia.edu/gems-gemology/fall-2024-lab-notes-multicore-nonbead-cultured-pearl.

Considering its external appearance, internal structure, and saltwater environment, the pearl was classified as a non-bead cultured pearl from the *Pinctada maxima* species.

Both natural and cultured pearls commonly exhibit multiple nuclei structures. Most natural pearls with multiple nuclei contain internal growth arc structures, and multicores of significant size inside the organic-rich concentric structures are generally related to non-bead cultured pearls. However, it is rare to encounter pearls with more than a couple of cores, making this pearl unique and noteworthy. Ongoing research is currently being conducted to further study the unusual chemistry readings recorded in the lot of pearls received.

Roxane Bhot Jain, Karan Rajguru, Abeer Al-Alawi, and Chunhui Zhou

Figure 20. This necklace contains 63 variously colored and shaped Mexican pearls from Pteria *and* Pinctada *species and the Pinnidae family, measuring from 4.88 mm to 10.75 × 9.32 mm.*

Natural Pearl Necklace from Baja California Sur, Mexico

A unique necklace containing 63 pearls of various colors, shapes, sizes and mollusk species (*Pteria* and *Pinctada* species, and Pinnidae family) was recently submitted to the Carlsbad laboratory for examination (figure 20). Ranging in size from 4.88 mm to 10.75 × 9.32 mm, all the pearls were nacreous and exhibited overlapping aragonite platelets under high magnification, and the majority displayed a pronounced orient or iridescence phenomenon.

Interestingly, several pearls displayed similar crosslines with various surface patterns, seen in figure 20. The crosslines appeared to be natural grooves with no signs of surface treatment. Further testing identified these as *Pteria* pearls.

Nine pearls of light yellowish brown to brown colors displayed a similar linear-looking nacre appearance caused by slender rectangular aragonite platelets, which has been observed on the nacreous surface of *Pinna* or pen pearls belonging to the Pinnidae family (figure 21; E. Strack, *Pearls*, Rühle-Diebener-Verlag, Stuttgart, Germany, 2006; N. Sturman et al., "Observations on pearls reportedly from the Pinnidae family (pen pearls)," Fall 2014 *G&G*, pp. 202–215). The nacre of pearls from the *Pteria* and *Pinctada* species generally consists of hexagonal or polygonal aragonite platelets.

Under long-wave ultraviolet radiation, many of the pearls exhibited weak to strong orangy red to red fluorescence, which is characteristic of the porphyrin pigment found in colored *Pteria* pearls (figure 22; L. Kiefert et al., "Cultured pearls from the Gulf of California, Mexico," Spring 2004 *G&G*, pp. 26–38). The fluorescence intensity of the *Pteria* pearls varied depending on their darkness and color saturation.

Figure 21. A linear-looking nacre is characteristic of nacreous Pinna *or pen pearls from the Pinnidae family; field of view 3.68 mm.*

Figure 22. The Pteria*,* Pinctada*, and* Pinna *pearls displayed distinct fluorescence colors under long-wave ultraviolet radiation: orangy red to red (*Pteria*), green to greenish yellow (*Pinctada*), and chalky yellow (*Pinna*).*

The samples with more intense colors displayed a stronger red reaction. In contrast, darker pearls from the *Pinctada* species exhibited weaker green to greenish yellow reactions. The pen pearls showed a weak to moderate chalky yellow fluorescence, consistent with the reaction of some pen pearls (Sturman et al., 2014).

Real-time X-ray microradiography (RTX) revealed various growth patterns of natural pearls. Many *Pteria* samples contained a typical large dark gray organic-rich area in the center, and a faint radial structure was also present within the dark area in some samples (figure 23). One pen sample exhibited an irregular dark gray void associated with light gray granular features that was previously observed in some natural nacreous pen pearls (Sturman et al., 2014) and in GIA's research collection.

Energy-dispersive X-ray fluorescence (EDXRF), ultraviolet/visible reflectance spectroscopy, and photoluminescence spectroscopy using a 514 nm laser excitation analyses indicated that all the pearls were of saltwater origin and naturally colored.

The client who submitted the necklace noted that the pearls were reportedly fished from the coastlines of the Mexican state of Baja California Sur, from both the Pacific Ocean and the Gulf of California (Sea of Cortez), over the course of eight years. The *Pteria* pearls were fished near San Carlos and Guerrero Negro, the pen pearls from the San Ignacio lagoon and Muleje, and the *Pinctada* pearls from Loreto. Based on the geographical information provided and the gemological characteristics observed, the mollusk species can be more precisely determined. The *Pteria* and *Pinctada* pearls likely came from *Pteria sterna* and *Pinctada mazatlanica*, respectively, as both species are indigenous along Mexico's Pacific coast and the Gulf of California (M. Cariño and M. Monteforte, "History of pearling in La Paz Bay, South Baja California," Summer 1995 *G&G*, pp. 88–105; Strack, 2006). Although the Pinnidae family is widespread globally, pen pearls from *Atrina tuberculosa* (often called *Atrina maura*) are local to Mexico and noted to produce pearls with a partially nacreous surface (Strack, 2006).

Mexico has been a rich source of pearls since ancient times (Cariño and Monteforte, 1995). Overfishing, changes in water environment, and dam construction have shortened the lifespan of indigenous mollusks and limited pearl production since the end of the nineteenth century (D. McLaurin-Moreno, "Sea of Cortez pearls: A historical overview," *Sixteenth Annual Sinkankas Symposium—Pearl*, Gemological Society of

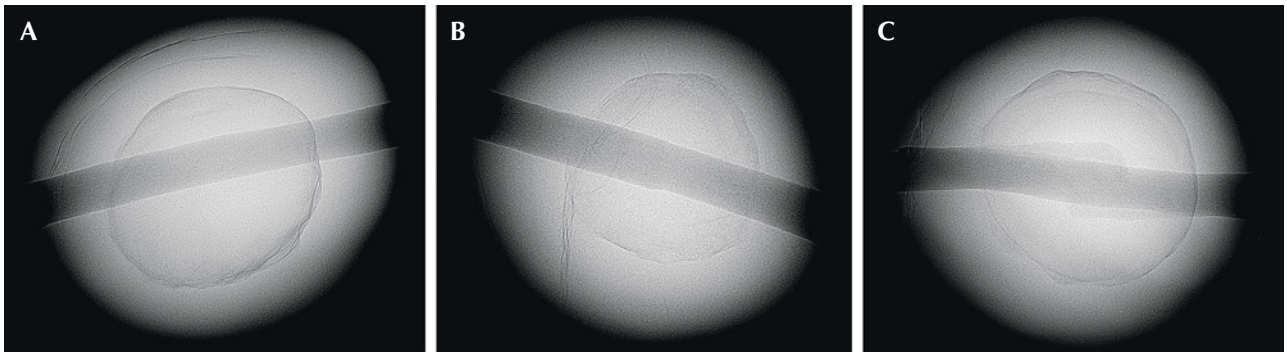

Figure 23. A large dark gray organic-rich area is a typical structure in natural Pteria *pearls, and sometimes a faint radial structure is found within the dark area.*

San Diego and GIA, pp. 6–29). These new pearls from native species signal the return of healthy mollusk beds.

Artitaya Homkrajae and Amiroh Steen

Iridescent Tubes in PEZZOTTAITE

A large 8.13 ct emerald-cut purplish pink pezzottaite ($CsLiBe_2Al_2Si_6O_{18}$) was submitted to the Carlsbad laboratory for gem identification (figure 24). Pezzottaite is a member of the beryl mineral group. This specimen had a measured refractive index of 1.600–1.610 and a specific gravity of 3.06. This stone was exceptional for its large size and quality, and gemological testing revealed no evidence of clarity treatment. The identity of the specimen was verified using Raman and Fourier-transform infrared spectroscopy, which also revealed the presence of H_2O in the crystal structure channels of the specimen, a common feature in pezzottaite. While the clarity of this pezzottaite was impressive for this mineral, especially without enhancement, the overall transparency was diminished by the presence of inclusions and small fractures. Some of these inclusions, such as the growth bands and tubules, could be considered distinctly beautiful features. Although the stone itself had a purplish pink hue, in darkfield illumination it appeared dark pink-purple (figure 25). The sample exhibited faint growth banding, with thin tube inclusions approximately perpendicular to the growth banding (i.e., tubes imperfectly parallel to the *c*-axis, crossing at shallow angles, and banding nearly perpendicular to the *c*-axis). At some viewing angles, the tube inclusions displayed vivid iridescence ranging from magenta, purple, neon blue, and green, to neon yellow and orange, given appropriate illumination. The iridescence was more vivid in darkfield

Figure 24. This 8.13 ct pezzottaite contains delicate growth banding (~horizontal) and tube inclusions (~vertical, seen best in lower left).

Figure 25. Iridescent tube inclusions (bottom left corner in figure 24) in pezzottaite, shown in darkfield illumination; field of view 2.5 mm.

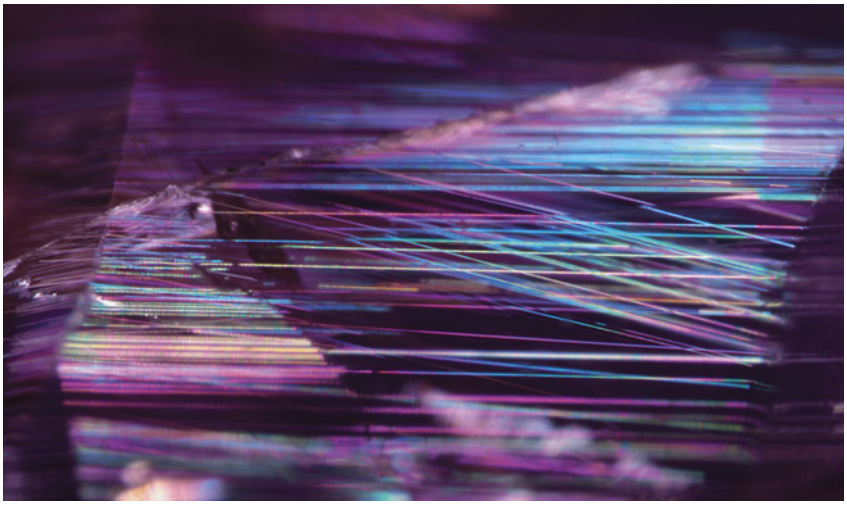

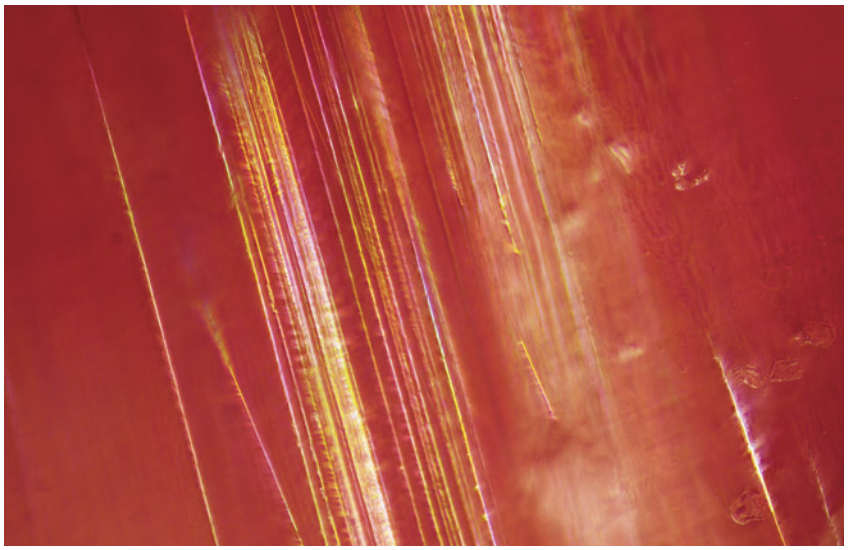

Figure 26. Iridescent growth tubes in pezzottaite with brightfield illumination; field of view 0.72 mm.

illumination, but brightfield lighting showed a pinkish orange background which made the tubes shimmer (figure 26). Although colorful in specialized microscope lighting, the tubular inclusions were semitransparent white to the unaided eye in common lighting conditions.

Rhiana Elizabeth Henry, Taryn Linzmeyer, and Jeffrey Hernandez

RUBY with Synthetic Overgrowth Lining Cavities

GIA's Bangkok laboratory recently received an 8.63 ct purplish red marquise double cabochon. The stone showed gemological properties consistent with ruby: a spot refractive index of 1.770 and a characteristic ruby spectrum using a handheld spectroscope. It was semitransparent and contained altered growth tubes, multiple fractures with flux residues, and some fractures with trapped flattened gas bubbles and areas of filled cavities. X-ray fluorescence revealed significant amounts of lead, mostly along fractures and filled cavities.

The author observed an unusual area of granular texture lining the filled cavity (areas of lower luster) (figure 27). This granular texture was caused by a reaction layer of synthetic overgrowth where surfaces were melted and recrystallized. This pattern can be found in any high-temperature heat-treated corundum. Synthetic overgrowth at the surface of a stone can sometimes be removed by repolishing.

Sudarat Saeseaw

PHOTO CREDITS
Annie Haynes—1, 20; Nathan Renfro—2; Raju Jain—3, 4A; Suraj Maurya—4 (B and C); Rhonda Wilson—6; Taryn Linzmeyer—7 (right), 26; Gaurav Bera—8, 9, 15, 18; Johnny (Chak Wan) Leung—11 (left); Lhapsin Nillapat—11 (right); Cheryl (Ying Wai) Au—12; Ravenya Atchalak—13, 14 (right); Nuttapol Kitdee—14 (left); Artitaya Homkrajae—21, 22; Adriana Robinson—24; Rhiana Elizabeth Henry—25; Polthep Sakpanich—27

Figure 27. An area of a filled cavity in ruby exhibiting a lower luster than the ruby and surrounded by a granular texture, caused by a reaction layer of synthetic overgrowth. Reflected light (left) and brightfield illumination (right); field of view 8.2 mm.

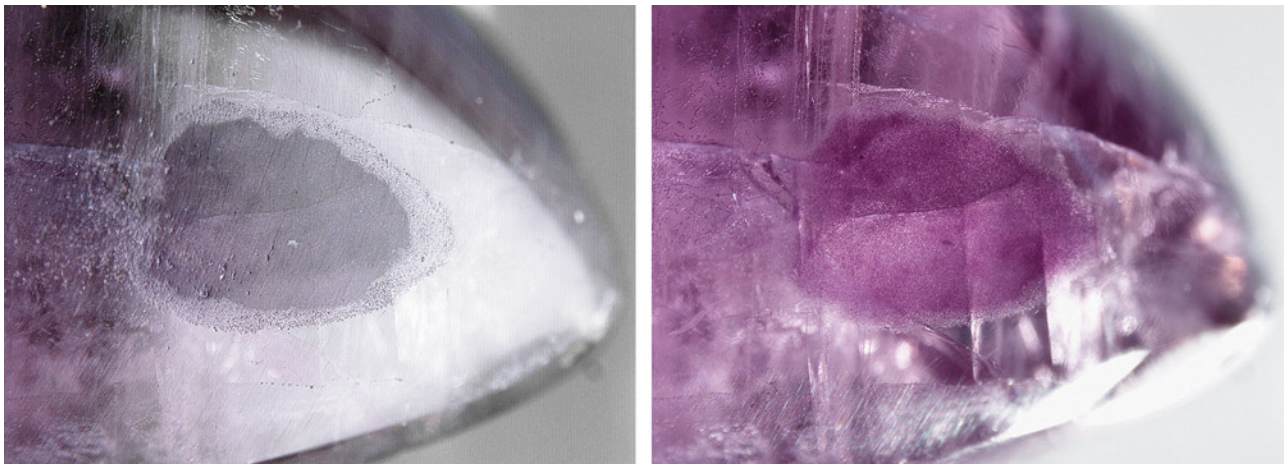

Protect Your Customers and Your Business.

The most effective defense against diamond deception.

In under two seconds, the easy-to-use **GIA iD100®** can identify a diamond as natural with 100% accuracy.

Speed, precision, and convenience – the ideal tool to add to your protocol.

Learn More

GIA.edu/iD100

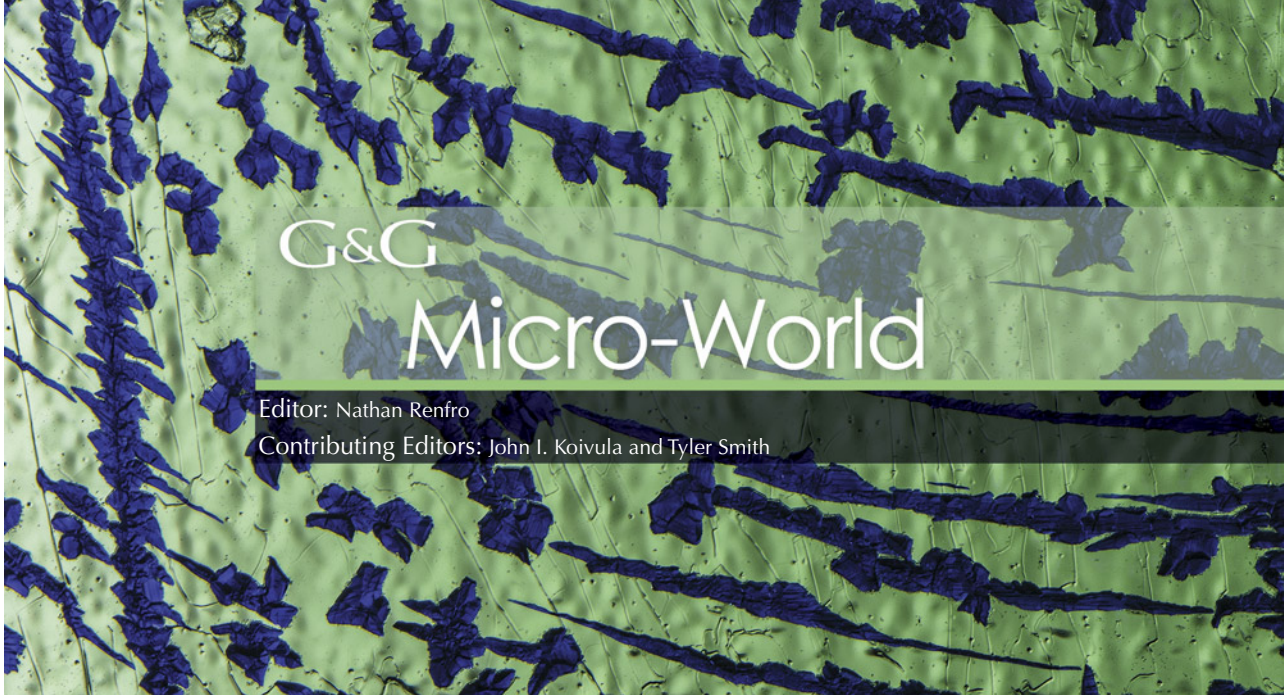

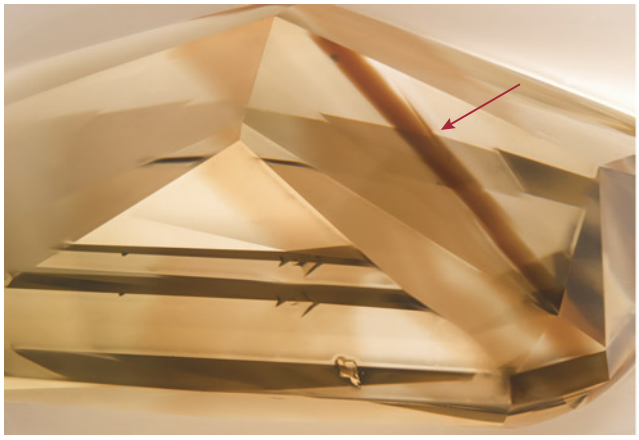

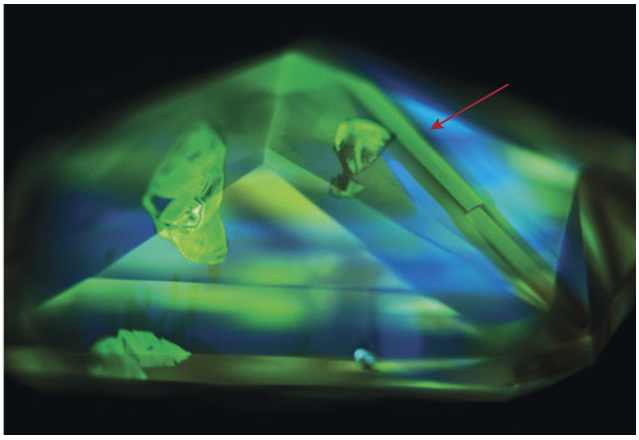

Figure 1. Left: The strong linear brown zoning (arrow) of the 2.21 ct Fancy Dark yellow-brown diamond was best viewed under diffused light, also revealing the stone's patchy bodycolor. Photomicrograph by Britni LeCroy and Jeffrey Hernandez; field of view 7.19 mm. Right: The associated DiamondView image shows a vibrant mixture of fluorescence patterns, with the brown zone displaying dull yellow-green fluorescence while retaining its linear structure (arrow). Image by Jeffrey Hernandez.

Brown Zoning in Diamond

The author recently encountered a 2.21 ct Fancy Dark yellow-brown rectangular diamond with unusually strong eye-visible linear brown zoning (figure 1, left). This stone provided a unique opportunity to document crystallographic defects coloring a diamond with various instrumentation and tools in separate lighting conditions. The diamond's ultraviolet/visible/near-infrared absorption spectra revealed a 480 nm absorption band, a defect gemologists know little about due to the complex mantle environment these diamonds come from (C.M. Breeding et al., "Naturally colored yellow and orange gem diamonds: The nitrogen factor," Summer 2020 *G&G*, pp. 194–219). Prior research has shown that the 480 nm band defect coincides with dull yellow-green fluorescence (M.Y. Lai et al., "Spectroscopic characterization of diamonds colored by the 480 nm absorption band," *Diamond and Related Materials*, Vol. 142, 2024, article no. 110825). Deep UV fluorescence imaging of this diamond showed several regions with dull yellow-green fluorescence corresponding with brown zoning. This defect was present not only in the brown band of

About the banner: The surface of this flame-fusion sapphire is decorated with unknown cobalt-colored dendrites. Photomicrograph by Nathan Renfro; field of view 12.82 mm.

Gems & Gemology, Vol. 60, No. 3, pp. 382–391.

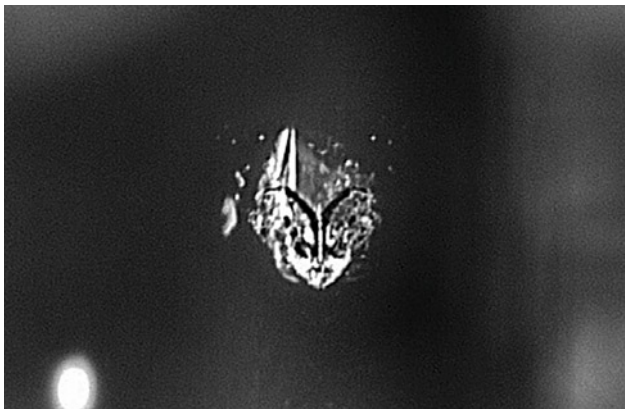

Figure 2. The mirroring of a feather inclusion in diamond, viewed through the step-cut facets of the pavilion, creates an apparent theater mask in a close-up view captured in monochrome. Photomicrograph by Kaivan Shah; field of view 3.00 mm.

color but also in the other areas of the stone that showed a dull yellow-green fluorescence (figure 1, right).

Figure 1 (right) also shows regions with blue fluorescence that are associated with the N3 defect (three substitutional nitrogen atoms adjacent to a vacancy). The bright green blocky color zones are associated with a concentrated H3 defect (two nitrogen atoms adjacent to a vacancy). Although the DiamondView image unveiled previously hidden defects, inert areas between the growth zones were not so easily explained. These images juxtaposed with one another provide a visually intriguing example of how defects in diamond can influence color.

Jeffrey Hernandez
GIA, Carlsbad

Mask Inhabiting a Natural Diamond

While diamond graders spend a good deal of time looking at inclusions, rarely do we see a clarity feature staring back at us, such as the example in figure 2. The 0.90 ct F-color type Ia natural diamond with VS_2 clarity contained a feather that reached the surface of the table. When viewed through the pavilion, the mirror image caused by the faceting created an effect resembling a distinctive theater mask. This striking inclusion showcases the wide variety of inclusions that are possible in diamond and leaves a memorable, almost haunting impression.

Kaivan Shah
GIA, Mumbai

Sally Eaton-Magaña
GIA, Carlsbad

Kaleidoscope of Butterflies and Tiny Fish in Diamonds

The author recently encountered two natural diamonds with interesting feather inclusions: a 1.55 ct round with G-color and I_1 clarity and a 0.30 ct round with F-color and VS_2 clarity.

The more heavily included diamond appeared to contain a swarm of butterflies. A feather breaking the pavilion surface was observed face-up through the crown, with mirror and prism images creating the appearance of a white butterfly (figure 3). Since the inclusion was visible through the upper half and bezel facets of the diamond, five prism images were formed, befitting the word "kaleidoscope" occasionally used to describe a group of butterflies.

The other diamond housed a small feather in the table with a mirror reflection (figure 4). The reflection along with

Figure 3. Mirrored and reflected fissures in a diamond take the form of a kaleidoscope of butterflies. Photomicrograph by Yash Jhaveri and Bijal Shah; field of view 4.20 mm.

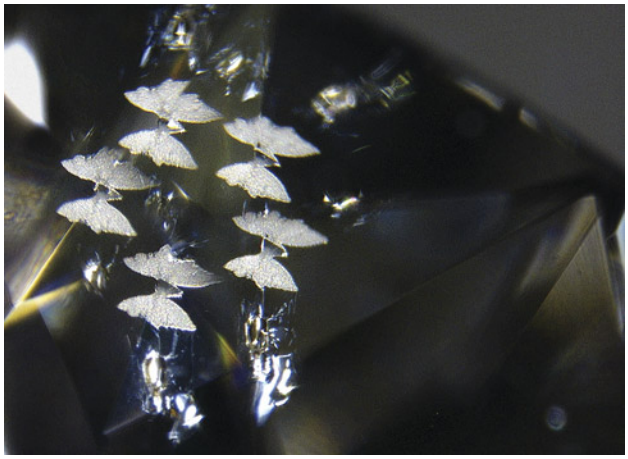

Figure 4. A mirrored feather in diamond resembles a small fish swimming through sunlit waters. The image was captured in monochrome. Photomicrograph by Russel Carvalho; field of view ~8 mm.

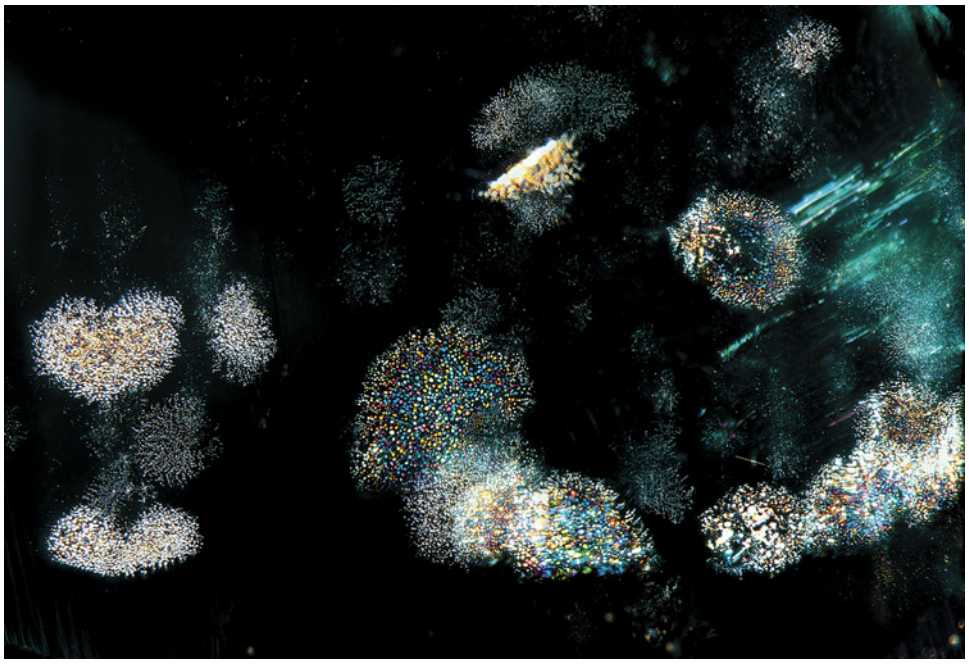

Figure 5. Interference thin films in Russian emerald resembling a sky filled with fireworks. Photomicrograph by Ungkhana Atikarnsakul; field of view 3.60 mm.

the actual inclusion resembled a tiny fish swimming under the warm rays of the sun. Feathers are commonly seen in diamonds, but such unique and precise shapes of fish and butterflies are uncommon.

Tejas Jhaveri
GIA, Mumbai

Fireworks Display in Russian Emerald

Russian emeralds can harbor unique inclusion scenes. Iridescent thin films that lie parallel to the basal pinacoid are considered conclusive evidence of this geographic origin. Microscopic observation of a 1.21 ct faceted emerald revealed multiple planes of interference thin films aligned parallel to the table (figure 5). Viewed under fiber-optic lighting, the scene was reminiscent of fireworks lighting up the night sky. Internal graining, fluid fingerprints, needles, and particles were also found in the stone, combining to form a visually interesting pattern.

Ungkhana Atikarnsakul
GIA, Bangkok

Unusual Hematite Lattice Pattern in Plagioclase Feldspar

Lattice patterns formed by hematite and magnetite platelets where the elongated blades intersect at an angle of 60° are well documented in orthoclase feldspars (S. Jin et al., "Iron oxide inclusions and exsolution textures of rainbow lattice sunstone," *European Journal of Mineralogy*, Vol. 34, 2022, pp. 183–200; J. Liu et al., "Revisiting rainbow lattice sunstone from the Harts Range, Australia," *Journal of Gemmology*, Vol. 36, No. 1, 2018, pp. 44–52). However, the author recently discovered a sample of plagioclase feldspar with similar hematite inclusions where the angle of intersection was closer to 90°. Thin-film interference caused the attractive rainbow colors of the hematite on display in this sunstone cabochon (figure 6). Chemical analysis using laser ablation–inductively coupled plasma–mass spectrometry revealed an oligoclase composition between $Ab_{82.5}An_{16.6}Or_{0.9}$ and $Ab_{83.6}An_{15.5}Or_{0.9}$. The cause of this unusual structure is unknown, as this type of inclusion would typically form as randomly oriented hexagonal platelets.

Rosie Young
Gemmological Certification Services, London

Figure 6. Elongated hematite platelets form a lattice pattern in a sunstone cabochon. Photomicrograph by Rosie Young; field of view 4.97 mm.

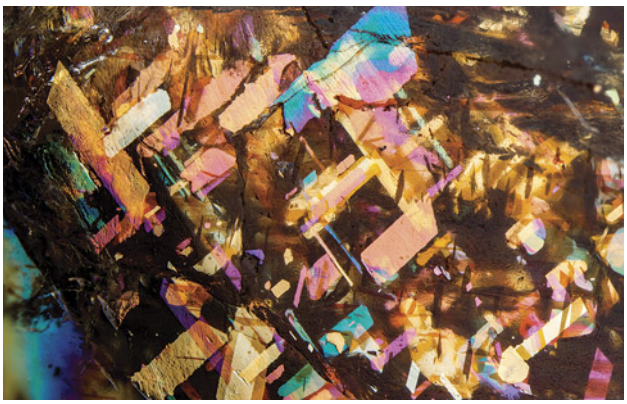

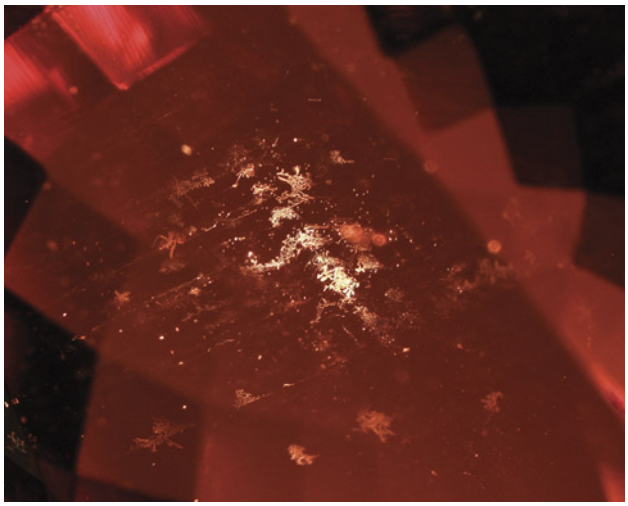

Figure 7. Skeletal formations of natural metallic reflective thin films in an 18.67 ct pinkish orange morganite. Photomicrograph by Taku Okada; field of view 8.10 mm.

Interesting Metallic Platelets in Morganite

Reflective thin films were observed in an 18.67 ct pinkish orange morganite (figure 7). Since morganite's subtle color is caused by traces of manganese, these films may have been natural metallic manganese, similar to the skeletal formations of natural metallic copper in Paraíba tourmaline (Summer 2023 *G&G* Micro-World, p. 229). Like many gems found in pegmatites (such as aquamarine, another beryl variety), morganite can form large crystals and usually does not contain eye-visible inclusions. Pegmatite is an igneous rock formed deep in the earth's crust from the fluids that remain after solidified crystals break away from hot granitic magma as it gradually cools. The fluids have low viscosity and contain many elements that are important components for gems. The elements can move quickly in the fluids, so pegmatites contain many large and clean gems.

At first glance, this morganite appeared to be eye clean. However, when the planar thin films aligned between the microscope objective lens and the fiber-optic light satisfied a total reflection condition, the skeletal platelets appeared. When examining gemstones through a microscope, gemologists are often surprised to discover unexpected inclusions.

Taku Okada
GIA, Tokyo

Written Characters in Black Opal

Opal sometimes contains play-of-color patches with unique and attractive patterns, such as an impressive 8.13 ct black opal measuring 15.93 × 10.88 × 7.52 mm recently examined by the author. Based on its gemological properties, microscopic observations, and strong phosphorescence to long-wave ultraviolet light, the stone was natural opal with no signs of assembled features.

Interestingly, blade-like play-of-color patches with a striking brushstroke pattern were present within the common (nonphenomenal) opal area on the back side (figure 8). Some of the patches intersected at nearly 90° and resembled Chinese characters. This pattern is rarely seen in precious opal and is known as a "Chinese writing pattern" in the trade. On the other side of the stone, the play-of-color formed another unique pattern, this one resembling the Latin letter "A" (figure 9). Brightfield il-

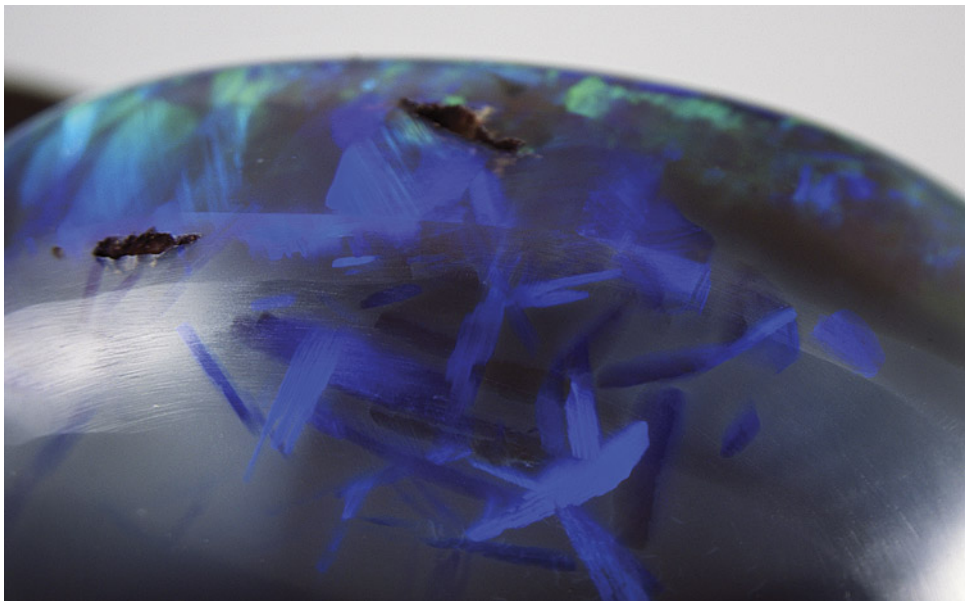

Figure 8. A pattern resembling Chinese characters in an 8.13 ct black opal. Note that blade-like play-of-color patches exist within common opal. Photomicrograph by Makoto Miura; field of view 12.06 mm.

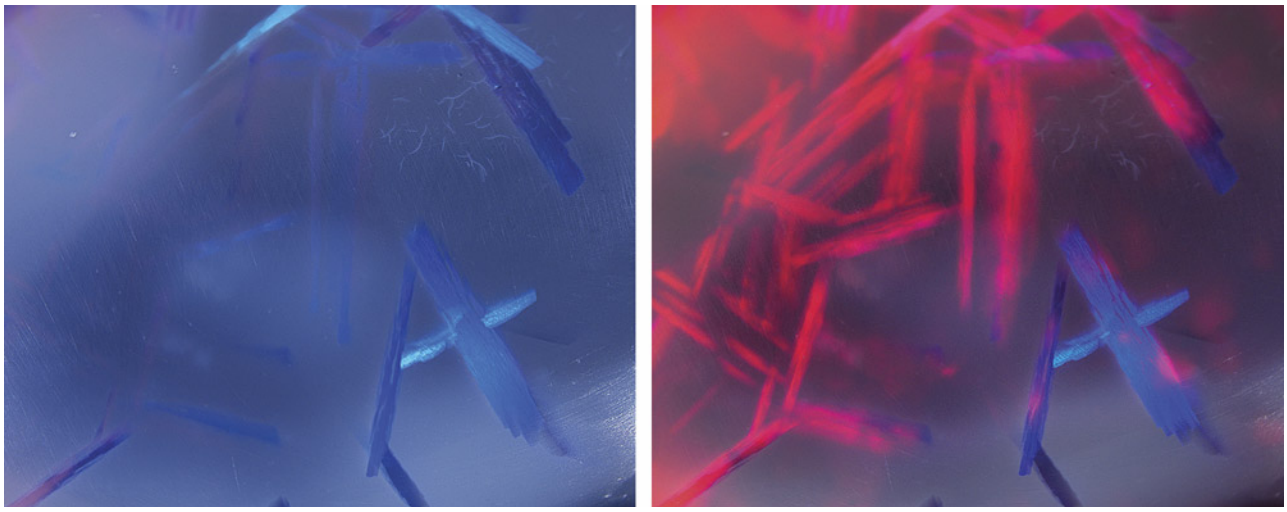

Figure 9. A pattern resembling the letter "A" was observed on the other side of the black opal. The left image was taken using fiber-optic illumination with a white diffuser, while the right image used a combination of fiber-optic and brightfield illumination. Photomicrographs by Makoto Miura; field of view 2.96 mm.

lumination revealed that these blade-like play-of-color patches were also contained within the common opal area (figure 9, right). The combination of reflected light with fiber-optic illumination and brightfield illumination caused the patterns to look like a natural inscription within precious opal. It is interesting to consider how play-of-color patches and common opal were both created from hydrothermal fluids.

Makoto Miura
GIA, Tokyo

"Frozen River" on the Surface of an *Atrina* Pearl

The author recently examined a group of dark-colored pearls reportedly produced by an *Atrina*-species mollusk from the Pinnidae family (known as "pen pearls"). The majority of pen pearls have nacreous surfaces and display characteristic linear-looking nacre under high magnification (N. Sturman et al., "Observations on pearls reportedly from the Pinnidae family (pen pearls)," Fall 2014 *G&G*, pp. 202–215). Some of the pearls examined in the group exhibited a near-colorless translucent frosted surface on certain areas. This structure is seldom observed on nacreous pearls from other mollusk species. Raman spectroscopy using 514 nm laser excitation revealed that the areas were composed of aragonite. A 0.62 ct dark brown pearl displayed the most interesting surface, composed of layered aragonite crystals in various sizes, resembling ice on a frozen river (figure 10).

Kwanreun Lawanwong
GIA, Bangkok

Anatase in Brazilian Quartz

Anatase crystals in quartz can be a fascinating sight. Their dipyramidal or acute pyramidal crystallographic habit and adamantine shine often create interference colors due to the inclusion's high refractive index compared to the host crystal. One notable example was recently observed in a 27.21 ct Brazilian quartz cabochon (figure 11). The blue interference color visible from every angle was remarkable, since isolated anatase crystals typically have a black, brown, reddish brown, or brownish yellow color. Anatase (along with

Figure 10. A "frozen river" caused by an overlay of aragonite crystals on the surface of a nacreous pearl from an Atrina *mollusk. Photomicrograph by Kwanreun Lawanwong; field of view 1.80 mm.*

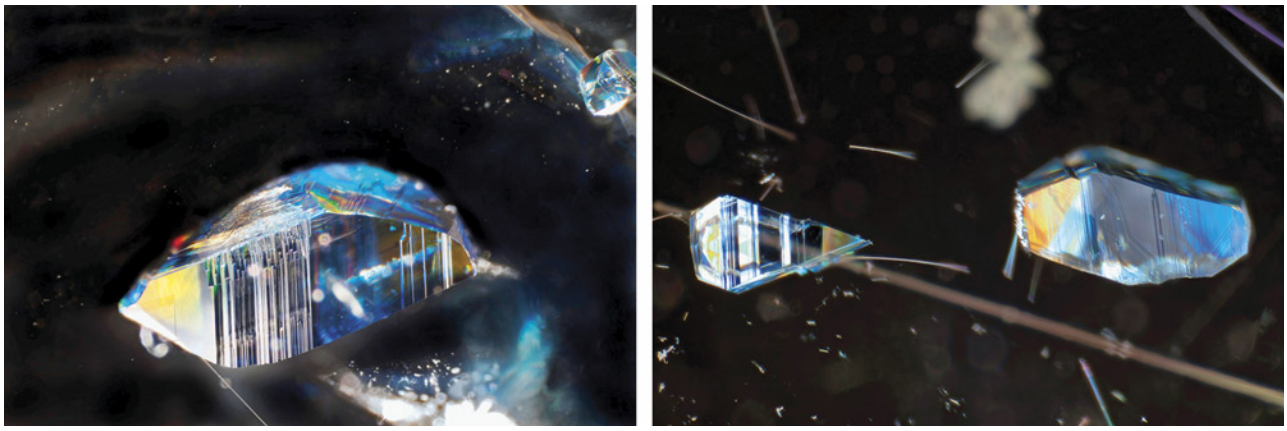

Figure 11. Left: This anatase crystal with a well-formed tetragonal habit in a Brazilian quartz shows adamantine luster and diffraction colors due to its high refractive index. Right: The crystals of anatase, one of the polymorphic forms of titanium dioxide, are associated with rutile needles shown in darkfield and oblique fiber-optic illumination. Photomicrographs by Liviano Soprani; field of view 1.8 mm.

rutile, brookite, akaogiite, and riesite) is one of the five polymorphic forms of titanium dioxide (TiO_2) found in nature and is almost always associated with rutile as an inclusion in quartz. However, rutile forms at high pressures and temperatures and is often found in igneous and metamorphic rocks, while anatase forms in hydrothermal phases at pressures and temperatures much lower than rutile (D.A.H. Hanaor and C.S. Sorrell, "Review of the anatase to rutile phase transformation," *Journal of Materials Science*, Vol. 46, 2011, pp. 855–874). The disordered orientation of the acicular rutile crystals and the relative distance from the euhedral anatase crystals suggest the protogenetic formation of rutile and the formation of anatase in a subsequent hydrothermal phase.

Liviano Soprani
Ravenna, Italy

Hedenbergite in Quartz

Quartz is known to host a wide variety of inclusions. In a large group of polished quartz samples recently examined, the authors observed groups of dark crystal inclusions that took the shape of a sea urchin. In some samples where the dark crystal reached the surface, the cross section of the crystal habit was rhomboid, indicating they were monoclinic. Under magnification, the inclusions were transparent to translucent and dark green to brownish green (figure 12). Raman spectra identified the inclusions as hedenbergite, confirmed by comparison with the RRUFF database. Hedenbergite, $CaFe^{2+}Si_2O_6$, is a member of the pyroxene group. Based on previous work (Winter 2023 *G&G* Micro-World, pp. 503–504), we realized that the material known in the trade as "urchin quartz" might contain inclusions other than hollandite.

Figure 12. These dark green acicular aggregates in quartz were identified as hedenbergite. Photomicrographs by Liyan He; fields of view 9.20 mm (left) and 8.30 mm (right).

Figure 13. A sphalerite crystal in quartz. Photomicrograph by Liyan He; field of view 11.40 mm.

Figure 14. Weighing between 3.07 and 10.53 ct, these four small transparent colorless spheres of rock crystal quartz each hosted an opaque black inclusion (one sphere contained two inclusions). Photo by Annie Haynes.

In the samples that contained hedenbergite, we also identified a translucent yellow to light brown inclusion in these samples (figure 13). The crystal was identified by Raman spectroscopy as sphalerite, consistent with the RRUFF database.

Liyan He
Guangdong Gemstones & Precious Metals Testing Center
Guangzhou, China

Wingtak Lui
Min De Minerals & Gem Research Co., Ltd.
Nanjing, China

"Rose" Quartz

The authors recently examined four small marble-sized colorless polished spheres of rock crystal quartz. Each sphere hosted a tiny, opaque black inclusion (figure 14), a feature that was the subject of this entry. The spheres weighed between 3.07 and 10.53 ct, with corresponding measurements ranging from 7.61 to 11.49 mm. They were supplied by Luciana Barbosa of the Gemological Center in Asheville, North Carolina, and were reported to have come from Zambia.

As shown in figure 15, microscopic observation of the four polished spheres revealed that the opaque black inclu-

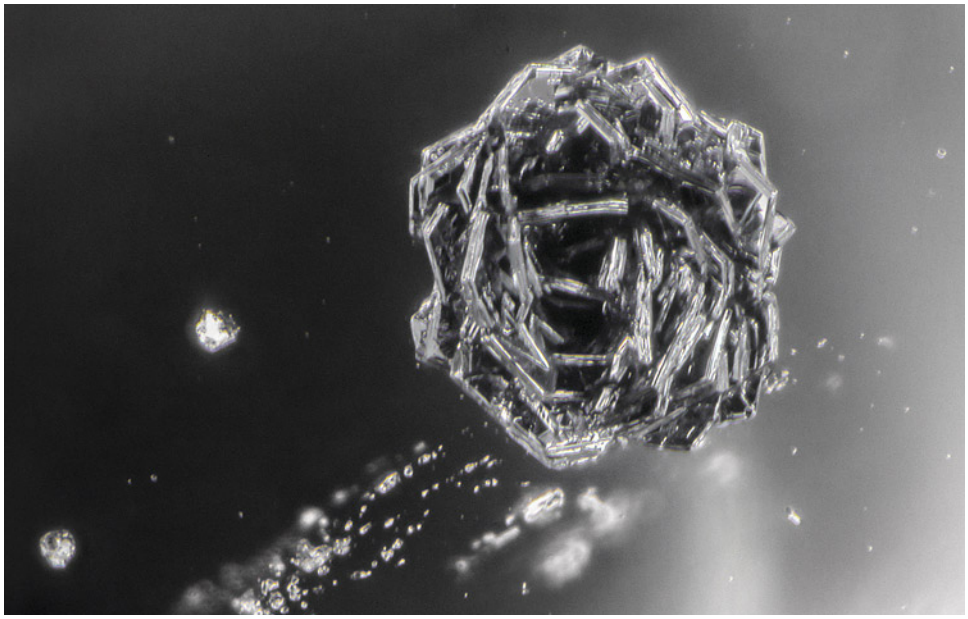

Figure 15. This opaque black hematite inclusion in one of the quartz spheres is composed of numerous platy inclusions arranged in the shape of a rose. Photomicrograph by Nathan Renfro; field of view 2.40 mm.

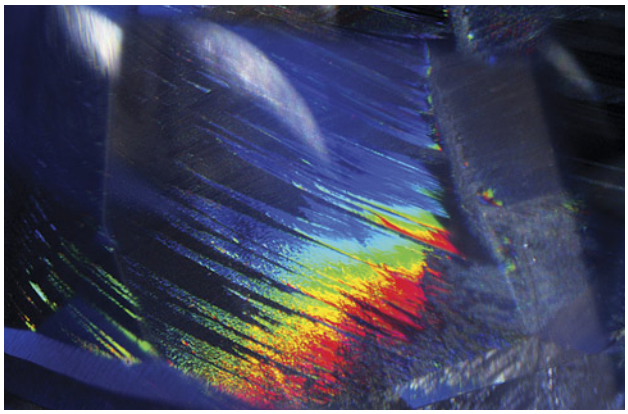

Figure 16. Iridescent partially healed fissure observed in a 4.13 ct blue sapphire. Photomicrograph by Kanako Otsuka; field of view 2.12 mm.

sions were actually composed of numerous platy euhedral crystals arranged in the shape of a rose. These inclusions were identified by Raman analysis as hematite. The roses' positioning along growth planes in the spheres shows that the hematite inclusions are syngenetic with their rock crystal quartz hosts.

John I. Koivula, Nathan Renfro, and Maxwell Hain
GIA, Carlsbad

Rainbow-Colored Partially Healed Fissure in Blue Sapphire

Thin-film interference caused by inclusions occasionally produces attractive scenes. In a 4.13 ct untreated blue sapphire from Sri Lanka, a partially healed fissure displayed vibrant iridescent colors due to this phenomenon under fiber-optic illumination (figure 16).

Healed fissures, known as fingerprints or feathers in gemology, are created by the natural healing process of surface-reaching fractures in the host gem material. Generally, when fluid involved in the healing process is trapped, fluid-filled inclusions such as negative crystals or thin internal fissures are formed (e.g., E. Roedder, "Ancient fluids in crystals," *Scientific American*, Vol. 207, No. 4, 1962, pp. 38–47). When the trapped fluid is thin enough, the difference in refractive index between the fluid and the host material causes thin-film interference and may result in vibrant colors.

Healed fissures are common in various gemstones and sometimes display iridescence (e.g., Spring 2021 *G&G* Micro-World, p. 68; Summer 2023 *G&G* Micro-World, p. 227). In this sapphire, the combination of a brushstroke-like texture and rainbow colors in a gradation from red to indigo produces a spectacular scene.

Kanako Otsuka
GIA, Tokyo

Rare Musgravite Crystal in Green Sapphire

A 6.59 ct faceted green stone, identified by standard gemological testing as sapphire, contained various inclusions such as needles, fingerprints, and a cluster of colorless and green crystals. The colorless crystals were identified as feldspar, and a transparent green prism-like crystal breaking the surface of the sapphire (figure 17) was confirmed as musgravite (magnesiotaaffeite) by Raman spectroscopy.

Musgravite, $(MgFe,Zn)_2BeAl_6O_{12}$, crystallizes in the trigonal system and is part of the taaffeite group. Musgravite

Figure 17. Green musgravite crystals observed in a faceted green sapphire. Darkfield and fiber-optic illumination. Photomicrograph by Titapa Tanawansombat; field of view 1.8 mm.

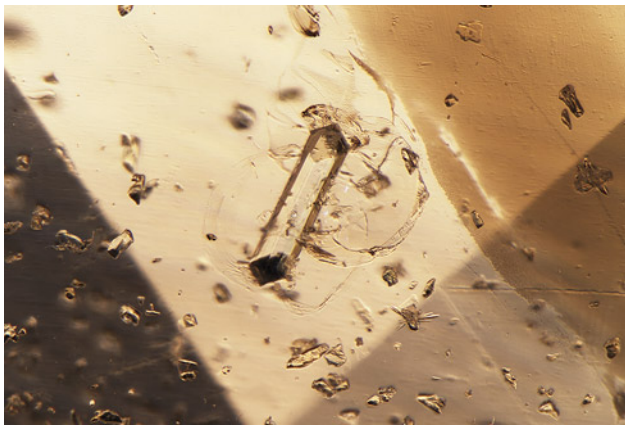

Figure 18. Prismatic diopside among a sea of diopside and danburite crystals in a rare orange sodalite. Photomicrograph by Joseph Hukins; field of view 1.56 mm.

Figure 19. The 2.83 ct orange sodalite exhibited short-lived tenebrescence after brief exposure to long-wave UV. Photos by Towfiq Ahmed.

is rarely found as an inclusion in corundum, making these crystals a unique observation for gemologists.

Titapa Tanawansombat
GIA, Bangkok

Diopside and Danburite in Rare Orange Sodalite

A rare orange sodalite was recently examined by the authors. The 2.83 ct stone, identified by Raman spectroscopy along with standard gemological testing, revealed a variety of unique inclusions upon microscopic examination.

A field of transparent crystals identified by Raman was found to consist of mostly diopside with a few intermixed danburites, which can be seen surrounding a larger euhedral, prismatic diopside in figure 18. Transparent facet-grade orange sodalite is uncommon, both for its color and high diaphaneity, as the complex tectosilicate sodalite is typically blue or colorless. The stone exhibited a short-lived reversible photochromism known as tenebrescence, changing from orange to pink after brief exposure to long-wave ultraviolet light and reverting to its stable orange color in a matter of minutes after removal of the long-wave UV (figure 19). Similar material reportedly from Afghanistan has been previously documented (M. Krzemnicki and C. Rochd, "Orange sodalite from Badakhshan, Afghanistan," *Journal of Gemmology*, Vol. 39, No. 1, 2024, pp. 20–22).

To the authors' knowledge, this is the first documented instance of diopside and danburite recorded as

Figure 20. This 46.32 ct color-change magnesioaxinite crystal from Tanzania contained interesting negative crystals. Photos by Rhonda Wilson; courtesy of Bill Vance.

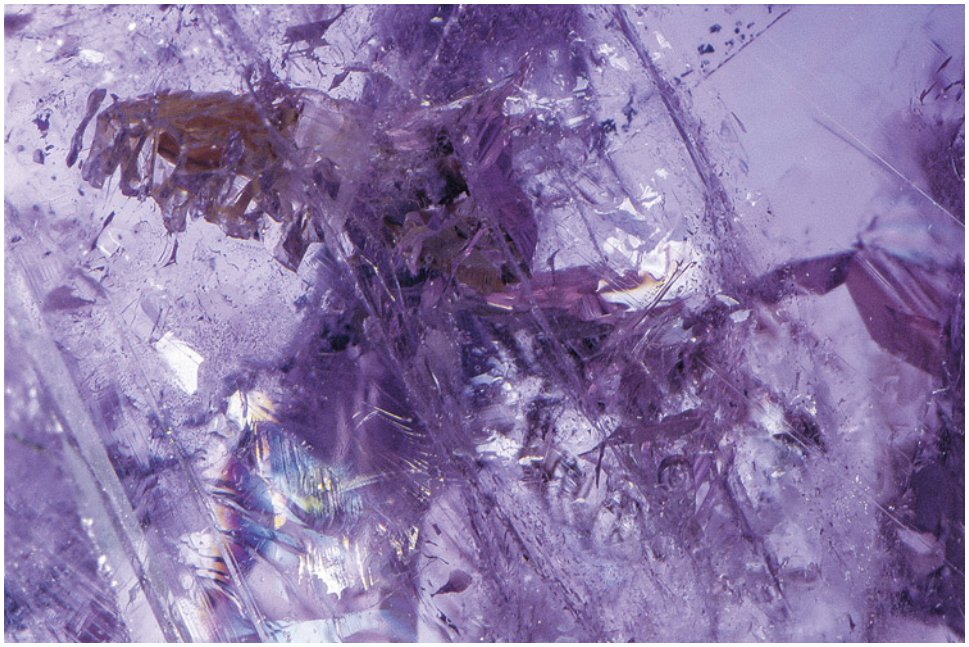

Figure 21. The irregular negative crystals in the magnesioaxinite crystal are filled with either epigenetic brown residue or liquid and gas components. Photomicrograph by Nathan Renfro; field of view 7.19 mm. Courtesy of Bill Vance.

inclusions together in sodalite and the second instance of prismatic transparent diopside (F. Blumentritt et al., "Properties and coloration of orange hackmanite from Afghanistan," *Journal of Gemmology*, Vol. 39, No. 2, 2024, pp. 160–168).

Joseph Hukins and Tyler Smith
GIA, New York

Quarterly Crystal: Magnesioaxinite

Gem-quality magnesioaxinite was first reported in 1975 (A. Jobbins et al., "Magnesioaxinite, A new mineral found as a blue gemstone from Tanzania," *Journal of Gemmology*, Vol. 14, No. 8, 1975, pp. 368–375). That report also noted a blue-to-violet color change. Magnesioaxinite is a member of the axinite group with the chemical formula $Ca_2MgAl_2BSi_4O_{15}OH$.

The authors recently examined a beautiful twinned 46.32 ct crystal with a blade-like morphology and an interesting inclusion scene (figure 20). A relatively large complex negative crystal containing a light brown epigenetic residue was observed, along with another negative crystal filled with a liquid and a mobile gas bubble (figure 21). Numerous colorful iridescent cracks were scattered throughout the crystal as well.

Magnesioaxinite is a desirable collector stone but quite scarce in the gem trade. It is also sometimes sold under the trade name "Vanceite" after gem dealer Bill Vance, who has been fascinated by this rare material since 2005, when he first encountered it mixed in a parcel of tanzanite. In addition to the color-change variety examined here, magnesioaxinate can also be pink or orange or zoned as a mixture of these colors.

Nathan Renfro and John I. Koivula

Editor: Evan M. Smith

The Extraordinary Backstory of Natural Diamonds: A Diamond Is (and Has Been) Forever

Evan M. Smith and James E. Shigley

Diamonds have a long history as a premier gemstone—a natural consequence of their beauty, rarity, and superlative physical properties such as extreme hardness. Diamonds that are mined for use as gemstones have an innate appeal and air of luxury. In ancient Rome, Pliny the Elder called diamond "the most valuable, not only of precious stones, but of all things in this world." The utility of diamond as a tool for cutting is also prized. It has even found niches in modern high-tech applications. However, our love affair with this transparent crystalline form of carbon is virtually blind to its geological backstory, arguably one of its most compelling facets.

In the decades since GIA introduced the Four *C*s quality-grading concept for polished diamonds in the 1940s, scientists' understanding of where, when, and how diamonds form has changed radically. They form deeper underground than virtually anything else you can touch. They are more ancient than initially thought, with some dating back to 3.5–3.3 billion years ago (three-quarters of the earth's age). Diamonds preserve evidence over both space and time of this ancient geologic origin in the form of pristine inclusions of minerals and geological fluids. Processes that contribute to diamond growth involve the movement of rocks and fluids inside the earth at a scale of hundreds of kilometers, a testament to the fact that our planet is dynamic and evolving rather than a static ball of rock. Much of this activity is attributable to plate tectonics and subduction, which is the slow sinking of oceanic plates into the mantle.

Editor's note: Questions or topics of interest should be directed to Evan Smith (evan.smith@gia.edu).

Gems & Gemology, Vol. 60, No. 3, pp. 392–399.

In a sense, geologists are beginning to unravel a fascinating new identity for diamonds, giving Pliny even more reason to have admired them. They have evolved from a curiosity to something of great scientific value and excitement. However, public awareness of this development has lagged. Here we review the story of diamond formation alongside other aspects of natural diamonds and their extraction from the earth, showcasing them in a new light.

Diamonds Are Deep: Carbon in the Mantle

At the earth's surface, graphite is the stable crystalline form of carbon, with a density of 2.26 g/cm^3. Diamond is a much more compact form of carbon, with a density of 3.52 g/cm^3, 56% higher than the density of graphite. Great confining pressure is required to stabilize the denser configuration of carbon atoms and crystallize diamond, which is why it forms deep in the mantle. Once formed, diamond remains in that form of carbon under all conditions that normally exist at the earth's surface.

The physical and chemical conditions of diamond formation have largely been constrained by studies of their mineral inclusions. Most diamonds crystallize within the base of old and thick parts of continents, called *cratons*, at depths of 150–200 km and temperatures of 900°–1300°C (Stachel and Harris, 2008). These are known as *cratonic* or *lithospheric* diamonds. Some rarer diamonds form at depths as deep as 200–800 km, below the lithosphere, and are called *sublithospheric* or *superdeep* diamonds (Shirey et al., 2024). Some unusual kinds of mineral inclusions are contained in sublithospheric diamonds, and these serve as the basis to constrain their depth of formation. Figure 1 illustrates just how vast these depths are. Virtually all the rocks and minerals observable at the earth's surface, including most gemstones, form at relatively shallow depths within the continental crust. In contrast, diamonds are easily the most

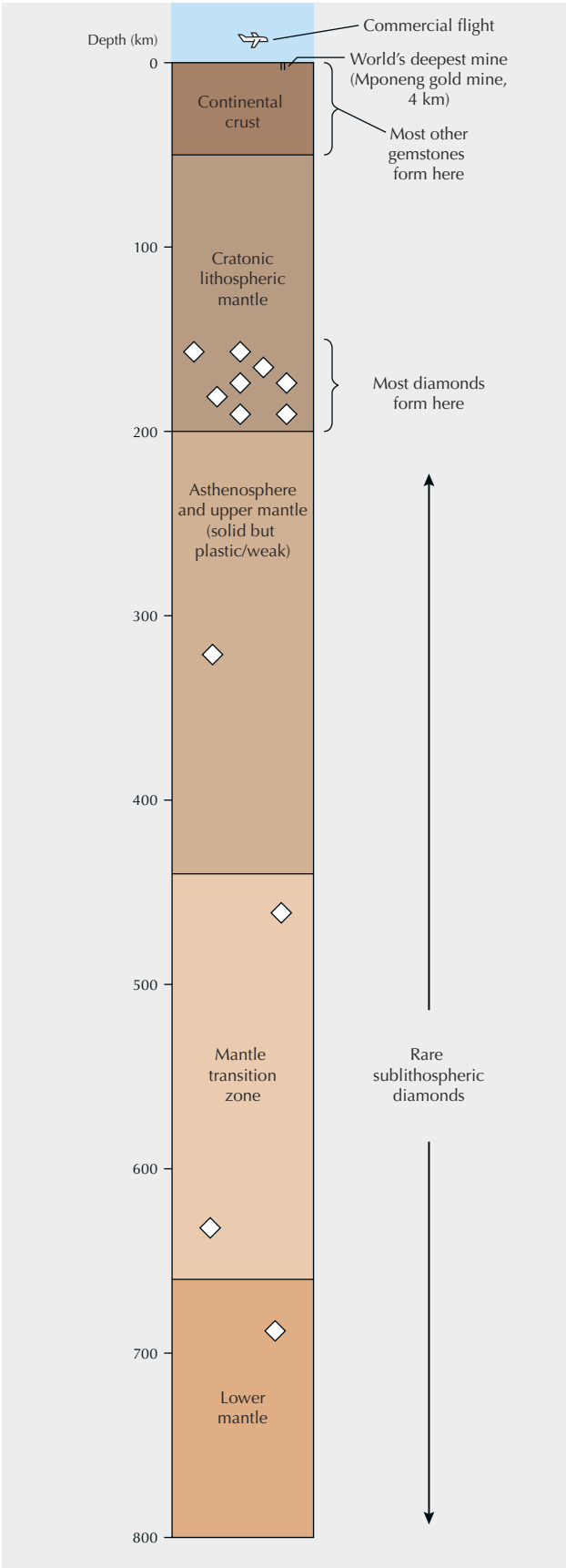

deeply derived things humans can touch. Much like meteorites from space, they are "alien" materials from deep underground and were only brought to the earth's surface by an unusual set of geologic circumstances.

Although diamonds originate very deep in the earth, when carried up by kimberlites or related volcanic eruptions, they can endure the upward journey because it is quick and survive indefinitely at the earth's surface because of their hardness, strength, and chemical robustness. Inclusions trapped inside diamonds can survive as well, being protected and shielded by their host. This makes inclusions in diamonds the most deeply derived well-preserved samples of the mantle. These inclusions can be not only minerals but also fluids or gases trapped at high pressures.

The range of possible residual pressures retained by some inclusions is nicely demonstrated by rare inclusions of nitrogen in either liquid or solid form, the latter having a pressure of 10.9 Gpa (Smith et al., 2013; Navon et al., 2017). For comparison, 1 gigapascal is about 10,000 times atmospheric pressure at sea level or about 10 times the pressure at the deepest part of the Mariana Trench in the Pacific Ocean.

Possibly the highest recorded pressure inside an inclusion (for a diamond above the earth's surface) is that of a phase called *ice-VII*, with a reported pressure of 24 GPa, equivalent to the ambient pressure at the bottom of the mantle transition zone (Tschauner et al., 2018). Inclusions from both the lithospheric and sublithospheric mantle are invaluable samples for scientific study because they are the only direct source of mantle information. They speak not only to diamond formation but also to the broader structure, composition, and processes of the mantle.

A more recent discovery based on inclusions has shown that some of the largest and highest-quality gem diamonds are derived from the sublithospheric mantle. Specifically, type IIb (boron-bearing) and so-called CLIPPIR (Cullinan-like, large, inclusion-poor, pure, irregular, and resorbed) diamonds have been found to contain high-pressure mineral assemblages indicating formation at depths between 360 and 800 km (Smith et al., 2016, 2017, 2018). Famous gem diamonds within these "superdeep" categories include the Hope, the Koh-i-Noor, the Lesedi La Rona, and the Cullinan. The faceted gems cut from the 3,106 ct Cullinan have been a cherished centerpiece of the British Crown Jewels

Figure 1. This cross section through ancient thickened continental lithosphere and underlying mantle shows the two major depth intervals of diamond formation. The majority of mined diamonds originate from the lithospheric mantle. Some rare diamonds originate from great depths in the sublithospheric mantle. Within both groups, diamond formation is likely to occur across a range of depths within the mantle. Note that the depth is drawn to scale to illustrate relative depths accurately.

for more than a century, based on their exquisite natural beauty and rarity. Now these diamonds have returned to the limelight, including coverage from the BBC (Gorvett, 2022), for their extreme depth of origin.

Diamonds Are Ancient

When De Beers introduced the slogan "A diamond is forever" in 1947, they were referring to diamond as a symbol of everlasting love. But four decades later, when the first measurements of diamond ages showed some to be more than three billion years old (Richardson et al., 1984), the romantic tagline became even more fitting. Prior to these measurements, there was considerable debate over whether the diamonds brought up in kimberlite magmas were phenocrysts (crystals grown directly from the magma) or xenocrysts (foreign, preexisting crystals simply picked up by the magma). The latter proved true—the three-billion-year-old diamonds must have grown and lain dormant in the mantle for billions of years before being swept to the surface in the Cretaceous-age (145–66 million years, or Ma) Kimberley and Finsch kimberlites.

Diamond growth may occur somewhat quickly compared to its age, building up a crystal layer by layer over thousands or perhaps millions of years. The subsequent period of mantle residence at conditions of high pressure and temperature can permit changes in the diamond morphology, internal structure, and atomic-scale defects. A well-known change affects the configuration of nitrogen atoms, the most abundant impurity in natural diamonds. Nitrogen atoms migrate from their isolated initial configurations to form pairs, and slowly the pairs reconfigure into groups of four atoms plus a vacancy. Taken collectively, these changes create the ancient geologic signature of natural diamonds, which cannot be created during very brief laboratory growth.

As shown in figure 2, diamonds have formed over a wide range of the earth's geologic history. The oldest dated examples are diamonds with an age of 3.5–3.3 Ga (billion years) from the Diavik and Ekati mines in northern Canada. For perspective, the age of the earth is 4.54 Ga. Many diamonds are ancient and predate the so-called Cambrian Explosion at 541 Ma, when a prolific increase in the complexity and abundance of life appears in the fossil record, one of the most significant time stamps in geology. However, not all diamonds fall within the Precambrian span of distant geologic time. Some fairly young diamond ages around 90 Ma have been measured at Jagersfontein and Koffiefontein in South Africa. Most deposits have multiple diamond populations that can vary in age. Jwaneng, Letlhakane, and Orapa in Botswana each contain six or more dated episodes of diamond formation (Smit et al., 2022).

It is also worth noting that the majority of fibrous diamonds, a non-gem diamond variety with abundant microinclusions that give them a translucent or opaque appearance, are understood to be close in age to their kimberlite hosts and therefore relatively young. It is even possible that diamonds are forming right now and may be carried to the surface by some future kimberlite millions of years from now. A recent review of diamond dating and ages is given by Smit et al. (2022).

Figure 2. Earth's geologic timescale, showing the formation times of select groups of diamonds. Note that many localities actually have multiple populations of diamonds that can vary in age. Unlike many geologic timelines that are distorted to fit information and labels, this one is linear and drawn to scale, from 4.54 billion years ago (Ga) to the present day. Timeline modified from Smit and Shirey (2019).

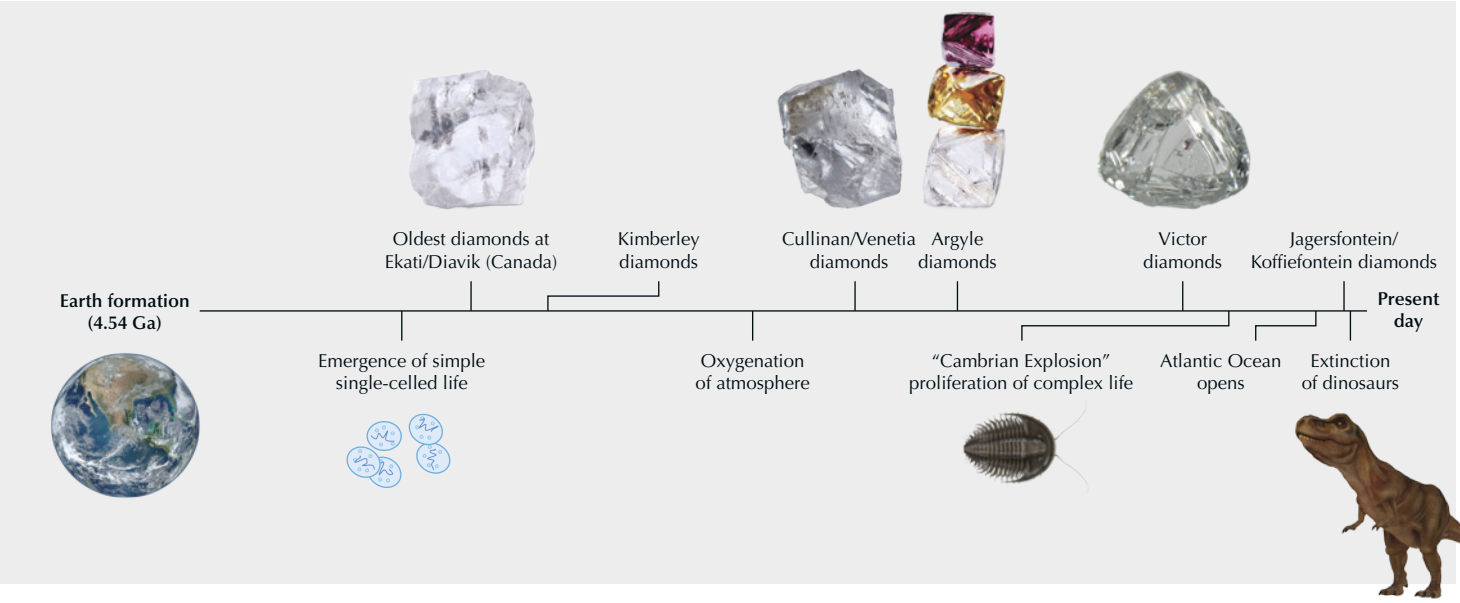

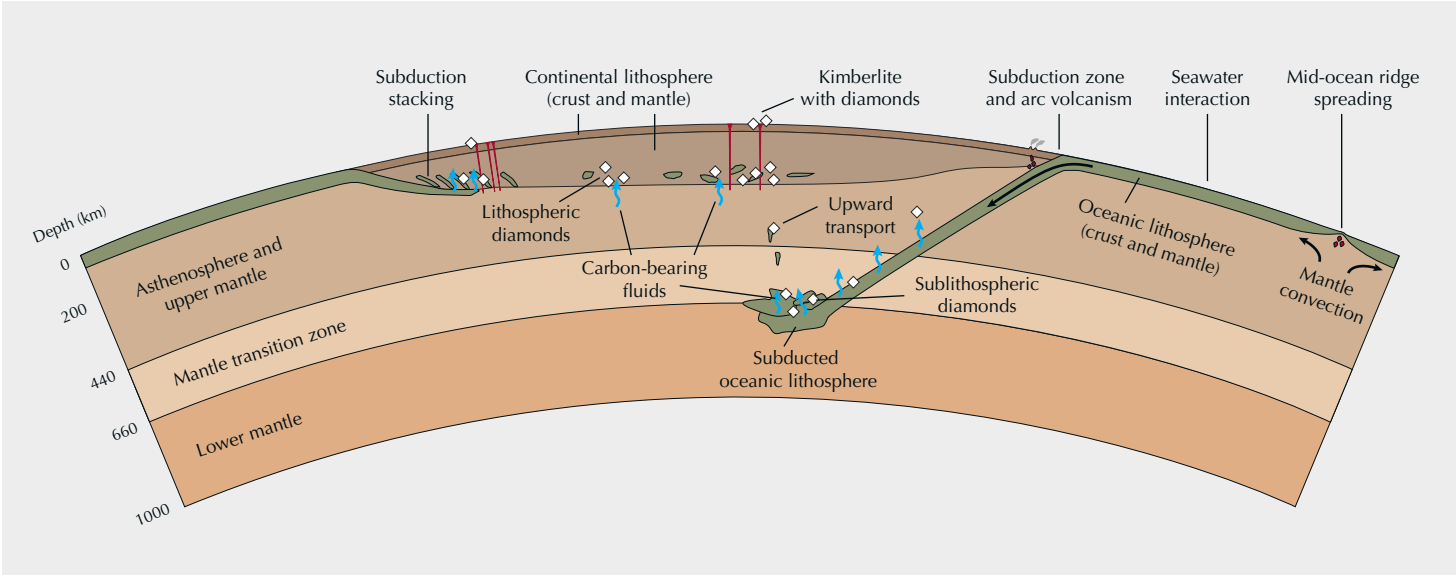

Figure 3. Generalized cross section of the earth showing diamond formation. There is an integral connection between plate tectonics, mantle dynamics, and diamonds. Settings and activities relating to diamond growth are often linked to large-scale processes, such as deep subduction recycling and continental growth and thickening (e.g., by subduction stacking). In both the continental lithosphere and the sublithospheric mantle, diamond formation is facilitated by carbon-bearing fluids. The composition of the carbon-bearing fluid can vary greatly, as can the mineralogy of the host rocks where diamonds grow. Earth's curvature and layers are drawn to scale.

The fact that diamonds can be dated is exciting, but the process is far from straightforward. Strictly speaking, the ages described here are mineral inclusion ages. The interpretation is that the age corresponds to how long the mineral has been trapped and sealed within the host diamond, thereby giving the age of diamond formation. Dating is based on exploiting radioactive elements in some inclusions that break down over time at a known rate, offering us the ability to read a built-in clock. For example, radioactive decay from the parent-daughter pairs Re-Os, Rb-Sr, and Sm-Nd are all used in diamond dating, from inclusions such as iron-nickel sulfide, clinopyroxene, and garnet. Given that only some inclusions are appropriate for this kind of analysis and the process is destructive, it is often challenging to date the diamonds from any given deposit. A comprehensive introduction to diamond dating can be found in Smit and Shirey (2019).

Large-Scale Processes of Diamond Formation

A key observation from decades of diamond studies is that diamonds can form in multiple distinct ways involving different host rocks, carbon sources, and diamond-forming reactions (Shirey et al., 2013). Interestingly, many of these diamond-forming processes appear to be linked to large-scale movements of solid rocks and fluid phases, such as the formation of continents and the release of melts and volatiles from tectonic plates as they sink and subduct into the mantle (e.g., Shirey and Richardson, 2011; Walter et al., 2011; Weiss et al., 2015; Shirey et al., 2024). Cross sections of the earth illustrating this activity often depict regions stretching hundreds or thousands of kilometers wide (figure 3).

In most cases, diamond growth in the mantle is said to be *metasomatic*, meaning it occurs as mobile carbon-bearing fluids invade preexisting solid host rocks and undergo changes that cause carbon to crystallize into a solid form. One of the most studied fluid types has been COH fluids (mixtures of carbon, oxygen, and hydrogen), which in simple terms can be thought of as a watery fluid mixture dominated by the molecules H_2O (water), CH_4 (methane), and CO_2 (carbon dioxide). Diamond formation in the lithosphere could occur from such a fluid as the temperature and pressure decrease when it percolates upward through mantle rocks by the following chemical reaction (Luth and Stachel, 2014):

$$CO_2 + CH_4 \longrightarrow 2H_2O + 2C \text{ (solid diamond)}$$

Changing conditions force the fluid-borne carbon in carbon dioxide and methane to recombine into solid native carbon as diamond. Other diamond-forming fluids thought to be relevant to diamond growth range in composition from hydrous, silicic, carbonatitic, and saline to potentially even metal-sulfide melts (Luth et al., 2022). Perhaps the most curious diamond-forming medium is the Fe-Ni-C-S metallic melt found as inclusions in some CLIPPIR diamonds, a sublithospheric variety that includes most top gem-quality type IIa diamonds (Smith et al., 2016). CLIPPIR diamonds are anomalous in being the only gem-quality diamonds that contain large (>10 µm) inclusions of the

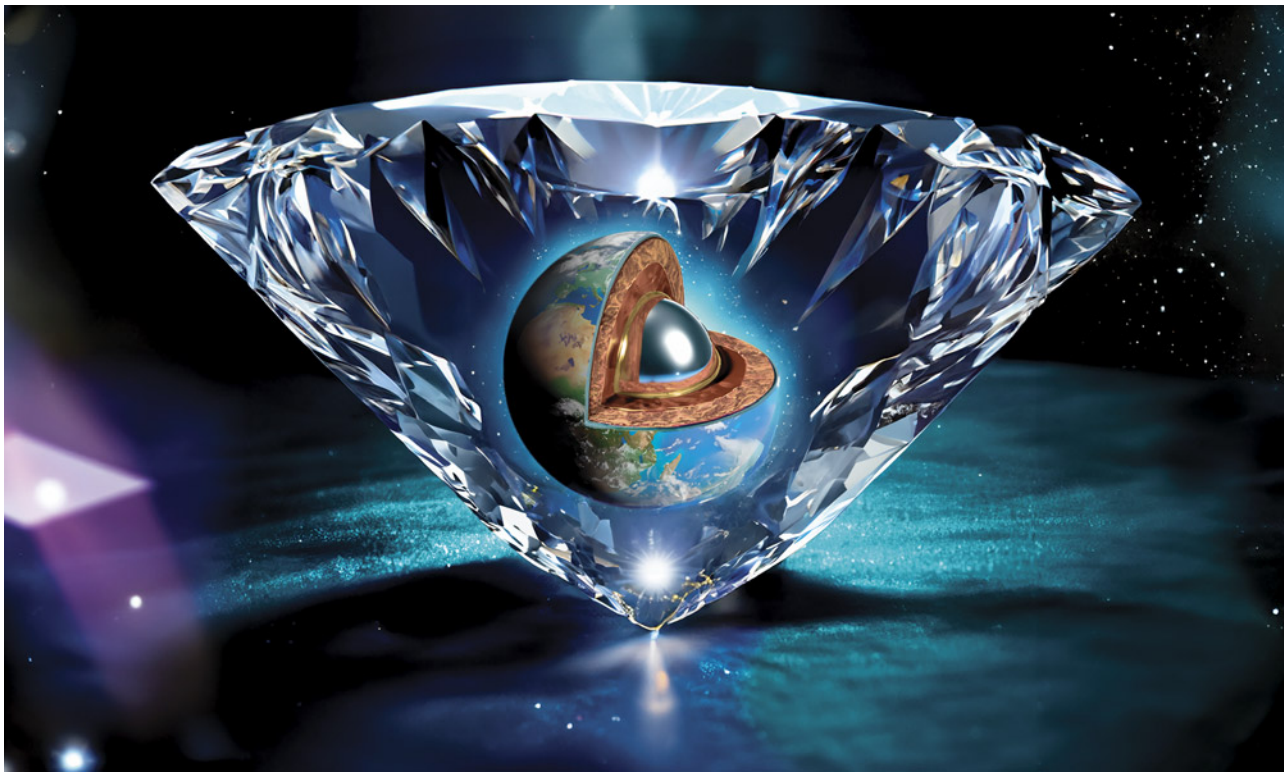

Figure 4. Peering inside a natural diamond can give scientists an unparalleled perspective into the earth's interior. Diamonds capture a lasting record of deep mantle processes over billion-year timescales, making them a unique window into geological space and time. Image created using Adobe Photoshop Generative AI.

growth medium. Coming back to the sense of spatial scale, CLIPPIR diamonds are an impressive example of large-scale movements. These crystals grow from ingredients delivered by descending oceanic plates that have been altered by seawater at the ocean floor and then subducted down to the mantle transition zone and the top of the lower mantle at 660 km (Smith et al., 2016, 2021). After growth, these diamonds are carried upward, potentially within low-density packages of rock derived from the subducted slab that rise under their own buoyancy. They may reside at the base of the continental lithosphere for an extended period (Timmerman et al., 2023) before later being drawn up to the earth's surface in a kimberlite.

It is no coincidence that diamond is linked to large-scale processes. After all, diamond is made of carbon, which plays an important role in lowering the melting point of mantle rocks, facilitating partial melting and the generation of magmas. Carbon's concentration in the mantle hovers around a few hundred parts per million but varies considerably with geological processes, such as volcanic activity. Carbon can also be introduced to the mantle by subducting slabs, both in sediments and altered oceanic crust. The balance of carbon entering the mantle through subduction and leaving the convecting mantle as magmas, volatiles, or metasomatic fluids forms the deep carbon cycle, which is critical in regulating atmospheric carbon dioxide over million-year timescales. The behavior of carbon influences geochemical cycles, mantle dynamics, and tectonic processes, not to mention the earth's ability to sustain life. Considering that ours is the only known planet with plate tectonics and an active deep carbon cycle, the formation of diamonds in the mantle may be somewhat unique to Earth. And peering into diamonds gives insights into the inner workings of our planet in a way that no other mineral can rival (figure 4).

Magmatic Journey to the Surface

While the multifarious crystallization of diamonds in the mantle is remarkable, yet another independent mechanism is responsible for bringing them up to the earth's surface. Early diamond mining in India, Indonesia, and Brazil was all alluvial, meaning that loose diamonds were extracted from river sediments or other sedimentary deposits. These diamonds were plucked clean from their primary sources by weathering and transported and mixed with assorted grains, obscuring their mantle origins. In 1867, alluvial diamonds were discovered in South Africa along the banks

of the Orange River, which set off a diamond rush that led to the discovery of weathered primary deposits in 1871 (Field et al., 2008). The new diamond-bearing igneous rocks became known as kimberlites, after the nearby town of Kimberley.

Kimberlites, and to a lesser extent lamproites and other related rocks, represent the most deeply derived magmas to erupt at the earth's surface. Although many details remain unresolved, they are thought to be produced by low-degree partial melting in the asthenosphere, which produces a carbonate-rich magma with an evolving composition en route to the surface (Giuliani et al., 2023). A high initial content of volatiles in the melt, chiefly water and carbon dioxide, serves as fuel to help crack overlying rocks and propel the magma to the earth's surface. The release of gases increases dramatically as the ascending magma approaches the surface. Over the roughly 200–300 km journey, the melt rips up pieces of rock and crystal grains, including diamonds occasionally, and may reach the surface rapidly, in a matter of just hours to days. With the element of chance involved, and considering the relatively high density of diamonds and mantle rocks as well as the fact that the magma threatens to oxidize or graphitize diamonds along the way due to the change in pressure and temperature, it is impressive that *any* diamonds make it all the way to the surface.

Diamonds are transported great distances vertically from the original settings in which they formed. Taking this into account helps explain the challenge of determining a diamond's geographic origin. Multiple layers of evidence from diamonds and their inclusions show considerable overlap in the conditions of diamond formation from one locality to the next on a worldwide basis. Unfortunately, this reality means there may not be any geographically distinct features that would allow scientists to analyze a diamond and ascertain its country or mine of origin (Smith et al., 2022).

Rarity

The popularity and availability of gem diamonds combined with some persistent myths have left some people wondering how rare natural diamonds really are. In terms of its natural abundance on earth, diamond is a relatively rare mineral. Prospectors and geologists who make a career searching for diamond deposits tend to come up dry. Considerable ongoing expenditures by mining and exploration companies to locate new deposits would be foolish if not for their rarity. Only through modern mining practices responding to global demand have diamonds become as available as they are today.

In total there are about 7,000 known kimberlites and related mantle-sourced magmatic rocks worldwide, but only about 1,000 are of potential economic interest for diamonds (Kjarsgaard et al., 2022). Of these, even fewer have the right combination of size, quality, and abundance of diamonds as well as favorable logistical factors that would make mining feasible (such as the deposit's depth, shape, and proximity to infrastructure). The question is always whether the sale of mined diamonds will actually outweigh the costs of exploration, mining, and reclamation and remediation when operations cease. Altogether there are fewer than 100 productive diamond mines past or present globally (Kjarsgaard et al., 2022). At most of these localities, the abundance of diamonds is still so low that they are almost never seen in the kimberlite—they only become visible at the final stages of ore processing. A decent ore grade is in the neighborhood of one carat per tonne, meaning a bathtub full of precious diamond-bearing kimberlite would contain on average one carat total weight of rough diamonds. More often than not, a tonne of ore contains multiple small diamonds, while seldom does it contain a gem-quality diamond exceeding one carat.

It is helpful to put diamonds in perspective by comparing them to another rare and precious material mined on an industrial scale: gold. By weight, about 125 times more gold is mined annually. Furthermore, only about one-third of the 110–130 million carats of diamond mined each year is actually of gem quality, with larger and higher-clarity diamonds being the scarcest. Global diamond production fluctuates year to year as mining output varies. The end of mining at Argyle in Australia in 2020 impacted the market, as will the expected end of production at Diavik in 2026. For now, the only new mine of similarly large scale is the Luele mine in Angola, which began production in 2023. Although diamonds may be actively forming deep in the mantle, it is important to recognize that the only diamonds available to humanity are the ones already at the surface. They are inherently finite in supply, and only a limited number of deposits are feasible to mine.

Mining and Its Impacts

Our world is underpinned by mining, an enormous industry largely hidden from view. Diamond mining has on several occasions entered the spotlight due to human rights concerns. In 2003, the Kimberley Process was established as an international certification scheme to prevent "conflict diamonds" from entering the mainstream rough diamond market. This has been a positive step forward, but it is not without challenges. Approximately 15% of global diamond production is from small-scale artisanal mining, and the people involved in these operations are most at risk of exploitation, violence, unsafe working conditions, and other problems. There are several corporate or industry initiatives focused on supporting and empowering artisanal diamond miners and communities, including Diamonds Do Good, the Diamond Development Initiative, Root Diamonds, and GemFair.

Less attention has been paid to some of the positive social impacts of diamond mining. Botswana is a great example. In 1967, only a year after Botswana gained inde-

pendence from British rule, a large diamond deposit at Orapa became a beacon of hope for one of the world's poorest countries at the time. Several additional deposits were soon found, and Botswana formed a partnership with De Beers. Today, Botswana is the top diamond producer by value, with the revenues providing significant economic benefits such as job creation and funding for critical infrastructure and social programs. The prudent management of diamond revenues has facilitated economic diversification, contributed to political stability, and positioned Botswana as a model for resource-rich developing countries.

In addition to social impact, diamond mining has an impact on the environment. Marketing efforts portray laboratory-grown diamonds as a "green" alternative to mined diamonds, but this is not a straightforward comparison. Both have environmental impacts, but their impacts are much different. Diamond mining is not as detrimental as many other forms of mining. Diamonds are extracted from rocks without the need for refining and smelting, as is the case for extracting copper or nickel from sulfide minerals, for instance. Diamond ore from a mine is crushed and diamonds are extracted mechanically, so the primary waste material is crushed rock. The recovery process uses water but few additional chemicals, if any. Curiously, the mineralogy of kimberlites is such that the weathering of this rock after crushing actually consumes carbon dioxide, with the potential to partially or even completely offset the carbon dioxide released by the mine (Mervine et al., 2018).

Artisanal diamond mining involves recovery from rivers or nearby sediments. The area affected by mining activity may be larger, but the depth that miners can reach with hand tools is limited to a few meters and the landscape is often reclaimed by vegetation when mining ceases. Larger mines targeting large alluvial deposits or primary deposits leave a larger footprint, typically some 20 to 30 square miles, often situated in remote areas. When a diamond mine closes, current best practices aim to restore the land to as natural a state as possible. The Argyle mine, one of the world's largest diamond mines, closed in 2020 after 37 years of operation. The owner, Rio Tinto, has a responsibility to reclaim and remediate the mine site, which involves dismantling the infrastructure, reshaping the land, and restoring vegetation. They are not permitted to simply abandon the site.

The Victor mine in Canada is another example of a recently closed diamond mine undergoing remediation. Victor was a relatively small but high-grade deposit. Mine construction began in 2006, and by 2019 the mining and processing was complete. With the infrastructure now demolished, rehabilitation of the site is well underway. The open pit has been transformed into a lake, and 1.4 million native trees and shrubs have been planted. For their remediation work at Victor, De Beers was recognized with the 2022 Tom Peters Memorial Mine Reclamation Award, presented by the Canadian Land Reclamation Association. Obviously it is impossible to truly "undo" damage to the environment, but the legally mandated steps taken by modern mining companies substantially reduce the long-term impact of diamond mining.

ACKNOWLEDGMENT

The authors wish to thank Dr. Jim Butler for his insightful comments and feedback.

REFERENCES

Field M., Stiefenhofer J., Robey J., Kurszlaukis S. (2008) Kimberlite-hosted diamond deposits of southern Africa: A review. *Ore Geology Reviews*, Vol. 34, No. 1, pp. 33–75, http://dx.doi.org/10.1016/j.oregeorev.2007.11.002

Giuliani A., Schmidt M.W., Torsvik T.H., Fedortchouk Y. (2023) Genesis and evolution of kimberlites. *Nature Reviews Earth & Environment*, Vol. 4, No. 11, pp. 738–753, http://dx.doi.org/10.1038/s43017-023-00481-2

Gorvett Z. (2022) How King Charles' diamonds reveal Earth's deep secrets. BBC, https://www.bbc.com/future/article/20220922-the-super-deep-royal-diamonds-revealing-earths-secrets

Kjarsgaard B.A., de Wit M., Heaman L.M., Pearson D.G., Stiefenhofer J., Janusczcak N., Shirey S.B. (2022) A review of the geology of global diamond mines and deposits. *Reviews in Mineralogy and Geochemistry*, Vol. 88, No. 1, pp. 1–117, http://dx.doi.org/10.2138/rmg.2022.88.01

Luth R.W., Stachel T. (2014) The buffering capacity of lithospheric mantle: Implications for diamond formation. *Contributions to Mineralogy and Petrology*, Vol. 168, No. 5, article no. 1083, http://dx.doi.org/10.1007/s00410-014-1083-6

Luth R.W., Palyanov Y.N., Bureau H. (2022) Experimental petrology applied to natural diamond growth. *Reviews in Mineralogy and Geochemistry*, Vol. 88, No. 1, pp. 755–808, http://dx.doi.org/10.2138/rmg.2022.88.14

Mervine E.M., Wilson S., Power I.M., Dipple G.M., Turvey C.C., Hamilton J.L., Vanderzee S., Raudsepp M., Southam C., Matter

J.M., Kelemen P.B., Stiefenhofer J., Miya Z., Southam G. (2018) Potential for offsetting diamond mine carbon emissions through mineral carbonation of processed kimberlite: An assessment of De Beers mine sites in South Africa and Canada. *Mineralogy and Petrology*, Vol. 112, No. 2, pp. 755–765, http://dx.doi.org/10.1007/s00710-018-0589-4

Navon O., Wirth R., Schmidt C., Jablon B.M., Schreiber A., Emmanuel S. (2017) Solid molecular nitrogen (δ-N_2) inclusions in Juina diamonds: Exsolution at the base of the transition zone. *Earth and Planetary Science Letters*, Vol. 464, pp. 237–247, http://dx.doi.org/10.1016/j.epsl.2017.01.035

Richardson S.H., Gurney J.J., Erlank A.J., Harris J.W. (1984) Origin of diamonds in old enriched mantle. *Nature*, Vol. 310, No. 5974, pp. 198–202, http://dx.doi.org/10.1038/310198a0

Shirey S.B., Richardson S.H. (2011) Start of the Wilson Cycle at 3 Ga shown by diamonds from subcontinental mantle. *Science*, Vol. 333, No. 6041, pp. 434–436, http://dx.doi.org/10.1126/science.1206275

Shirey S.B., Cartigny P., Frost D.J., Keshav S., Nestola F., Nimis P., Pearson D.G., Sobolev N.V., Walter M.J. (2013) Diamonds and the geology of mantle carbon. *Reviews in Mineralogy and Geochemistry*, Vol. 75, No. 1, pp. 355–421, http://dx.doi.org/10.2138/rmg.2013.75.12

Shirey S.B., Pearson D.G., Stachel T., Walter M.J. (2024) Sublithospheric diamonds: Plate tectonics from Earth's deepest mantle samples. *Annual Review of Earth and Planetary Sciences*, Vol. 52, No. 1, pp. 249–293, http://dx.doi.org/10.1146/annurev-earth-032320-105438

Smit K., Shirey S.B. (2019) Diamonds from the Deep: How old are diamonds? Are they forever? *G&G*, Vol. 55, No. 1, pp. 102–109.

Smit K.V., Timmerman S., Aulbach S., Shirey S.B., Richardson S.H., Phillips D., Pearson D.G. (2022) Geochronology of diamonds. *Reviews in Mineralogy and Geochemistry*, Vol. 88, No. 1, pp. 567–636, http://dx.doi.org/10.2138/rmg.2022.88.11

Smith E.M., Kopylova M.G., Frezzotti M.L., Afanasiev V.P. (2013) Nitrogen bubbles in the mantle: Evidence from diamond inclusions. *GAC MAC Winnipeg 2013,* Abstract No. 141.

Smith E.M., Shirey S.B., Nestola F., Bullock E.S., Wang J., Richardson S.H., Wang W. (2016) Large gem diamonds from metallic liquid in Earth's deep mantle. *Science*, Vol. 354, No. 6318, pp. 1403–1405, http://dx.doi.org/10.1126/science.aal1303

Smith E.M., Shirey S.B., Wang W. (2017) The very deep origin of the world's biggest diamonds. *G&G*, Vol. 53, No. 4, pp. 388–403, http://dx.doi.org/10.5741/gems.53.4.388

Smith E.M., Shirey S.B., Richardson S.H., Nestola F., Bullock E.S., Wang J., Wang W. (2018) Blue boron-bearing diamonds from Earth's lower mantle. *Nature*, Vol. 560, No. 7716, pp. 84–87, http://dx.doi.org/10.1038/s41586-018-0334-5

Smith E.M., Ni P., Shirey S.B., Richardson S.H., Wang W., Shahar A. (2021) Heavy iron in large gem diamonds traces deep subduction of serpentinized ocean floor. *Science Advances*, Vol. 7, No. 14, article no. abe9773, http://dx.doi.org/10.1126/sciadv.abe9773

Smith E.M., Smit K.V., Shirey S.B. (2022) Methods and challenges of establishing the geographic origin of diamonds. *G&G*, Vol. 58, No. 3, pp. 270–288, http://dx.doi.org/10.5741/gems.58.3.270

Stachel T., Harris J.W. (2008) The origin of cratonic diamonds—Constraints from mineral inclusions. *Ore Geology Reviews*, Vol. 34, No. 1-2, pp. 5–32, http://dx.doi.org/10.1016/j.oregeorev.2007.05.002

Timmerman S., Stachel T., Koornneef J.M., Smit K.V., Harlou R., Nowell G.M., Thomson A.R., Kohn S.C., Davies J.H.F.L., Davies G.R., Krebs M.Y., Zhang Q., Milne S.E.M., Harris J.W., Kaminsky F., Zedgenizov D., Bulanova G., Smith C.B., Cabral Neto I.C., Silveira F.V., Burnham A.D., Nestola F., Shirey S.B., Walter M.J., Steele A., Pearson D.G. (2023) Sublithospheric diamond ages and the supercontinent cycle. *Nature*, Vol. 623, No. 7988, pp. 752–756, http://dx.doi.org/10.1038/s41586-023-06662-9

Tschauner O., Huang S., Greenberg E., Prakapenka V.B., Ma C., Rossman G.R., Shen A.H., Zhang D., Newville M., Lanzirotti A., Tait K. (2018) Ice-VII inclusions in diamonds: Evidence for aqueous fluid in Earth's deep mantle. *Science*, Vol. 359, No. 6380, pp. 1136–1139, http://dx.doi.org/10.1126/science.aao3030

Walter M.J., Kohn S.C., Araujo D., Bulanova G.P., Smith C.B., Gaillou E., Wang J., Steele A., Shirey S.B. (2011) Deep mantle cycling of oceanic crust: Evidence from diamonds and their mineral inclusions. *Science*, Vol. 334, No. 6052, pp. 54–57, http://dx.doi.org/10.1126/science.1209300

Weiss Y., McNeill J., Pearson D.G., Nowell G.M., Ottley C.J. (2015) Highly saline fluids from a subducting slab as the source for fluid-rich diamonds. *Nature*, Vol. 524, No. 7565, pp. 339–

GEM NEWS INTERNATIONAL

Contributing Editors
Gagan Choudhary, *IIGJ-Research & Laboratories Centre, Jaipur, India* (gagan.choudhary@iigjrlc.org)
Guanghai Shi, *School of Gemmology, China University of Geosciences, Beijing* (shigh@cugb.edu.cn)

COLORED STONES AND ORGANIC MATERIALS

Gemfields emerald and ruby auctions. In May and June 2024, GIA was able to attend viewings of rough gemstones prior to Gemfields auctions in Bangkok. The first viewing offered emeralds from Gemfields' Kagem mine in Zambia, and the second featured rubies from the MRM mine in Mozambique (figure 1). Both viewings were immediately followed by the tender, where bids were submitted online and the winners of each parcel were notified.

Many international buyers attended the auctions, with strong interest from Indian and Israeli companies in the emeralds, while Thai and Indian companies focused mostly on the rubies. Several firms from Europe, China, and other Asian nations also submitted bids on parcels.

During both auctions, production from recent months was offered in pre-graded parcels. These lots are created by experienced professionals who have often spent decades working with the respective gemstones. The first factor in sorting is the size of the stones. Larger stones usually hold higher value, so these are often in very high demand by companies that specialize in fine single stones. Several substantial emerald crystals were available, including one that weighed 479 g (figure 2).

While these exceptional specimens stand out, the true power of skilled gemstone sorting is evident in the larger parcels. Emerald quality is determined by the richness of green color and the clarity (figure 3). When inspecting rubies, color is the most important factor, with different grades assigned based on the intensity of color, the orientation of color, and secondary color components (orangy or purplish). In the case of Mozambique rubies, the color ranges broadly from bright, intense pinkish red to a darker, more "closed" burgundy red (figure 4). Inclusions, especially dense silky bands, bring an extra dimension to ruby grading. This precise grading results in parcels that contain similar-looking finished gemstones in terms of color, size, or both. In some cases, fine gemstones of similar quality but different sizes are offered together because they would create a perfectly matched set (e.g., a larger stone suitable for a ring with two matching earrings and a necklace layout featuring smaller stones).

All products are offered untreated, with the exception of oiling. Oil is routinely used to inspect rough because it can minimize surface reflections and allow better observation of the clarity of the rough gems. While oil generally does not penetrate deep into fractures as it does during intentional fracture-filling treatment, rough buyers typically deep-clean the rough before starting the manufacturing process. All of these rubies are untreated. (Gemfields previously offered some treated parcels but discontinued this practice a few years ago.)

Rough emerald valuation is complex because of the abundant fractures that run through a crystal, and a single crystal will often result in many polished emeralds. This is especially true for the larger pieces of rough emerald. With rubies, a single piece of rough usually results in a single finished gem.

The seemingly unremarkable parcel shown in figure 3 attracted significant attention at the emerald auction. At first sight, this parcel might be overlooked due to the small size of the stones, with some as small as 0.5 g. But on closer examination, all of these stones were unusually clean and had a rich color; such emeralds are very rare and in high demand. This 500 g parcel could be turned into exceptional faceted emeralds.

At these high-stakes auctions, winning or losing a parcel can be determined by variations as small as 0.5% of the total price. While single stones of notable size gather the highest price per carat, the economic impact of larger parcels of smaller gems is often greater. These parcels re-

Editors' note: Interested contributors should send information and illustrations to Stuart Overlin at soverlin@gia.edu.

Gems & Gemology, Vol. 60, No. 3, pp. 400–429.

Figure 1. Fine emerald (>60 ct) and ruby (13 ct) crystals offered at the 2024 Gemfields auctions in Bangkok. Photos by Wim Vertriest.

quire much more manufacturing time (and cost), and the profits gained from them are often needed to keep cutting workshops in operation. Missing out on a large parcel could result in the suspension of manufacturing operations, potentially leading to the loss of the valuable skilled labor required to optimize the rough-to-cut process.

During the event, buyers are allowed a specific time slot to inspect stones. This often involves an entire team of specialists, including heat treaters, preformers, and polishers. The final value of a stone will be determined by its color, shape, and size. Cutting, especially the preforming, is the most important aspect of this process. Experienced cutters assist the company owners by offering input on

Figure 2. Large emerald crystals from the Kagem mine in Zambia. The three crystals have a combined weight of 106 g, while the large single crystal weighs 479 g. In these stones, visible fractures and inclusions will determine how the pieces are processed into smaller preforms before going to polishing. Photos by Wim Vertriest.

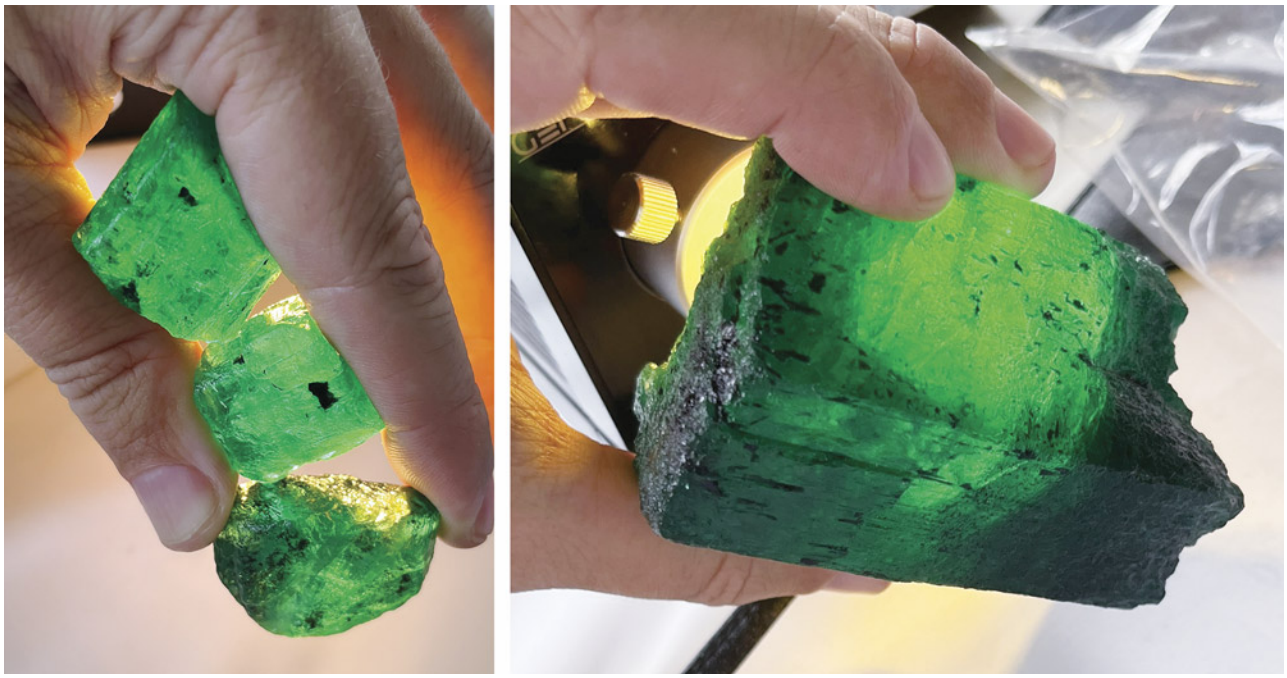

Figure 3. Large parcel of smaller emeralds of very high clarity; the average size of the crystals is between 2.8 and 4 mm. Photo by Wim Vertriest.

what can be done with a piece of rough. For example, the same crystal could yield a 4 ct pear shape or a 3.5 ct cushion. Making such decisions is crucial because the final price of the fashioned gem will be different. This difference must be reflected in the bid placed on the parcel. Considering that certain parcels consist of a few hundred stones, this is a painstaking exercise where minute details can tip the scales one way or another.

Another aspect of valuing the rough involves the impact of potential treatment. The extent of fracture filling can affect the value of an emerald and must be taken into account. The price premium for an untreated stone must be weighed against the value of a stone with a cleaner look from a certain degree of fracture filling or improvement in color due to heating during the manufacturing process. Many buyers are aware that certain grades of ruby will require treatment to improve the color (e.g., rubies with a strong purple tint). The final ruby color is an enormous value factor, which is why a heat treatment expert is often part of the decision-making team at the ruby auction. Striking the right balance between improved color and the price premium for an untreated stone becomes more complex with every auction.

During the May–June tenders, Gemfields offered high-quality rubies and medium- to high-quality rubies. The ruby sales totaled nearly US$69 million, with 97% of the offered goods finding a buyer. The emerald sale included only higher quality rough and totaled US$35 million, with 93% of the lots offered sold.

Figure 4. Range of rubies produced by the MRM mine in Mozambique: pinkish red material (top, 3.5–5.0 ct) and darker, more "closed" red rubies (bottom, 2.5–3.5 ct). Photos by Wim Vertriest.

Wim Vertriest
GIA, Bangkok

Arzakite inclusion in ruby from Mogok. Rubies with intense color and high transparency, such as those from the Mogok mining district in Myanmar, form in metamorphosed carbonate platforms during the retrograde metamorphism stage. This occurs at temperatures of ~620°–670°C and pressures of ~2.6–3.3 kbar (V. Garnier et al., "Marble-hosted ruby deposits from central and southeast Asia: Towards a new genetic model," *Ore Geology Reviews*, Vol. 34, 2008, pp. 169–191). The protolith comprises carbonates enriched in detrital Fe-Cr-V-bearing clays, shales with organic matter, and intercalated evaporitic layers.

Previous studies of primary fluid inclusions trapped by ruby at Mogok (G. Giuliani et al., "Fluid inclusions in ruby from Asian marble deposits: Genetic implications," *European Journal of Mineralogy*, Vol. 27, 2015, pp. 393–404) indicated the contemporary trapping of two carbonic immiscible fluid inclusions: mono- to two-phase fluid inclusions in the CO_2-H_2S ± COS ± S_8 ± H_2O system and multi-solid carbonic fluid inclusions in the Na-K-Ca-CO_3-SO_4-NO_3-Cl-F-(CO_2-H_2S) system. The multiple solids are mainly mixtures of Na-Ca-Al-carbonates (such as shortite and dawsonite), sulfates, phosphates, nitrates, fluorides, and chlorides (such as halite). They are the trapped recrystallized residues of molten salts formed during the metamorphism of evaporitic lenses (chlorides and sulfates) intercalated in the carbonate-shale rocks. The carbon dioxide is released by devolatilization of the original limestones during metamorphism. H_2S originated from the partial or total dissolution of evaporites and subsequent sulfate reduction by organic carbon, which produced graphite and pyrite. The formation of pyrite sequestered iron and led to the formation of iron-poor ruby.

In 2018, American Gemological Laboratories examined a 33.98 ct freeform carved ruby cabochon from Mogok measuring 24.08 × 18.48 × 8.30 mm (figure 5, left). The medium-quality, semitransparent to translucent stone was heavily included with numerous small cavities and whitish fillers on the base (figure 5, right). Energy-dispersive X-ray fluorescence analysis (in wt.% oxide) revealed low trace concentrations of gallium (0.004), iron (0.020), and titanium (0.026), with higher vanadium (0.071) and chromium (0.607). A large and highly reflective, soft yellowish syngenetic inclusion, measuring about 0.5 × 0.2 mm, was evident on the base (figure 5, right). Raman analysis of the inclusion, taken with 514 nm laser excitation, gave a spectrum (figure 6) that we compared to a couple of samples from the RRUFF database and the Raman data of arzakite intimately associated with graphite in nodules of tsavorite from the Scorpion mine in Kenya (R. Thomas et al., "Genetic significance of the 867 cm^{-1} out-of-plane Raman mode in graphite associated with V-bearing green grossular," *Mineralogy and Petrology*, Vol. 112, 2018, pp. 633–645). The best match identified it as arzakite, with Raman peaks at 210, 275, 390, and 590 cm^{-1}. Fourier-transform infrared analysis also highlighted the presence of diaspore and kaolinite in the ruby.

Arzakite, the sulfohalogenide of mercury ($Hg_3S_2(Br,Cl)_2$), forms a chemical series with lavrentievite ($Hg_3S_2(Cl,Br)_2$), originally reported from the Arzakskoye deposit, Uyuk Range, in the eastern Siberia region of Russia (V.I. Vasil'ev et al., "Lavrentievite and arzakite, new natural mercury sulfohalides," *Geologiya i Geofizika*, Vol. 25, 1984, pp. 54–63). It is a supergene mineral found in rhyolite-dacite porphyries and formed between 100°C and 200°C in relatively near-surface conditions.

Figure 5. The 33.98 ct carved ruby cabochon from Mogok (left) and its highly reflective, soft yellowish arzakite inclusion and whitish fillers on the base (right). Photos by Christopher Smith.

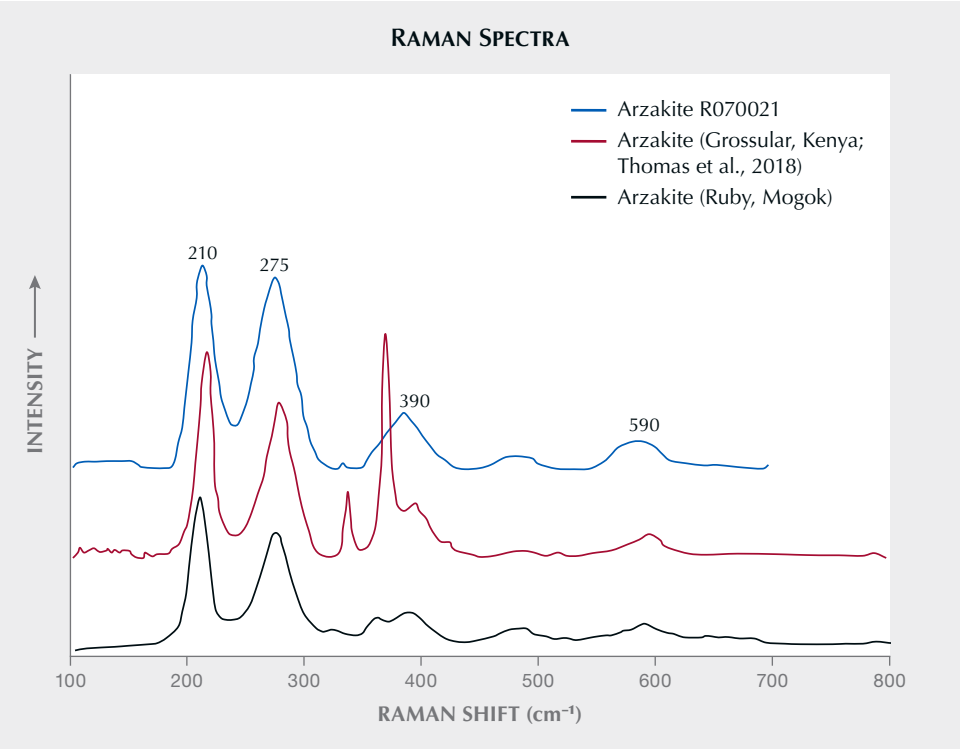

Figure 6. The Raman spectrum (514 nm laser excitation) of an arzakite inclusion in a ruby from Mogok. These peak positions are similar to those observed for an arzakite inclusion in a green grossular (tsavorite) from Kenya by Thomas et al. (2018) and a RRUFF reference spectrum.

The nature and chemical composition of inclusions and fluids associated with ruby in marble from Mogok highlighted the formation of sulfurous fluids and/or molten salts in a closed system with low fluid mobility. The Na–K–Ca–Li–CO_3–SO_4–NO_3–Cl–F fluid systems are powerful fluxes that lowered the temperature of chloride- and fluoride-rich ionic liquids. They provided transport over a very short distance of aluminum and/or silica and transition metals (Cr-V) contained in phengites and organic matter included in anhydrite and salts during prograde metamorphism. The presence of organic matter associated with evaporites is key for the formation of arzakite and sulfides. Evaporites played the role of fluxes, resulting in the formation of an alkaline saline magma in a closed system, much like a pressure cooker, where all the needed ingredients combined at high temperature to extract the chemical elements from the initial protoliths with their redistribution according to atomic and chemical compatibility. In these growth conditions, volatile elements such as mercury cannot escape from the system and (with sulfur) may preferentially form a new stable mineral. The halogens bromine and chlorine of arzakite, elements that are conservative in solution, originated from the evaporites, especially salts as halite (figure 7).

In nature, mercury is known to accumulate in sedimentary contexts (i.e., fluid mud and/or organic matter), especially with organic carbon. Some black shales present anomalous mercury concentrations associated with polymetallic sulfide-rich shales (R. Yin et al., "Anomalous mercury enrichment in Early Cambrian black shales of South China: Mercury isotopes indicate a seawater source," *Chemical Geology*, Vol. 467, 2017, pp. 159–167). Mercury can be used as a proxy to understand the formation of sulfide-rich shales. In the case of South China, a seawater origin is advanced to explain the anomalous mercury contents observed in the black shales (178–505 ppb) and the polymetallic sulfide-rich samples (10900–20700 ppb). These contexts of mercury accumulation also match with arzakite's sedimentary environment. However, mercury is very sensitive to temperature, and arzakite in the present case is a high-temperature metamorphic mineral. According to previous studies showing mercury contents in sedimentary rocks, all the mercury should be degassed by 650°C (B. Marie et al., "Determination of mercury in one hundred and sixteen geological and environmental reference materials using a direct mercury analyser," *Geostandards and Geoanalytical Research*, Vol. 39, 2015, pp. 71–86). The only way to preserve mercury during such an amphibolite metamorphism event is to attain a closed system, in this case with the fusion of evaporites.

This is the first time a Hg-S-bearing inclusion has been described in ruby. The presence of arzakite is a product of the genesis of ruby in marbles, in which the metamorphism of the sedimentary protolith occurred at very high temperature in a closed system where fluids could not escape. The fusion of the mixture of the protolith nucleated an alkaline-salty magma where all the chemical elements combined, forming ruby and minerals such as arzakite.

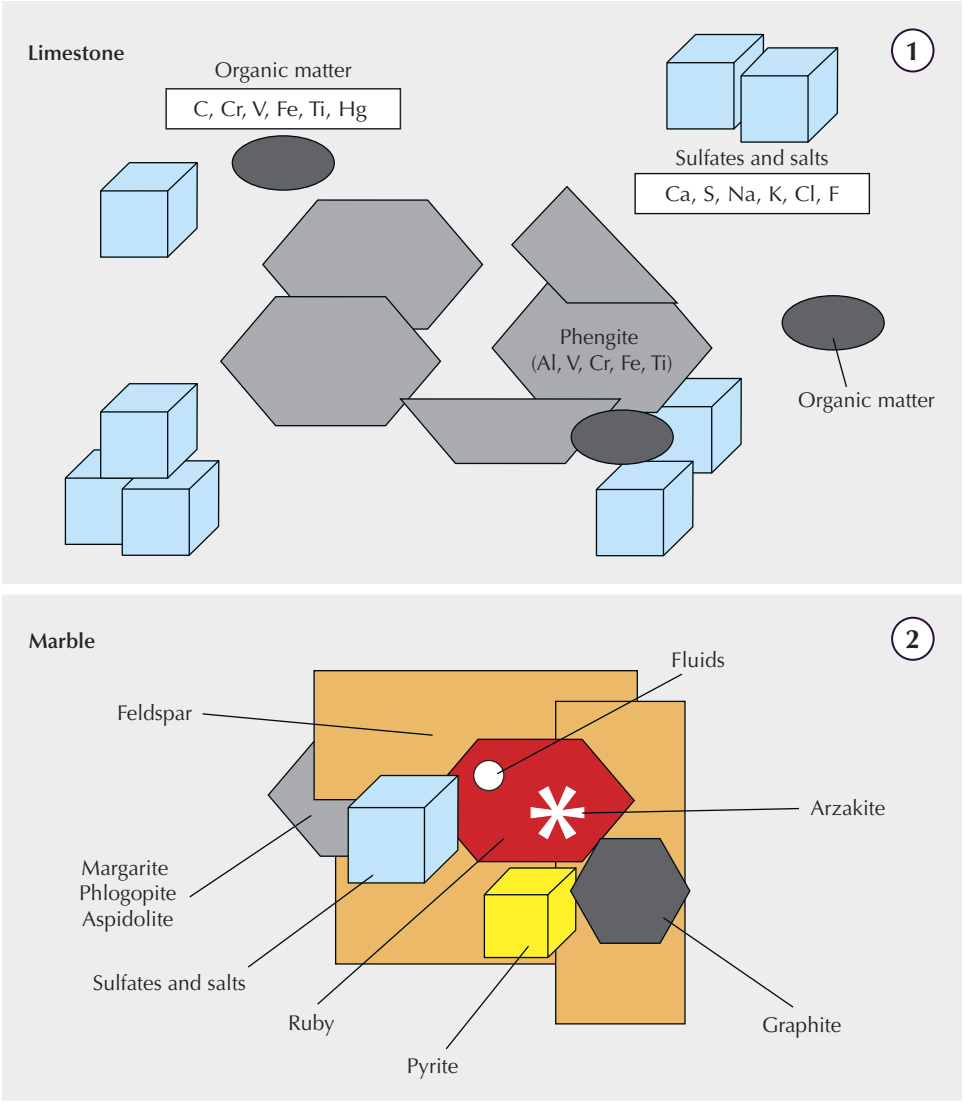

Figure 7. The model of formation of ruby deposits from the sedimentary stage of the protolith with the deposition of carbonates, dolomitic carbonates, organic matter–bearing shale, and marine and non-marine evaporites (stage 1) to the Himalayan metamorphism of the ruby protolith (stage 2); modified from Garnier et al. (2008). The arzakite inclusion is contained in ruby. The photomicrograph on the bottom shows a molten salts–bearing fluid inclusion in ruby with inclusions of calcite (Cal), graphite (C), apatite, halite, fluorite, dawsonite, shortite, and a CO_2-H_2S-bearing fluid phase (CO_2). Photomicrograph by Gaston Giuliani; field of view 0.49 mm.

This finding underscores the importance of detailed inclusion studies offering critical insights into the formation of gems such as Mogok ruby.

Gaston Giuliani
Université Paul Sabatier, Toulouse, France
Université de Lorraine, CRPG/CNRS,
Vandœuvre-lès-Nancy, France

Christopher P. Smith
American Gemological Laboratories (AGL), New York

Julien Boulliung
Université de Lorraine, CRPG/CNRS

Zoned trapiche emerald with goshenite overgrowth. GIA's Tokyo laboratory recently examined a 12.62 ct trapiche emerald with areas of the near-colorless beryl variety goshenite (figure 8). The stone was carved in the shape of a modified hexagram measuring 23.66 × 19.65 × 5.66 mm.

The internal features consisted of tubes, graphite, and jagged three-phase inclusions composed of a cube of halite (NaCl), a carbon dioxide (CO_2) gas bubble, and water (H_2O). Both the green and the near-colorless areas showed similar Raman spectra consistent with a beryl structure and spot refractive index readings of 1.57, matching that of beryl. The nearly identical Raman spectra patterns and intensity ratios indicated that the crystal axes of both areas were aligned. Some of the inclusions such as tubes were also in agreement with the internal fibrous growth structure of both the green and the near-colorless arm areas. These points suggested that both green and near-colorless arms were almost in the same crystallographic direction (figure 9).

The green core and green arms showed hexagonal weak green color bands. Absorption lines and bands related to trivalent vanadium (V^{3+}) and chromium (Cr^{3+}) were detected by a handheld spectroscope and an ultraviolet/visible absorption spectrometer in the green area but not in the near-colorless area. Chemical analyses using energy-dispersive X-ray fluorescence (EDXRF) demonstrated that the green trapiche area was consistent with a Colombian origin and the near-colorless goshenite area was poorer in minor elements of sodium, magnesium, vanadium, chromium, and iron while richer in potassium and cesium than the green core and arms (table 1). (The behavior of rubidium is unknown with this chemical measurement method.)

Figure 8. A 12.62 ct trapiche emerald with areas of near-colorless goshenite. Photo by Shunsuke Nagai.

Next, we considered the processes that might have formed such a zoned trapiche emerald. The finest trapiche emeralds are found in the Colombian deposits on the western side of the Eastern Cordillera Basin (e.g., Muzo, Coscuez, and Peñas Blancas), characterized by folding and thrusting along tear faults at the time of the Eocene-Oligocene boundary between 38 and 32 million years ago. Accumulation of hot H_2O-NaCl-CO_2 fluids at the tip of décollement faults in black shale host rock led to maximum fluid overpressure and subsequent sudden decompression associated with the collapsing of rock, forming emerald-bearing vein systems. The rapid growth of trapiche arms

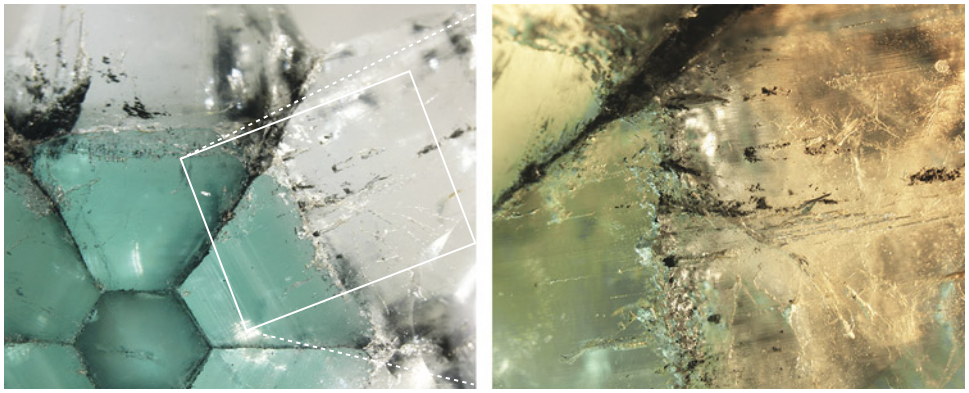

Figure 9. Left: Green color banding in the green internal arm areas of the trapiche emerald; field of view 1.18 cm. Right: Black and whitish inclusions in the green and near-colorless areas; field of view 5.95 mm. Photomicrographs by Makoto Miura (left) and Taku Okada (right).

TABLE 1. Comparison of chemical compositions (in wt.%) of the trapiche emerald and goshenite areas by EDXRF[a] and partial molar volumes of ions in water.

Area	SiO_2	Al_2O_3	Cr_2O_3	Fe_2O_3	V_2O_3	MgO	Na_2O	K_2O	Rb_2O	Cs_2O
Trapiche emerald	67.77 (19)	16.00 (12)	0.145 (9)	0.159 (5)	0.200 (10)	0.82 (7)	0.87 (11)	0.039 (3)	0.0003 (2)	0.001 (6)
Goshenite	68.09 (19)	16.71 (12)	0.006 (2)	0.054 (3)	0.009 (3)	0.39 (6)	0.65 (10)	0.078 (3)	0.0001 (1)	0.010 (5)
	Si^{4+}	Al^{3+}	Cr^{3+}	Fe^{3+}	V^{3+}	Mg^{2+}	Na^+	K^+	Rb^+	Cs^+
Partial molar volume (cm^3/mol)[b]	na[c]	na	–36.7[d]	–36.5[d]	na	–21.55[e]	–0.87[e]	9.06[e]	14.3[e]	21.42[e]

[a]*Chemical compositions were calculated assuming a BeO content of 14 wt.% and the uncertainties are given as least significant figures in parentheses*
[b]*At infinite dilution at 298 K and 1 bar*
[c]*na = not available*
[d]*Swaddle and Mak (1983)*
[e]*Shock et al. (1997)*

was shown to start at the beginning of decompression (e.g., I. Pignatelli et al., "Colombian trapiche emeralds: Recent advances in understanding their formation," Fall 2015 *G&G*, pp. 222–259).

Pignatelli et al. (2015) performed EDX elemental mapping using an electron probe microanalyzer for sodium, magnesium, aluminum, vanadium, and chromium on a trapiche beryl, which consisted of a near-colorless core and arms and green overgrowth areas. The green overgrowth areas were richer in sodium, magnesium, vanadium, and chromium than the near-colorless core and arms. The behavior of these trace elements corresponds to the color and is consistent with our EDXRF results on the present stone, which showed an inverse color distribution. In addition to these trace elements, we examined potassium and cesium and found for the first time that they behaved in a manner opposite to that of sodium, magnesium, vanadium, chromium, and iron.

Such chemical differences could be due to either compositional changes in the incoming fluids themselves in a simple open system or fluid differentiation associated with emerald crystallization in a closed system. Various chemical elements will behave differently to changes in pressure or temperature of the mineralizing aqueous fluid in such a system. For instance, elements such as potassium and cesium, with a so-called positive partial molar volume, will be released from the fluid due to increased pressure and/or decreased temperature (e.g. table 1; T.W. Swaddle and M.K.S. Mak, "The partial molar volumes of aqueous metal cations: Their prediction and relation to volumes of activation for water exchange," *Canadian Journal of Chemistry*, Vol. 61, No. 3, 1983, pp. 473–480; E.L. Shock et al., "Inorganic species in geologic fluids: Correlations among standard molal thermodynamic properties of aqueous ions and hydroxide complexes," *Geochimica et Cosmochimica Acta*, Vol. 61, No. 5, 1997, pp. 907–950). These elements are concentrated in the colorless goshenite areas. On the other hand, V^{3+} and Cr^{3+}, with a so-called negative partial molar volume, would have reacted in the opposite way and are depleted in the goshenite but enriched in the emerald areas, indicating a change in the pressure and/or temperature of the fluid as it crystallized either goshenite or emerald. The classical chemical thermodynamic considerations above may provide insight into the differences in behavior among trace elements and the growth history that zoned gems such as this stone have undergone in fluids or melts.

This trapiche emerald offers a unique example to consider trace element behavior and geological conditions during crystal growth, as well as the diversity of trapiche emerald formation.

Taku Okada and Makoto Miura
GIA, Tokyo

Almandine garnet from Phu Tho, Vietnam. During the early 2000s, garnet was discovered and mined along with black tourmaline and aquamarine in the northern Vietnamese province of Phu Tho. Its undesirable appearance led to a suspension of mining activities, but mining resumed in 2021 with more promising results. Phu Tho borders the province of Yen Bai, which has produced a wide range of gem materials such as ruby, sapphire, spinel, and tourmaline. Despite their proximity, the geological settings are much different, and Phu Tho produces tourmaline, beryl, and garnet.

Rough garnet from Phu Tho possesses typical cubic crystal shapes with either trapezohedral or elongated habit.

Figure 10. The trapezohedral habit of garnet from Phu Tho. The trapezohedral habit is suitable for cutting as cabochons or beads, while the elongated habit (not shown) would be appropriate for carving. Photos by Nguyen Thanh Nhan.

The authors purchased a total of 28 samples, including 26 euhedral trapezohedral crystals (figure 10) and two enormous rough samples, from a garnet miner in Phu Tho. One crystal was cut into a cabochon measuring 17.23 × 14.82 × 9.37 mm and weighing 24.30 ct. The other 25 crystals were kept intact, ranging from 11 to 29 mm with a total weight of 218.58 g. The two large samples were elongated and up to 30 cm in length. Most of the garnet is found in black mica schist. Although the materials formed within the host rock, the crystals can be detached easily into loose crystals. The Phu Tho garnet displays colors from medium dark to very dark red to purple-red. Its transparency ranges from translucent to opaque, with no transparent material found, and the luster is vitreous to greasy.

Standard gemological testing of the samples showed a refractive index of 1.78 to over the limit of the refractometer, specific gravity ranging from 4.01 to 4.12, an almandine spectrum, and an inert reaction under ultraviolet light (long-wave and short-wave). Microscopic examination revealed several solid black inclusions and oriented needles of rutile, some fingerprints, and feathers filled with iron stains. These results confirmed almandine garnet. Raman spectroscopy showed distinct peaks at 123 and 1456 cm^{-1}, consistent with almandine.

Because of their dark tone and low transparency, Phu Tho garnets are more suitable for cutting as cabochons, beads, and ornamental carvings (figure 11). Asterism was observed in several samples from Phu Tho, with four- or six-rayed stars caused by oriented rutile needles intersecting at angles of 120° and 60°. Interestingly, the occurrence of both four- and six-rayed stars within a polished sample is not rare. In the studied samples, we counted a maximum of five six-rayed stars and two four-rayed stars on one side of a garnet. The display of multiple stars within garnet was previously reported by K. Schmetzer et al. ("Star garnets and star garnet cat's-eyes from Ambatondrazaka, Madagascar,"

Figure 11. Vietnamese garnet from Phu Tho displays a medium dark brown-red, translucent to opaque appearance. The polished octahedral crystal weighs 450 g, the carving weighs 234 g, and the four-rayed star garnet weighs 26 ct. Photo by Pham Minh Tien.

Figure 12. Two views of the 2.43 ct orangy pink morganite with bright yellow and dark brown inclusions lying in a plane. Photos by Sandie Clain, © LFG; courtesy of Gravier & Gemmes.

Journal of Gemmology, Vol. 28, No. 1, 2002, pp. 13–24), and so far this phenomenon has only been found in garnet.

Although most Phu Tho garnet is not suitable for high-quality jewelry making, giant crystals or well-formed crystals on host rock could be valuable as ornamental objects or mineral specimens.

Pham Minh Tien and Nguyen Thanh Nhan
Liu Gemological Research and Application Center (LIULAB)
Ho Chi Minh City

Helvine inclusions in morganite. A group of remarkable bright yellow inclusions in a partially polished 2.43 ct orangy pink morganite from Madagascar (figure 12) recently caught our attention. The beryl was identified by a combination of classical gemology and spectroscopy. The partial hexagonal prism contained hundreds of yellow crystals aligned on a plane. Although it was difficult to evaluate their complex polyhedral morphology, many had triangular faces (figure 13). Using reflected light, several of the crystals were found to reach the surface of a polished face. In addition, a few very dark brown, somewhat elongated crystals were observed in the same plane.

Raman spectra were obtained with a Jobin Yvon T6400 Raman spectrometer, with diode-pumped solid-state (DPSS) laser excitation at 458 and 561 nm, at 2 cm^{-1} resolution. Three major peaks at about 130, 180, and 890 cm^{-1} and smaller matching features were observed. These were identified as helvine using the RRUFF database (Lafuente et al., 2015, https://rruff.info/about/downloads/HMC1-30.pdf) and CrystalSleuth software (figure 14). Similar spectra were obtained on three different surface-reaching inclusions using both excitation wavelengths. The dark crystals were identified as hubnerite, $Mn^{2+}(WO_4)$, also through Raman spectroscopy using the same software, with a dominant band around 882 cm^{-1}.

Because of the very bright color of the yellow inclusions, we attempted to detect their absorption with a visible absorption spectrum. Ultraviolet/visible/near-infrared (UV-Vis-NIR) spectra were acquired over 365–1000 nm using a mobile instrument with an integrating sphere (Magilabs GemmoSphere), with 0.1 seconds acquisition time, 50 accumulations, and spectral resolution of about 1.5 nm. The spectrum presents strong, relatively sharp absorption features at about 420, 446, and 477 nm, with broader bands at about 567 and 830 nm (figure 15). The absorptions at 420, 446, and 477 nm match those for the helvine-genthelvite series documented previously (U. Hålenius, "Absorption of light by exchange coupled pairs of tetrahedrally coordinated divalent manganese in the helvite-genthelvite solid solution," *Periodico di Mineralogia*, Vol. 80, No. 1, 2011, pp. 105–111). Their strong violet and blue absorption induced the vivid yellow color. The features at about 567 nm (Mn^{3+}), 830 nm (iron-related), and 965 nm (water-related) come from the beryl matrix (D.L. Wood and K. Nassau, "The characterization of beryl by visible and infrared absorption spectroscopy," *American Mineralogist*, Vol. 53, No. 5-6, pp. 777–800).

Helvine is a cubic beryllosilicate with the chemical formula $Be_3Mn^{2+}_4(SiO_4)_3S$. It belongs to the helvine group of minerals, where divalent manganese can be replaced by di-

Figure 13. Bright yellow inclusions with polyhedral shapes, often with triangular faces, accompanied by a small number of very dark brown crystals. Photomicrograph by Aurélien Delaunay; field of view 2.2 mm.

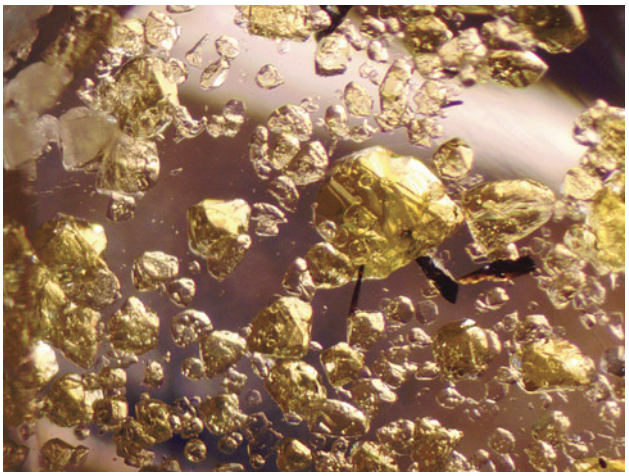

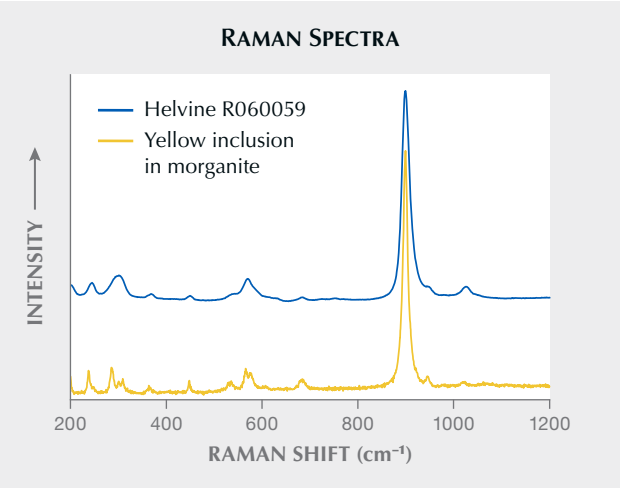

Figure 14. Comparison of the Raman spectrum of the yellow inclusions and the RRUFF reference Raman spectrum for helvine.

valent iron or zinc. Its intrinsic saturated yellow color (the name comes from the Latin *helvus*, for "yellow") is due to exchange-coupled pairs of tetrahedrally coordinated Mn^{2+} ions (Hålenius, 2011). This explains why the color remained strong even with a short optical path in the inclusions. Helvine crystals are usually tetrahedral, thus with only triangular faces, which is consistent with the preliminary visual observations. Yet the morphology was quite different from what is recorded in the Mindat database (https://www.mindat.org/min-40167.html), probably because these inclusions can be considered microcrystals. Small crystals often show fast-growing faces that are absent from larger ones (I. Sunagawa, *Crystals: Growth, Morphology and Perfection*, 2005, Cambridge University Press, Cambridge, UK). Helvine is known to occur in highly complex pegmatites, hence its association with beryl in the present specimen. Hubnerite may sometimes grow within pegmatites as well. Note that helvine and morganite beryl are beryllium-containing. Together with hubnerite, they accommodate manganese (as the coloring agent for morganite). The plane containing these unusual inclusions probably represents a manganese-rich growth spurt, also with tungsten and sulfur.

Emmanuel Fritsch (Emmanuel.Fritsch@cnrs-imn.fr)
Nantes Université, CNRS
Institut des Matériaux de Nantes Jean Rouxel (IMN)
Nantes, France

Stefanos Karampelas, Aurélien Delaunay, and Ugo Hennebois
Laboratoire Français de Gemmologie (LFG)
Paris

Figure 15. UV-Vis-NIR absorption spectrum of the morganite containing the helvine inclusions. The helvine-related Mn^{2+} features at 420, 446, and 477 nm cause the inclusions' yellow color, while the Mn^{3+} broad band at around 567 nm provides the pink component to the beryl host. The bands at around 830 and 965 nm are also beryl-related.

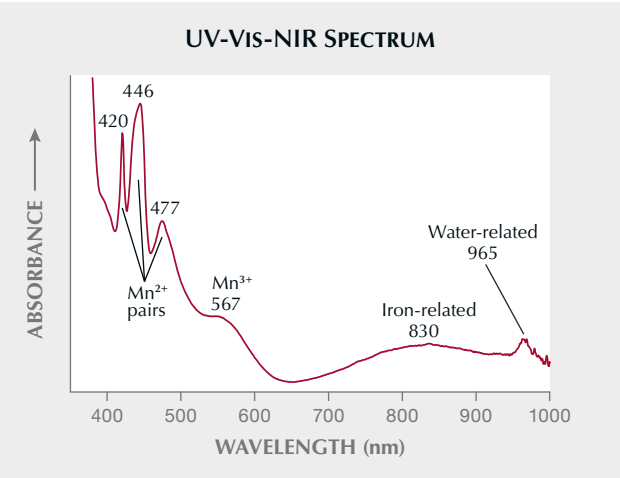

Mineral assemblage of "Paraíba matrix." Since entering the market in the late 1980s, Paraíba tourmaline has been sought after for its electric blue-green tone. A product called "Paraíba matrix" or "Paraíba in quartz" emerged about three years ago. Two examples of this material, pear-shaped cabochons weighing 4.23 and 3.67 ct (samples PB1 and PB2, respectively), were purchased from the September 2023 Hong Kong Jewellery and Gem Fair (figure 16). The blue minerals in these samples showed an attractive neon-blue color with low clarity surrounded by opaque or transparent white minerals. Dark red minerals were also scattered in the matrix.

Figure 16. Two pieces of "Paraíba matrix" weighing 4.23 ct (sample PB1, left) and 3.67 ct (PB2, right). Photo by Xinchenlu Ai.

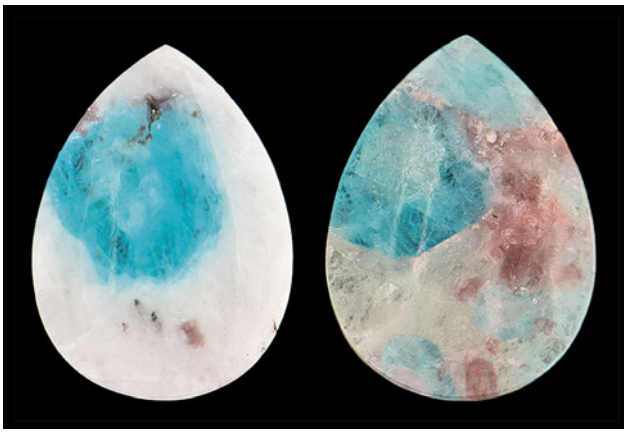

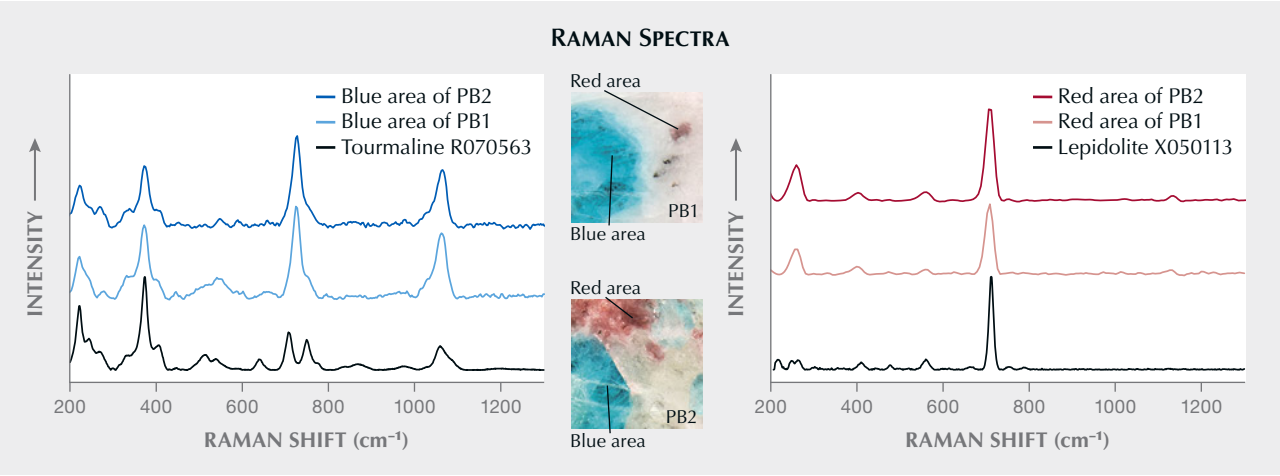

Figure 17. Raman spectra of the embedded blue and dark red minerals in the "Paraíba matrix" samples, with standard RRUFF reference spectra included for comparison. Spectra are offset vertically for clarity.

Raman spectroscopy identified the blue mineral as tourmaline (figure 17, left), and X-ray fluorescence (XRF) spectroscopy showed that it contained copper and manganese. These results, combined with the material's bright neon-blue color, confirmed the blue mineral as Paraíba tourmaline. In both samples, the Paraíba tourmaline displayed color banding, with bluish white cores surrounded by neon-blue rims. The Raman spectra of the dark red mineral in both samples were consistent with that of lepidolite in the RRUFF database (figure 17, right). The Raman spectrum of the opaque white part of PB1 was consistent with albite (figure 18, left), while that of the transparent white part of PB2 was consistent with quartz (figure 18, right).

Based on the Raman and XRF tests of both samples, the "Paraíba matrix" was mainly composed of blue Paraíba tourmaline, dark red lepidolite, opaque white albite, and transparent white quartz. Thus, the white matrix minerals were not all quartz, as suggested by the trade name "Paraíba in quartz." The Paraíba tourmalines in these samples cannot be cut and polished into faceted gemstones due to their low clarity. Cutting and polishing these unique pieces into cabochons can provide more affordable options for fashion jewelry designers and customers.

Xinchenlu Ai and Xiaojing Lai
Gemmological Institute
China University of Geosciences, Wuhan

A minute foraminifera shell in a natural non-nacreous black pearl. Nacre can form around nearly any irritant that infiltrates a shell, resulting at times in pearls with unique internal structures. In very rare cases, foraminifera shell (also known as "test") can serve as the nuclei of pearls produced by different mollusks (Spring 2023 GNI, pp. 143–145). These tiny single-celled marine microorganisms can be found on the seafloor and are usually about half a millimeter to one millimeter long.

Figure 18. Raman spectra of the white matrix in the two "Paraíba matrix" samples, with standard RRUFF reference spectra included for comparison. Spectra are offset vertically for clarity.

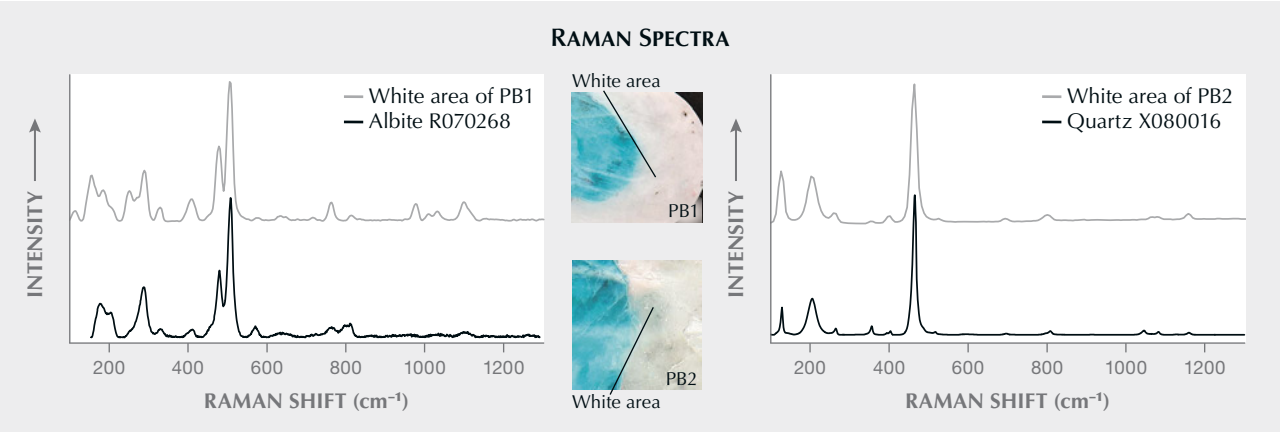

Figure 19. A black non-nacreous pearl measuring 1.55 × 1.43 mm and weighing 0.02 ct. Photo by Gaurav Bera.

GIA's Mumbai laboratory recently received a lot of non-nacreous brown and black pearls of various shapes, collected by a Bahraini diver over a period of six years. The lot was submitted for scientific examination and contained pearls from both the *Pinctada radiata* and *Pinna* species (pen pearls) fished from Bahrain. Real-time X-ray microradiography (RTX) revealed different types of cores and acicular (radial) structures in most of the pearls. One very intriguing structure was observed in a black near-round pearl weighing 0.02 ct and measuring 1.55 × 1.43 mm, reportedly from a *Pinctada radiata* mollusk (figure 19).

The pearl had a glossy appearance with a few pits and no surface-reaching cracks. Viewed under high magnification with a fiber-optic light, it showed a non-nacreous surface, presenting cellular outlines with fine small lines within each cell (figure 20, left). When exposed to X-ray fluorescence, the pearl showed an inert reaction. Energy-dispersive X-ray fluorescence spectrometry revealed a manganese level of 76 ppm and a higher strontium level of 1160 ppm, indicative of a saltwater origin. Under long-wave and short-wave ultraviolet radiation, the pearl showed an inert reaction. However, DiamondView imaging revealed a remarkable cellular structure within. A bluish reaction was observed at the boundaries outlining the cellular columnar structures with thin, short lines within the cells (figure 20, right). This cellular surface structure appeared different from the pseudohexagonal cellular outline found in pen pearls (N. Sturman et al., "Observations on pearls reportedly from the Pinnidae family (pen pearls)," Fall 2014 *G&G*, pp. 202–215). Based on the authors' previous observations, this type of structure is more typically found on the surface of non-nacreous pearls from the *Pinctada radiata* mollusk.

Raman spectroscopy using 514 nm laser excitation was performed on two spots. The first spot revealed peaks at 150 and 280 cm^{-1} with the associated band at 1086 cm^{-1}. The second spot also revealed a peak at 1086 cm^{-1} associated with aragonite and calcite, but there were no other clear peaks to identify which of the two calcium carbonate polymorphs was present in that area of the pearl.

Interestingly, RTX imaging and X-ray computed microtomography (μ-CT) analysis revealed a minute foraminifera shell at the pearl's core, measuring approximately 0.44 × 0.38 mm. The shell exhibited a double thin-walled structure, surrounded by an organic-rich area and an acicular (radial) structure with fine growth arcs crossing it. The radiating acicular structure covered the entire area of the pearl (figure 21, A and C). When observed from the top

Figure 20. Left: Non-nacreous surface of the black pearl; field of view 3.4 mm. Right: DiamondView image showing a bluish reaction of the outline of the cellular structure. Photos by Anukul Belanke.

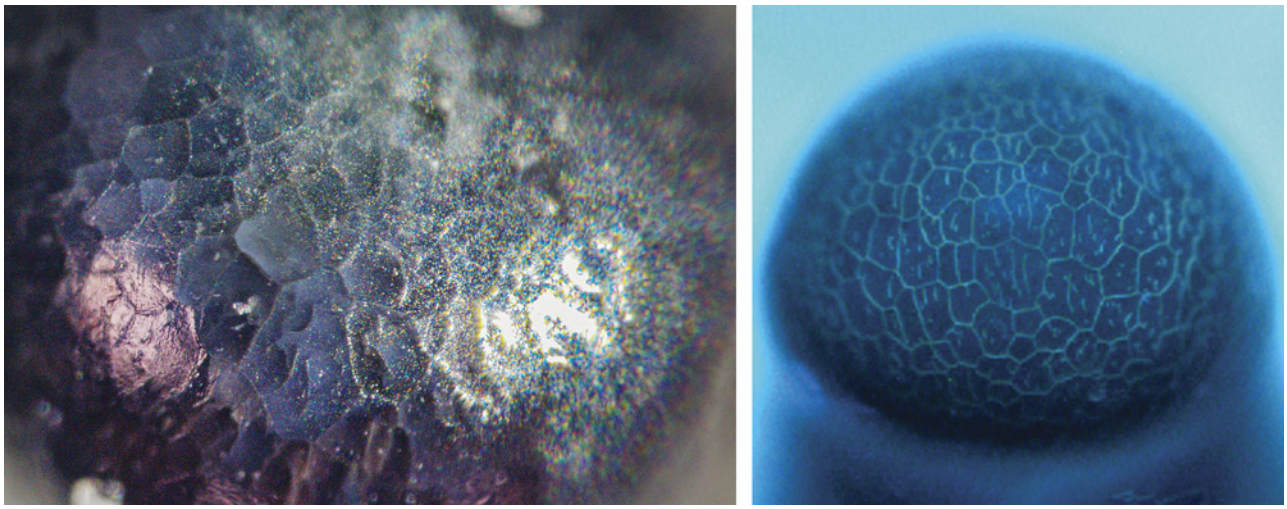

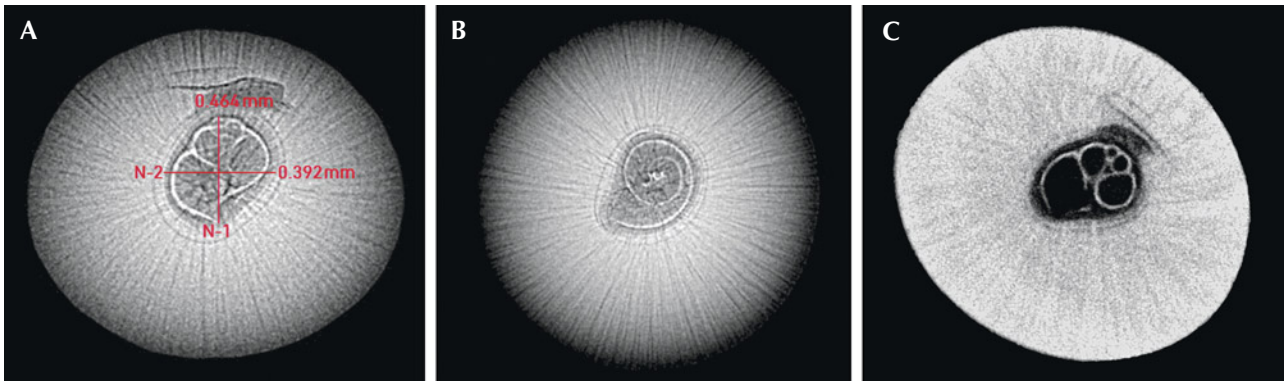

Figure 21. A: RTX image showing the measurements of the foraminifera shell at the center surrounded by an acicular structure. B: RTX image of the pearl along its length, revealing the spiral top formation of the foraminifera shell. C: µ-CT image of the foraminifera shell and acicular structure.

view, the RTX image showed the spiral shape of the shell's apex (figure 21B). Given its chamber shape and tiny size, the shell was identified as a foraminifera (K. Kimoto et al., "Precise bulk density measurement of planktonic foraminiferal test by X-ray microcomputed tomography," *Frontiers in Earth Science*, Vol. 11, 2023, article no. 1184671). Additionally, µ-CT scan images were rendered using specialized software (C. Zhou et al., "New 3-D software expands GIA's pearl identification capabilities," *GIA Research News*, May 13, 2016), which showed a clearer visualization of the external morphology of the foraminifera shell within the pearl (figure 22), as shown in the video at www.gia.edu/gems-gemology/fall-2024-gemnews-foraminifera-shell-in-natural-non-nacreous-pearl.

Black non-nacreous pearls from *Pinctada radiata* are extremely rare, and it is very uncommon to see such intriguing internal structures with foraminifera shells surrounded by acicular structures. The presence of this non-nacreous seed pearl with such a structure adds to GIA's comprehensive research database, contributing to the ongoing studies of unique formations found in natural pearls from the wild.

Abeer Al-Alawi, Anukul Belanke, Lubna Sahani, and Roxane Bhot Jain
GIA, Mumbai

Emiko Yazawa
GIA, New York

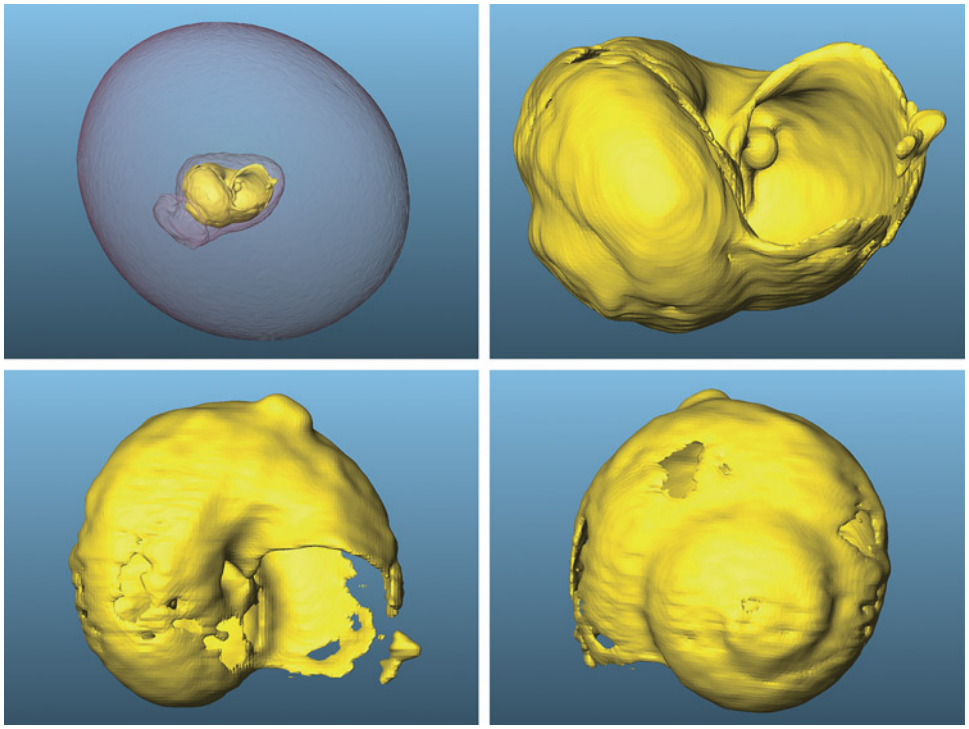

Figure 22. 3D images constructed from µ-CT scans showing the tiny foraminifera shell's morphology.

Figure 23. Left: This gourd-shaped saltwater bead cultured pearl (2.04 g and 15.90 mm high) displays two different colors. Right: Magnification indicates that the two parts grew together naturally. Photos by Yanhan Wu.

An unusual saltwater bead cultured pearl. A saltwater pearl with an unusual appearance was discovered in the pearl market in the city of Zhuji, in China's Zhejiang Province. It was shaped like a gourd, consisting of a silver gray part and a black part with green overtone (figure 23, left). The pearl's unusual color and shape raised suspicions about whether it had been artificially processed.

The pearl weighed 2.04 g and had a height of 15.90 mm. The gray part measured 6.79 × 6.12 × 5.07 mm and the black part 10.64 × 10.75 × 10.83 mm. Upon magnification, it appeared the two parts grew together naturally, rather than being artificially attached (figure 23, right).

No silver was detected with energy-dispersive X-ray fluorescence in either part, indicating that the pearl had not been treated with silver nitrate dye. The ultraviolet/visible/near-infrared (UV-Vis-NIR) reflectance spectra of both parts showed absorptions at 279, 405, 500, and 700 nm (figure 24, left), consistent with previous studies on the absorption of saltwater cultured pearls (S. Karampelas et al., "UV-Vis-NIR reflectance spectroscopy of natural-color saltwater cultured pearls from *Pinctada Margaritifera*," Spring 2011 *G&G*, pp. 31–35). In the visible light region, only the cause of the 405 nm band has been identified; it is attributed to a kind of porphyrin called uroporphyrin (Y. Iwahashi et al., "Porphyrin pigment in black-lip pearls and its application to pearl identification," *Fisheries Science*, Vol. 60, No. 1, 1994, pp. 69–71). The black part was more absorbed than the gray part due to its richer color.

The Raman spectra displayed bands at 1085 and 704 cm^{-1} (figure 24, right), corresponding to the ν_1 symmetric and the ν_4 in-plane bending modes of the carbonate ion (CO_3^{2-}) in aragonite (J. Unvros et al., "Characterization of

Figure 24. Left: The UV-Vis-NIR reflection spectra of the two parts of the pearl showed the same absorption positions and differences in intensity. Spectra are offset vertically for clarity. Right: Raman spectroscopy displayed the bands of aragonite and organic components.

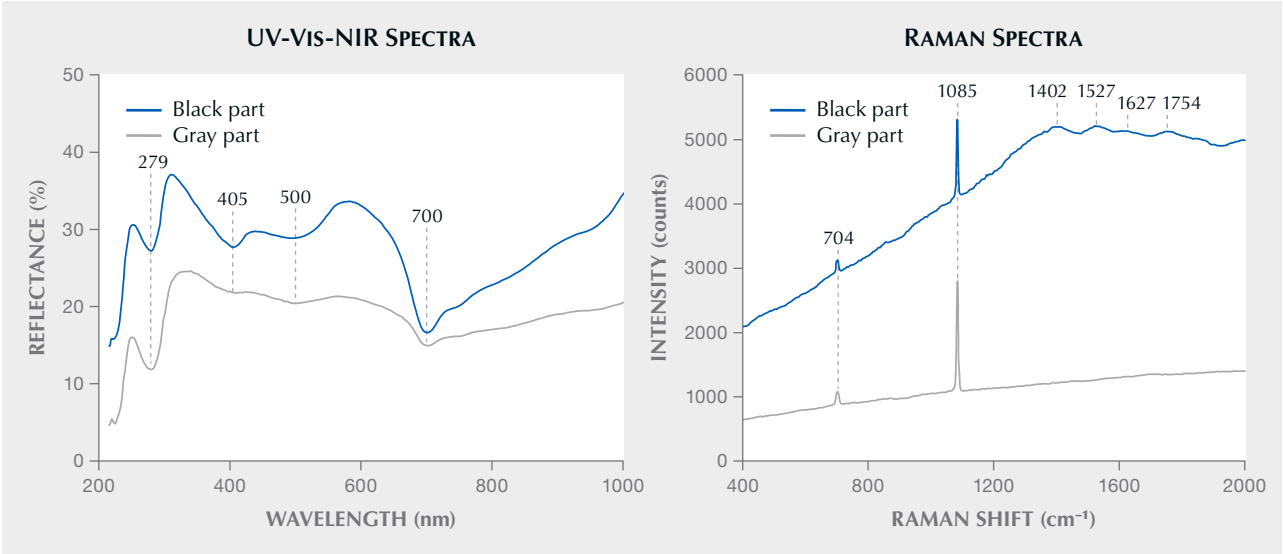

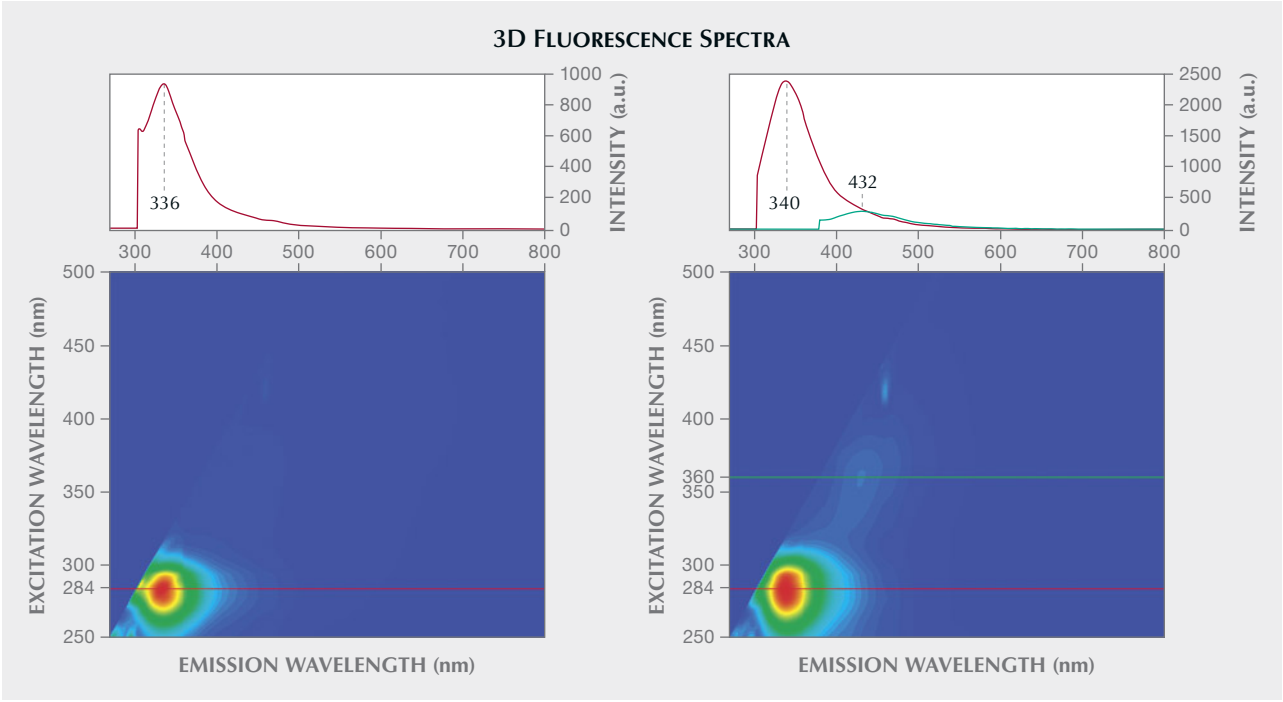

Figure 25. 3D fluorescence spectra of the black part of the pearl (left) and the gray part (right).

some biogenic carbonates with Raman spectroscopy," *American Mineralogist*, Vol. 76, 1991, pp. 641–646). Compared to the gray part, several broad bands were observed in the black part at 1800–1400 cm^{-1}, with centers at approximately 1754, 1627, 1527, and 1402 cm^{-1}. These Raman features were attributed to various types of organic components, such as conchiolin and porphyrin, and their intensity clearly increased with the color tone (W. Wang et al., "Identification of 'chocolate pearls' treated by Ballerina Pearl Co.," Winter 2006 *G&G*, pp. 222–235). These could exclude the possibility of irradiation treatment and other staining treatments.

Under long-wave ultraviolet radiation, both parts exhibited purplish blue fluorescence. However, the gray part exhibited significantly more intense fluorescence than the black part. The 3D fluorescence spectra confirmed this. The strongest fluorescence in the black part was at 336 nm (figure 25, left), while the strongest in the gray part was at 340 nm (figure 25, right). The fluorescence intensity between the two differed by more than 2.5 times. The gray part still had weak fluorescence centers at 432 nm, while the black part did not.

Although the study showed that the pearl's fluorescence may be attributable to the organic compounds contained within the nacreous layers (J. Hiramatsu et al., "Non-destructive assessment of the effects of heat and sunlight on akoya pearl quality," *Seibutsu Kogaku*, Vol. 88, No. 8, 2010, pp. 378–383), the cause of the different fluorescence characteristics is unknown.

The X-ray computed microtomography (μ-CT) scan in figure 26 shows that the outer layer of the two parts was connected by nacre, while the inner layer was composed of voids and organic components. Both parts had a distinct bead nucleus. The organic matter between the bead nucleus and the nacre had a dark gray circular shape. The nacre thickness in both parts was 3–4 mm.

Figure 26. μ-CT scan images of the saltwater bead cultured pearl at different depths.

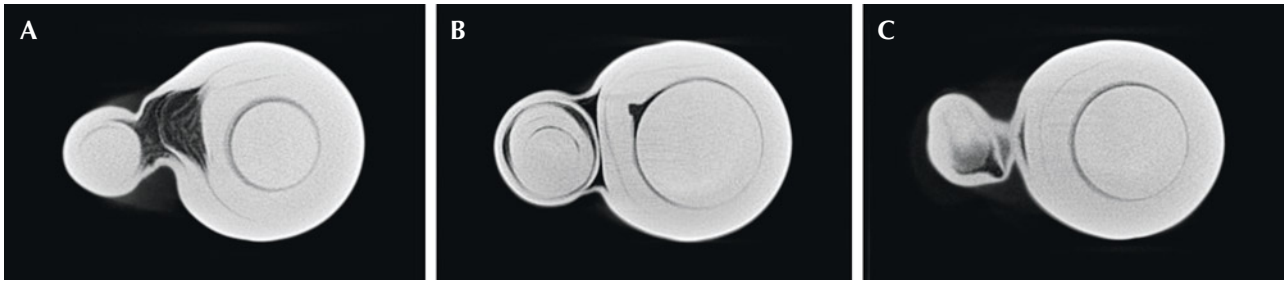

Many mechanisms combine to affect the color of pearls during their growth process (Z. Wang et al., "How cultured pearls acquire their colour," *Aquaculture Research*, Vol. 51, 2020, pp. 3925–3934), making it difficult to pinpoint the exact mechanism. This research can be used to further study the relationship between organic compounds and the color and fluorescence reactions of saltwater pearls, excluding variables such as mollusk type and environmental factors.

Yanhan Wu and Xianyu Liu
College of Jewelry, Shanghai Jian Qiao University
Yanling Yang
Sichuan University

New production of sapphire from Matepwende, Tanzania. In February 2024, Mark Saul (Amor Gems, Kenya) informed author VP about a sapphire rush near Matepwende village, located in the Namtumbo district in Songea, in southern Tanzania. News of a rush involving several thousand migrant miners from all around the country was soon publicized on Tanzanian television.

The following month in Bangkok, VP acquired a parcel of "F-type" reference samples (according to the GIA classification system) (W. Vertriest et al., "Field gemology: Building a research collection and understanding the development of gem deposits," Winter 2019 *G&G*, pp. 490–511; V. Pardieu, "Field gemology, the evolution of data collection," *InColor*, No. 46, 2020, pp. 100–106) reportedly from the new deposit for preliminary study (figure 27). Some were used for a heat treatment experiment in Thailand, and 27 others were sent to author AP for gemological study.

While samples were being studied at GIA, VP visited the new deposit in early June 2024 with geologists Leonard Cornuz and Yedidia Mgema. The site is in a remote area about five hours' drive from Songea using dirt roads during the dry season. It is 7 km north of the Ruvuma River bordering Mozambique. Geologically, it lies at the boundary between the Luwegu sedimentary sub-basin (part of the Selous basin) and the metamorphic Usagaran Belt. A uranium prospective license covers most of the deposit.

The deposit is a primary hard rock deposit where blue sapphires are associated with feldspar and mica in pegmatites intruding into gneisses (figure 28). Most of the sapphires are inside the pegmatites, while others are found in a mica-rich reaction zone between the pegmatite and the gneiss, indicating a desilicated pegmatite deposit (G. Giuliani et al., "The geology and genesis of gem corundum deposits," in L.A. Groat, Ed., *The Geology of Gem Deposits*, 2007, Mineralogical Association of Canada Short Course Series). Most of the mining activity occurred in the nearby detrital deposit over and near the pegmatites and in the limited secondary deposits along streams. The site of the rush covered approximately 1 square kilometer. About 400 artisanal miners (mostly from the Songea or Tunduru) were in the area during VP's visit, down from 1,000 a few weeks earlier at the height of the rush. About half were directly involved in mining, while the others were buying gems or providing supplies to the miners.

Figure 27. Blue sapphires from the Matepwende area in southern Tanzania. Most of the production consists of low-clarity material in matrix. Only a very small percentage (usually weighing less than 1 ct) is clean enough to be faceted. Photo by Vincent Pardieu.

The best facet-grade, fine-color sapphire seen during the expedition was a deep blue stone weighing about 2 ct, while the other fine stones were under 1 ct. We also saw kilos of heavily fractured and twinned corundum specimens up to 500 g, locally called "cabochons," that are broken to extract fragments of blue facetable material to be used for calibrated stones (figure 29). Most of these stones were industrial-, carving-, or bead-grade. According to locals, the deposit has been a known source of this material for more than 30 years. While some of the stones have an attractive blue coloration, most have a grayish overtone. Regarding clarity, most stones exhibit polysynthetic twinning and fractures, and more than half are also milky/silky. A heat treatment experiment under reducing conditions was conducted in Thailand by Karim Guer-

Figure 28. A: Large grayish blue sapphire crystals (about 5 cm) in white feldspar. B: Geologists check a sapphire-rich pegmatite in an artisanal mining excavation near Matepwende. C: A small deep blue facet-grade sapphire fragment within a heavily fractured sapphire crystal associated with (whitish) feldspar and (dark) mica. Photos by Vincent Pardieu.

chouche from Premacut Ltd. The stones did not improve with heat treatment.

Author AP used 12 sapphires from the deposit for a preliminary study, splitting the material into two groups

Figure 29. Left: Two miners with kilos of sapphire rough. Right: The result of their work after breaking the heavily fractured sapphires into attractive parcels of small sapphire. Photos by Vincent Pardieu.

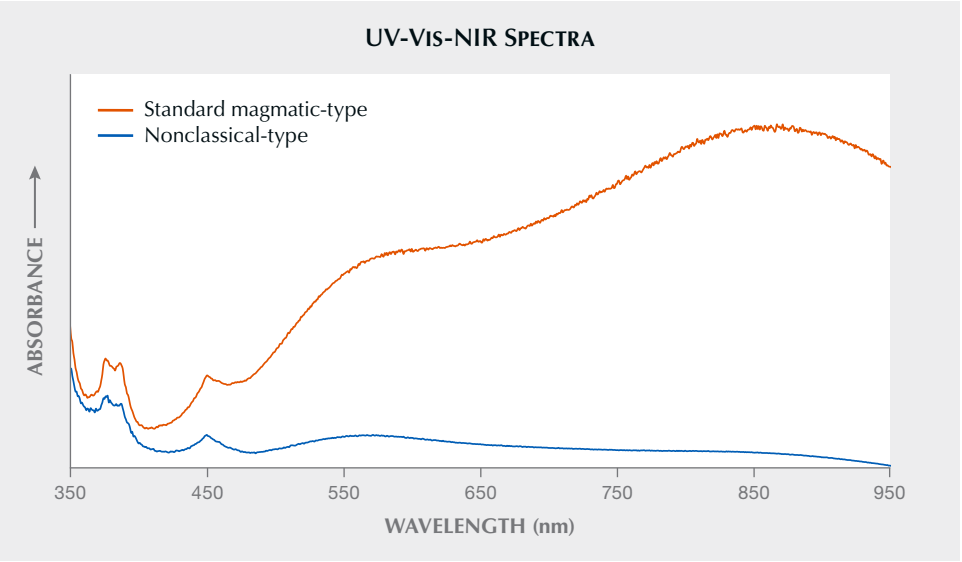

Figure 30. Representative UV-Vis-NIR spectra of Matepwende sapphire. Half of the samples showed a standard magmatic-type UV-Vis-NIR spectrum with a prominent 880 nm band and Fe^{3+}-related features, while the other half showed a nonclassical spectrum without a prominent 880 nm band but with prominent Fe^{3+}-related features.

based on their ultraviolet/visible/near-infrared (UV-Vis-NIR) spectra (figure 30). One group of six samples had UV-Vis-NIR spectra more typically seen in basalt-related sapphires, such as those from Australia or Thailand, with a prominent broad band absorption at 880 nm and significant Fe^{3+}-related features at 377, 388, and 450 nm. These are often called "magmatic-type" or "CMG" sapphires. The other group of six samples lacked the prominent 880 nm band but still had significant Fe^{3+}-related features. These are often called "nonclassical" (NCL) sapphires, and they include sapphires from Montana in the United States and both Umba and Songea in Tanzania.

The inclusion characteristics were different between these groups. The CMG-type sapphire from Matepwende generally displayed platelet-type inclusions and reflective silk that appeared white under strong fiber-optic light (figure 31). Twinning was also common in this group. The NCL-type sapphire from Matepwende, on the other hand, had reflective silk, sometimes in linear bands or stringer-type inclusions that appeared brassy or yellow with reflected fiber-optic light (figure 32). In these NCL-type Matepwende sapphires, the silk also took on a grayish cast with transmitted brightfield light.

Despite these differences, the trace element chemistry of both groups was very similar and matched more closely with that expected of basalt-related blue sapphire, with relatively low magnesium and elevated iron and gallium (table 1). Fourier-transform infrared (FTIR) spectra for both groups were also very similar. All the sapphires had a prominent 3309 cm^{-1} peak and a pair of peaks at 3394 and 3379 cm^{-1}. A few samples showed the presence of boehmite in FTIR as well. The difference in UV-Vis-NIR spectra between these two groups was unexpected, given that they were reportedly from the same deposit. The authors had never witnessed such a case, where a single geographical locality produced sapphires displaying two distinct types of UV-Vis-

Figure 31. Platelet-type inclusions (left) and reflective silk (right) in the Matepwende sapphires with a magmatic-type UV-Vis-NIR spectrum. Photomicrographs by Aaron Palke; fields of view 1.58 mm (left) and 1.26 mm (right).

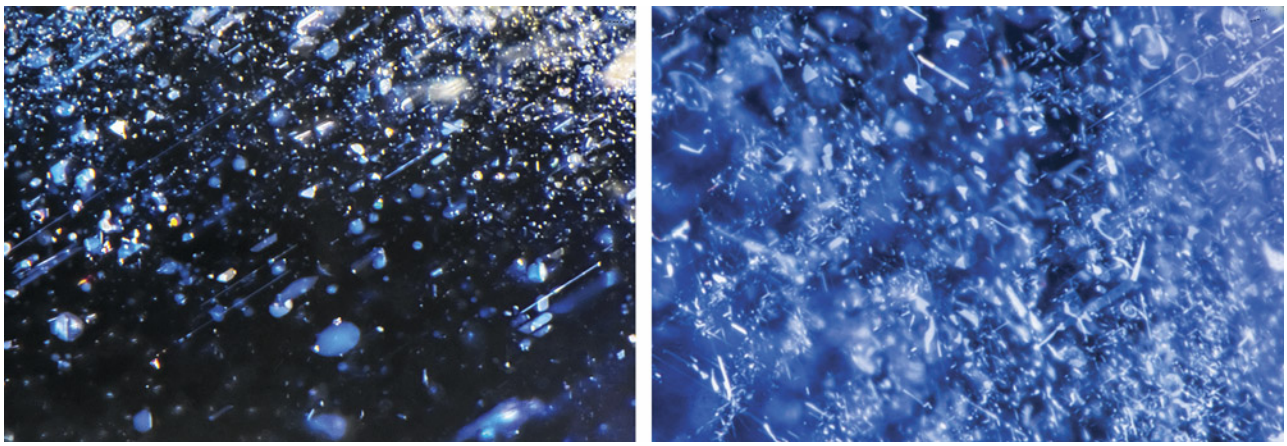

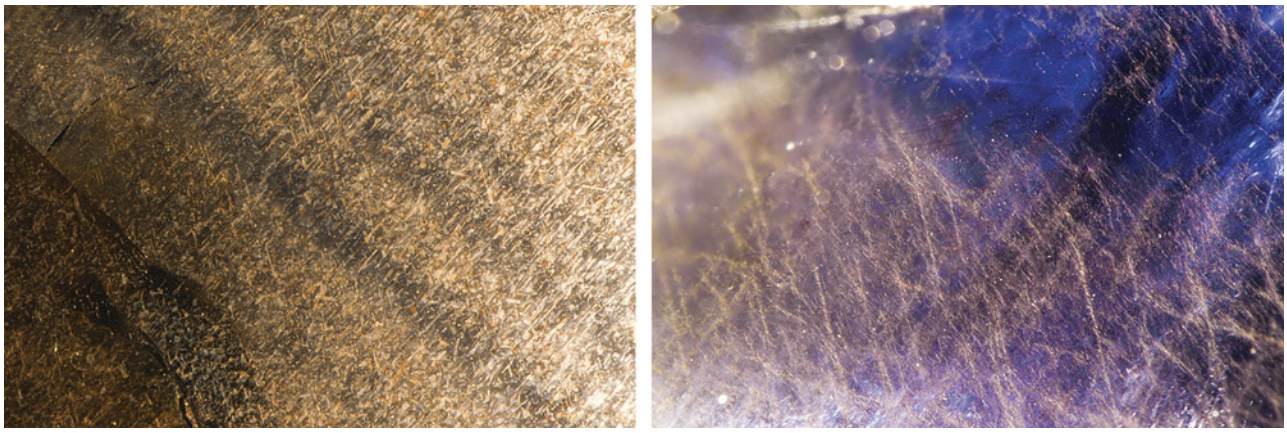

Figure 32. Bronzy reflective silk in dense linear bands (left) and as stringers (right) in the Matepwende sapphires with a nonclassical-type UV-Vis-NIR spectrum. Photomicrographs by Aaron Palke; fields of view 1.99 mm (left) and 2.90 mm (right).

NIR spectra. However, the similarity in trace element chemistry and FTIR spectra suggests a genetic link between these two groups of sapphire from Matepwende. Based on observations during the visit to the deposit, one possible explanation is that the CMG sapphires could have formed inside the pegmatite, while the NCL samples could have formed inside the reaction zone. A study of the material collected at the mine from the pegmatites and reaction zones could help to confirm this hypothesis.

Aaron Palke
GIA, Carlsbad

Vincent Pardieu
VP Consulting WLL, Bahrain

DIAMONDS

Master diamond cutter Harvey Lieberman. For half a century, Harvey Lieberman has perfected the subtle art of cutting colored diamonds and bringing out their vivid hues and tones. Lieberman, nearing retirement, has sat at the same cutting bench (formerly his father's bench) for 35 years in the renowned William Goldberg diamond cutting factory (figure 33). Goldberg (1925–2003) was a legend in his own right, often hailed as the father of New York's Diamond District.

Lieberman is part of an elite community at the Goldberg cutting factory. Any given week might find Mutty Bornstein, Willy Lopez, Shmiel Wurzberger, or Eliezer Gottlieb at work. Each is a master cutter of both colorless and colored diamonds. Their camaraderie and shared passion for the craft make the factory a thriving hub of expertise and collaboration.

Lieberman graduated from Queens College in New York with a theater arts degree in 1974. He planned to wait tables, audition, and chase that big break. (Lieberman still does some occasional acting in off-Broadway productions.) But his father, being practical, told him, "Let me at least

TABLE 1. Trace element concentrations (in ppma) of Matepwende sapphires, measured by LA-ICP-MS.

	Mg	Ti	V	Cr	Fe	Ga
Sapphire with magmatic UV-Vis-NIR spectra						
Range	0.24–8.64	1.6–9.5	0.3–1.7	0–9.33	1190–1588	26.8–35.7
Average	2.02	5.57	0.88	3.80	1321.78	32.52
Median	0.57	4.90	0.82	2.75	1272.50	33.05
Sapphire with nonclassical UV-Vis-NIR spectra						
Range	0.51–2.62	5–25	0.69–2.93	0.49–4.12	1103–1603	27.8–50.3
Average	1.11	10.39	1.43	1.55	1366.33	35.37
Median	0.60	7.90	0.75	0.85	1397.00	29.65
Detection limit (ppma)	0.01	0.03	0.002	0.04	0.59	0.001

Figure 33. Harvey Lieberman at the diamond cutting bench where he has worked for the past 35 years—the same bench his father used before him. Photo by Pedro Padua.

teach you a trade." And with that, Lieberman apprenticed with his father, a master cutter on West 47th Street, learning the intricacies of cutting colorless diamonds.

His introduction to the craft at age 24 was cutting macles (twinned diamonds). Lieberman struggled with these uncooperative diamonds, whose crystal structures are knotted, watching as they ruined one cutting wheel after another. It was difficult, frustrating work. After nearly a year, he quit. He spent the next two years traveling, trying to sell gold and diamonds to jewelers, but it was not his calling. After two years of false starts, Lieberman returned to his father's side, ready to give diamond cutting another shot. This time, though, he was armed with a better attitude and much more patience.

When his father became the foreman at Goldberg's cutting factory, he brought Harvey along. The senior Lieberman did more than just cut and polish; he traveled to London, granted the rare privilege of attending De Beers sights. These were exclusive events where only a handful of companies could purchase rough diamonds directly from De Beers. Harvey joined him and had a front-row seat to the inner workings of the diamond industry, from the raw power of uncut gems to the dazzling brilliance of a perfectly cut stone. This became his world.

Everything changed when Lieberman first laid eyes on colored diamonds brought to him by his uncle, who had worked with the renowned Stanley Doppelt and Louis Glick. Doppelt and Glick would take in the yellow rough, painstakingly cutting it into smaller pieces to downplay the color. But his uncle had a different vision. He began cutting to maximize the color, pioneering a new market for vibrant yellow diamonds. This was Lieberman's introduction to the magic of amplifying color through cutting.

Initially it was trial and error, and each stone was a new test—especially regarding the delicate pinks. One prominent dealer who sourced pink diamonds from Argyle would bring them to Lieberman to bring out the color. With that, Lieberman embarked on a journey to unlock the full potential of colored diamonds. Improving the color grade from intense to vivid became a goal. One time, Lieberman received an Argyle 2.14 ct Fancy Deep pink. After cutting it, he ended up with a stone just under 2 carats that had transformed into a pure red. The value improved nearly tenfold.

Lieberman worked under his father for a while and then for Louis Glick, who sent him to a De Beers sight and tenders in Africa (where non–De Beers mines sell rough diamonds, some in remote armed compounds). He was then assigned to start a factory in Africa. After a few years, he brought his family back to the U.S. and rejoined Goldberg, who had kept the same bench for Harvey after his father passed away.

Lieberman has since worked with blues (figure 34 and figure 35, left), pinks (figure 35, right), reds, greens, and others. He has made color grades go from light to intense, all by changing how the diamond is cut. In the world of diamonds, color is everything. And improving that color is an art form few have mastered. Lieberman is one of the

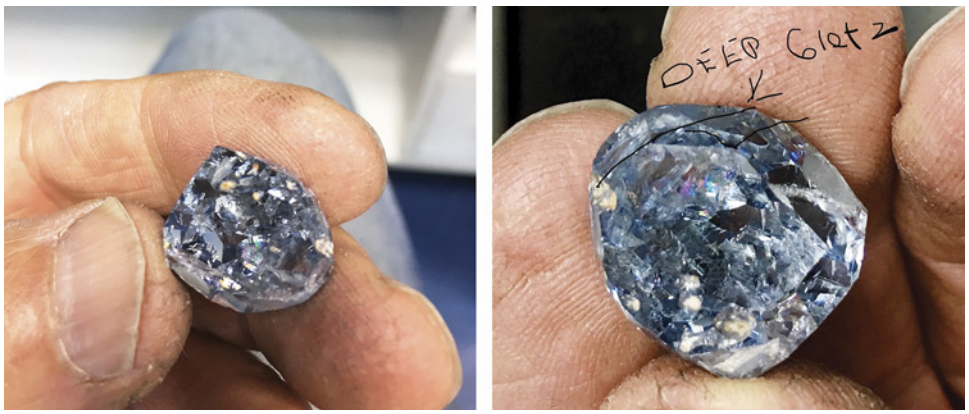

Figure 34. Lieberman examines a 40 ct rough blue diamond that yielded a 15 ct heart. The lines on the right photo indicate where the stone might be sawn. Photos courtesy of Harvey Lieberman.

Figure 35. Left: The 15 ct vivid blue heart-shaped diamond cut from the rough shown in figure 34. Right: A 9 ct vivid pink and a 5.5 ct deep pink cut by Lieberman. Photos courtesy of Harvey Lieberman.

select few. With years of experience, he has transformed diamonds of all kinds, bringing out their hidden beauty. But sometimes, he looks at a diamond and has to tell the owner it cannot be improved. That candor makes his expertise especially valuable.

The works of Lieberman and his Goldberg factory collaborators have graced the halls of the Smithsonian (including the 5.1 ct Moussaieff Red diamond) and been highlighted at numerous auctions. One was a 1.92 ct Fancy red radiant cut diamond with VS_2 clarity, the second most expensive red per carat at the time, sold at a Phillips New York auction. The Pumpkin diamond, a 5.54 ct Fancy Vivid orange cushion cut, was bought by Harry Winston at a Sotheby's auction. These are just a few of their masterpieces.

This interview with Harvey Lieberman was captured on video as part of GIA's Oral History Project to be used by future historians. To see more, go to www.gia.edu/gems-gemology/fall-2024-gemnews-harvey-lieberman.

Al Gilbertson
GIA, Carlsbad

"Out of the Darkness"…and into the light of diamond fluorescence. GIA's Carlsbad laboratory recently had the opportunity to examine "Out of the Darkness," a diamond art piece created in 2021 by South African artist Johnathan Schultz (figure 36). This unique design hosting 9,225 diamonds, totaling just over 895 carats, is laid out as a reproduction of Nelson Mandela's fingerprint (figure 37). The representation measures approximately 20 × 15 in. (51 × 38 cm). Schultz incorporated gold and diamonds in the piece as an homage to some of his home country's most valuable resources. According to the artist, all of the diamonds are round brilliants with G–H color and VS or better clarity. Each was mounted in a white gold martini setting with the posts removed. The mounted diamonds were then soldered together to produce the ebbs and flows of the individual lines in the fingerprint. Using a few carefully selected posts that were left in place, the strands were attached to clear acrylic in just the right pattern to replicate one of Mandela's fingerprints preserved from his 1962 arrest.

Figure 36. Artist Johnathan Schultz working on "Out of the Darkness," a reproduction of Nelson Mandela's fingerprint with more than 9,200 diamonds set in white gold. Photo by Michael Craigwood; courtesy of Johnathan Schultz.

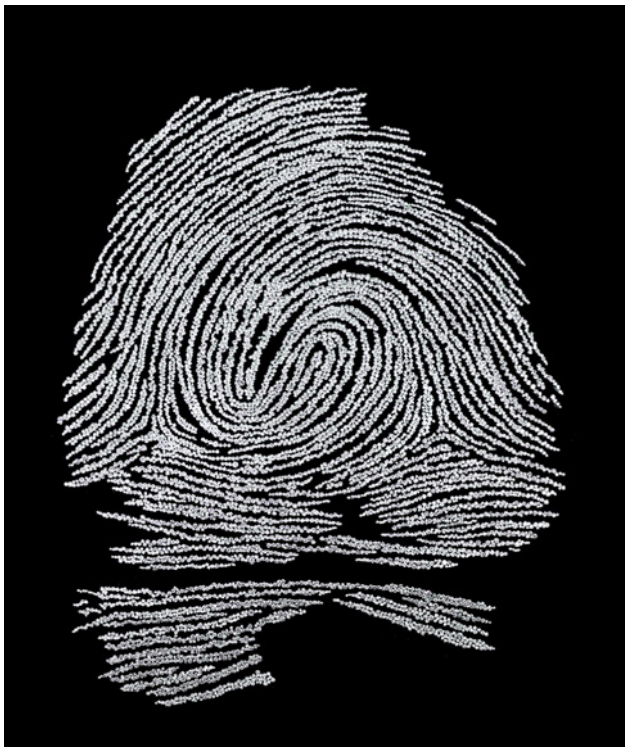

Figure 37. Johnathan Schultz's "Out of the Darkness" contains 9,225 diamonds laid out in an artistic representation of Nelson Mandela's fingerprint. The fingerprint measures approximately 20 × 15 in. (51 × 38 cm). Photo by Rhonda Wilson and Annie Haynes.

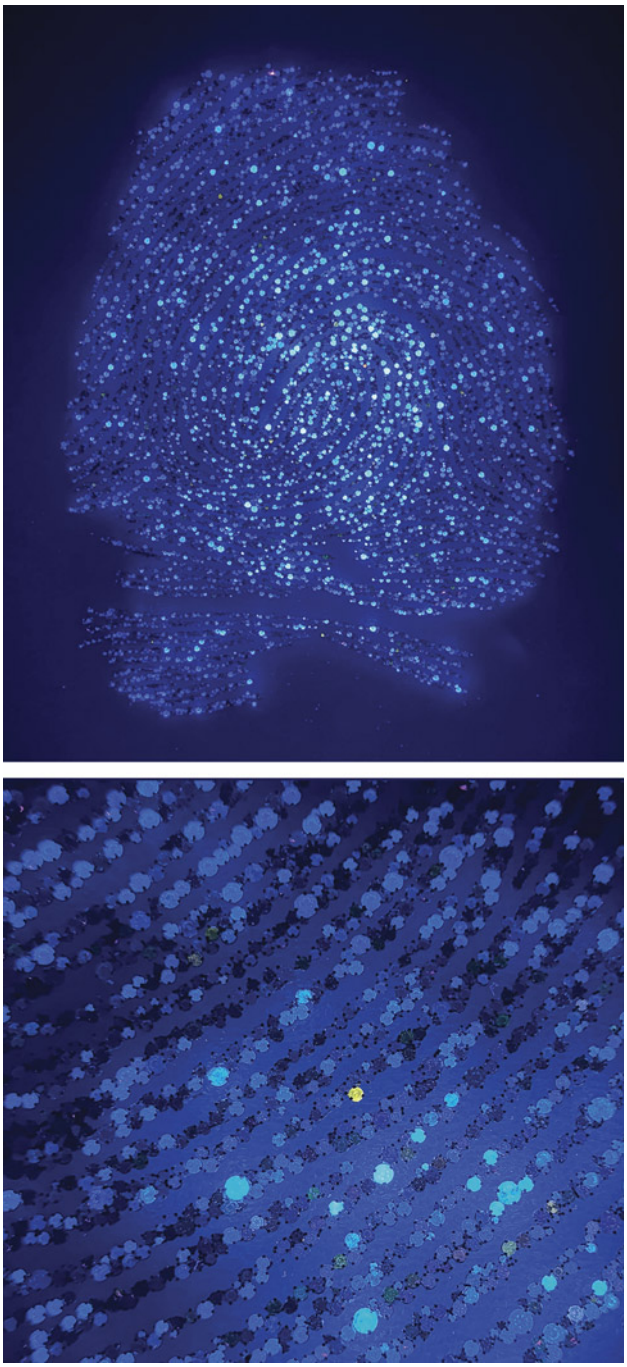

Figure 38. The fluorescence reaction of the diamonds under long-wave UV (365 nm excitation). Photos by Christopher M. Breeding.

While the work itself is extraordinary and among the largest diamond art pieces ever made, it also provided GIA with an excellent opportunity to employ testing and instrumentation in rare and challenging ways. Testing small mounted diamonds to determine if they are natural or laboratory-grown is never easy, but when attached in such large numbers in a fragile and valuable art piece, the challenge is magnified. Using the flexible instrument probe of the GIA iD100, the subset of diamonds examined were identified as natural. The iD100 uses the fluorescence properties of natural diamonds to accurately and conclusively determine their natural origin.

During testing, Schultz was introduced to a different aspect of his art: the beauty of diamond fluorescence. A handheld long-wave LED ultraviolet light revealed the array of color hidden in the fingerprint produced by the fluorescence of the diamonds (figure 38). While mostly blue due to nitrogen atoms in the diamond structure, the diamonds' fluorescence colors also included some yellow, orange, pink, whitish, and greenish glowing hues. The combination made for a spectacular, almost night-sky appearance that seemed to inspire creative ideas for his next endeavor with diamonds.

Using innovative technology and expertise, we were able to not only identify the nature of the diamonds in this art piece but also offer the artist a new perspective, showing that the beauty of diamond is further enhanced by the science of diamond.

Christopher M. Breeding
GIA, Carlsbad

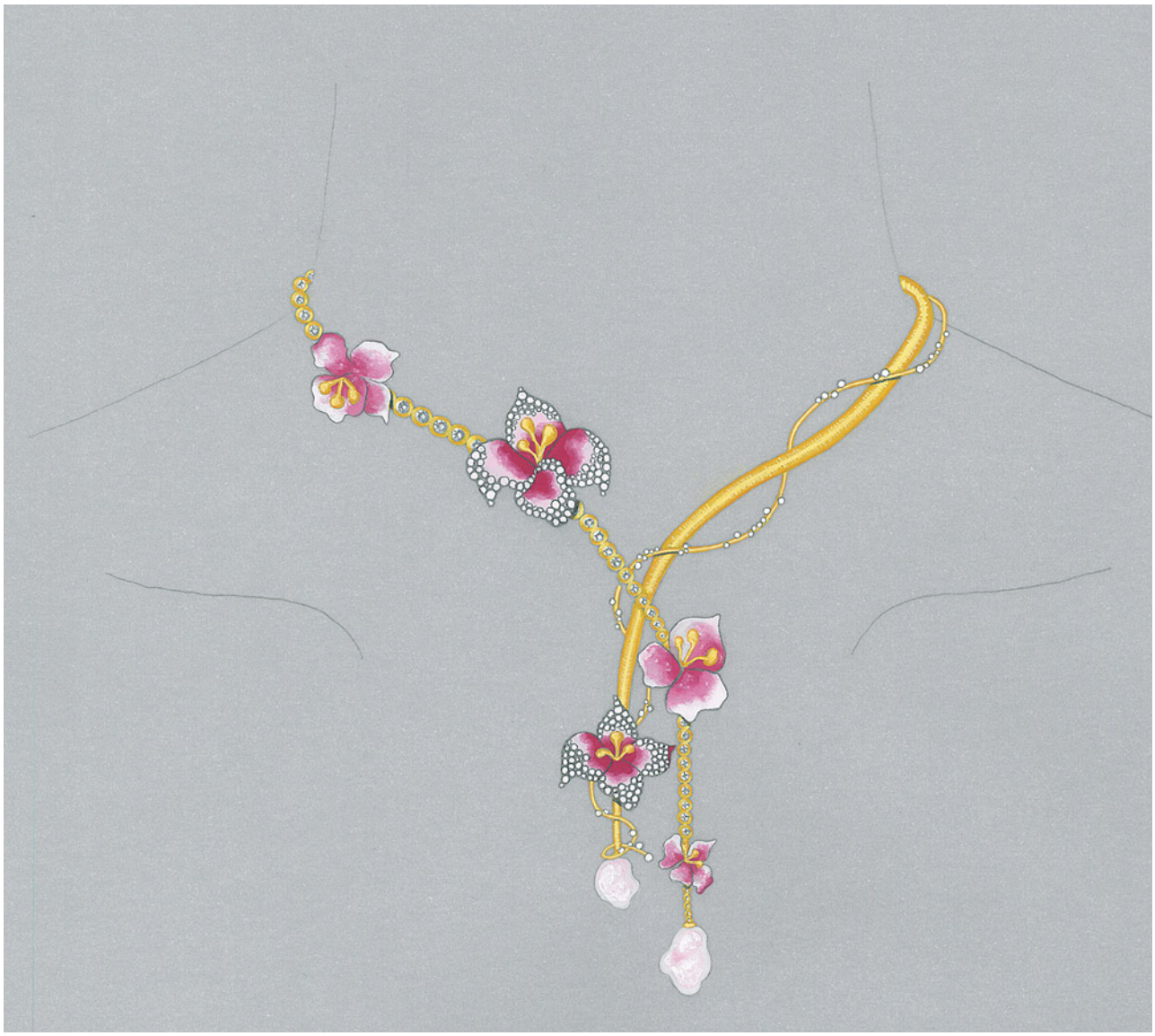

Figure 39. Srushti Shah's design sketch for a necklace featuring 18K yellow gold, baroque pearls, diamonds, light pink garnets, and colored glass enamel.

JEWELRY DESIGN

GIA student design showcase. One of GIA's "student choice" awards was recently presented to Srushti Shah, a graduate of the Jewelry Design program at the London campus. Shah's design combines 18K yellow gold, baroque pearls, diamonds, light pink garnets, and colored glass enamel to create a vine of cherry blossoms draped around the neck (figure 39). Shah noted, "This necklace design draws on the symbolism of cherry blossoms, embodying the cycle of life and generational connections. The five cherry blossoms on the necklace represent significant milestones in the journey of life, inspired by Antoine de Saint-Exupéry's *The Little Prince*. Diamonds reflect the wonder of childhood. The gold vines capture the exploration and learning that shape our growth. Freshwater pearls, symbols of wisdom gained through life's experiences, represent love and relationships. Enamel brings the blooms to life, echoing resilience in facing life's challenges. Baby pink garnets in the flowers evoke the gentle hues of spring, celebrating reflection and legacy."

SYNTHETICS AND SIMULANTS

"Cotton pearl" imitations. For centuries, pearls have been one of the most imitated gems. Traditionally created by coating spherical glass beads with pearlescent paint, these

Figure 40. Left: A variety of cotton pearls imitating akoya, golden South Sea, and Tahitian pearls. Right: A necklace featuring pistachio-colored cotton pearls. Photos by Annie Haynes.

imitations were designed to resemble the color, luster, and heft of genuine pearls. This continued with the advent of plastic beads and, more recently, coated shell beads (Summer 2014 Lab Notes, pp. 153–154). A new simulant has since been gaining popularity in the fashion jewelry market: "cotton pearls" (figure 40).

Cotton pearls are available in a variety of colors and sizes, allowing them to imitate nearly every pearl species. These beads are created from cotton fibers or other fibrous textile materials that are tightly packed and concentrically layered. Their internal structure can be revealed by real-time X-ray microradiography (RTX), as shown in figure 41. The image displays concentric bands composed of fine fibers as well as a bright white edge representing the higher-density coating on the bead's exterior. The star-shaped "drill hole" is likely a remnant of the manufacturing process rather than an actual drill hole. It is possibly in the shape of the spindle on which the fibers are rotated, creating concentric layering. To examine the interior, a bead was cut in half perpendicular to the "drill hole." This

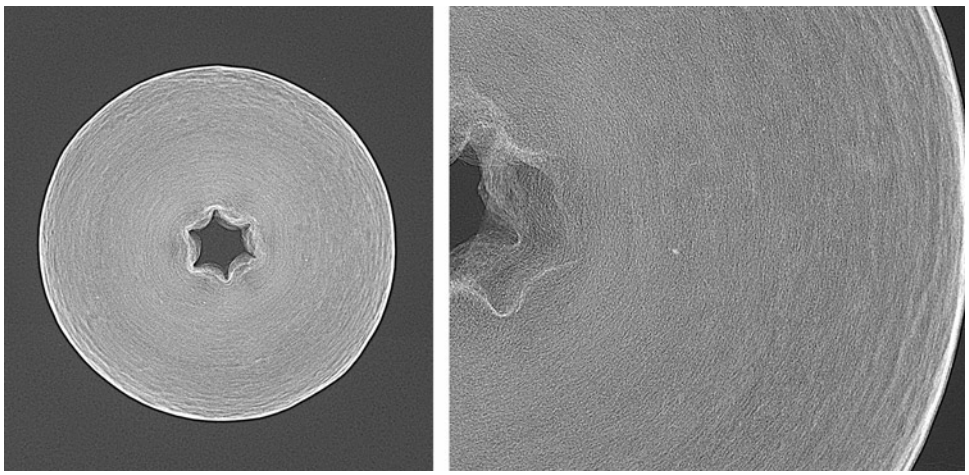

Figure 41. Left: RTX image of a cotton pearl featuring a star-shaped center hole, likely a manufacturing remnant. Fine concentric banding can be seen along with a bright white outer edge representing the higher-density surface coating. Right: A closer view of the bead reveals a fine fibrous texture.

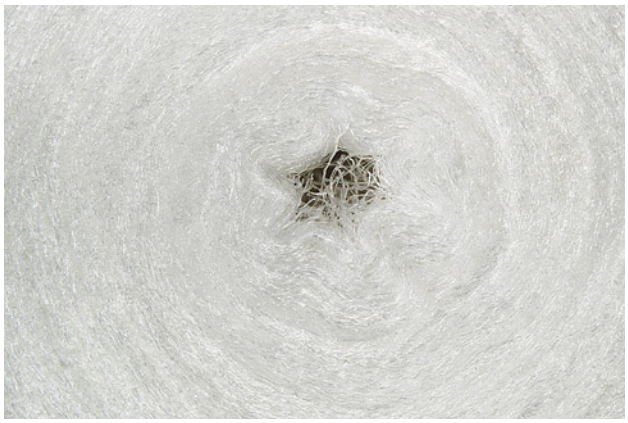

Figure 42. A cross section of a cotton pearl viewed perpendicular to the "drill hole." Fine white fibers with a concentric layered structure were observed throughout the interior, resembling what was seen in the RTX image. Photomicrograph by Britni LeCroy; field of view 7.19 mm.

exposed tightly packed white fibers throughout with faint concentric layering (figure 42), consistent with observations from the RTX images.

Cotton pearls are lightweight and comfortable to wear, particularly compared to glass or shell imitations of large pearls such as South Sea or Tahitian. They are also surprisingly strong and did not deform when pressed firmly between the fingers. Additionally, the textured surface of cotton pearls gives them a convincing visual impression.

If imitation is the sincerest form of flattery, then pearls certainly continue to inspire admiration and innovation.

Britni LeCroy
GIA, Carlsbad

Pearls marketed as "Venezuelan pearls." The term "Venezuelan pearls" is applied to natural saltwater pearls harvested from the *Pinctada imbricata* mollusk, also known as the Atlantic pearl oyster. They are found primarily in the western Atlantic, from Bermuda and Florida to northern South America. The mollusk size ranges from 5 to 7 cm and produces pearls ranging from less than 2 mm (seed pearls) up to 9 mm (*CIBJO Pearl Guide*, 2022). Some traders claim that many pearls sold as "Venezuelan pearls" in the world markets today, mainly India and the Middle East, are sometimes mixed with pearls from other *Pinctada* species (typically lower- to medium-quality *Pinctada maxima* pearls). Others claim that actual pearls from Venezuela are also sold as "Basra pearls," which are sourced from *Pinctada radiata* and are highly valued in India and the Middle East due to their appearance and luster.

GIA's Mumbai laboratory studied a parcel of 988 reportedly "Venezuelan pearls" from one of the main suppliers of this material (figure 43). The internal structures were examined with real-time X-ray microradiography (RTX),

Figure 43. A lot of pearls sold as "Venezuelan pearls," ranging from 2.05 × 1.88 mm to 6.87 × 5.23 × 4.23 mm. Photo by Gaurav Bera.

and 97 samples were selected for further study. The majority of the button-shaped and semi-baroque pearls were white to light cream and cream in color, and most exhibited strong orient. Their weight ranged from 0.05 to 1.06 ct, with sizes from 2.05 × 1.88 mm to 6.87 × 5.23 × 4.23 mm. Most of the samples exhibited a good luster with a smooth surface, and a few revealed minor surface blemishes. Under high magnification, the samples showed various patterns of overlapping aragonite platelets on the surface, which are typically observed in nacreous pearls.

Energy-dispersive X-ray fluorescence on the 97 selected samples revealed low manganese levels ranging from below detection limit to 29 ppm, with a few ranging from 32.5 to 69.8 ppm. Higher strontium levels were also observed, from 1177 to 2988 ppm, with a few samples ranging from 3056 to 3437 ppm. When exposed to X-ray fluorescence, most of the samples showed an inert reaction, while a few exhibited an extremely faint yellowish green reaction. Under long-wave ultraviolet radiation, all the pearl samples luminesced various degrees of bluish green.

Raman spectroscopy revealed a doublet at 701/704 cm^{-1} and a peak at 1086 cm^{-1}, with a few pearls showing a weak peak at 1464 cm^{-1} indicative of aragonite. Additionally, the spectra of one light cream and one cream pearl showed weak polyenic pigment peaks at 1135 and 1530 cm^{-1}. These observations were previously documented for pearls from *Pinctada fucata* (akoya) and *Pinctada radiata* (A. Al-Alawi et al., "Saltwater cultured pearls from *Pinctada radiata* in Abu Dhabi (United Arab Emirates)," *Journal of Gemmology*, Vol. 37, No. 2, 2020, pp. 164–179). Due to the pearls' smaller size, ultraviolet/visible/near-infrared spectra were collected for only 54 of them. Some of these displayed weak bands around 320, 395, and 420 nm, while others showed a prominent feature at 460 nm, similar to previously studied samples from *Pinctada imbricata*.

RTX analyses revealed a combination of structures that were typical of those observed in natural pearls from *Pinctada* species, as shown in figure 44. In this study, around 44% of the pearls revealed faint gray dense cores surrounded by growth arcs and organic-rich gaps at their outer edges. The samples displayed tight and minimal internal growth structures, some with thicker concentric growth arc formations following the shape of the pearl, representing approximately 16% of the group. Additionally, around 13% showed multi-nuclei structures, exhibiting a combination of different types of cores, while a few revealed interesting crystalline structures.

The most challenging to identify were void structures and linear features, which were found in only 6% of the samples. Some of these were long features that, to some extent, mirrored the outline of the pearl. The linear features originated from the tip of the pearls and were surrounded by a few growth arcs. These were similar to the odd linear structures observed in natural pearls from various mollusk species in GIA's research database. A total of 18% of the pearls revealed irregular centrally positioned voids of varying sizes. Voids are frequently observed in saltwater non-bead cultured (NBC) pearls, particularly those from *Pinctada* species. Therefore, it was important to further study these samples using X-ray computed microtomography (μ-CT) imaging, which indicated that many voids were filled with fine, light gray organic-rich matter, unlike the empty voids typically observed in NBC pearls

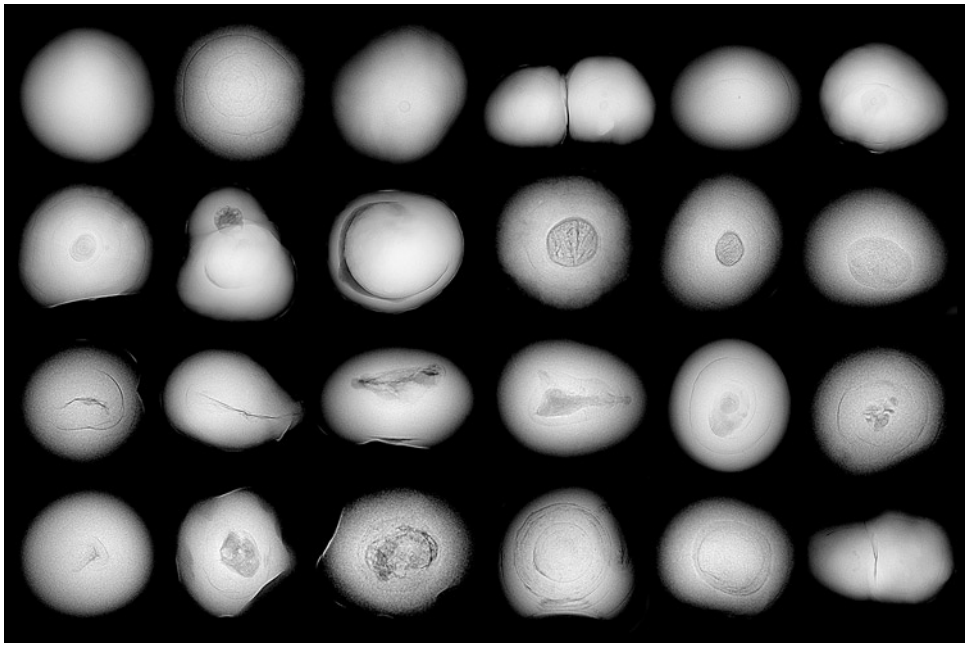

Figure 44. RTX imaging of various structures examined in the lot. The first row displays pearls with growth arcs and small faint cores, the second row shows different cores and crystalline structures, and the third row presents various linear and void features. The bottom row shows voids filled with organic matter, pearls with growth arcs, and faint cores in the multi-nuclei structure.

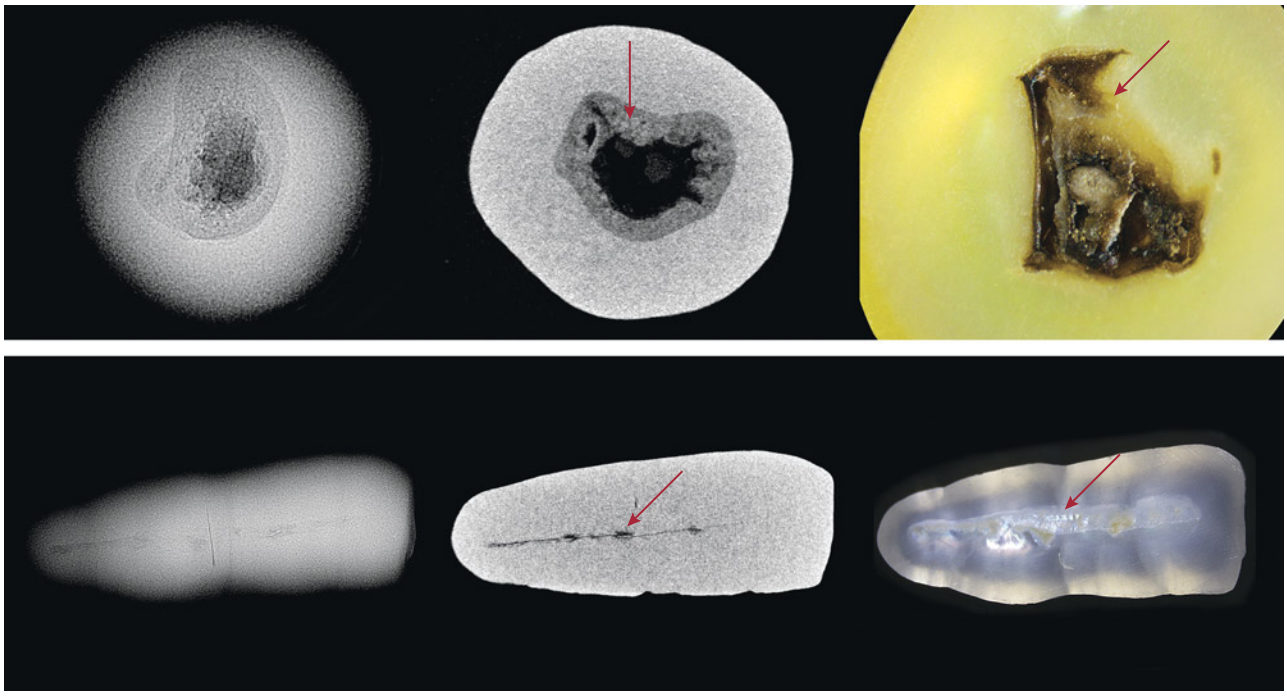

Figure 45. Left to right: RTX images, µ-CT images, and photomicrographs of two cut pearls. Top: Pearl A reveals a complex irregular void feature surrounded by an organic-rich area (arrow). Bottom: Pearl B exhibits an elongated linear structure with a knot-like feature (arrow). Photomicrographs by Karan Rajguru; field of view 1.3 mm and 3 mm, respectively.

(A. Homkrajae et al., "Internal structures of known *Pinctada maxima* pearls: Cultured pearls from operated marine mollusks," Fall 2021 *G&G*, pp. 186–205).

To further study these challenging internal structures, two pearls were ground down. The dark gray void-like area seen in the RTX image of pearl A was composed of a solid organic material that appeared as a light and dark brown area in the cross section (figure 45, top row). Pearl B, which showed an elongated linear structure in the RTX image, had a hollow space with organic-rich pockets (figure 45, bottom row).

Based on comparison with research samples from GIA's database, some of the samples from this lot had internal structures similar to those from *Pinctada imbricata*, but others displayed overlap with structures found in *Pinctada radiata* and *Pinctada maxima*. Although a few samples showed borderline void and linear internal structures, similar to NBC pearls from *Pinctada maxima*, the majority had structures seen in natural pearls from the other *Pinctada* species. These findings suggest that the potential mixing of these pearls, whether intentional or accidental, may be attributed to their remarkably similar external appearance. Consequently, more advanced testing utilizing laser ablation–inductively coupled plasma–mass spectrometry will be necessary to effectively differentiate between the pearls from the different *Pinctada* species mollusks mixed within the studied lot of pearls. Therefore, GIA's ongoing research serves as a valuable resource for identifying pearls from different mollusks.

Karan Rajguru, Abeer Al-Alawi, Gauri Sarvankar, and Roxane Bhot Jain
GIA, Mumbai

CONFERENCE REPORTS

IJK 2024. International Jewellery Kobe (IJK), held at the Kobe International Exhibition Hall every spring, is one of the premier international jewelry trade shows in the Kansai region of western Japan. Since Kobe is known for its pearl industry, pearl dealers exhibited in more than 100 booths out of 441 total. Overall, the show drew nearly 14,000 visitors.

Many vendors exhibited akoya bead cultured pearls, mostly in 6–8 mm sizes. With unusually large akoya bead cultured pearls from 11.0 to 12.2 mm seen at the Tucson show earlier this year (Summer 2024 GNI, pp. 255–256), the authors searched for similar sizes but only found them as large as 9.0–9.5 mm (figure 46). Some dealers said that 11 mm would be the largest size found at the show.

Meanwhile, small sizes (less than 10 mm) of Tahitian and golden South Sea bead cultured pearls are currently on

Figure 46. A strand of akoya pearls and a pair of earrings ranging in size from 9.02 to 9.49 mm. Photo by Asumi Sanbonmatsu; courtesy of Kuwayama.

the market (figure 47). The smallest Tahitian at the show was 7 mm, and the smallest golden South Sea pearl was 8 mm. The small Tahitian pearls featured various shapes, colors, and overtones, with very good to excellent luster, and some pits and blemishes on the surface (figure 47, left). According to one salesperson, these small Tahitian pearls

Figure 47. Tahitian pearl strands in 7–9 mm size (left) and golden South Sea pearl strands in 8–10 mm size (right). Photos by Moemi Ogawa; courtesy of Tanaka Pearl.

Figure 48. A conch pearl necklace offered at IJK. Photo by Asumi Sanbonmatsu; courtesy of Fiore Y.A.C.

were from the Philippines. He noted that pearl farmers are producing small Tahitian and golden South Sea pearls due to an unprecedented increase in demand. However, high-quality small pearls are still rare. On the other hand, very few South Sea white pearls were found below 10 mm in diameter, which might suggest a low demand due to the availability of akoya.

One vendor offered uniquely designed conch pearl jewelry (figure 48). These conch pearls had typical porcelaneous structures such as granulate, silk, and the highly prized flame structure.

The next IJK show will be held May 15–17, 2025.

Moemi Ogawa and Asumi Sanbonmatsu
GIA, Tokyo

Splendors from the Deep: Historic Treasures from a Spanish Shipwreck

Aaron C. Palke, Sona Tajiryan, Mel King, and Emily Lane

Each summer, when the waters off Florida's east coast are calm enough for shallow diving, treasure hunters from 1715 Fleet Queens Jewels explore the seafloor for artifacts lost in a Spanish shipwreck from 1715. The company is licensed to operate in an offshore area between the towns of Sebastian Inlet and Fort Pierce, where they mostly recover gold and silver coins and nuggets but have also unearthed jewelry adorned with precious gems (figure 1). GIA's Carlsbad laboratory recently had the opportunity to study six pieces of jewelry recovered by the team, providing a glimpse into the treasures and skilled craftsmanship of colonial Spain.

History

Christopher Columbus's four voyages to the New World between 1492 and 1502 sparked the Age of Discovery, a centuries-long period of exploration and colonization. The Spanish Empire, which funded Columbus's journeys, initially sought a westward maritime trade route to Asia. Instead, the exploration led to an unprecedented expansion of trade routes between the Americas, Europe, and Asia, catalyzing globalization. The export of silver, mainly from Bolivia (Potosí) and Mexico, dominated transatlantic trade beginning in the late sixteenth century, with Spanish galleons transporting it—along with gold, gems, pearls, and other commodities—to Europe. While these Spanish treasure fleets supported the empire's finances, they faced the considerable risk of tropical storms and hurricanes on the route to Spain.

One of the most historic and archaeologically significant Spanish fleets was destroyed by a fierce hurricane in the summer of 1715. Anchored at Havana, the 1715 Fleet was a formation of galleons from the Tierra Firme fleet and the New Spain fleet, as well as the French warship *Griffon* (https://1715fleetsociety.com/history). Eleven vessels set sail for Cádiz, Spain, carrying 14 million silver coins, as well as gold and other commodities (Newton, 1976). Three days later, the fleet was devastated by a hurricane; some of the ships sank, while others were driven toward the reefs along the eastern coast of Florida. The *Griffon* was the only ship to survive the disaster and arrive safely at a European port.

Modern salvage efforts begun in the late 1950s yielded a massive amount of Spanish New World silver and gold coins struck by the colonial mints of Potosí, Lima, and Mexico City, among others (Craig, 2000a,b). Loose stones, mainly emeralds, as well as silver and gold jewelry items have also been recovered.

The discovery of emeralds and emerald jewelry during these salvage efforts is not surprising. After conquering Bogotá in 1538, the Spaniards eventually gained control of Colombia's rich emerald deposits. By the mid-1500s, Colombian emeralds, primarily from the famed Muzo mines, were being transported to European and Asian markets, adorning the European royalty and Indian Mughals. The nature of the jewelry recovered from the shipwreck suggests a thriving manufacturing industry in the New World employing expert artisans using locally sourced materials.

Figure 1. Captain Grant Gitschlag holds an amethyst and emerald ring recovered from the 1715 Spanish shipwreck (also shown in figure 3). Photo courtesy of 1715 Fleet Queens Jewels.

Figure 2. This gold and emerald pendant contains 61 Colombian emeralds with 33 stones missing, presumably lost during its residence on the seafloor for more than 300 years. The pendant is approximately 3.5 in. (8.9 cm) wide. Photo by Emily Lane.

Gemstone Treasures

The most stunning example studied was a gold and emerald pendant containing 61 of the original 94 emeralds (figure 2). A second piece, a gold ring set with a Colombian emerald surrounded by two amethysts (figure 3), was also examined. All three stones in the ring were emerald cut with faceting styles common in Colombian emerald of this era, showcasing the color with a simple one-tiered step-cut pattern. The stones in both pieces were fixed in a bezel setting, with metal scraped or pushed over their edges to keep them in place. In some cases, this was evident from gold pushed into small cavities or fractures in the gem (figure 4A). The stones and the surrounding metal showed signs of wear from the slow action of water and sand, with pieces of gold flaked off near the girdle (figure 4, B and C).

Figure 3. An emerald and amethyst gold ring recovered from the shipwreck. Photo by Robert Weldon.

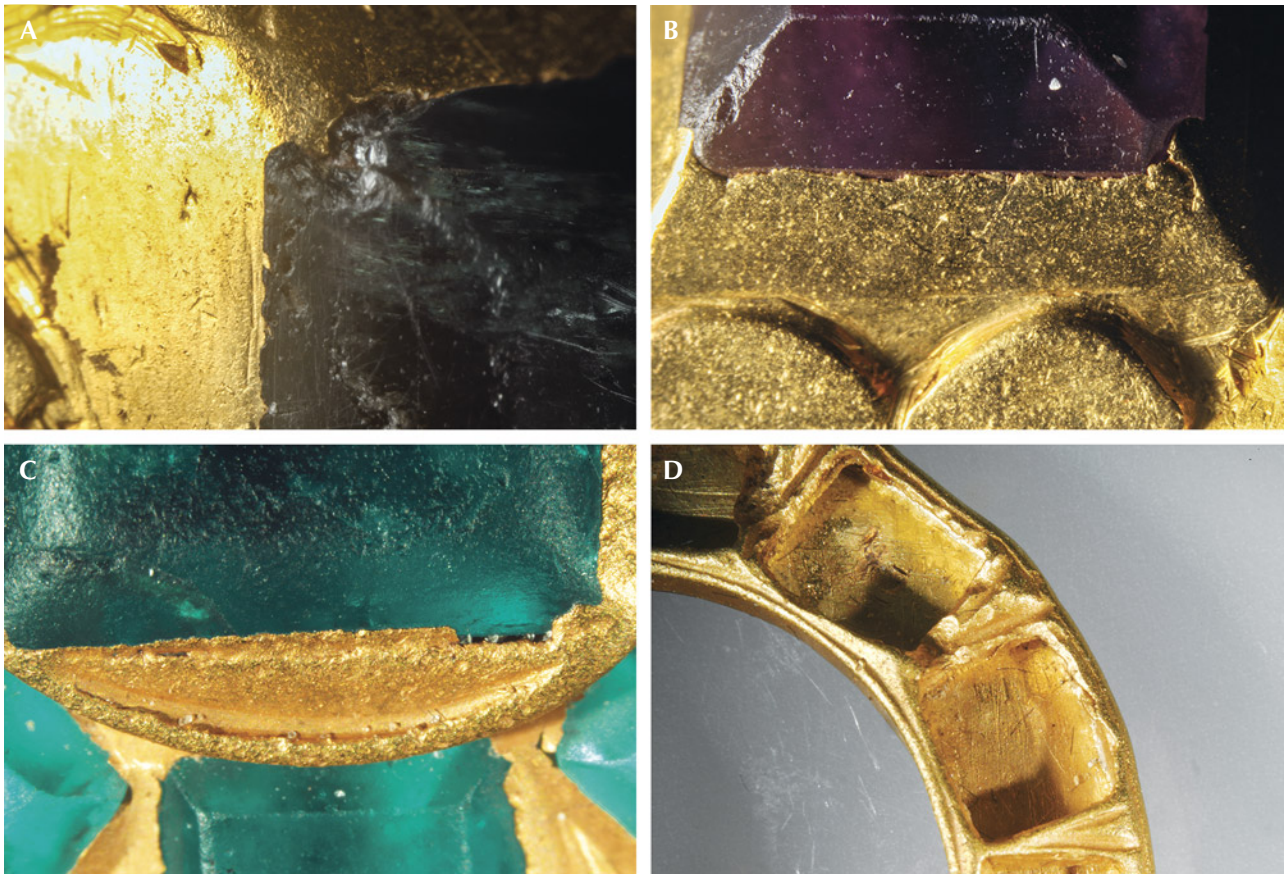

Figure 4. Details of the setting styles in the amethyst and emerald ring (A and B) and the emerald pendant (C and D). Photomicrographs by Aaron Palke; fields of view 4.79 mm (A), 7.19 mm (B), 10.00 mm (C), and 19.27 mm (D).

Figure 5. Inclusions in two emeralds from the pendant shown in figure 2. The jagged three-phase inclusions support a Colombian origin. Photomicrographs by Aaron Palke; fields of view 1.76 mm (left) and 1.99 mm (right).

The identity of the stones was confirmed by Raman spectroscopy and corroborated with ultraviolet/visible (UV-Vis) absorption spectroscopy, X-ray fluorescence (XRF) spectrometry, and microscopic observations. The UV-Vis absorption spectrum of the emerald in the ring showed typical chromium and vanadium absorption features as well as the chromium fluorescence feature at ~685 nm, typical for emerald. XRF measurements of these emeralds' chemistry supported a Colombian origin, given the very low concentrations of iron and potassium. While many of the emeralds had too poor of a polish to allow for inclusion observations, most showed jagged three-phase fluid inclusions, further confirming their Colombian origin (figure 5).

Figure 6. Two gold chains and a plain gold ring from the 1715 shipwreck. Photo by Emily Lane.

Gold and Silver Jewelry

Two gold chains, a gold ring, and silver cloak buttons recovered from the shipwreck were also studied (figures 6 and 7). The larger, thicker chain was assembled by mechanically bending and twisting thick gold wire into itself (figure 8, A and B). The manufacturing process for the small, finer chain was much more complicated, as one end of each link was clearly soldered in place (figure 8C). The careful soldering of the links, allowing for flexibility and movement, showcases the remarkable skill of these early jewelry artisans.

One interesting aspect of the jewelry was its metal composition. Except for the silver cloak buttons, most of the pieces were gold. Testing the metals with XRF gave precise measurements of their composition. The jewelers mainly used a high gold content with nonstandard karatage (typically from 20.1 to 21.5K, but with one 13.2K piece). Copper and silver made

Figure 7. A set of intricately engraved silver cloak buttons. Photo by Emily Lane.

Figure 8. Gold chains showing the style of chain assembly used by jewelry makers in the New World. Photomicrographs by Aaron Palke; fields of view 19.27 mm (A), 19.27 mm (B), and 14.52 mm (C).

up the non-gold components of the alloys. The silver in the cloak buttons was also a nonstandard composition compared to modern jewelry, testing as 942 silver with copper making up the balance. The nonstandard gold and silver compositions likely result from the use of precious metals directly refined from natural sources, closely mirroring their Earth-derived composition.

A Glimpse into the Past

These pieces are just a small sampling of the remarkable treasures recovered from the Spanish galleons of the 1715 Fleet. Salvage efforts are ongoing every summer, and who knows where or when the next bounty will be revealed. Each artifact offers a fascinating glimpse into the craftsmanship, trade, and history of colonial Spain, shedding new light on a bygone era.

REFERENCES

Craig A.K. (2000a) *Spanish Colonial Gold Coins in the Florida Collection*. University Press of Florida, Gainesville.

——— (2000b) *Spanish Colonial Silver Coins in the Florida Collection*. University Press of Florida, Gainesville.

Newton L.W. (1976) Juan Esteban de Ubilla and the Flota of 1715. *The Americas*, Vol. 33, No. 2, pp. 267–281, http://dx.doi.org/10.2307/980786

A Brilliant Future Is Here.

Online Courses from GIA Experts

Start learning from anywhere with self-paced online courses created by the leader in gemological research. Designed for working professionals, GIA® courses on diamonds, colored stones, pearls, and jewelry deliver knowledge you need to advance your career.

Choose Your Sample Lesson

GIA.edu/online-ed

Scenes from 90 Years of *Gems & Gemology*

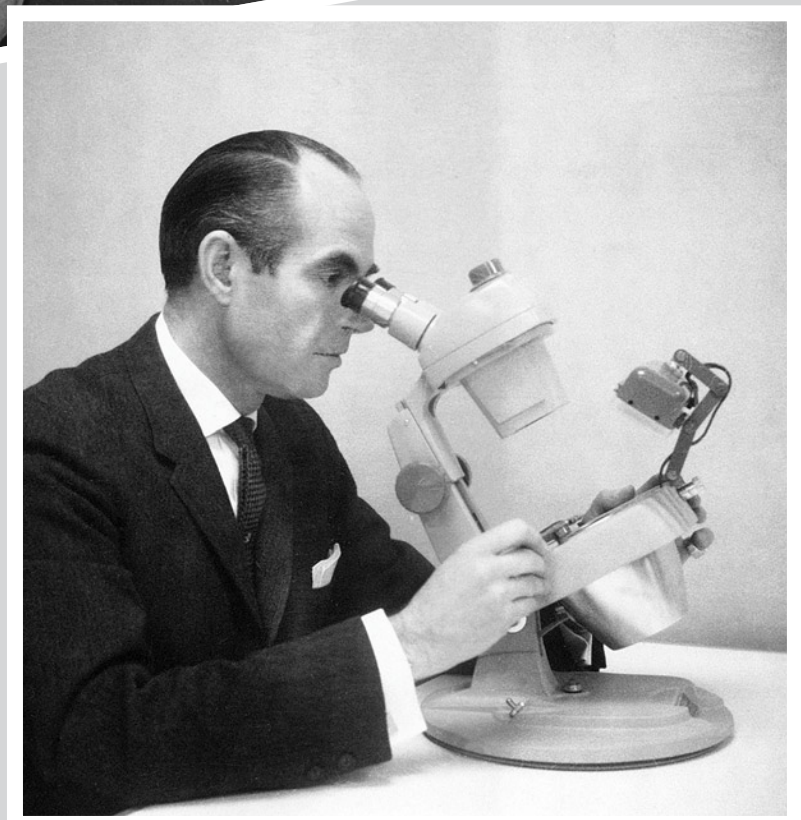

Top: *G&G* founder Robert M. Shipley. Bottom left: Richard T. Liddicoat, editor-in-chief from 1952 to 2002. Bottom right: G. Robert Crowningshield.

Top left: Lester Benson. Top right: Kurt Nassau. Bottom: the *G&G* editorial office in 1949.

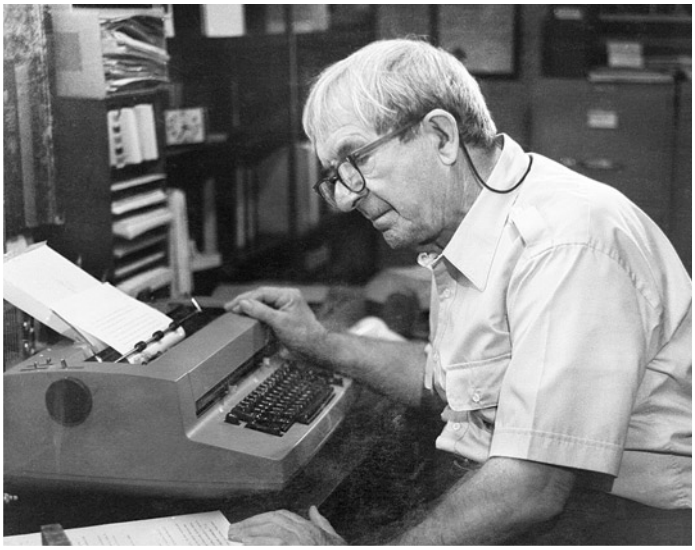

Top left: John Sinkankas. Top right: Alice Keller, Shane McClure, and Martin Cooper. Bottom: Photographers Harold and Erica Van Pelt.

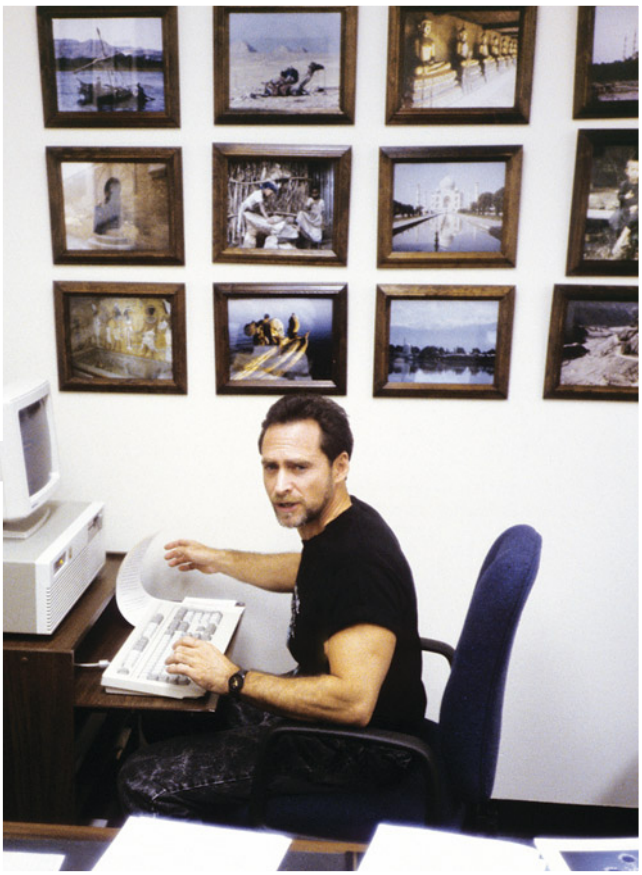

Top left: Bram Janse, Richard T. Liddicoat, and Al Levinson. Top right: Robert Kane and Edward J. Gübelin. Middle left: Emmanuel Fritsch using the FTIR spectrometer. Middle right: Robert Kammerling. Bottom: Dona Dirlam.

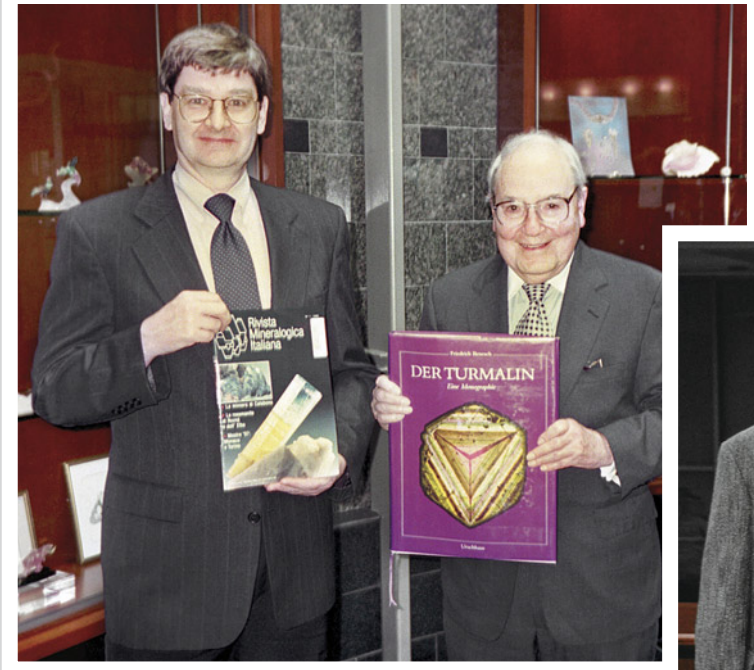

Top left: George Rossman and Richard T. Liddicoat. Top right: Jim Shigley, Shane McClure, and John Koivula. Bottom: Alice Keller, who directed *G&G* from 1981 to 2011.

Top left: Brendan Laurs. Top right: Tom Moses. Middle: Duncan Pay, the journal's editor-in-chief since 2013. Bottom: Robert Weldon.

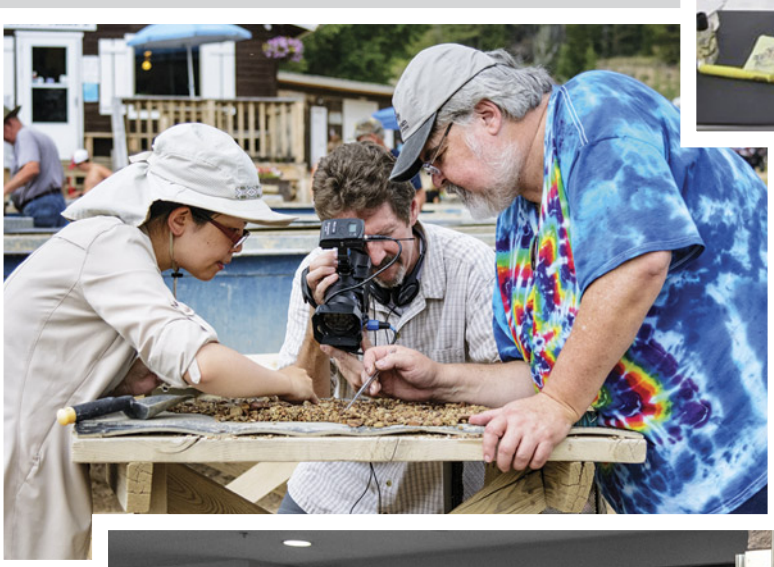

Top left: Chi Huynh and Stuart Overlin. Top right: Faizah Bhatti. Middle: Tao Hsu, Kevin Schumacher, and Shane McClure on location in Montana. Bottom: Stuart Overlin and Brooke Goedert at the Tucson gem show.